Fabrication of Flexible Hybrid Energy Harvester for Powering Low-Powered Devices

A thesis submitted for fulfilment of the degree of

Doctor of Philosophy in Science

To

Department of Physics

Jadavpur University

By

Sourav Maity

Functional Materials and Devices Division

CSIR-Central Glass and Ceramic Research Institute

Jadavpur, Kolkata-700 032, India

2023

CERTIFICATE FROM THE SUPERVISOR

This is to certify that the thesis entitled "***Fabrication of Flexible Hybrid Energy Harvester for Powering Low-Powered Devices***" submitted by Sri. Sourav Maity (Registration no: **SOPHY1103920** and Index no: **39/20/Phys./27**) who got his name registered on 14th October 2020 for the award of Ph.D. (Science) degree of Jadavpur University, is absolutely based upon his own work under the supervision of Dr. Shrabanee Sen, Principal Scientist, Functional Materials and Devices Division, CSIR- Central Glass and Ceramic Research Institute (CGCRI), Kolkata, West Bengal-700032, India and that neither this thesis nor any part of it has been submitted for either any degree/diploma or any other academic award anywhere before.

Shrabanee Sen
12/12/23

Dr. Shrabanee Sen

Principal Scientist
FMDD, CSIR-CGCRI,
Kolkata, West Bengal-700032

Dr. Shrabanee Sen
Principal Scientist
Functional Materials and Devices Division
CSIR-Central Glass & Ceramic Research Institute
Kolkata - 700 032


Dedicated to my beloved
parents

Acknowledgements

At this stage of accomplishment, first and foremost I must acknowledge my department, I feel blessed to have had the chance to carry my Ph.D. research here which is enjoyable, challenging and valuable at the same time. I would like to express my deepest gratitude to my supervisor, Dr. Shrabanee Sen. I am extremely fortunate to have her as my advisor and mentor. I am delighted to gratefully thank her for her excellent supervision and cooperation. The time and guidance that she provided me throughout the duration of my Ph.D. study are immeasurable. She always supported and helped me irrespective of my situation throughout my entire Ph.D. tenure. I am grateful to her for giving me the freedom during my Ph.D. work.

I take the opportunity to express my gratitude to Dr. Mrinal Pal, Head, Functional Materials and Device Division, CSIR-CGCRI for his constant encouragement. He, being very supportive, always helped me whenever I needed it. I would like to express my gratitude to Dr. K. Muraleedharan (former Director, CSIR - CGCRI) and Dr. Suman Kumari Mishra (present Director, CSIR - CGCRI) for giving me the opportunity to pursue my Ph. D. work in this esteemed Institute with its sophisticated facilities.

I am extremely thankful to the Head, Department of Physics, Jadavpur University for allowing me to be registered in this department. I would also like to acknowledge all the faculty members of this department who introduced me with the different aspects of research related topics during the course work. I also very much grateful to Dr. Sumana Ghosh, Senior Principal Scientist, Bio-ceramics & Coating Division, CSIR-CGCRI for giving me valuable suggestions as the member of RAC committee during my Ph.D. work.

It's a great pleasure to thank my seniors labmates Dr. Epsita Kar, Dr. Abhishek Sasmal, Dr. Shewli Pratihar, Dr. Puja Ghosh, for all the valuable discussions. They have helped me a lot in any situation whenever I need and I appreciate it very much. I am very much thankful to all my juniors Pounomi, Animesh, Soumya, Deepak, Siddharth for their altruistic help. I am deeply indebted to Shuvankar Da, Aditi Di, Taniya Di, Gourav, Ganga for the countless supports they have provided me throughout my entire journey of Ph.D.

I wish to express my sincere thanks to Uttam and Sumanta, my longtime friends and companions from my college days for their support and encouragement during my studies and research work.

Now I take this opportunity to express my deepest gratitude to my Maa and Baba for their blind support. And most importantly I want to thank my sister Dora. I would like to thank my love, my special one, for her continuous inspiration, support, encouragement throughout my journey. I know any word in the English vocabulary cannot express their contributions in my life.

I am extremely thankful to INSPIRE, DST, Government of India (Grant No. DST/INSPIRE Fellowship/2018/IF180801) for providing me the financial support through research fellowship to complete my research work.

Once again, I want to thank each and every one for their constant support, I could never have achieved this without them.

Sourav Maity
12.12.2023

Sourav Maity
December, 2023

Abstract

The rapid surge in portable electronic devices, wearable multimedia gadgets, and various medical apparatus, has created a flourishing demand for energy generation technologies that are slim, lightweight, portable, and flexible. Here we have developed high-performance piezoelectric assisted triboelectric hybrid energy harvesters (HEH) with specific attributes, including increased output properties in terms of output voltage and current, flexibility, and versatile functionality. Innovative applications for HEH technology that can offer cost-effective, safe, convenient solutions to address energy challenges, specific sensing, and smart applications were explored. As functional layers for HEH devices PVDF and PDMS were utilized due to their high negative surface charge density. To induce higher piezoelectricity inside the polymer matrix, ceramic inclusion strategy was implemented. At first, ceramic Barium Titanate ($BaTiO_3$)-based filler material, the strontium-doped $BaTiO_3$ was characterized. Optimized composition ($Ba_{0.6}Sr_{0.4}TiO_3$) in terms of high dielectric permittivity, low loss tangent, and low leakage current was used as a filler in PVDF for piezoelectric energy harvesting and mechanosensing. The limitation posed by BST40's centrosymmetric crystal structure was addressed by introducing $(Ba_{0.85}Ca_{0.15})(Ti_{0.90}Hf_{0.10})O_3$ (BCHT) particles. These BCHT particles had a notably high piezoelectric charge coefficient of 333 pC/N and were incorporated as fillers to create flexible BCHT/PVDF composites. The BCHT/PVDF functional layer was utilized to efficiently fabricate a piezo-tribo hybrid energy harvester for biomechanical movement sensing. It was also well suited in applications like smart switches for controlling smart home appliances and in smart parking sensors which can efficiently differentiate any “vacant” or “filled” state in a parking slot. The idea of piezoelectric-assisted triboelectric hybrid energy harvester was again implemented in another HEH device where lead-free morphotropic phase boundary composition $BaTi_{0.89}Sn_{0.11}O_3$ (BTS) was used as filler material. Due to four phase coexistence, BTS showed piezoelectric charge coefficient (d_{33}) of ~ 412 pC/N. BTS loaded PDMS consisted hybrid energy harvester device was utilized for biomechanical energy harvesting, writing pad sensing, and as a power source for wireless power transmission. Hence, this thesis is set to introduce a groundbreaking dimension to the realm of piezo-tribo

hybrid energy harvesting. The proposed multifunctional solutions incorporate biomechanical movement sensing, writing pattern detection, leveraging the device as a power source for wireless power transmission, and integrating the fabricated device into wireless smart home and smart parking sensor applications. This contribution is anticipated to significantly impact self-powered electronics, robotics, real-time healthcare monitoring, and advancements in artificial intelligence technologies.

Table of contents

Page No.

List of Figures

List of Tables

Chapter 1

Introduction

1.1 Motivations

The rapid expansion of globalization has sparked two pressing challenges: the depletion of fossil fuels and the mounting crisis of global warming [1–5]. Our world is progressing towards severe issues related to pollution and the diminishing reserves of carbon-based energy resources. In the past century, due to the swift growth of industrialization and urbanization, there has been an aggressive consumption of global energy [1,3]. In these critical times, as the world grapples with the dual challenges of reducing CO_2 emissions and addressing electricity deficits, decisive measures are of paramount importance. To confront these pressing issues, the field of efficient energy harvesting has a central focus on the realm of green and sustainable energy science. Large-scale energy harvesting endeavors mainly center around the capture of energy from renewable sources like solar, wind, thermal, and mechanical systems [2–11]. While these energy resources have the potential to provide eco-friendly power on a large scale, they face challenges related to cost-effectiveness, and portability [9,10,12,13]. Many of these resources entail high initial installation costs, are not friendly to birds and bats, and demand substantial land or space for their deployment. Furthermore, the rapid surge in portable electronic devices, mobile phones, flexible displays, wearable multimedia gadgets, and various medical apparatus, has created a flourishing demand for energy generation technologies that are slim, lightweight, portable, and flexible [9,11,13]. These technologies are widely utilized in wireless sensing, infrastructure monitoring, healthcare systems, and security applications. These devices are also gaining tremendous attention in self-powered sensing applications. These sleek, lightweight devices are exceptionally well-suited for powering portable and flexible electronics that operate at lower frequencies which will also reduce the burden of the battery[14–24]. Keeping these aspects in mind, researchers are in tremendous search for devices and technologies that can power up their energy needs on their own. In this viewpoint, energy harvesting is the backbone, elaborated in the next portion.

Chapter 1

1.2 Concept of energy harvesting

Energy harvesting is the procedure of capturing and transforming different types of energy from the nearby environment into electrical energy that can power electronic devices or charge batteries [25]. Below are some essential aspects of energy harvesting.

Energy harvesting has a rich history, with various milestones:

Early Exploration (19th-20th Century): The concept of tapping into ambient energy sources dates back to the 19th century. Early experiments by scientists like Thomas Seebeck and Jean-Charles-Athanase Peltier laid the groundwork for thermoelectric energy conversion.

Piezoelectric Advances (Mid-20th Century): Piezoelectric materials, which generate electricity when subjected to mechanical stress, gained attention in the mid-20th century. They found use in devices like piezoelectric lighters and underwater sonar equipment.

Space Era (1950s-1960s): Energy harvesting was employed in early space missions to power instruments and sensors. Radioisotope thermoelectric generators convert heat from decaying radioactive isotopes into electricity.

Commercialization (1970s): The 1970s saw the first commercial applications of energy harvesting. Electronic watches and calculators integrated with photovoltaic cells to power low-energy displays.

Microelectronics and Wireless Sensors (Late 20th Century): As low-power microelectronics advanced, the demand for energy harvesting grew. Research efforts focused on enhancing the efficiency and practicality of these systems.

Solar Power Revolution (Late 20th Century to Present): Solar energy harvesting saw significant progress. Photovoltaic technology improvements and cost reductions made solar energy more accessible and efficient.

IoT advancement (21st Century): The rise of small, low-power IoT devices drove the need for reliable energy harvesting solutions. Research and development surged to make these systems more dependable and scalable.

Diverse Applications (21st Century): Energy harvesting found use in various fields, from environmental monitoring and healthcare devices to wearables and smart

infrastructure. It's applications for replacing batteries in remote and challenging environments have increased.

These energy-harvesting technologies continue to evolve. Ongoing research focuses on improving efficiency, scalability, and cost-effectiveness, exploring new materials and techniques for enhanced energy conversion and storage. In this era of smart IoT, energy harvesting has transitioned from early concepts to a practical and eco-friendly solution for powering a wide range of electronic devices that are self-powered [14,15,17,26]. Out of several ideas to reach a sustainable reality, energy harvesting from waste energy like sun energy, geothermal energy, wind energy, ocean waves, hydro currents in from rivers, biomechanical energies, etc. have a very promising aspect. Among these strategies, in the realm of low power requirement devices, omnipresent energy endeavors like human daily life movements, heartbeat, vibrations, and ocean waves can give us a major solution.

1.2.1 Electromechanical energy harvesting

If we talk about energy harvesting from mechanical energy resources, there are three major technologies, electromagnetic, piezoelectric, and electrostatic energy harvesting. Among them, electromagnetic induction is the process of harnessing energy by utilizing a coil or wire to collect power from fluctuating magnetic fields generated by mechanical movement. As the coil interacts with the magnetic field through motion, it generates an electric current [27–29]. Examples are bicycle dynamos, hand-crank flashlights, etc. Piezoelectric materials generate electrical voltage when subjected to mechanical stress or deformation. This technology is commonly used in applications where vibrations, impacts, or mechanical motion are available sources of energy[30–42]. Electrostatics is used in the energy harvesting strategy, called triboelectric energy harvesting. It is mainly used in energy harvesting, and several smart sensor application purposes [10–13,15,21,43–46]. Considering the fruitful aspects of energy generation capabilities of energy harvesters, researchers around the world are working on the progress of this technology. Keeping in mind this technological prospect, our dissertation will mainly deal with this energy harvesting as well as some smart sensing applications. Here, we will only focus on piezoelectric and triboelectric energy harvesting technologies due to their operational similarities and fundamental mechanisms [47–53].

1.2.1.1 Piezoelectric energy harvesting

Since this dissertation deals with hybrid energy harvesting where piezoelectricity as well as triboelectricity are hybridized, the basic mechanism, and fabrication of piezoelectric energy harvesting technologies are included in this section. Piezoelectric energy harvesting is focussed on piezoelectricity where piezoelectric materials owing to their non-centrosymmetric crystal structure generate electricity on the application of mechanical stimuli. So, for piezoelectric energy harvesting, the material should be only piezoelectric materials. In the next portion, we will discuss on the piezoelectricity.

1.2.1.1.1 What is piezoelectricity?

The Piezoelectric Effect is the property of certain materials to produce an electric charge when subjected to mechanical stress. The term "Piezoelectric" is derived from the Greek words "piezein," meaning "to squeeze or press," and "piezo," meaning "push"[54]. An interesting feature of the Piezoelectric Effect is its reversibility. This means that materials that exhibit the direct Piezoelectric Effect (generating electricity under mechanical stress) also demonstrate the converse Piezoelectric Effect (producing stress when an electric field is applied). When a piezoelectric material is subjected to mechanical stress, it causes a repositioning of the positive and negative charge centers within the material, resulting in the creation of an external electrical field. Conversely, when an external electrical field is applied, it either stretches or compresses the piezoelectric material. The first one is called the direct piezoelectric effect whereas the second one is called the converse piezoelectric effect. This effect occurs due to the linear interaction between the mechanical and electrical properties in crystalline materials that lack inversion symmetry[55,56]. The constant governing this linearly proportional relationship is known as the piezoelectric coefficient, denoted as "d." This coefficient is a third-rank tensor that connects a first-rank tensor or vector (representing electric displacement or field) with a second-rank tensor (representing stress or strain). Consequently, the piezoelectric equations can be expressed as follows

$$D_k = d_{kij} T_{ij} \quad (1.1)$$

$$S_{ij} = d_{kij} * E_k \quad (1.2)$$

(where "i," "j," and "k" represent indices from 1 to 3) [22]:

D_k represents electric displacement (C/m^2).

E_k represents the electric field component (V/m).

S_{ij} represents strain components.

T_{ij} stands for stress components (N/m^2).

d_{kij} or d_{kij}* denotes components of the piezoelectric charge or strain constant.

It's worth noting that the subscripts used for piezoelectric constants are commonly represented using the reduced Voigt matrix notation "d_{km}," where "k" signifies the component of electric displacement D or electric field E in the Cartesian reference frame (x_1, x_2, x_3). The index "m," ranging from 1 to 6, is utilized to describe mechanical stress or strain. Specifically, m = 1, 2, and 3 correspond to the normal stresses along the x_1, x_2, and x_3 axes, while m = 4, 5, and 6 correspond to the shear stresses T_{23}, T_{13}, and T_{12}, respectively. Both "d" and "d*" are referred to as the piezoelectric constant or coefficient, although they have distinct units: "pC/N" and "pm/V" (here, "p" signifies pico, 10^{-12}), respectively[55,56].

Many advanced piezoelectric materials exhibit ferroelectric properties wherein these materials possess a natural electric polarization that can be altered by applying an external electric field. As depicted in Fig. 1.1, it's important to note that dielectrics encompass a broad group of materials. Dielectric materials are essentially electrical insulators that can become polarized when subjected to an external electric field, particularly when placed between the plates of a capacitor. Piezoelectric materials are a subgroup of dielectrics, but they exhibit a unique property: when stress is applied to a piezoelectric crystal with a non-centrosymmetric crystal structure, it results in a separation of positive and negative charges. Pyroelectric materials are distinct in that they can generate a temporary voltage when subjected to temperature changes. This occurs because the magnitude of polarization in a pyroelectric crystal can be altered by variations in temperature. In contrast, for piezoelectric crystals, it is mechanical stimulation that leads to changes in polarization, resulting in the accumulation of charges on their surfaces. Ferroelectric materials represent a subset of pyroelectric materials. Every ferroelectric material is also a pyroelectric material, and every pyroelectric material is piezoelectric. However, not all piezoelectric materials are pyroelectric, and not all pyroelectric materials are ferroelectric. The categorization of

these materials is determined by the symmetry of their crystal structures. All crystalline substances fall into one of the 32 crystallographic point groups. Out of the thirty-two potential crystal classes, twenty-one lack a center of symmetry, and among these, twenty crystal classes demonstrate direct piezoelectric properties. Materials with these crystal structures can generate surface charges when mechanical stress is applied to them. The single non-centrosymmetric crystal class that doesn't exhibit piezoelectricity falls under the cubic crystal class 432. Among these twenty non-centrosymmetric crystal classes with piezoelectric properties, ten are considered polar

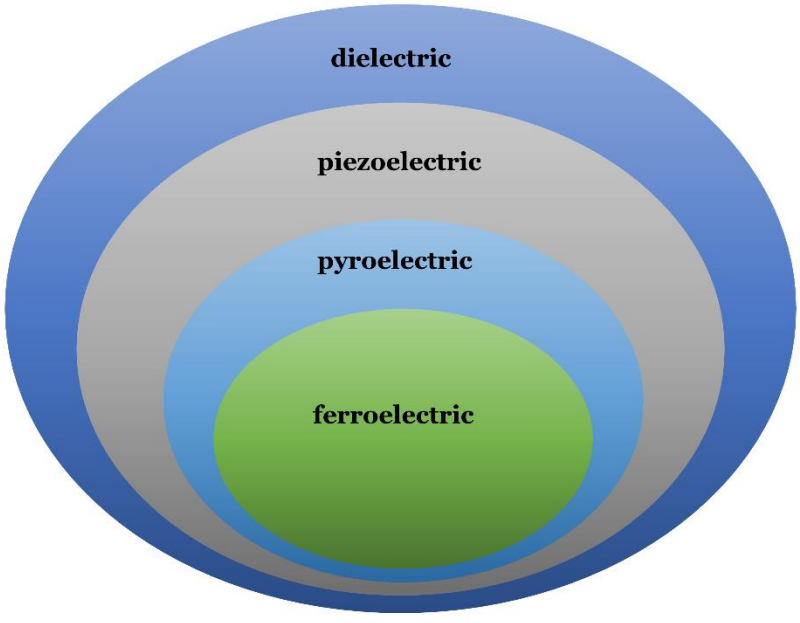

Fig. 1.1 *Mapping among ferroelectric, pyroelectric, piezoelectric, and dielectric materials.*

classes because they possess inherent polarization even in the absence of applied mechanical stress, which arises from a non-zero electric dipole moment within the unit cell of their structures. Materials belonging to these ten crystal classes with spontaneous polarization (non-zero dipole moments) can have their polarization altered by changes in temperature, making them part of the pyroelectric group. If the dipole moments of materials in these ten polar crystal structures can be reversed by the application of an external electric field, they are classified as ferroelectric materials. In the case of polar piezoelectric crystals, which inherently possess a non-zero dipole moment without the need for applied mechanical stress, the piezoelectric effect occurs through changes in the magnitude and/or direction of the dipole density. Conversely, non-polar piezoelectric crystals do not exhibit a non-zero dipole moment without

external stimuli. In these non-polar crystals, any polarization other than zero is induced by the application of an external mechanical load. It can be understood that externally applied mechanical stress essentially transforms the material from a non-polar crystal class (with a zero net dipole density) into a polar one, resulting in a non-zero net dipole density [54–58]

Hence, researchers primarily focus on materials that exhibit piezoelectric properties as these materials are well-suited for generating power from ambient mechanical vibrations.

1.2.1.1.2 Piezoelectric materials

Piezoelectric materials are suitable for energy harvesting, some common ones include quartz, barium titanate (BT), lead titanate (PT), cadmium sulfide (CdS), lead zirconate titanate (PZT), lead lanthanum zirconate titanate (PLZT), poly(vinylidene) fluoride (PVDF). Among these, BT was the first discovered, and PZT is frequently employed for piezoelectric energy harvesting. Although piezoelectric ceramics have superior electromechanical properties compared to piezoelectric polymers, they are inherently brittle. Nevertheless, the modern world demands materials that are flexible, lightweight, and low in toxicity. These piezoelectric materials can be categorized into two groups: natural and artificial, as depicted in Table 1.1.

Table 1.1 Various types of piezoelectric materials

<table>
<tr><th rowspan="2">Natural</th><th colspan="2">Manmade/artificial</th></tr>
<tr><th>Pb-based</th><th>Pb-free</th></tr>
<tr><td>Quartz</td><td rowspan="2">Lead Titanate (PT)</td><td>Barium Titanate ($BaTiO_3$)</td></tr>
<tr><td>Sucrose</td><td>Zinc Oxide (ZnO)</td></tr>
<tr><td>Rochelle Salt</td><td rowspan="2">Lead Zirconate Titanate (PZT)</td><td>Barium Calcium Titanate – Barium Zirconium Titanate (BCT-BZT)</td></tr>
<tr><td>Tendon</td><td>Bismuth Ferrite ($BiFeO_3$)</td></tr>
<tr><td rowspan="2">Silk</td><td rowspan="2">Lead Lanthanum Zirconate Titanate (PLZT)</td><td>Bismuth Sodium Titanate (BNT)</td></tr>
<tr><td>Zinc Stannate ($ZnSnO_3$)</td></tr>
<tr><td>DNA</td><td rowspan="3">Lead Magnesium Niobium Oxide- Lead Titanate (PMN-PT)</td><td>Lithium Niobate ($LiNbO_3$)</td></tr>
<tr><td>Dry bone</td><td>Aluminium Nitrate (AlN)</td></tr>
<tr><td></td><td>Polyvinylidene Fluoride (PVDF)</td></tr>
</table>

1.2.1.1.3 Mechanism of piezoelectric energy harvesting

Now, for the fabrication of piezoelectric energy harvesters, piezoelectric materials should be sandwiched between two electrodes. On the application of stress upon the device, piezoelectric dipoles will try to align along the direction of the applied force. Simultaneously there will be a piezoelectric charge induction at the two electrodes. Now to balance this charge electrons will move from one electrode to the other through the external circuit connection. However, on the force removal step, the electrons will move in the reverse direction. This periodic force application and removal lead to the piezoelectric energy generation[31–33,39,40,57]. The mechanism is depicted in Fig. 1.2.

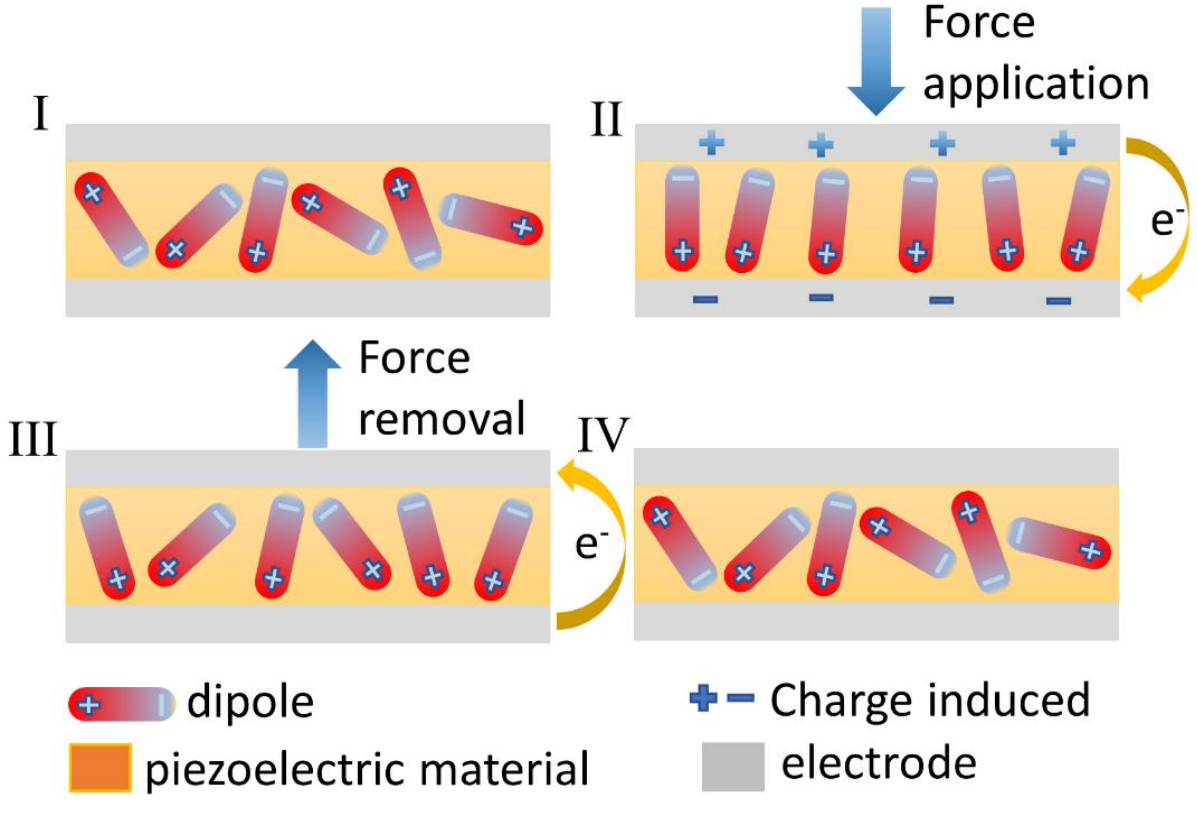

Fig. 1.2 *Mechanism of piezoelectric energy harvesting*

1.2.1.2 Triboelectric energy harvesting

1.2.1.2.1 What is triboelectricity?

Several years ago, researchers were drawn to the intriguing phenomenon known as the triboelectric effect, in which the mechanical friction between two objects in motion

generates electricity [59,60]. This effect has been recognized for quite some time and was originally thought to be solely electrostatic [59–61]. Although triboelectricity has been observed for a long time, it was previously considered a nuisance, leading to extensive efforts to mitigate it, such as in the context of powder and recycled material handling [60]. Recently triboelectricity has been used for self-powering a wide range of highly advanced devices. The Triboelectric Nanogenerator (TENG) was initially developed by Wang and his colleagues in 2012 to transform disorganized, and unused low-frequency energy into electrical power[62]. TENG operates by harnessing the interaction between contact electrification (CE) and electrostatic induction, offering several benefits, such as affordability, easy manufacturing, a wide array of material options, and a wide range of potential applications. In essence, TENG is a discipline that leverages Maxwell's displacement current as the driving mechanism to efficiently convert mechanical energy into electric power or signals[60–64]. By physically contacting two dissimilar materials, electrostatic charges are generated on their surfaces. When these materials are mechanically separated, the resulting triboelectric charges can lead to a potential drop. This potential difference can, in turn, induce the movement of electrons between electrodes located on the top and bottom surfaces of the two materials. There are four fundamental modes of triboelectric energy harvesting named the (1) Vertical Contact Separation Mode, (2) Lateral Sliding Mode, (3) Single Electron Mode, (4) Freestanding Tribo-Electric Layer Mode.

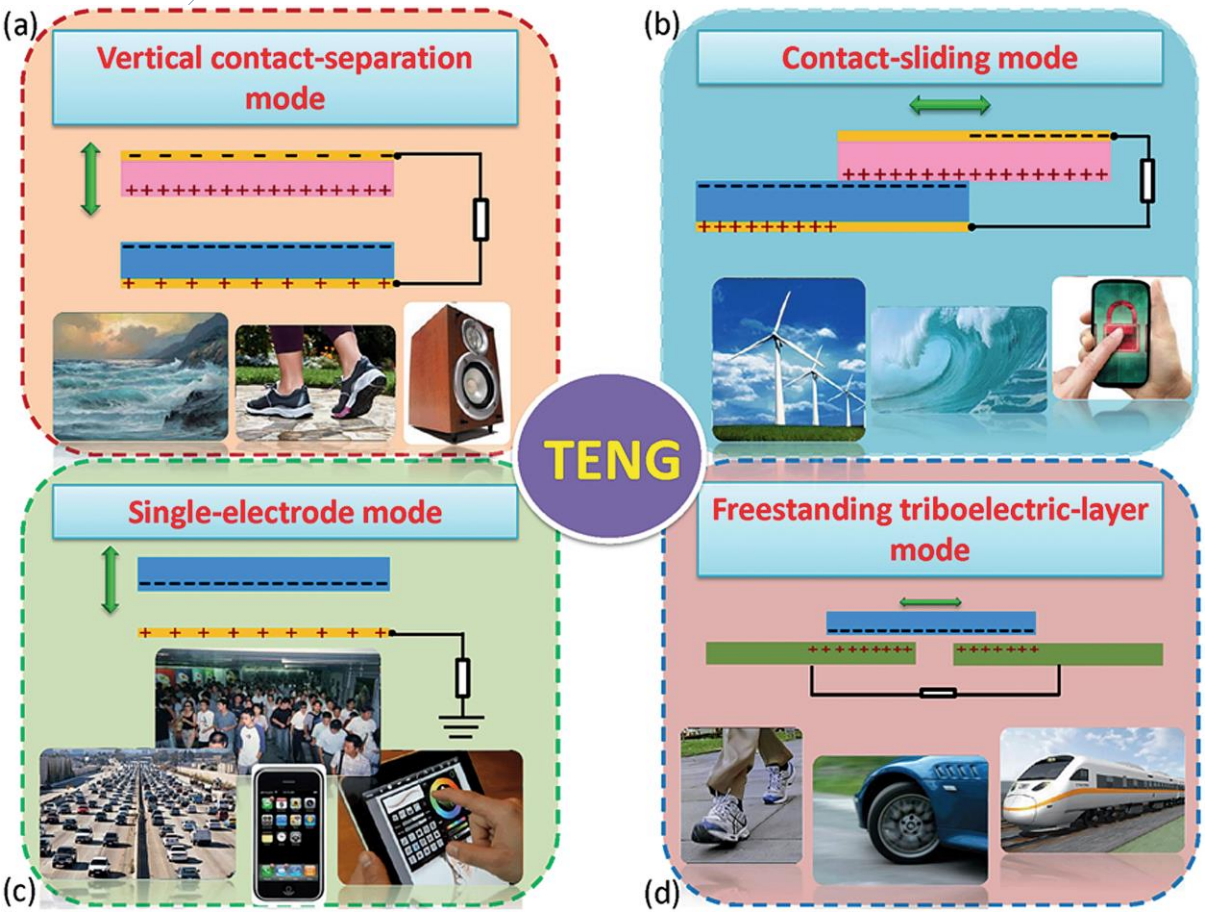

Fig. 1.3 *The 4 basic Modes of Triboelectric Nanogenerators: (a) vertical contact separation mode (b) contact-sliding mode; (c) single electrode mode and (d) free-standing triboelectric-layer mode [65].*

a. Vertical contact separation mode

The original operational mode for Triboelectric Nanogenerators (TENGs) was the vertical contact-separation mode [61,66]. In this mode, when two dielectric films with differing electron affinities (minimum one layer should be dielectric) physically contact each other, they become oppositely charged on their surfaces. As the two surfaces are separated by a gap, electrodes on the top and bottom of the films generate a potential difference. When these two electrodes are connected by an electrical load, electrons from one electrode flow to the other to equalize the electrostatic field. When the gap is closed again, the potential difference created by the triboelectric charges disappears, causing the induced electrons to return. Repeated contact and separation of the two materials cause induced electrons to oscillate between the two electrodes, generating an alternating current (AC) output in the external circuit. The vertical

contact-separation mode has been widely employed for energy harvesting from diverse sources, including finger typing, human walking, and biomedical systems [67–71]. Additionally, it has been adapted for the development of self-powered sensor systems, encompassing magnetic sensors, pressure sensors, vibration sensors, catechin detection sensors, and acoustic sensors [72–76].

b. Lateral sliding mode

The lateral sliding mode of the Triboelectric Nanogenerator (TENG) involves producing electricity through the triboelectric effect by moving two materials horizontally relative to each other. This is in contrast to the vertical contact-separation mode, where the materials touch and then separate. In the lateral sliding TENG, as the materials slide horizontally against each other, the friction generates charges, resulting in the production of electrical power. It has applications in velocity sensors, motion sensors, etc [59,61,66]

c. Single electrode mode

The vertical contact-separation mode and in-plane sliding mode of triboelectric nanogenerators both require the moving objects to be connected to an electrode and a lead wire. This configuration significantly restricts the versatility and potential applications of TENGs for harnessing energy from any freely moving object, as the object must be linked to the entire system through an interconnect. To address this issue, a solution was devised in the form of the single electrode mode TENG. With its distinctive capability, the single electrode mode has been employed for energy harvesting from various sources such as airflow, rotating tires, raindrops, and turning book pages [77–80].

d. Freestanding triboelectric layer mode

The freestanding tribo layer mode is a configuration within a Triboelectric Nanogenerator (TENG) where the triboelectric layer is not affixed to any substrate or supporting structure. Instead, this layer is self-supporting, enabling it to move or deform independently in response to mechanical stimuli like vibrations, pressure, or airflow [81–83]. By coming into contact or undergoing relative motion with another material, the freestanding tribo layer generates electricity, creating a potential difference that can be utilized for energy harvesting. This is different from the in-plane

sliding mode, which can lead to material wear and the generation of heat when continuously operating for an extended period.

1.2.1.2.2 Triboelectric materials

Table 1.2 Materials in triboelectric series

Positive	Negative
Polyformaldehyde 1.3-1.4	Continued
Ethylecellulose	Polyester (Dacron) Polyisobutylene
Polyamide 11Polyamide 6-6	Polyurethane Aexiblesponge
Melanime formol	Polyethylene Terephthalate
Wool , knitted	Polyvinyl butyral
Silk, woven	Polychlorobutadiene
Aluminium	Natural rubber
Paper	Polyacrilonitrile
Cotton, woven	Acrylonitrile-vinyl chloride
Steel	Polybisphenol carbonate
Wood	Polycholoether
Hard rubber	Polyvinylidene chloride (Saran)
Nickel, copper	Polystyrene
Sulfur	Polyethylene
Brass, silver	Polypropylene
Acetate, rayon	Polyimide (Kapton)
Polymethyl methacrylate	Polyvinyl Chloride (PVC)
Polyvinyl alcohol	Polydimethylsiloxane (PDM S)
continued	Polytetrafluoroethylene (Teflon)

Positive

Negative

Now the output generated from a triboelectric energy harvester (TEH) device depends on the two triboelectric layers. That's why material choice play a vital significance in the fabrication of TEH device [84]. The primary choice for the two materials is that one material should be characterized by a high positive surface charge density and the counterpart should have with high negative surface charge density. Table 1.2 displays the various triboelectric materials in a comprehensive order of their surface charge density [85]. The table describes that if we move from the bottom towards the upper

side in the left column the surface charge density gets higher. Similarly in the right column if we move from up to the lower side, negative surface charge density increases.

1.2.1.2.3 Theory of triboelectric energy harvesting

The driving force behind Triboelectric energy harvesters (TEHs) is Maxwell's displacement current, which results from the time-varying electric field and a polarization term associated with the medium. In the case of TEHs, triboelectric charges are generated on surfaces due to the contact electrification between two different materials. To incorporate the influence of contact electrification-induced electrostatic charges into Maxwell's equations, an additional term, denoted as P_s, was introduced into the displacement vector D by Wang in 2017 [86], represented as

$$D = \epsilon_0 E + P + P_s \tag{1.3}$$

Here, the initial polarization vector P arises from the influence of an external electric field, while the additional term P_s primarily stems from the presence of surface charges that are not dependent on the existence of an electric field. By substituting Equation (1.3) into Maxwell's equations and defining

$$D' = \epsilon_0 E + P \tag{1.4}$$

Now the reconstructed Maxwell equation will be

$$\nabla \cdot D' = \rho' \tag{1.5}$$

$$\nabla \cdot B = 0 \tag{1.6}$$

$$\nabla \times E = -\frac{\partial B}{\partial t} \tag{1.7}$$

$$\nabla \times H = J' + \frac{\partial D'}{\partial t} \tag{1.8}$$

Where volume charge density $\rho' = \rho - \nabla \cdot P_s$ (1.9)

and current density $J' = J + \frac{\partial P_s}{\partial t}$ (1.10)

In Equation (1.10), the component that influences the output current of the TEH is associated with the driving force denoted as $\frac{\partial P_s}{\partial t}$, and this element is commonly referred to as the "Wang term" in displacement current.

In Equation (1.8), the displacement is composed of two components. The term, $\frac{\partial D'}{\partial t}$, represents the displacement current arising from the time-varying electric field and the medium polarization induced by the electric field. This component can give rise to a corresponding magnetic field and is the fundamental origin of electromagnetic waves, a concept first introduced by Maxwell. The term, $\frac{\partial P_s}{\partial t}$, accounts for the displacement current that results from factors unrelated to electric fields, primarily originating from external strain fields. At high frequencies, particularly in wireless communication, the first term dominates and is responsible for the generation of electromagnetic waves. On the other hand, the second term operates at lower frequency conditions, making it major in energy harvesting[86].

Over the past decade, research on TEH has increased very fast due to its wide material choice, easy fabrication, and above all its applications in self-powered sensors. Though the power generation capability of TEH devices is much higher than the PEH devices, applications of this device as a power source that can reduce the hazardous implications of battery-based devices are still lacking owing to its low output power, packaging issues, stability factors, etc. Due to these reasons, several approaches like material optimization, device structure manipulation, etc are being implemented to augment the power density from nW/cm² to μW/cm² and to reach the mW/cm² range. Among these strategies, synergistic enhancement of PEH and TEH devices through hybridization gained a prior node from worldwide researchers[47,49–53]. Here, the dissertation deals with the piezoelectric-assisted triboelectric hybrid energy harvester.

1.2.1.3 Hybrid energy harvesting

1.2.1.3.1 Hybridization

Of late, combining piezoelectricity with triboelectricity in a single device takes a major boost since the deformation of a material and contact friction can take place simultaneously which is the backbone of their strategy respectively. Now as far as hybrid energy harvesting (HEH) is concerned, there are two types of hybridization one is external hybridization whereas the other one is internal hybridization. In the context of external hybridization, these two types of devices are linked in a manner where they function independently but collectively contribute to the total electrical power output. Nevertheless, the design of hybrid energy harvesters with this approach leads to the

creation of large-sized devices with impedance contrast between the two distinct components, PEH and TEH. To address these shortcomings, the present research leverages internal hybridization to create the final hybrid energy harvesting device. In this hybridization approach, a single functional layer is harnessed, exhibiting characteristics associated with both piezoelectric and triboelectric effects. Because of its straightforward manufacturing process and simple circuit connections, the construction of hybrid energy harvester (HEH) devices using a single piezo-tribo hybrid functional layer is widely favored [16,17,26,87,88].

1.2.1.3.2 Materials selection

As we have previously mentioned for internal HEH devices material should be such that it possesses piezoelectric as well as triboelectric properties. In that regard as a triboelectric layer, polymer materials are the premier choices due to their electron-donating characteristics. In the realm of flexible energy storage and energy harvesting applications, Poly(vinylidene fluoride) (PVDF) stands out as the predominant polymer material among several others, such as its co-polymers, Polyvinyl chloride (PVC), and Polyamide (Nylon-11) [89,90]. This is primarily attributed to PVDF's extensive popularity owing to its exceptional characteristics, including remarkable flexibility, high electric breakdown strength, favorable ferroelectric, and piezoelectric properties, as well as its cost-effectiveness when compared to alternative piezoelectric polymers [15,87,91]. Polyvinylidene fluoride (PVDF) is a semi-crystalline polymer with five distinct crystalline phases, namely α, β, γ, δ, and ε. Typically, PVDF tends to crystallize in the non-polar α phase when subjected to standard room temperature and pressure conditions. In terms of molecular conformation, the α phase features the helical TGTG′ (T- trans, G- gauche+, G′-gauche) structure, while the β phase consists of an all-trans (TTT) conformation, and the γ phase is characterized by T_3GT_3G' conformations. When PVDF polymer chains are organized into crystalline lattices, a net dipole moment is created in the β, γ, and δ phases, endowing them with polar properties. In contrast, the α phase lacks a net dipole moment and is considered non-polar. Among these polar phases, the β phase exhibits the highest spontaneous polarization per unit cell, making it particularly well-suited for displaying superior piezoelectric and ferroelectric properties. However, to construct efficient energy-harvesting devices using PVDF-based polymers, it becomes mandatory to induce a transformation from the non-polar α phase to the polar β phase. Consequently, various strategies have been

utilized to achieve this transition, such as electrospinning, the application of a strong electric field (poling), and the integration of piezoelectric materials [87,92]. Among these approaches, the incorporation of ceramic piezoelectric materials has emerged as a particularly viable solution, owing to its ease of processing and cost-effectiveness [61]. Consequently, various ceramic materials such as $BaTiO_3$ [87], $BiFeO_3$ [93], ZnO [94], $Cs_3Bi_2Br_9$ [16], $ZnSnO_3$ [95], etc. are incorporated in PVDF. As dielectric permittivity and surface charge play the leading role in hybrid energy harvesting, so to enhance these characteristics is our first aim. Using the ceramic incorporation different PVDF-based composites were used to fabricate different energy-harvesting devices. Xiang et al developed a piezoelectric triboelectric nanogenerator (PTENG) that utilized a polyvinylidene fluoride (PVDF) film doped with 10% of barium titanate nanoparticles, along with polyamide 6 (PA6) as the functional layers [96]. This modification had a significant impact on the device's performance. The introduction of $BaTiO_3$ nanoparticles led to the following improvements: the peak voltage generated by the PTENG increased substantially, rising from 384 V to a value of 900 V and the charge density also saw a notable increase, climbing from 26.4 mC/cm² to 34.4 mC/cm². These enhancements in peak voltage and charge density are indicative of the improved performance and efficiency of the PTENG, which can have applications in energy harvesting and other areas where piezoelectric effects are utilized.

Again, according to the triboelectric series [84,85] Polydimethylsiloxane (PDMS) is also a well known negative triboelectric polymer material that has gained tremendous applications due to its flexibility, elasticity, biocompatibility, and its optical transparency. Though this material has no piezoelectricity, owing to its high negative surface charge density, it is one of the vastly used triboelectric materials. In some instances, pristine materials are not able to achieve the desired level of performance. To enhance electronic properties, such as piezoelectric and dielectric attributes, in the context of advancing flexible electronics, composite designs featuring functional nano/micro-fillers are employed. Yang and Daoud conducted research in which they directly grew zinc oxide (ZnO) nanorod arrays on a PDMS/PVDF composite film to enhance its performance [97] Before the growth of ZnO nanorods, they exposed the substrate to ultraviolet (UV) treatment to improve its hydrophilicity. The process involved spin-coating a ZnO seed solution onto the prepared substrate, followed by the hydrothermal growth of ZnO nanorods. A comparison of the open-circuit voltage

between the devices with and without ZnO nanorod arrays revealed a substantial increase of 21.8 V. This outcome verifies the beneficial role played by the interfacial ZnO nanorod array in enhancing the output performance of the piezoelectric triboelectric nanogenerator. This improvement is attributed to the expanded effective contact area and the enhanced contact electrification charges facilitated by the presence of the ZnO nanorod array. These findings hold promise for the effective harnessing of mechanical energy using hybrid devices. To enhance the dielectric properties of a material, colossal dielectric $Bi_4Ti_3O_{12}$ particles were incorporated into the PDMS matrix [17]. This modification resulted in a substantial increase in the material's dielectric constant. The hybrid nanogenerator, which combined the poled PDMS composite with aluminium, exhibited significant improvements in both voltage and current signals delivered compared to individual piezoelectric nanogenerator (PENG) and triboelectric nanogenerator (TENG) devices. This illustrates the effectiveness of modifying natural materials to create a highly efficient nanogenerator for energy harvesting applications. In a study by Jirayupat et al [98], they incorporated zinc oxide nanowires (ZnO NWs) into a TENG structure consisting of Au/PDMS/Au-Al. Since ZnO NWs exhibit piezoelectric properties, the combined device demonstrated a significant enhancement in its output performance. Specifically, the output voltage and current of the hybrid device improved by approximately a factor of two when compared to a TENG based solely on pure PDMS. Again, Patnam et al demonstrated that Ca and Zr doped $BaTiO_3$ incorporation inside PDMS augmented the output generation capability of the hybrid device from an output voltage of 295 V to 550 V and output current from 16 μA to 34 μA [52]. Whereas the generated maximum output power density was reached to a value of 23.6 W/m² due to the filler loading. Therefore, from the above discussion, we can confirm the positive prospect of output augmentation for a hybrid energy harvester through piezoelectric filler loading inside the triboelectric layer.

Table 1.3 Summary of some recently reported hybrid energy harvesters

Triboelectric material	Piezoelectric material	Output voltage	Output current	Output power	ref
PDMS	$BaTiO_3$ nanoparticles	280 V	5.6 μA	0.04 mW/cm²	[53]

Triboelectric material	Piezoelectric material	Output voltage	Output current	Output power	ref
PDMS	Ca and Zr doped $BaTiO_3$	550 V	34 µA	23.6 W/m^2	[52]
Chitosan and PTFE	$BaTiO_3$ nanorods and Chitosan	247.2 V	36.7 $\mu A/cm^2$	1.568 mW/cm^2	[50]
PDMS, MWCNT, ZnO nanoflower	ZnO nanoflower	400 V	30 µA		[51]
Ni/Cu coated PET fabric and PVDF	PVDF	210 V	45 µA	2.1 mW	[99]
Textured PDMS and human skin	PVDF	750 V	400 µA	3.7 W/m^2	[100]
PVDF TrFE and Polyamide 6	Poled PVDF TrFE	1100 V	32 µA	5.2 W/m^2	[101]
PTFE	PVDF	220 V	60 µA	1.7 mW	[102]
PDMS and nitrile baffle	PVDF	138 V		878 mW/m^3	[103]
PTFE	Poled PVDF TrFE	210 V	395 µA	6 mW/cm^2	[49]
Silicone rubber	PZT	15 V	2 µA	80 µW	[104]
Poled PVDF	Poled PVDF	180 V	5.3 µA	127 µW	[47]
PDMS	Poled PVDF	5.2 V	500 nA		[105]
PDMS and nylon	ZnO nanorod		280 nA		[106]
FEP	Piezoelectric fiber sheet	210 V		238 µW	[107]
PVA/PVDF nanofiber, PDMS and nylon	PVDF	220 V	1.1 µA	80 mW/m^2	[48]
FEP and nylon	Poled $BaTiO_3$	6 V	1.5 µA	11 nW	[108]
$Cs_3Bi_2Br_9$/PVDF-HFP/SEBS	$Cs_3Bi_2Br_9$/PVDF-HFP	400V	1.63 $\mu A/cm^2$	2.34 W/m^2	[16]
Nafion functionalized $BaTiO_3$/PVDF	Nafion functionalized $BaTiO_3$	307 V	1.8 $\mu A/cm^2$	1.12 mW/cm^2	[15]
Mxene/PVDF TrFE and nylon-11	Mxene/PVDF-TrFE	270 V	140 mA/cm^2	4.02 W/m^2	[109]

Triboelectric material	Piezoelectric material	Output voltage	Output current	Output power	ref
PVDF HFP, silicone rubber	Ca and Zr doped $BaTiO_3$	34 V	1.12 mA/m^2	167.7 mW/m^2	[87]
PVDF	KNN with MWCNT	54.1	29.4 µA	164.74 $µw/cm^2$	[110]
PDMS	$BaTiO_3$	72.2	1.82 µA	5.5 $µW/cm^2$	[111]
PDMS	Al-doped $BaTiO_3$	580 V	44 µA	28.1 W/m^2	[112]
PDMS	$BaTiO_3$, MWCNT/PVDF	19.26 V	0.84 mA/cm^2	4.61 mW/cm^2	[113]
PDMS	$Bi_4Ti_3O_{12}$	300 V	4.7 µA		[17]
PANI/PVDF-TrFE	PVDF-TrFE	246 V	122 µA	6.69 W/m^2	[114]
PDMS	$LiNbO_3$	600 V	50 µA	25 W/m^2	[115]
PVDF	Silk	500 V	12 µA	0.31 mW/cm^2	[116]
PDMS	Ca and Zr doped $BaTiO_3$	127 V	67.1 mA/m^2	7.5 W/m^2	[117]
$BaTiO_3$/MWCNT/PVDF	$BaTiO_3$	48.46 V	1.22 mA/m^2	29.27 mW/m^2	[118]
PDMS	ZnO nanoflakes	470 V	60 µA $/cm^2$	28.2 mW/cm^2	[119]
PDMS and PTFE	Li doped ZnO, MWCNT	60.1 V	75 µA		[120]

Table 1.3 depicts several recently reported piezoelectric-assisted triboelectric hybrid energy harvester devices. From that table, it can be confirmed that as far as the triboelectric materials are concerned, PVDF, PDMS, and PTFE are the prior choices, and for ceramic inclusion, piezoelectric materials are favored.

1.2.1.3.3 Mechanism

If we discuss the structure of the device, it has the same device structure of a vertical contact separation-based triboelectric energy device. But here the only disparity is that one of the triboelectric layers must be a piezoelectric material [17].

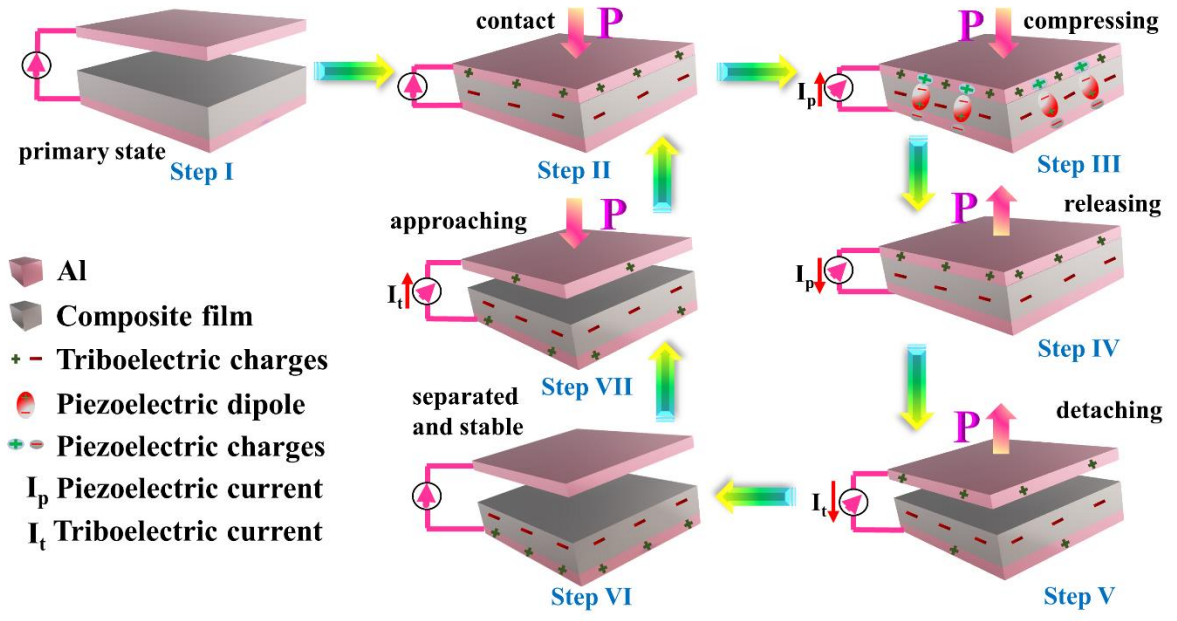

Fig. 1.4 *Mechanism of hybrid energy harvesting*

Now, the probable working mechanism of the HEH based on the combined effect of the piezoelectric and triboelectric phenomenon of the composite film is schematically illustrated in Fig. 1.4. As shown in Fig. 1.4, there is a separation between the composite film and Al electrode inside the device. Here, the Al attached to the PET sheet acts as the top electrode whereas the composite/Al/PET acts as the bottom part of the device. The Al electrode acts as the positive and the composite acts as the negative triboelectric layer of the device. The entire mechanism can be divided into the following steps.

Step-I, initially, without the application of any pressure from outside there is no charge on the electrodes, no potential difference exists between them and the output voltage is zero.

Step-II, on the application of external pressure, both the top and bottom parts of the device will touch each other which leads to the generation of an equal and opposite number of charges depending upon their respective affinity. Based on the triboelectric series Al will get a positive triboelectric charge and the composite gets a negative triboelectric charge.

Step-III, in addition to the above triboelectrification process, due to the application of external pressure the inherent dipoles inside the composite will try to marshal themselves along the direction of pressure under stress-induced polarization. This leads to the induction of charges in the upper and bottom electrodes of the device due

to piezoelectricity. That is why electrons will move from the upper electrode to the lower electrode and consequently, there will be piezoelectric current (I_p).

Step-IV, upon releasing the applied stress, first, the applied pressure on the device will release, this will result in the re-orientations of the arranged dipoles in their original orientation, resulting in I_p in the opposite direction.

Step-V, now with further releasing of the pressure, to maintain electric equilibrium electrons will flow from the bottom to the upper electrode. Simultaneously there will be the generation of I_t in the opposite direction.

Step-VI, the composite layer and upper electrode will reach their stable position resulting in no movements of electrons.

Step-VII, because of the applied pressure there is a breakage in the equilibrium condition which in turn results in a triboelectric current in the opposite direction to the previous from the bottom electrode to the upper electrode through the load. The output generation through the HEH device consists of these stages and the periodic application of pressure and releasing it will generate alternating output which can be detected at the outer load circuit [16,26]. In this entire procedure, the coupling of piezoelectric as well as triboelectric effect will occur which leads to the synergetic output voltage of HEH. In this context, it should be highlighted that the alignment of the dipoles of the composite film under applied pressure was considerably augmented by the presence of triboelectric charges which further enhances the dipolar polarization and accumulation of more and more negative surface charges on the surface of the composite film. As a result, the final output voltage of the typical HEH device is enhanced.

1.2.1.3.4 Materials Selected

Here as we have mainly focussed on flexible piezoelectric triboelectric hybrid energy harvester, we have excluded the use of PTFE as a functional layer due to its low mechanical strength. As a functional matrix, we have opted for PVDF and PDMS based composite films. For choosing the filler material we went through several viewpoints.

a. As the dissertation deals with the piezoelectric assisted triboelectric hybrid energy harvester, the filler material should have a high piezoelectricity. This inherent piezoelectricity will simultaneously augment the piezoelectricity of the

PVDF and PDMS based composite films. In that regard, $PbZrTiO_3$ (PZT), $BaTiO_3$, $BiFeO_3$, $LiNbO_3$, ZnO are the primary choices.

b. The next consideration is to assess the biocompatibility of the selected material. Though in the present scenario, PZT is characterized as the front runner as far as the piezoelectricity is concerned, we have kept out PZT due to its lead toxicity.
c. The next attribute that should be noticed is the relative permittivity of the filler material. As polymer materials are trademarked materials with low relative permittivity, we must choose ceramic materials consisting of high relative permittivity which will help in higher charge storing. That is why ZnO, $LiNbO_3$, and $BiFeO_3$ are eliminated due to their low dielectric permittivity.

Therefore, the material that fulfills these requirements is the $BaTiO_3$. Due to its perovskite structure, $BaTiO_3$ has charge defects that act as the charge storing centers. Due to these superiorities, $BaTiO_3$ is used explicitly in hybrid energy harvesting applications. Though pristine $BaTiO_3$ is used in vast energy harvesting applications, its most promising aspect is its modifiable nature. The perovskite lattice structure of $BaTiO_3$ allows for the intentional incorporation of various dopant ions, having excellent capability to accommodate ions of different sizes, creating significant opportunities for modification [121]. Though there are various dopant ions that can be implanted in $BaTiO_3$ lattice, here in the present dissertation work we have chosen Sr^{2+} doped $BaTiO_3$ due to its robust non-linear dielectric permittivity, small dielectric loss tangent, highly tunable, and sensible thermal stability of dielectric permittivity which are very useful during the development of tunable microwave devices [122,123]. Moreover, the structural properties of $BaTiO_3$ strongly depend on the concentration of Sr^{2+} ion doping in the Ba^{2+} site which in turn greatly affects its electrical properties [124,125]. While there has been some previous investigation into Sr^{2+}-doped $BaTiO_3$, there remains a requirement for a comprehensive analysis and the identification of connections among its various characteristics. This motivates us to use $Ba_{0.6}Sr_{0.4}TiO_3$ (BST40) (which is optimized) as a filler in PVDF for energy harvesting applications. In the context of energy harvesting, the BST40/PVDF composite film exhibited limited potential, primarily stemming from the constraints associated with the centrosymmetric crystal structure of BST40. To overcome the limitation arising from the centrosymmetric crystal structure of BST40, $(Ba_{0.85}Ca_{0.15})(Ti_{0.90}Hf_{0.10})O_3$ (BCHT) was introduced. Though $BaTiO_3$ is a very widely used filler material as far as hybrid

energy harvesting is concerned, the use of morphotropic phase boundary consisted filler materials is not much explored. Due to this multiple-phase coexistence, these materials show very high piezoelectricity. That's why BCHT particles were synthesized. These BCHT particles exhibited a significantly high piezoelectric charge coefficient of 333 pC/N and were incorporated as fillers to create flexible BCHT/PVDF composites. As far as our literature survey is concerned there is no report of using this material in hybrid energy harvesting applications. This strategic addition greatly bolstered the capabilities of piezoelectric energy harvesting, as the perovskite BCHT particles acted as nucleation centers, aligning the PVDF polymer chains in a trans conformation. Further, again to elaborate our material aspect we have introduced $BaTi_{0.89}Sn_{0.11}O_3$ (BTS) at the morphotropic phase boundary was prepared using a modified Pechini method. As a result of the presence of four different phases, BTS exhibited a piezoelectric charge coefficient (d_{33}) of approximately 412 pC/N. In this instance, we have shifted our attention towards an alternative negative triboelectric polymer matrix, namely, PDMS, instead of PVDF.

1.3 State of the art and scope of the thesis

The advent of triboelectric nanogenerator technology (developed by the Wang group in 2012), in conjunction with the introduction of the PENG by the Wang research group in 2006, has been widely acknowledged as a revolutionary development in the domains of energy harvesting and sensing. Various research methods, including bibliometrics, patent analysis, and technology road-mapping, have been employed to investigate its trends, impacts, and strategies for achieving large-scale commercialization [126–128]. The results of these studies reveal that the progression of nanogenerator technology is becoming increasingly interdisciplinary, necessitating contributions not only from materials science and nanotechnology but also from areas such as computer science, information systems, and various other fields [126–128]. The recent state of the art can be summarized like that,

a. New material search

As the strategy of HEH devices is nearly the same as that of TEH devices, research on new innovative triboelectric material with higher surface charge density is going on.

b. Structure optimization

Output enhancement through various structural modifications is a new trend of research in hybrid energy harvesting. The incorporation of various other energy harvesting technologies like solar energy is also in the development stage.

c. Wearable and flexible energy harvesters

Harvesting energy from various biomechanical sources research in the field of wearable and flexible energy harvesting has gained tremendous consideration. These gadgets can be incorporated into garments, footwear, and other wearable items to capture and store energy generated by the movement of the wearer.

d. Self-powered sensor

Hybrid energy harvesters have been incorporated into a range of sensors, including pressure sensors, strain sensors, environmental sensors, and writing pad sensors to facilitate self-sustained and wireless sensing systems.

e. High voltage power source

Due to the promise shown by hybrid energy harvesters in fruitfully generating high output voltage, research in this field is very much in progress. Research in wireless power transfer is gaining attention using this device.

f. Applications

HEH devices are under investigation for numerous applications, such as self-sustained electronic devices, distant monitoring systems, and IoT gadgets. They hold promise for supplying energy to low-power devices and sensors in remote or challenging-to-access areas.

Despite active research and the rapid development of HEH technology worldwide, it is in its infancy, and its widespread practical application requires further fundamental and technical advancements. One of the most critical parameters for energy harvesters, the output power density of TENG, is constrained by its intrinsic high-voltage and low-current characteristics. Additionally, there are material-related challenges including flexibility, that need to be addressed.

During my doctoral research, full dedication was given for advancing high-performance HEH technology and uncovering innovative applications. The ultimate aim is to offer accessible and cost-effective solutions to address the fundamental energy sustainability challenges in the era of the Internet of Things (IoT). The summary of the scope of the dissertation is

a. Fabrication of flexible hybrid energy harvester device where the synergistic enhancement of piezoelectricity and triboelectricity take place.
b. Inclusion of $BaTiO_3$-based filler materials that have high piezoelectricity.
c. Illustration of diverse applications in real-life scenarios like charging a capacitor, lighting LEDs, and powering up several low-powered electronic gadgets (i.e., digital watch, electronic calculator, digital screw gauge, digital hygrometer, etc.).
d. Demonstration of biomechanical energy harvesting from several daily life human movements like walking, jogging, and jumping as well as wrist movement, finger movement, ankle movement, and elbow movements.
e. Displaying of utilization of the HEH device in writing pad sensing which can differentiate letters written on it.
f. Demonstration of using the device as a smart sensor for a smart parking system which can show the vacant or filled state of a parking slot in a parking area.
g. Utilization of the fabricated device as a power source in a wireless power transfer system.

As previously mentioned, the primary focus of this dissertation is confined to the enhancement of several electronic properties of filler materials. While there are significant opportunities for exploring the surface treatment of the filler material, it falls beyond the current scope of our dissertation. In the thesis work only the vertical contact separation strategy is used for hybrid energy harvester fabrication, the application of using other techniques is out of the current scope. For device fabrication structural modification of the polymer matrix has a prominent essence but it is beyond our current scope of thesis.

1.4 Objective of the Dissertation

The thesis work is structured in such a way as to achieve the main intent which is to successfully hybridize the piezoelectric with triboelectric energy harvesting and

optimize the hybrid energy harvester device in utilizing it as a biomechanical energy harvester, smart switch to operate smart home appliances and smart parking sensor, biomechanical movement sensor, writing pad sensor, and a power source in wireless power transmission. Chapter 1 describes a brief introduction to piezoelectric energy harvesting, triboelectric energy harvesting, and hybridization of piezoelectricity with triboelectric energy harvester. Materials synthesis, composite film preparation, fabrication of the hybrid energy harvesting device, and its characterization techniques are described in Chapter 2. Ceramic Barium titanate ($BaTiO_3$)-based filler material, mainly the Strontium doped $BaTiO_3$ will be characterized in the next part (Chapter 3). After that, strontium-doped $BaTiO_3$ will be used as a filler in PVDF for piezoelectric energy harvesting and mechanosensing (Chapter 4). In the next step a piezoelectric material, Calcium (Ca) and Hafnium (Hf) doped $BaTiO_3$ is loaded inside PVDF to efficiently fabricate a piezo-tribo hybrid energy harvester for biomechanical movement sensing, and a wireless smart device application (Chapter 5). Chapter 6 of my thesis deals with the Tin doped $BaTiO_3$ loaded PDMS composed hybrid energy harvester device for biomechanical energy harvesting, using it as a writing pad sensor, and utilizing the device as a power source for wireless power transmission. This thesis work in this way will open up a new window in the field of piezo-tribo hybrid energy harvesting with multifunctional solutions for biomechanical movement sensing and energy harvesting, writing pattern sensing, using the device as a power source in wireless power transmission, and employing the fabricated device in wireless smart home and smart parking sensor applications which will play a pivotal role in self-powered electronics, robotics, real-time health-care monitoring, and artificial intelligence technologies.

The arrangement of the thesis is as follows:

Chapter 1: Introduction: short description of piezoelectric materials, piezoelectric energy harvester, triboelectric materials, triboelectric energy harvester, hybridization of piezoelectric with triboelectric energy harvester.

Chapter 2: Synthesis of ceramic particles, preparation of composite films, fabrication of piezoelectric-triboelectric hybrid energy harvester, characterization techniques.

Chapter 3: Sr^{2+} doped $BaTiO_3$ incorporated PVDF: an efficient piezoelectric energy harvester and mechanosensor.

Chapter 4: Multiphase Coexisted Perovskite/PVDF-based Piezo-Tribo Hybrid Energy Harvester: A Wearable Flexi-Electronic for Real-Time Wireless Smart Applications.

Chapter 5: Morphotropic Phase Boundary-Assisted Lead-Free $BaTiO_3$/PDMS Based Hybrid Energy Harvester: A Portable Power Source for Wireless Power Transmission

Chapter 6: Conclusion: Recap of the whole work and future perspectives.

Chapter 1

References

[1] M.Z. Jacobson, Review of solutions to global warming, air pollution, and energy security, Energy Environ Sci. 2 (2009) 148–173. https://doi.org/10.1039/b809990c.

[2] K. Hansen, C. Breyer, H. Lund, Status and perspectives on 100% renewable energy systems, Energy. 175 (2019) 471–480. https://doi.org/10.1016/j.energy.2019.03.092.

[3] P.A. Østergaard, N. Duic, Y. Noorollahi, H. Mikulcic, S. Kalogirou, Sustainable development using renewable energy technology, Renew Energy. 146 (2020) 2430–2437. https://doi.org/10.1016/j.renene.2019.08.094.

[4] J. Yu, Y.M. Tang, K.Y. Chau, R. Nazar, S. Ali, W. Iqbal, Role of solar-based renewable energy in mitigating CO2 emissions: Evidence from quantile-on-quantile estimation, Renew Energy. 182 (2022) 216–226. https://doi.org/10.1016/j.renene.2021.10.002.

[5] A. Rahman, O. Farrok, M.M. Haque, Environmental impact of renewable energy source based electrical power plants: Solar, wind, hydroelectric, biomass, geothermal, tidal, ocean, and osmotic, Renewable and Sustainable Energy Reviews. 161 (2022). https://doi.org/10.1016/j.rser.2022.112279.

[6] D.J. Arent, A. Wise, R. Gelman, The status and prospects of renewable energy for combating global warming, Energy Econ. 33 (2011) 584–593. https://doi.org/10.1016/j.eneco.2010.11.003.

[7] K. Hansen, C. Breyer, H. Lund, Status and perspectives on 100% renewable energy systems, Energy. 175 (2019) 471–480. https://doi.org/10.1016/j.energy.2019.03.092.

[8] N.L. Panwar, S.C. Kaushik, S. Kothari, Role of renewable energy sources in environmental protection: A review, Renewable and Sustainable Energy Reviews. 15 (2011) 1513–1524. https://doi.org/10.1016/j.rser.2010.11.037.

[9] H. Ryu, H.J. Yoon, S.W. Kim, Hybrid Energy Harvesters: Toward Sustainable Energy Harvesting, Advanced Materials. 31 (2019). https://doi.org/10.1002/adma.201802898.

[10] S.A. Graham, S.C. Chandrarathna, H. Patnam, P. Manchi, J.W. Lee, J.S. Yu, Harsh environment–tolerant and robust triboelectric nanogenerators for mechanical-energy harvesting, sensing, and energy storage in a smart home, Nano Energy. 80 (2021). https://doi.org/10.1016/j.nanoen.2020.105547.

[11] L. Liu, X. Guo, C. Lee, Promoting smart cities into the 5G era with multi-field Internet of Things (IoT) applications powered with advanced mechanical energy harvesters, Nano Energy. 88 (2021). https://doi.org/10.1016/j.nanoen.2021.106304.

[12] C. Lin, J. Yu, Z. Hua, J. Lan, H. Huang, D. Lu, S. Cao, X. Ma, Development progress, performance enhancement routes, and applications of paper-based triboelectric nanogenerators, Chemical Engineering Journal. 430 (2022). https://doi.org/10.1016/j.cej.2021.132559.

[13] J. Tian, X. Chen, Z.L. Wang, Environmental energy harvesting based on triboelectric nanogenerators, Nanotechnology. 31 (2020). https://doi.org/10.1088/1361-6528/ab793e.

[14] X. Cao, Y. Xiong, J. Sun, X. Xie, Q. Sun, Z.L. Wang, Multidiscipline Applications of Triboelectric Nanogenerators for the Intelligent Era of Internet of Things, Nanomicro Lett. 15 (2023). https://doi.org/10.1007/s40820-022-00981-8.

[15] P. Pandey, D.H. Jung, G.J. Choi, M.K. Seo, S. Lee, J.M. Kim, I.K. Park, J.I. Sohn, Nafion-mediated barium titanate-polymer composite nanofibers-based triboelectric nanogenerator for self-powered smart street and home control system, Nano Energy. 107 (2023). https://doi.org/10.1016/j.nanoen.2022.108134.

[16] F. Jiang, X. Zhou, J. Lv, J. Chen, J. Chen, H. Kongcharoen, Y. Zhang, P.S. Lee, Stretchable, Breathable, and Stable Lead-Free Perovskite/Polymer Nanofiber Composite for Hybrid Triboelectric and Piezoelectric Energy Harvesting, Advanced Materials. 34 (2022). https://doi.org/10.1002/adma.202200042.

[17] S. Hajra, A.M. Padhan, M. Sahu, P. Alagarsamy, K. Lee, H.J. Kim, Lead-free flexible Bismuth Titanate-PDMS composites: A multifunctional colossal dielectric material for hybrid piezo-triboelectric nanogenerator to sustainably

power portable electronics, Nano Energy. 89 (2021). https://doi.org/10.1016/j.nanoen.2021.106316.

[18] E. Kar, P. Ghosh, S. Pratihar, M. Tavakoli, S. Sen, Nature-Driven Biocompatible Epidermal Electronic Skin for Real-Time Wireless Monitoring of Human Physiological Signals, ACS Appl Mater Interfaces. (2023). https://doi.org/10.1021/acsami.3c00509.

[19] B. Shi, Z. Liu, Q. Zheng, J. Meng, H. Ouyang, Y. Zou, D. Jiang, X. Qu, M. Yu, L. Zhao, Y. Fan, Z.L. Wang, Z. Li, Body-Integrated Self-Powered System for Wearable and Implantable Applications, ACS Nano. 13 (2019) 6017–6024. https://doi.org/10.1021/acsnano.9b02233.

[20] T. Tat, A. Libanori, C. Au, A. Yau, J. Chen, Advances in triboelectric nanogenerators for biomedical sensing, Biosens Bioelectron. 171 (2021). https://doi.org/10.1016/j.bios.2020.112714.

[21] X. Cao, Y. Xiong, J. Sun, X. Xie, Q. Sun, Z.L. Wang, Multidiscipline Applications of Triboelectric Nanogenerators for the Intelligent Era of Internet of Things, Nanomicro Lett. 15 (2023). https://doi.org/10.1007/s40820-022-00981-8.

[22] P. Pandey, K. Thapa, G.P. Ojha, M.K. Seo, K.H. Shin, S.W. Kim, J.I. Sohn, Metal-organic frameworks-based triboelectric nanogenerator powered visible light communication system for wireless human-machine interactions, Chemical Engineering Journal. 452 (2023). https://doi.org/10.1016/j.cej.2022.139209.

[23] S. Mondal, T. Paul, S. Maiti, B.K. Das, K.K. Chattopadhyay, Human motion interactive mechanical energy harvester based on all inorganic perovskite-PVDF, Nano Energy. 74 (2020). https://doi.org/10.1016/j.nanoen.2020.104870.

[24] C. Qiu, F. Wu, C. Lee, M.R. Yuce, Self-powered control interface based on Gray code with hybrid triboelectric and photovoltaics energy harvesting for IoT smart home and access control applications, Nano Energy. 70 (2020). https://doi.org/10.1016/j.nanoen.2020.104456.

[25] Y. Bai, H. Jantunen, J. Juuti, Energy harvesting research: The road from single source to multisource, Advanced Materials. 30 (2018). https://doi.org/10.1002/adma.201707271.

[26] J. Yun, J. Park, M. Ryoo, N. Kitchamsetti, T.S. Goh, D. Kim, Piezo-triboelectric hybridized nanogenerator embedding MXene based bifunctional conductive filler in polymer matrix for boosting electrical power, Nano Energy. 105 (2023). https://doi.org/10.1016/j.nanoen.2022.108018.

[27] P. Maharjan, T. Bhatta, M. Salauddin Rasel, M. Salauddin, M. Toyabur Rahman, J.Y. Park, High-performance cycloid inspired wearable electromagnetic energy harvester for scavenging human motion energy, Appl Energy. 256 (2019). https://doi.org/10.1016/j.apenergy.2019.113987.

[28] B. Yang, C. Lee, W. Xiang, J. Xie, J. Han He, R.K. Kotlanka, S.P. Low, H. Feng, Electromagnetic energy harvesting from vibrations of multiple frequencies, Journal of Micromechanics and Microengineering. 19 (2009). https://doi.org/10.1088/0960-1317/19/3/035001.

[29] C.R. Saha, T. O'Donnell, H. Loder, S. Beeby, J. Tudor, Optimization of an electromagnetic energy harvesting device, IEEE Trans Magn. 42 (2006) 3509–3511. https://doi.org/10.1109/TMAG.2006.879447.

[30] A. Sasmal, S. Maity, P. Maiti, A. Arockiarajan, S. Sen, Nano to micrometer range particle size effect on the electrical and piezoelectric energy harvesting performances of hydroxide mediated crosslinked PVDF composites, Chemical Engineering Journal. 468 (2023) 143794. https://doi.org/10.1016/j.cej.2023.143794.

[31] C. Covaci, A. Gontean, Piezoelectric energy harvesting solutions: A review, Sensors (Switzerland). 20 (2020) 1–37. https://doi.org/10.3390/s20123512.

[32] W. Deng, Y. Zhou, A. Libanori, G. Chen, W. Yang, J. Chen, Piezoelectric nanogenerators for personalized healthcare, Chem Soc Rev. (2022). https://doi.org/10.1039/d1cs00858g.

[33] Q. Xu, J. Wen, Y. Qin, Development and outlook of high output piezoelectric nanogenerators, Nano Energy. 86 (2021). https://doi.org/10.1016/j.nanoen.2021.106080.

[34] W. Zhai, J. Nie, L. Zhu, Enhanced Flexible Poly(vinylidene fluoride-trifluorethylene) Piezoelectric Nanogenerators by SnSe Nanosheet Doping and

Solvent Treatment, ACS Appl Mater Interfaces. 13 (2021) 32278–32285. https://doi.org/10.1021/acsami.1c08347.

[35] S. Xu, Y.W. Yeh, G. Poirier, M.C. McAlpine, R.A. Register, N. Yao, Flexible piezoelectric PMN-PT nanowire-based nanocomposite and device, Nano Lett. 13 (2013) 2393–2398. https://doi.org/10.1021/nl400169t.

[36] E. Kar, N. Bose, S. Das, N. Mukherjee, S. Mukherjee, Enhancement of electroactive β phase crystallization and dielectric constant of PVDF by incorporating GeO2 and SiO2 nanoparticles, Physical Chemistry Chemical Physics. 17 (2015) 22784–22798. https://doi.org/10.1039/c5cp03975d.

[37] S. Tiwari, A. Gaur, C. Kumar, P. Maiti, Enhanced piezoelectric response in nanoclay induced electrospun PVDF nanofibers for energy harvesting, Energy. 171 (2019) 485–492. https://doi.org/10.1016/j.energy.2019.01.043.

[38] S.S. Nardekar, K. Krishnamoorthy, P. Pazhamalai, S. Sahoo, S. Jae Kim, MoS2 quantum sheets-PVDF nanocomposite film based self-poled piezoelectric nanogenerators and photovoltaically self-charging power cell, Nano Energy. 93 (2022). https://doi.org/10.1016/j.nanoen.2021.106869.

[39] G. Tian, W. Deng, Y. Gao, D. Xiong, C. Yan, X. He, T. Yang, L. Jin, X. Chu, H. Zhang, W. Yan, W. Yang, Rich lamellar crystal baklava-structured PZT/PVDF piezoelectric sensor toward individual table tennis training, Nano Energy. 59 (2019) 574–581. https://doi.org/10.1016/j.nanoen.2019.03.013.

[40] C. Chen, Z. Bai, Y. Cao, M. Dong, K. Jiang, Y. Zhou, Y. Tao, S. Gu, J. Xu, X. Yin, W. Xu, Enhanced piezoelectric performance of BiCl3/PVDF nanofibers-based nanogenerators, Compos Sci Technol. 192 (2020). https://doi.org/10.1016/j.compscitech.2020.108100.

[41] J. Fu, Y. Hou, X. Gao, M. Zheng, M. Zhu, Highly durable piezoelectric energy harvester based on a PVDF flexible nanocomposite filled with oriented BaTi2O5 nanorods with high power density, Nano Energy. 52 (2018) 391–401. https://doi.org/10.1016/j.nanoen.2018.08.006.

[42] N.A. Hoque, P. Thakur, P. Biswas, M.M. Saikh, S. Roy, B. Bagchi, S. Das, P.P. Ray, Biowaste crab shell-extracted chitin nanofiber-based superior piezoelectric

nanogenerator, J Mater Chem A Mater. 6 (2018) 13848–13858. https://doi.org/10.1039/c8ta04074e.

[43] S. Dai, X. Li, C. Jiang, J. Ping, Y. Ying, Triboelectric nanogenerators for smart agriculture, InfoMat. 5 (2023). https://doi.org/10.1002/inf2.12391.

[44] M.F. Lin, K.W. Chang, C.H. Lee, X.X. Wu, Y.C. Huang, Electrospun P3HT/PVDF-HFP semiconductive nanofibers for triboelectric nanogenerators, Sci Rep. 12 (2022). https://doi.org/10.1038/s41598-022-19306-1.

[45] Y. Su, G. Chen, C. Chen, Q. Gong, G. Xie, M. Yao, H. Tai, Y. Jiang, J. Chen, Self-Powered Respiration Monitoring Enabled By a Triboelectric Nanogenerator, Advanced Materials. 33 (2021). https://doi.org/10.1002/adma.202101262.

[46] A. Chen, C. Zhang, G. Zhu, Z.L. Wang, Polymer Materials for High-Performance Triboelectric Nanogenerators, Advanced Science. 7 (2020). https://doi.org/10.1002/advs.202000186.

[47] D.W. Lee, D.G. Jeong, J.H. Kim, H.S. Kim, G. Murillo, G.H. Lee, H.C. Song, J.H. Jung, Polarization-controlled PVDF-based hybrid nanogenerator for an effective vibrational energy harvesting from human foot, Nano Energy. 76 (2020). https://doi.org/10.1016/j.nanoen.2020.105066.

[48] X. Li, Z.H. Lin, G. Cheng, X. Wen, Y. Liu, S. Niu, Z.L. Wang, 3D fiber-based hybrid nanogenerator for energy harvesting and as a self-powered pressure sensor, ACS Nano. 8 (2014) 10674–10681. https://doi.org/10.1021/nn504243j.

[49] C. Zhao, Q. Zhang, W. Zhang, X. Du, Y. Zhang, S. Gong, K. Ren, Q. Sun, Z.L. Wang, Hybrid piezo/triboelectric nanogenerator for highly efficient and stable rotation energy harvesting, Nano Energy. 57 (2019) 440–449. https://doi.org/10.1016/j.nanoen.2018.12.062.

[50] S. Pongampai, T. Charoonsuk, N. Pinpru, P. Pulphol, W. Vittayakorn, P. Pakawanit, N. Vittayakorn, Triboelectric-piezoelectric hybrid nanogenerator based on BaTiO3-Nanorods/Chitosan enhanced output performance with self-charge-pumping system, Compos B Eng. 208 (2021). https://doi.org/10.1016/j.compositesb.2020.108602.

[51] D.H. Kim, B. Dudem, J.S. Yu, High-Performance Flexible Piezoelectric-Assisted Triboelectric Hybrid Nanogenerator via Polydimethylsiloxane-Encapsulated Nanoflower-like ZnO Composite Films for Scavenging Energy from Daily Human Activities, ACS Sustain Chem Eng. 6 (2018) 8525–8535. https://doi.org/10.1021/acssuschemeng.8b00834.

[52] H. Patnam, B. Dudem, N.R. Alluri, A.R. Mule, S.A. Graham, S.J. Kim, J.S. Yu, Piezo/triboelectric hybrid nanogenerators based on Ca-doped barium zirconate titanate embedded composite polymers for wearable electronics, Compos Sci Technol. 188 (2020). https://doi.org/10.1016/j.compscitech.2019.107963.

[53] M. Sahu, V. Vivekananthan, S. Hajra, K. Khatua, S.-J. Kim, Porosity modulated piezo-triboelectric hybridized nanogenerator for sensing small energy impacts, (2020). https://doi.org/10.1016/j.apmt.2020.10.

[54] P. Ueberschlag, PVDF piezoelectric polymer, n.d. http://www.emerald-library.com/ft.

[55] theory of piezoeleectricity, (n.d.).

[56] H. JAFFE, Piezoelectric Ceramics, Journal of the American Ceramic Society. 41 (1958) 494–498. https://doi.org/10.1111/j.1151-2916.1958.tb12903.x.

[57] Z. Yang, S. Zhou, J. Zu, D. Inman, High-Performance Piezoelectric Energy Harvesters and Their Applications, Joule. 2 (2018) 642–697. https://doi.org/10.1016/j.joule.2018.03.011.

[58] D. Damjanovic, Ferroelectric, dielectric and piezoelectric properties of ferroelectric thin films and ceramics, 1998.

[59] S. Pan, Z. Zhang, Fundamental theories and basic principles of triboelectric effect: A review, Friction. 7 (2019) 2–17. https://doi.org/10.1007/s40544-018-0217-7.

[60] V. Slabov, S. Kopyl, M.P. Soares dos Santos, A.L. Kholkin, Natural and Eco-Friendly Materials for Triboelectric Energy Harvesting, Nanomicro Lett. 12 (2020). https://doi.org/10.1007/s40820-020-0373-y.

[61] C. Wu, A.C. Wang, W. Ding, H. Guo, Z.L. Wang, Triboelectric Nanogenerator: A Foundation of the Energy for the New Era, Adv Energy Mater. 9 (2019). https://doi.org/10.1002/aenm.201802906.

[62] F.R. Fan, Z.Q. Tian, Z. Lin Wang, Flexible triboelectric generator, Nano Energy. 1 (2012) 328–334. https://doi.org/10.1016/j.nanoen.2012.01.004.

[63] S. Wang, L. Lin, Z.L. Wang, Nanoscale triboelectric-effect-enabled energy conversion for sustainably powering portable electronics, Nano Lett. 12 (2012) 6339–6346. https://doi.org/10.1021/nl303573d.

[64] W.G. Kim, D.W. Kim, I.W. Tcho, J.K. Kim, M.S. Kim, Y.K. Choi, Triboelectric Nanogenerator: Structure, Mechanism, and Applications, ACS Nano. 15 (2021) 258–287. https://doi.org/10.1021/acsnano.0c09803.

[65] Y. Zi, Z.L. Wang, Nanogenerators: An emerging technology towards nanoenergy, APL Mater. 5 (2017). https://doi.org/10.1063/1.4977208.

[66] Z.L. Wang, J. Chen, L. Lin, Progress in triboelectric nanogenerators as a new energy technology and self-powered sensors, Energy Environ Sci. 8 (2015) 2250–2282. https://doi.org/10.1039/c5ee01532d.

[67] W. Yang, J. Chen, G. Zhu, J. Yang, P. Bai, Y. Su, Q. Jing, X. Cao, Z.L. Wang, Harvesting energy from the natural vibration of human walking, ACS Nano. 7 (2013) 11317–11324. https://doi.org/10.1021/nn405175z.

[68] G. Zhu, P. Bai, J. Chen, Z. Lin Wang, Power-generating shoe insole based on triboelectric nanogenerators for self-powered consumer electronics, Nano Energy. 2 (2013) 688–692. https://doi.org/10.1016/j.nanoen.2013.08.002.

[69] T.C. Hou, Y. Yang, H. Zhang, J. Chen, L.J. Chen, Z. Lin Wang, Triboelectric nanogenerator built inside shoe insole for harvesting walking energy, Nano Energy. 2 (2013) 856–862. https://doi.org/10.1016/j.nanoen.2013.03.001.

[70] J. Zhong, Q. Zhong, F. Fan, Y. Zhang, S. Wang, B. Hu, Z.L. Wang, J. Zhou, Finger typing driven triboelectric nanogenerator and its use for instantaneously lighting up LEDs, Nano Energy. 2 (2013) 491–497. https://doi.org/10.1016/j.nanoen.2012.11.015.

[71] X.S. Zhang, M. Di Han, R.X. Wang, F.Y. Zhu, Z.H. Li, W. Wang, H.X. Zhang, Frequency-multiplication high-output triboelectric nanogenerator for sustainably powering biomedical microsystems, Nano Lett. 13 (2013) 1168–1172. https://doi.org/10.1021/nl3045684.

[72] Z.H. Lin, Y. Xie, Y. Yang, S. Wang, G. Zhu, Z.L. Wang, Enhanced triboelectric nanogenerators and triboelectric nanosensor using chemically modified TiO2 nanomaterials, ACS Nano. 7 (2013) 4554–4560. https://doi.org/10.1021/nn401256w.

[73] Y. Yang, L. Lin, Y. Zhang, Q. Jing, T.C. Hou, Z.L. Wang, Self-powered magnetic sensor based on a triboelectric nanogenerator, ACS Nano. 6 (2012) 10378–10383. https://doi.org/10.1021/nn304374m.

[74] Z.H. Lin, G. Zhu, Y.S. Zhou, Y. Yang, P. Bai, J. Chen, Z.L. Wang, A self-powered triboelectric nanosensor for mercury ion detection, Angewandte Chemie - International Edition. 52 (2013) 5065–5069. https://doi.org/10.1002/anie.201300437.

[75] J. Chen, G. Zhu, W. Yang, Q. Jing, P. Bai, Y. Yang, T.C. Hou, Z.L. Wang, Harmonic-resonator-based triboelectric nanogenerator as a sustainable power source and a self-powered active vibration sensor, Advanced Materials. 25 (2013) 6094–6099. https://doi.org/10.1002/adma.201302397.

[76] L. Lin, Y. Xie, S. Wang, W. Wu, S. Niu, X. Wen, Z.L. Wang, Triboelectric active sensor array for self-powered static and dynamic pressure detection and tactile imaging, ACS Nano. 7 (2013) 8266–8274. https://doi.org/10.1021/nn4037514.

[77] H. Zhang, Y. Yang, X. Zhong, Y. Su, Y. Zhou, C. Hu, Z.L. Wang, Single-electrode-based rotating triboelectric nanogenerator for harvesting energy from tires, ACS Nano. 8 (2014) 680–689. https://doi.org/10.1021/nn4053292.

[78] Y. Yang, G. Zhu, H. Zhang, J. Chen, X. Zhong, Z.H. Lin, Y. Su, P. Bai, X. Wen, Z.L. Wang, Triboelectric nanogenerator for harvesting wind energy and as self-powered wind vector sensor system, ACS Nano. 7 (2013) 9461–9468. https://doi.org/10.1021/nn4043157.

[79] Q. Liang, X. Yan, Y. Gu, K. Zhang, M. Liang, S. Lu, X. Zheng, Y. Zhang, Highly transparent triboelectric nanogenerator for harvesting water-related energy reinforced by antireflection coating, Sci Rep. 5 (2015). https://doi.org/10.1038/srep09080.

[80] Q. Zhong, J. Zhong, B. Hu, Q. Hu, J. Zhou, Z.L. Wang, A paper-based nanogenerator as a power source and active sensor, Energy Environ Sci. 6 (2013) 1779–1784. https://doi.org/10.1039/c3ee40592c.

[81] S. Niu, Y. Liu, X. Chen, S. Wang, Y.S. Zhou, L. Lin, Y. Xie, Z.L. Wang, Theory of freestanding triboelectric-layer-based nanogenerators, Nano Energy. 12 (2015) 760–774. https://doi.org/10.1016/j.nanoen.2015.01.013.

[82] L. Zhang, C. Su, X. Cui, P. Li, Z. Wang, L. Gu, Z. Tang, Free-standing triboelectric layer-based full fabric wearable nanogenerator for efficient mechanical energy harvesting, ACS Appl Electron Mater. 2 (2020) 3366–3372. https://doi.org/10.1021/acsaelm.0c00646.

[83] S. Wang, Y. Xie, S. Niu, L. Lin, Z.L. Wang, Freestanding triboelectric-layer-based nanogenerators for harvesting energy from a moving object or human motion in contact and non-contact modes, Advanced Materials. 26 (2014) 2818–2824. https://doi.org/10.1002/adma.201305303.

[84] H. Zou, Y. Zhang, L. Guo, P. Wang, X. He, G. Dai, H. Zheng, C. Chen, A.C. Wang, C. Xu, Z.L. Wang, Quantifying the triboelectric series, Nat Commun. 10 (2019). https://doi.org/10.1038/s41467-019-09461-x.

[85] M.A. Parvez Mahmud, N. Huda, S.H. Farjana, M. Asadnia, C. Lang, Recent Advances in Nanogenerator-Driven Self-Powered Implantable Biomedical Devices, Adv Energy Mater. 8 (2018). https://doi.org/10.1002/aenm.201701210.

[86] Z.L. Wang, On Maxwell's displacement current for energy and sensors: the origin of nanogenerators, Materials Today. 20 (2017) 74–82. https://doi.org/10.1016/j.mattod.2016.12.001.

[87] Y. Wu, J. Qu, W.A. Daoud, L. Wang, T. Qi, Flexible composite-nanofiber based piezo-triboelectric nanogenerators for wearable electronics, J Mater Chem A Mater. 7 (2019) 13347–13355. https://doi.org/10.1039/c9ta02345c.

[88] M. Sahu, V. Vivekananthan, S. Hajra, K.S. Abisegapriyan, N.P. Maria Joseph Raj, S.J. Kim, Synergetic enhancement of energy harvesting performance in triboelectric nanogenerator using ferroelectric polarization for self-powered IR signaling and body activity monitoring, J Mater Chem A Mater. 8 (2020) 22257–22268. https://doi.org/10.1039/d0ta06215d.

[89] M. Smith, S. Kar-Narayan, Piezoelectric polymers: theory, challenges and opportunities, International Materials Reviews. 67 (2022) 65–88. https://doi.org/10.1080/09506608.2021.1915935.

[90] K.S. Ramadan, D. Sameoto, S. Evoy, A review of piezoelectric polymers as functional materials for electromechanical transducers, Smart Mater Struct. 23 (2014). https://doi.org/10.1088/0964-1726/23/3/033001.

[91] S. Ippili, V. Jella, A.M. Thomas, C. Yoon, J.S. Jung, S.G. Yoon, ZnAl-LDH-induced electroactive β-phase and controlled dielectrics of PVDF for a high-performance triboelectric nanogenerator for humidity and pressure sensing applications, J Mater Chem A Mater. 9 (2021) 15993–16005. https://doi.org/10.1039/d1ta02966e.

[92] A. Sasmal, S. Sen, P.S. Devi, Frequency dependent energy storage and dielectric performance of Ba-Zr Co-doped BiFeO3loaded PVDF based mechanical energy harvesters: Effect of corona poling, Soft Matter. 16 (2020) 8492–8505. https://doi.org/10.1039/d0sm01031f.

[93] A. Sasmal, A. Patra, S. Maity, S. Pratihar, S. Sen, Multiferroic BiFeO3-based hydrophobic polymer composites for polarization rationalization-induced piezo-tribo hybrid energy harvesting and versatile self-powered mechanosensing, Sustain Energy Fuels. 6 (2022) 4652–4668. https://doi.org/10.1039/d2se00947a.

[94] H.H. Singh, N. Khare, Improved performance of ferroelectric nanocomposite flexible film based triboelectric nanogenerator by controlling surface

morphology, polarizability, and hydrophobicity, Energy. 178 (2019) 765–771. https://doi.org/10.1016/j.energy.2019.04.150.

[95] N. Soin, P. Zhao, K. Prashanthi, J. Chen, P. Ding, E. Zhou, T. Shah, S.C. Ray, C. Tsonos, T. Thundat, E. Siores, J. Luo, High performance triboelectric nanogenerators based on phase-inversion piezoelectric membranes of poly(vinylidene fluoride)-zinc stannate (PVDF-ZnSnO3) and polyamide-6 (PA6), Nano Energy. 30 (2016) 470–480. https://doi.org/10.1016/j.nanoen.2016.10.040.

[96] X. Tao, H. Jin, M. Ma, L. Quan, J. Chen, S. Dong, H. Zhang, C. Lv, Y. Fu, J. Luo, Significantly Enhanced Performance of Triboelectric Nanogenerator by Incorporating BaTiO3 Nanoparticles in Poly(vinylidene fluoride) Film, Physica Status Solidi (A) Applications and Materials Science. 216 (2019). https://doi.org/10.1002/pssa.201900068.

[97] X. Yang, W.A. Daoud, Triboelectric and Piezoelectric Effects in a Combined Tribo-Piezoelectric Nanogenerator Based on an Interfacial ZnO Nanostructure, Adv Funct Mater. 26 (2016) 8194–8201. https://doi.org/10.1002/adfm.201602529.

[98] C. Jirayupat, W. Wongwiriyapan, P. Kasamechonchung, T. Wutikhun, K. Tantisantisom, Y. Rayanasukha, T. Jiemsakul, C. Tansarawiput, M. Liangruksa, P. Khanchaitit, M. Horprathum, S. Porntheeraphat, A. Klamchuen, Piezoelectric-Induced Triboelectric Hybrid Nanogenerators Based on the ZnO Nanowire Layer Decorated on the Au/polydimethylsiloxane-Al Structure for Enhanced Triboelectric Performance, ACS Appl Mater Interfaces. 10 (2018) 6433–6440. https://doi.org/10.1021/acsami.7b17314.

[99] T. Huang, C. Wang, H. Yu, H. Wang, Q. Zhang, M. Zhu, Human walking-driven wearable all-fiber triboelectric nanogenerator containing electrospun polyvinylidene fluoride piezoelectric nanofibers, Nano Energy. 14 (2014) 226–235. https://doi.org/10.1016/j.nanoen.2015.01.038.

[100] M.S. Rasel, P. Maharjan, J.Y. Park, Hand clapping inspired integrated multilayer hybrid nanogenerator as a wearable and universal power source for

portable electronics, Nano Energy. 63 (2019). https://doi.org/10.1016/j.nanoen.2019.06.012.

[101] W. Yang, W. Gong, C. Hou, Y. Su, Y. Guo, W. Zhang, Y. Li, Q. Zhang, H. Wang, All-fiber tribo-ferroelectric synergistic electronics with high thermal-moisture stability and comfortability, Nat Commun. 10 (2019). https://doi.org/10.1038/s41467-019-13569-5.

[102] M.T. Rahman, M. Salauddin, P. Maharjan, M.S. Rasel, H. Cho, J.Y. Park, Natural wind-driven ultra-compact and highly efficient hybridized nanogenerator for self-sustained wireless environmental monitoring system, Nano Energy. 57 (2019) 256–268. https://doi.org/10.1016/j.nanoen.2018.12.052.

[103] H. Deng, J. Ye, Y. Du, J. Zhang, M. Ma, X. Zhong, Bistable broadband hybrid generator for ultralow-frequency rectilinear motion, Nano Energy. 65 (2019). https://doi.org/10.1016/j.nanoen.2019.103973.

[104] J. He, T. Wen, S. Qian, Z. Zhang, Z. Tian, J. Zhu, J. Mu, X. Hou, W. Geng, J. Cho, J. Han, X. Chou, C. Xue, Triboelectric-piezoelectric-electromagnetic hybrid nanogenerator for high-efficient vibration energy harvesting and self-powered wireless monitoring system, Nano Energy. 43 (2018) 326–339. https://doi.org/10.1016/j.nanoen.2017.11.039.

[105] Y. Zou, J. Liao, H. Ouyang, D. Jiang, C. Zhao, Z. Li, X. Qu, Z. Liu, Y. Fan, B. Shi, L. Zheng, Z. Li, A flexible self-arched biosensor based on combination of piezoelectric and triboelectric effects, Appl Mater Today. 20 (2020). https://doi.org/10.1016/j.apmt.2020.100699.

[106] O. Yue, X. Wang, X. Liu, M. Hou, M. Zheng, Y. Wang, B. Cui, Spider-Web and Ant-Tentacle Doubly Bio-Inspired Multifunctional Self-Powered Electronic Skin with Hierarchical Nanostructure, Advanced Science. 8 (2021). https://doi.org/10.1002/advs.202004377.

[107] Q. Wang, H.X. Zou, L.C. Zhao, M. Li, K.X. Wei, L.P. Huang, W.M. Zhang, A synergetic hybrid mechanism of piezoelectric and triboelectric for galloping wind energy harvesting, Appl Phys Lett. 117 (2020). https://doi.org/10.1063/5.0014484.

[108] Y. Ji, K. Zhang, Y. Yang, A One-Structure-Based Multieffects Coupled Nanogenerator for Simultaneously Scavenging Thermal, Solar, and Mechanical Energies, Advanced Science. 5 (2018). https://doi.org/10.1002/advs.201700622.

[109] S.M.S. Rana, M.T. Rahman, M. Salauddin, S. Sharma, P. Maharjan, T. Bhatta, H. Cho, C. Park, J.Y. Park, Electrospun PVDF-TrFE/MXene Nanofiber Mat-Based Triboelectric Nanogenerator for Smart Home Appliances, ACS Appl Mater Interfaces. 13 (2021) 4955–4967. https://doi.org/10.1021/acsami.0c17512.

[110] A.M. Abdullah, M.U.K. Sadaf, F. Tasnim, H. Vasquez, K. Lozano, M.J. Uddin, KNN based piezo-triboelectric lead-free hybrid energy films, Nano Energy. 86 (2021). https://doi.org/10.1016/j.nanoen.2021.106133.

[111] P. Zhang, W. Zhang, L. Deng, H. Zhang, A triboelectric nanogenerator based on temperature-stable high dielectric BaTiO3-based ceramic powder for energy harvesting, Nano Energy. 87 (2021). https://doi.org/10.1016/j.nanoen.2021.106176.

[112] B. Dudem, L.K. Bharat, H. Patnam, A.R. Mule, J.S. Yu, Enhancing the output performance of hybrid nanogenerators based on Al-doped BaTiO3 composite films: A self-powered utility system for portable electronics, J Mater Chem A Mater. 6 (2018) 16101–16110. https://doi.org/10.1039/c8ta04612c.

[113] X. Yang, W.A. Daoud, Synergetic effects in composite-based flexible hybrid mechanical energy harvesting generator, J Mater Chem A Mater. 5 (2017) 9113–9121. https://doi.org/10.1039/c7ta01524k.

[114] S. Yu, Y. Zhang, Z. Yu, J. Zheng, Y. Wang, H. Zhou, PANI/PVDF-TrFE porous aerogel bulk piezoelectric and triboelectric hybrid nanogenerator based on in-situ doping and liquid nitrogen quenching, Nano Energy. 80 (2021). https://doi.org/10.1016/j.nanoen.2020.105519.

[115] P. Manchi, S.A. Graham, B. Dudem, H. Patnam, J.S. Yu, Improved performance of nanogenerator via synergetic piezo/triboelectric effects of lithium niobate microparticles embedded composite films, Compos Sci Technol. 201 (2021). https://doi.org/10.1016/j.compscitech.2020.108540.

[116] Y. Guo, X.S. Zhang, Y. Wang, W. Gong, Q. Zhang, H. Wang, J. Brugger, All-fiber hybrid piezoelectric-enhanced triboelectric nanogenerator for wearable gesture monitoring, Nano Energy. 48 (2018) 152–160. https://doi.org/10.1016/j.nanoen.2018.03.033.

[117] S.R. Gopal, T.S. Velayutham, W.C. Gan, J.Y. Cheong, A.E. Soh, A hybrid piezoelectric and triboelectric nanogenerator with lead-free BZT-BCT/PDMS composite and PVA film for scavenging mechanical energy, RSC Adv. 13 (2023) 7921–7928. https://doi.org/10.1039/d3ra00077j.

[118] X. Yang, W.A. Daoud, Synergetic effects in composite-based flexible hybrid mechanical energy harvesting generator, J Mater Chem A Mater. 5 (2017) 9113–9121. https://doi.org/10.1039/c7ta01524k.

[119] W. He, Y. Qian, B.S. Lee, F. Zhang, A. Rasheed, J.E. Jung, D.J. Kang, Ultrahigh Output Piezoelectric and Triboelectric Hybrid Nanogenerators Based on ZnO Nanoflakes/Polydimethylsiloxane Composite Films, ACS Appl Mater Interfaces. 10 (2018) 44415–44420. https://doi.org/10.1021/acsami.8b15410.

[120] A.R. Chowdhury, A.M. Abdullah, I. Hussain, J. Lopez, D. Cantu, S.K. Gupta, Y. Mao, S. Danti, M.J. Uddin, Lithium doped zinc oxide based flexible piezoelectric-triboelectric hybrid nanogenerator, Nano Energy. 61 (2019) 327–336. https://doi.org/10.1016/j.nanoen.2019.04.085.

[121] M. Acosta, N. Novak, V. Rojas, S. Patel, R. Vaish, J. Koruza, G.A. Rossetti, BaTiO3-based piezoelectrics: Fundamentals, current status, and perspectives, 041305 (2017).

[122] D. Zhang, W. Hu, C. Meggs, B. Su, T. Price, D. Iddles, M.J. Lancaster, T.W. Button, Fabrication and characterisation of barium strontium titanate thick film device structures for microwave applications, J Eur Ceram Soc. 27 (2007) 1047–1051. https://doi.org/10.1016/j.jeurceramsoc.2006.05.051.

[123] P. Bao, T.J. Jackson, X. Wang, M.J. Lancaster, Barium strontium titanate thin film varactors for room-temperature microwave device applications, J Phys D Appl Phys. 41 (2008). https://doi.org/10.1088/0022-3727/41/6/063001.

[124] S. Sasikumar, S. Saravanakumar, S. Asath Bahadur, D. Sivaganesh, Electronic structure, optical and chemical bonding properties of strontium doped Barium Titanate, Optik (Stuttg). 206 (2020) 163752. https://doi.org/10.1016/j.ijleo.2019.163752.

[125] M. Ben Chamekh, Z. Ben Achour, A. Thamri, R. Chtourou, E. Dhahri, O. Touayar, Structural and electrical characterization of strontium doped barium titanate for radiometric measurement, Chem Phys Lett. 761 (2020) 138008. https://doi.org/10.1016/j.cplett.2020.138008.

[126] A. Ahmed, I. Hassan, T. Ibn-Mohammed, H. Mostafa, I.M. Reaney, L.S.C. Koh, J. Zu, Z.L. Wang, Environmental life cycle assessment and techno-economic analysis of triboelectric nanogenerators, Energy Environ Sci. 10 (2017) 653–671. https://doi.org/10.1039/c7ee00158d.

[127] H. Askari, A. Khajepour, M.B. Khamesee, Z. Saadatnia, Z.L. Wang, Piezoelectric and triboelectric nanogenerators: Trends and impacts, Nano Today. 22 (2018) 10–13. https://doi.org/10.1016/j.nantod.2018.08.001.

[128] H. Peng, X. Fang, S. Ranaei, Z. Wen, A.L. Porter, Forecasting potential sensor applications of triboelectric nanogenerators through tech mining, Nano Energy. 35 (2017) 358–369. https://doi.org/10.1016/j.nanoen.2017.04.006.

Chapter 2

Synthesis, device fabrication, and characterizations

This chapter aims to describe the detailed experimental procedures for the synthesis of different Barium Titanate-based particles and PVDF/PDMS-based composites. The fabrication techniques of several PVDF/PDMS composite-based piezoelectric, triboelectric, and hybrid energy harvester devices have also been included in this chapter. In addition to that, this chapter also describes the different types of characterization methods/tools (with instrument specification) adopted for the fulfillment of the entire work.

2.1. Synthesis of materials:

Facile and reproducible synthesis procedures have been adopted to produce the required Barium Titanate ($BaTiO_3$) based filler particles for PVDF and PDMS-based composites. Mainly, solid state and modified Pechini methods were employed in this work to synthesize Barium Titanate-based materials. The polymer composites were prepared using a simple mixing-solution casting-drying technique.

2.1.1. Solid State method:

A solid-state method is a synthesis procedure where reagent materials are mixed in a solid phase without the need for any solvents to produce the required product. The solid mixed oxide reaction method usually consists of the mixing of reagent oxides or carbonates using the ball milling method and calcination at high temperatures [1,2].

Advantages of the Solid-State Method:

1. **Purity and Homogeneity:** This method usually involves working with crystalline or solid materials, which can lead to greater purity and homogeneity in the final product. This is especially beneficial where the properties of a material can be highly dependent on its purity and uniformity.
2. **Less Environmental Impact:** Solid-state methods can result in reduced waste generation and the use of hazardous solvents, leading to smaller environmental damage.

3. **Ease of handling:** Solid materials are easier to handle than liquid solvent-based reaction methods.
4. **Precursor Compatibility:** Certain reactants or precursors might not be stable in solution, making solid-state methods the preferred choice. Solid-state reactions can allow the use of unstable compounds that would react prematurely in a liquid solvent.

Due to these advantages, the solid-state reaction method is very often used in materials science.

Ball Milling Procedure:

Ball milling is a mechanical method extensively employed for grinding powders to achieve finer particles and for combining different materials. This procedure involves introducing powders into a container alongside small, rigid balls composed of materials like ceramics. The container and balls are set in rotation, generating a cascading motion where the balls collide with the powders during their movement. This collision results in the reduction of particle size and the amalgamation of the materials.

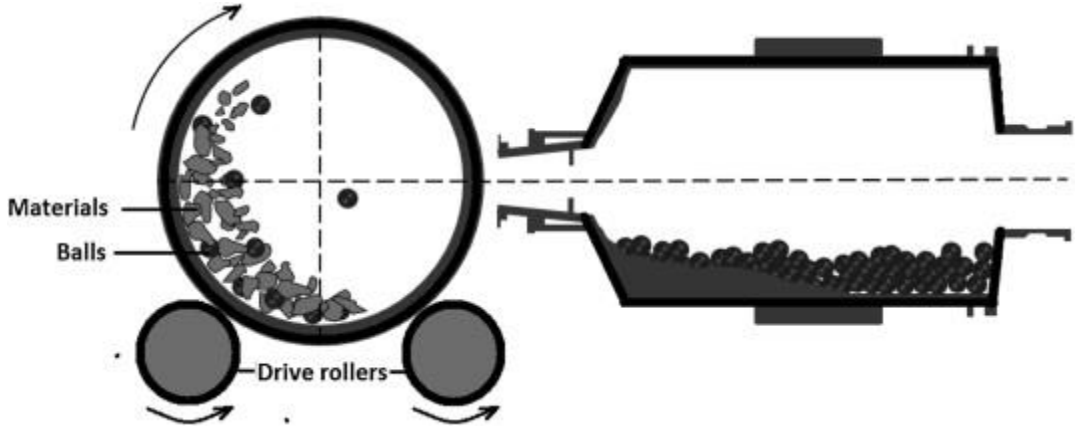

***Fig. 2.1** Image of the Ball Milling Unit. [Ref. 3]*

Synthesis of $Ba_{(1-x)}Sr_xTiO_3$ (x=0.0, 0.2, 0.4, 0.6, 0.8, 1.0) particles using Solid State Method:

Analytical grade $BaCO_3$ (Sigma Aldrich, purity ≥ 99%), $SrCO_3$ (Fluka purity 98%), and TiO_2 (Sigma Aldrich, purity 99%) were the initial raw materials for the synthesis of Barium Titanate and Barium Strontium Titanate. Acetone (Merck) was used as the liquid medium during solid-state mixing. During the fabrication of bulk pellets, Poly(vinyl alcohol) (PVA) (Sigma Aldrich) was used as a binder.

Fig. 2.2 shows the schematic of the synthesis procedure through the solid-state method. Conventional mixed oxide reaction technique was utilized to synthesize $Ba_{(1-x)}Sr_xTiO_3$, where, x=0, 0.2, 0.4, 0.6, 0.8, 1 (henceforth indicated as BT, BST20, BST40, BST60, BST80, ST, respectively). In a typical synthesis procedure, the raw materials were first taken in stoichiometric proportion and mixed. The mixture was then ball milled (inside a Teflon bottle) in acetone medium (15 ml) for 24 h at 200 rpm using zirconia balls of different sizes. The resulting semi-liquid mixture was dried in an oven at 90°C for 24 h. By varying the stoichiometric amount of the raw materials corresponding to the value of 'x', all the mixtures were prepared by following the same technique. Then the dried powders were calcined at 1200°C for 8 h with a heating rate of 2°C/min. For some specific characterizations, the calcined powders were then pelletized (diameter ~ 13 mm) by applying uniaxial pressure of ~ 5 ton/cm². During the fabrication of pellets, a certain amount of PVA dissolved in water was used as the binder. These pellets were sintered at 1350°C for 6 h (keeping the pellets on the calcined powder bed) with an intermediate temperature of 650°C (for 2 h) to remove the binder from them. Resultant pellets were used for morphological and elemental investigations. To investigate the electrical characterizations, both flat sides of the pellets were electroded by standard silver paste.

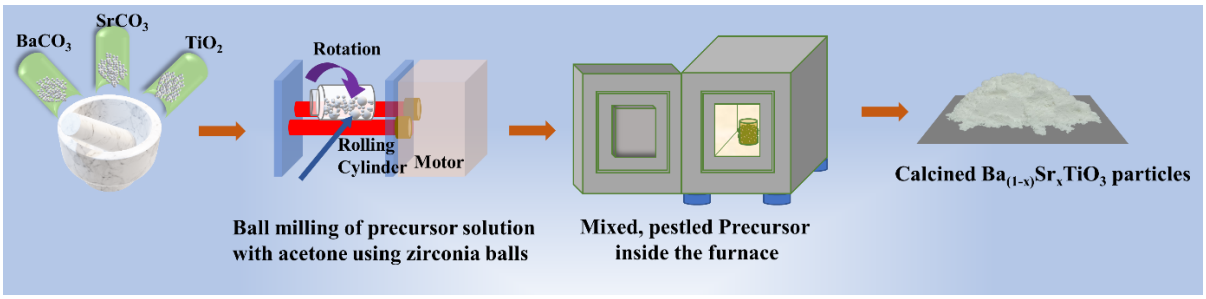

Fig. 2.2 *Synthesis of $Ba_{(1-x)}Sr_xTiO_3$ (x=0.0, 0.2, 0.4, 0.6, 0.8, 1.0) particles using Solid State Method.*

2.1.2. Modified Pechini method:

Sol-gel based synthesis routes are very well known and employed. In the sol-gel-based Pechini method, there is the formation of metal complexes and polymerization of organics. Then the polymeric resin is produced through polyesterification between metal complex, citric acid, and ethylene glycol. After calcination of this resin desired final product is produced [4,5]. The required calcination temperature to get the pure crystalline phase without any impurity ranges is below (<1000°C) the required

temperature for the solid-state reaction method. In addition to that, the Pechini method holds certain advantages over other techniques are mentioned below

Advantages:

1. Excellent control over perovskite structures along with very homogeneous solutions even with multicomponent oxides comprising of higher number of cations.
2. This method enables the synthesis of materials with complex compositions that may not be easily achievable through traditional methods. It allows for the incorporation of multiple metal ions with high precision.
3. Compositional control is also a great merit of this synthesis technique.
4. Calcination temperature lies in the moderate range below 1000°C.

Considering these preferable advantages BTS was synthesized using the Pechini method which resulted in high crystallinity without the presence of any secondary phases along with composition nearly in the required ratio.

2.1.2.1 Synthesis of $BaTi_{0.89}Sn_{0.11}O_3$ (BTS) and $Ba_{0.85}Ca_{0.15}Ti_{0.90}Hf_{0.10}O_3$ (BCHT) particles using Modified Pechini Method

2.1.2.1.1 Synthesis of BTS using Modified Pechini Method

Fig. 2.3 depicts the sequential synthesis procedure of $BaTi_{0.89}Sn0.11\ O_3$ (BTS). Owing to the several advantages such as low calcination temperature and higher compositional control on perovskite structure modified Pechini method was utilized to synthesize BTS particles. In this synthesis procedure Barium Acetate ($Ba(CH_3COO)_2$, Sigma Aldrich (99%)), Tin Chloride Pentahydrate ($SnCl_4{\cdot}5H_2O$; Sigma Aldrich (99%)), Titanium Isopropoxide ($Ti\{OCH(CH_3)_2\}_4$); Sigma Aldrich (99%)) was used as the starting raw materials. At first two solutions of Barium Citrate and Titanium Citrate were produced using Citric Acid Monohydrate ($C_6H_8O_7{\cdot}H_2O$; Merck 99%) and Ethylene Glycol ($C_2H_6O_2$; Merck 99%) solvent. The molar ratio of the Ba^{2+} /Ti^{4+}: Citric Acid: Ethylene Glycol used to prepare the solution was 1:4:16. These two solutions were then mixed and a particular amount of $SnCl_4{\cdot}5H_2O$ was added to the solution under constant stirring (250 rpm). Thereafter temperature of the solution was increased from RT (25°C) to 220°C gradually. After the formation of the gel, it was transferred to an oven and kept at 250°C for 4 h for drying. Formation of black solid observed due to resin decomposition when kept at 300°C inside a furnace for 16 h. After pestling the black solid into black powder using agate mortar it was transferred

to a programmable furnace for calcination at 950°C for 3 h. The synthesized powders were then grinded into fine powders using mortar and indexed as BTS. The obtained BTS particles were at first grinded using a mortar pestle. The powders were pelletized using a uniaxial pressure of ~3 ton/cm^2 in a hydraulic press pelletizer using PVA (2 wt% solution in DI water) as the binder. The pellets were then sintered at a temperature of 1350°C for 2 hours placing synthesized BTS powder as the bed. To remove the binder from the pellets, the intermediate temperature in the sintering process was set at 650°C. After completing the sintering process, electroding on both sides of the pellets was done with high-quality silver paint and annealed at 400°C to get the final pellets. These pellets were used for electrical characterization (dielectric, ferroelectric, and piezoelectric properties) of BTS.

2.1.2.1.2. Synthesis of BCHT using Modified Pechini Method

These typical procedures require Barium Acetate ($Ba(CH_3COO)_2$), Calcium Nitrate Tetrahydrate ($Ca(NO_3)_2{\cdot}4H_2O$), Titanium(IV) Isopropoxide ($C_{12}H_{28}O_4Ti$), and Hafnium(IV) Chloride ($HfCl_4$) as the raw materials. Initially, two separate solutions of Barium Citrate and Titanium Citrate were prepared by mixing Barium and Titanium precursors in Citric Acid Monohydrate ($C_6H_8O_7{\cdot}H_2O$) and Ethylene Glycol ($C_2H_6O_2$) solution homogeneously, where the ratio of positive ion: Citric Acid Monohydrate: Ethylene Glycol was 1: 4: 16, respectively. Once complete dissolution was achieved the second solution was poured dropwise into the first solution. A required amount of Hafnium Chloride and Calcium Nitrate Tetrahydrate solution in a water medium was also prepared and mixed with the previous solution. Thereafter, the acquired precursor solution was kept under steady stirring at 250 rpm and the temperature of the hot plate was raised stepwise from RT (30°C) to 200°C. The obtained gel was then dried at 250°C and then transferred to a furnace at 300°C. The obtained black solidified lumps were then ground into powder using a mortar pestle following calcination at 950°C for 3 h. To obtain the required fine particles the synthesized powders were again pestled using an agate mortar and collected as BCHT. The BCHT particles were then pressed into pellets with a high pressure of ~3 ton/cm^2 using a hydraulic press machine and PVA (a 2 wt% solution in DI water) as glue. The pellets were heated at 1350°C for 2 h on a bed of BCHT powder, with an intermediate temperature of 650°C to remove the PVA. Next, silver paint was applied on both sides of the sintered pellets and treated at 400°C to make the final pellets. To measure the

piezoelectric coefficient (d_{33}), the pellets were put in a silicon bath and given 1 kV of voltage for 1 h.

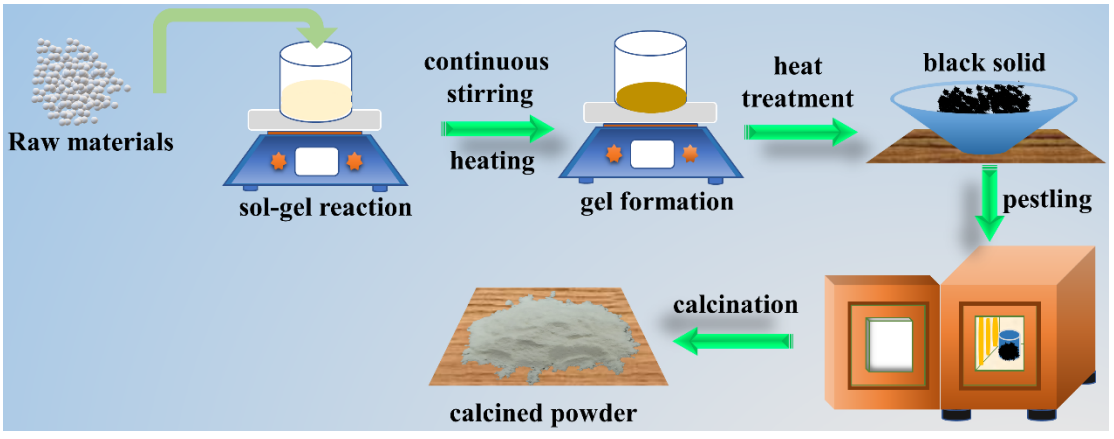

Fig. 2.3 *Synthesis of BTS & BCHT particles using modified Pechini method.*

Table 2.1 Synthesis conditions of different filler particles.

Name of the material	Synthesis procedure	Materials required	Calcination temperature	Time
BST40 particles	**Solid state**	1. Barium Carbonate ($BaCO_3$) 2. Strontium Carbonate ($SrCO_3$) 3. Titanium Oxide (TiO_2)	1200°C	23 h
BTS and BCHT particles	**Modified Pechini method**	For BTS 1. Barium Acetate ($Ba(CH_3COO)_2$ 2. Tin Chloride Pentahydrate ($SnCl_4{\cdot}5H_2O$) 3. Titanium Isopropoxide ($Ti(OCH(CH_3)_2)_4$) For BCHT 1. Barium Acetate ($Ba(CH_3COO)_2$)	950°C 950°C	17 h 17 h

		2. Calcium Nitrate Tetrahydrate ($Ca(NO_3)_2 \cdot 4H_2O$) 3. Titanium (IV) Isopropoxide ($C_{12}H_{28}O_4Ti$) 4. Hafnium (IV) Chloride ($HfCl_4$)		

2.2. Preparation of composite films:

2.2.1. Preparation of PVDF-based composites:

There are several methods available for the synthesis of polymer and polymer composite films, such as solution casting method, hot pressing method, film blowing, and thermal evaporation method to name a few. Among these different synthesis procedures, solution casting technique is the most facile technique for the synthesis of films of a polymer and its composite. Therefore, this simple solution casting method has been employed for the synthesis of neat PVDF and PVDF composite films in this present investigation.

In this typical synthesis procedure, initially, 0.49 g of PVDF was dissolved in a specific amount (6 ml) of DMF with vigorous stirring (600 rpm) at 60°C until complete dissolution. On the other hand, varying amounts of fillers (BST40, BTS, and BCHT) were dispersed in that PVDF-DMF solution by rigorous magnetic stirring (600 rpm) for at least 48 h followed by 1 h of sonication in separate containers to obtain a homogeneous mixture so that uniform dispersion and interaction of the fillers with PVDF can be achieved. Afterward, the whole mixture was cast on properly cleaned and dried glass slides, and the solution was heat treated to evaporate the solvent at 90°C for 4 h. Finally, the composite films were peeled off from the glass slides to get the required self-standing composite films. This synthetic procedure yields well-dispersed fillers incorporated in PVDF films. The neat PVDF film was also prepared by following the same procedure without impregnating any filler particles. The discussed synthesis procedures are schematically illustrated in Fig.2.4.

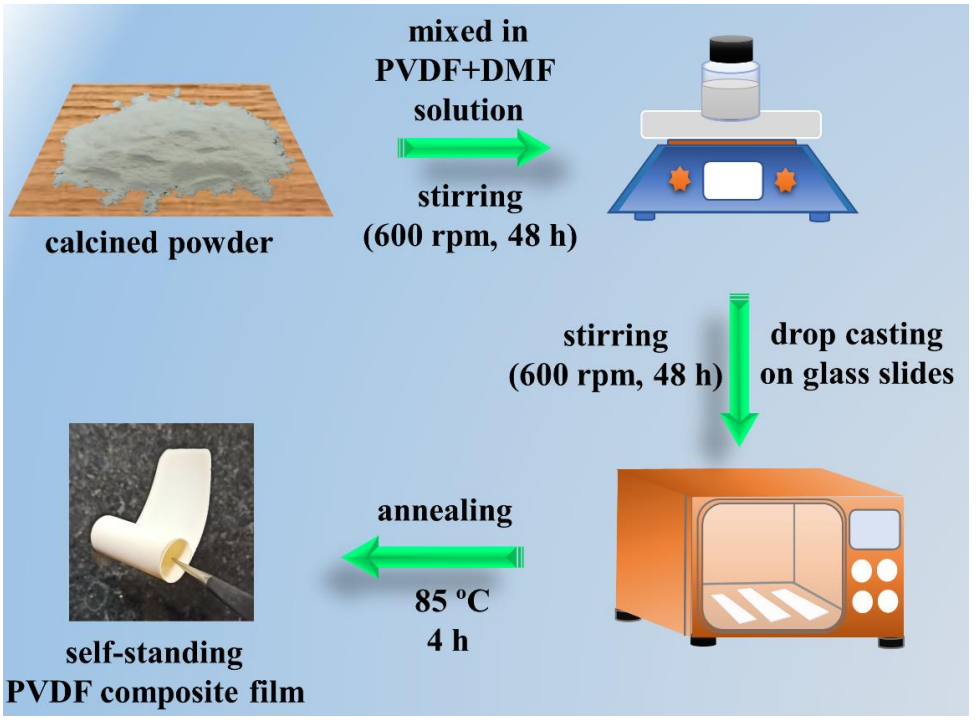

Fig. 2.4 *Synthesis of PVDF-based composite films.*

2.2.2. Preparation of BTS/PDMS composites:

To prepare PDMS-based composite films familiar solution casting technique was used. Different wt% of BTS powders (5, 10, 15, and 20 wt%) were homogeneously mixed with the PDMS solution (PDMS base and curing agent in a ratio of 10:1). This suspension was then poured into a pre-cleaned petri dish and kept inside a vacuum oven to eliminate any air bubbles and heated to 60°C for 4 hours. Then the self-standing films were peeled off from the Petri dish to get the required BTS/PDMS composite film.

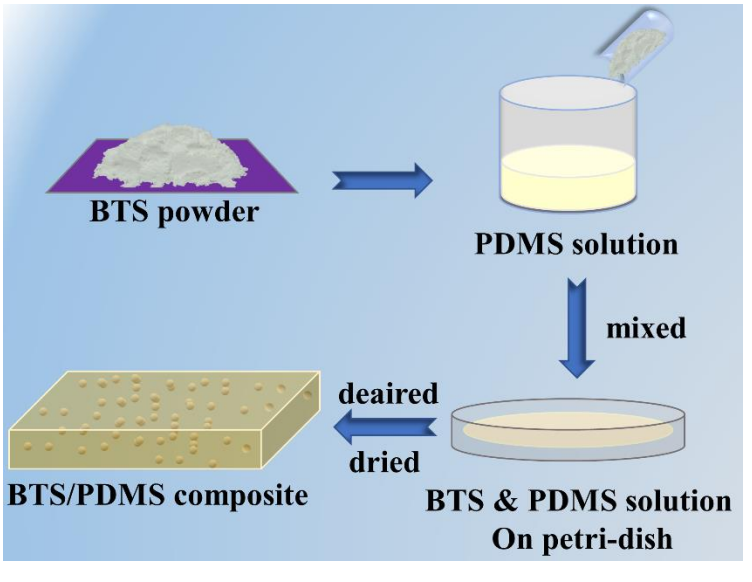

Fig. 2.5 *Synthesis of PDMS-based composite films*

2.3. Fabrication of piezoelectric energy harvesters (PEH)

Throughout the present work, flexible piezoelectric energy harvester (PEH) devices are utilized. As a consequence, in this section, a detailed fabrication procedure for the flexible nanogenerator is provided. This PEH fabrication is based on the typical sandwich structure. Initially, the synthesized composite film has been cut into small pieces of a particular area (2 cm x 3 cm). Such a piece of the composite film was then sandwiched between two flexible electrodes (Ag paste or Al tape) to fabricate the electrode–composite–electrode (ECE) stack. Adhesive electrodes (with definable area) were attached on both sides of the film. Finally, the ECE stack is being encapsulated (using a PET sheet) to protect the stack from any kind of external physical damage. A schematic of the facile fabrication procedure is shown in Fig.2.6.

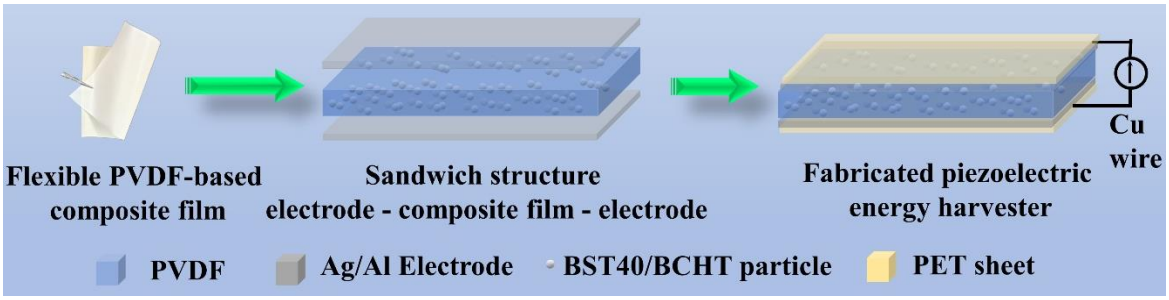

Fig. 2.6 *Schematic of fabrication procedure of piezoelectric energy harvester (PEH).*

2.4. Fabrication of triboelectric energy harvesters (TEH)

For the fabrication of TEH, at first, a stacked layer of an Aluminium electrode (Al tape) and a bare PVDF/PDMS film was attached with a PET sheet (dimension~ 4.5 cm x 5.5 cm) using a two-sided adhesive tape. This entire structure (PVDF or PDMS film/Al/PET) acted as the bottom part of the TEH device, where PVDF/PDMS film acted as the negative triboelectric layer, Al as the bottom electrode, and PET as the substrate. However, the upper part consists of Al/PET, where Al tape is carefully affixed to the PET sheet to avoid any air gap. Here, Al acted as the positive triboelectric layer as well as the upper electrode, and PET acted as the substrate. These two parts (upper and bottom) were then placed together in such a way that the negative (PVDF/PDMS) and positive tribo-layers (Al) face each other maintaining a specific distance (~5 mm). Here two sponge spacers were used to maintain the specific distance between the two layers of the TEH device. The final dimension of the fabricated device was ~ 4.5 cm x 5.5 cm x 0.5 cm.

2.5. Fabrication of piezoelectric-triboelectric hybrid energy harvesters (HEH)

As discussed earlier, the hybridization of piezoelectricity with triboelectricity in a hybrid energy harvester is internal hybridization. That is why the fabrication technique of the HEH device is the same as that of the TEH device. To couple the piezoelectricity with triboelectricity, BCHT/PVDF or BTS/PDMS composite films were used in the bottom layer of the HEH device instead of bare PVDF or PDMS films as in the case of TEH devices. In the case of BCHT/PVDF, Aluminium (Al) was used as the upper layer while for BTS/PDMS, normal printer paper was utilized as the positive tribo layer. Fig. 2.7 shows the fabrication process of a BCHT/PVDF-based HEH device.

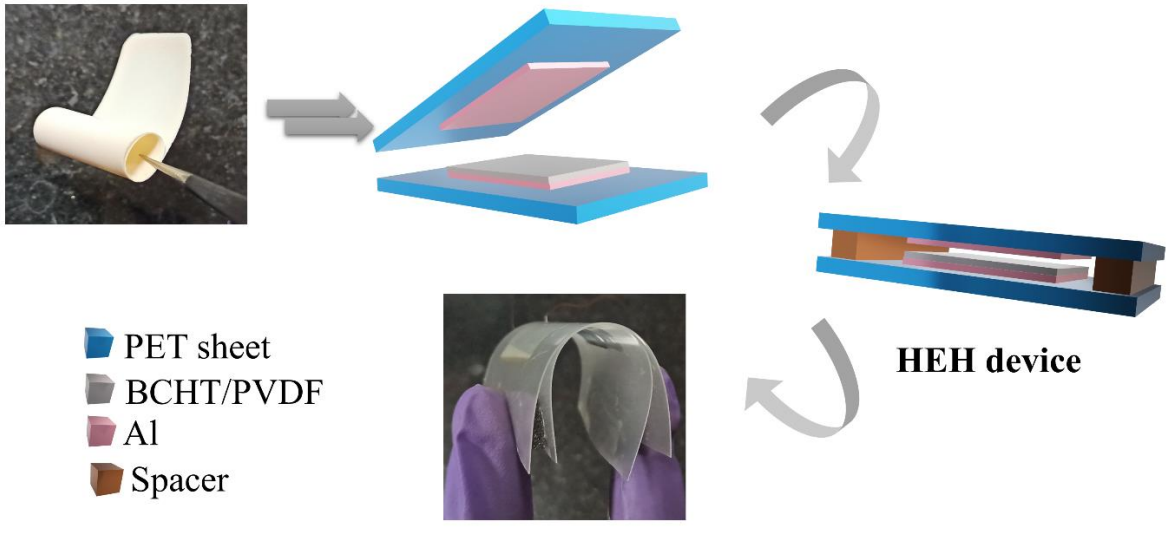

Fig. 2.7 *Schematic of fabrication procedure of hybrid energy harvester (HEH).*

2.6. Characterization techniques

To avoid the repeated appearance of the experimental techniques in the respective chapters, the various experimental details of the present investigation have been put together and placed in this chapter. Different analytical tools were used to characterize the filler's structure, morphology, and different properties. The synthesized PVDF composite films were characterized thoroughly to have a clear idea about their structural, morphological, optical electrical, ferroelectric, piezo-electric, and microwave shielding properties.

2.6.1. Structural and morphological characterizations

2.6.1.1. X-ray diffraction (XRD)

X-ray diffraction (XRD) is a powerful structural characterization technique used to investigate crystalline structures. It is a non-destructive analytical technique that provides unprecedented detailed information on the crystal structures, orientations, size, and unit cell lattice parameters, phases, and chemical composition of materials. All types of materials nanostructures, films, or in the bulk form can be studied using X-rays.

The basis of the formation of an X-ray diffraction pattern lies in Bragg's law, which is as follows:

$$2d \sin\theta = n\lambda \qquad (2.1)$$

This relation holds when a constructive interference is observed from a crystal lattice. In equation 2.1 'd' is the distance between the two consecutive planes of the crystal, 'λ' is the wavelength of the incident X-radiation, θ is the angle of incidence of the X-ray on the crystal lattice, and 'n' is an integer (Fig. 2.8).

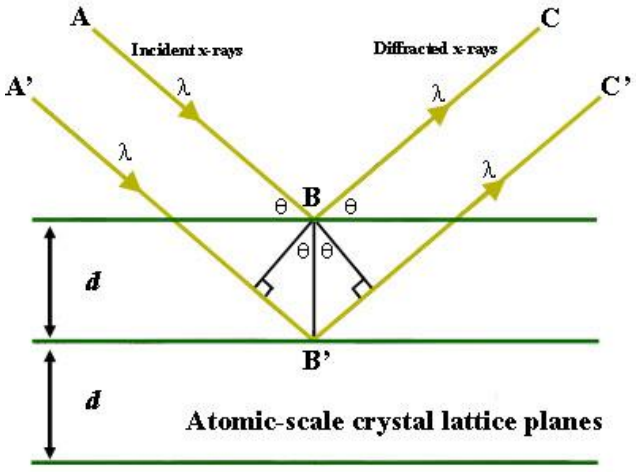

Fig. 2.8 *Bragg's Law reflection. The diffracted x-rays exhibit constructive interference when the distance between paths ABC and A'B'C' differs by an integer no. of the wavelengths (λ). [ref. 7]*

In this investigation, the X-ray diffraction measurements of the filler particles and composite films were carried out using an 'Xray diffractometer of PAN Analytical, X'pert PRO MPD' parallel beam X-ray diffractometer with conventional Bragg – Brentano goniometer geometry with a θ-2θ scanning mechanism. The X-radiation

source was Cu-K_α with wavelength (λ) = 1.540598 Å (40 kV and 40 mA). For the θ-2θ mechanism, the X-ray tube is stationary, the sample moves by the angle θ, and at the same time, the detector moves by the angle 2θ (Fig. 2.9). The peak positions (2θ or 'd' values) of the XRD patterns, obtained for a particular sample, were matched with the standard JCPDS database corresponding to the material; to find out the crystallographic nature of the synthesized material. In this regard, it is mentioned that the XRD data was Reitveld refined using the Fullprof software package for crystallographic analysis.

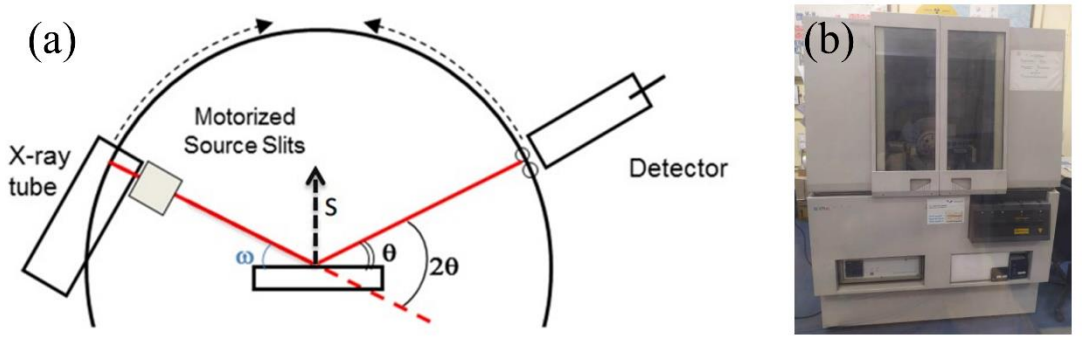

Fig. 2.9 *(a) Schematic of Bragg- Brentano geometry, (b) digital image of X-ray diffractometer. [ref.8]*

2.6.1.2. Fourier Transformed Infrared Spectroscope (FTIR):

The output performance of a polymer-based piezoelectric nanogenerator mostly depends on the electroactive phase contents, as the piezoresponse of a polymeric material increases with increasing electroactive phase content. Fourier transform infrared (FTIR) absorption spectroscopy is the most useful tool to investigate such electroactive phases of a polymeric material.

In this method, vibrational spectroscopy serves as the measurement approach for identifying the specific bonds within a composite material. When exposed to infrared (IR) radiation, certain molecules possessing a permanent dipole moment exhibit a distinct response at the frequency corresponding to their vibrational mode. Additionally, molecules lacking a permanent dipole moment can also partake in vibration at a characteristic frequency under the influence of IR radiation. Illustrated in Fig. 2.10, the incident beams undergo reflection at the interface of stationary and movable mirrors, generating an optical path difference. Upon traversing the sample, the light beam carries a phase vibration contingent on its frequency and is captured by a detector. Subsequently, this frequency-induced vibration is transformed into

intensity oscillations using the Fourier transform method, resulting in an "interferogram." This interferogram is then translated into a wavenumber-dependent spectrum through software, namely the Cooley-Tukey algorithm. In comparison to traditional IR spectrometers, Fourier Transform Infrared (FTIR) (Perkin Elmer FTIR instrument) spectroscopy boasts enhanced resolution, quicker operational speed, and improved signal-to-noise ratios. For the present work, the FTIR samples are prepared by using the drop-casting method with a thickness of ~ 20-30 μm. In this work, a FTIR Spectrum 2, Perkin Elmer instrument has been used for measuring the FTIR spectra with a scan rate of 8 cm^{-1}/sec within the 400 to 4000 cm^{-1} spectral range.

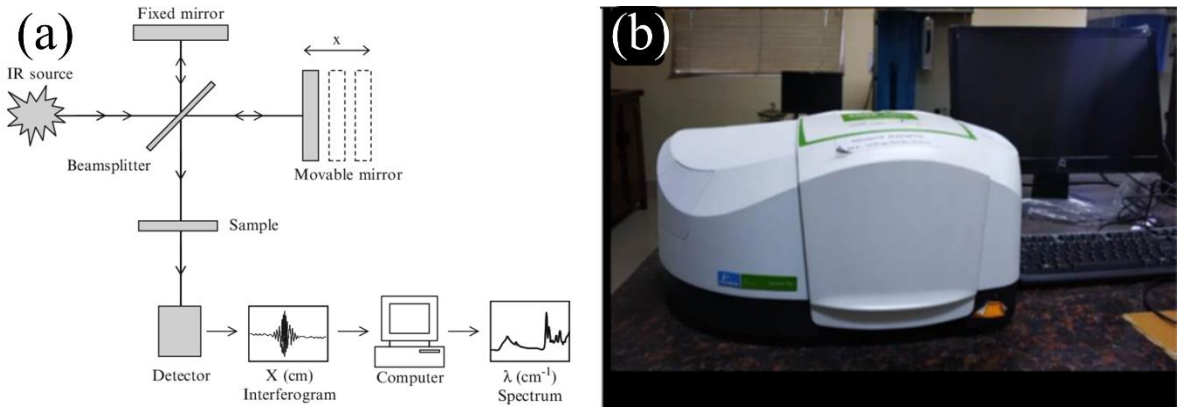

Fig. 2.10 *(a) Schematic of Fourier transformed infrared (FTIR) spectrometer (b) Digital photograph of FTIR instrument (Perkin Elmer FTIR instrument) [ref. 9].*

In this work, the recorded FTIR spectra of different PVDF composite films have been utilized to find out the fraction of the electroactive β phase in the composites. This β phase fraction (F(EA)) was calculated using Lambert-Beer law as given by [6],

$$F(EA) = \frac{A_{EA}}{\left(\frac{K_{EA}}{K_{NEA}}\right) A_{NEA} + A_{EA}} \qquad (2.2)$$

Where A_{NEA} and A_{EA} are the absorbance at 764 cm^{-1} and 840 cm^{-1} respectively, K_{NEA} ($6.1 \times 10^4 cm^2\ mol^{-1}$) and K_{EA}($7.7 \times 10^4\ cm^2 mol^{-1}$) were the absorption coefficients at the respective wave numbers [6].

2.6.1.3. Raman spectroscopy

Raman spectroscopy is a sophisticated analytical technique that offers a deep and insightful window into the molecular world. Named after its discoverer, Sir C. V. Raman, the technique is founded on the phenomenon of light scattering, where photons interact with molecules in a sample and emerge with altered energies,

providing a wealth of information about molecular vibrations and chemical compositions.

At the heart of Raman spectroscopy lies the concept of molecular vibrations. Molecules are in a constant state of motion, with atoms oscillating around their equilibrium positions. These vibrations include stretching, where bonds between atoms are alternately extended and compressed, and bending, where the angles between these bonds fluctuate. Each type of bond and functional group in a molecule has specific vibrational modes associated with it. When a sample is irradiated with monochromatic light, typically from a laser, some of the scattered light will exhibit frequency shifts due to interactions with these molecular vibrations.

There are two main outcomes of Raman scattering: Stokes and anti-Stokes scattering. In Stokes scattering, the scattered photons lose energy, resulting in longer wavelengths (lower frequencies) than the incident light. This is the more common type of scattering as it aligns with the second law of thermodynamics, which states that molecules tend to occupy lower energy states. On the other hand, anti-Stokes scattering involves photons gaining energy during scattering, leading to shorter wavelengths (higher frequencies) than the incident light. However, this process is less likely due to the lower population of higher energy vibrational states. Fig. 2.11 shows the schematic of the Raman spectrometer. In the present studies, Micro Raman Spectrometer of RENISHAW was used as the Raman spectrometer with a laser source of wavelength 785 nm.

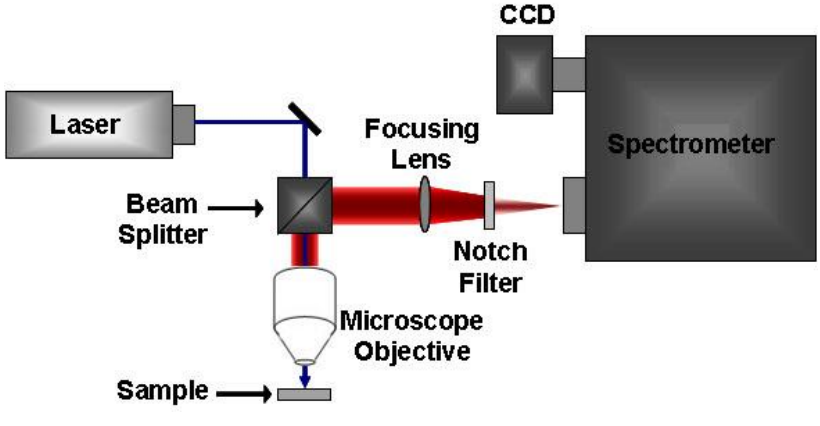

Fig. 2.11 *Schematic of Raman spectrometer. [ref. 10]*

The resulting Raman spectrum is a graphical representation of intensity against frequency shift (usually in wavenumbers or wavelengths). Peaks in the spectrum correspond to different molecular vibrations, providing valuable information about

the types of bonds present in the sample. These peaks can be used to identify functional groups, confirm molecular structures, and even detect subtle changes in molecular environments.

2.6.1.4. Field Emission Scanning Electron Microscope (FESEM):

The scanning electron microscope (SEM) plays a pivotal role in the examination of microscopic characteristics and the analysis of surface topography. Within the SEM, an electron gun generates an electron beam within a highly evacuated column, maintaining a pressure below $1x10^{-7}$ Pascal. This vacuum environment enables unobstructed electron movement along the column, minimizing scattering effects and preventing undesired discharges within the instrument. The design of this vacuum is intricately tied to the electron source, as it directly impacts the longevity of the cathode emitter. The primary purpose of the electron gun is to furnish a concentrated and steady electron current in the form of a fine beam. There exist two main categories of emission sources for this purpose: thermionic emitters and field emitters. These emission sources influence the efficiency and performance of the SEM.

The fundamental distinction between SEM and FESEM lies in the type of emitter used. In SEM, emitter selection is the key differentiator. Thermionic Emitters function by passing an electrical current through a filament, which heats up. This filament is typically made of tungsten (W) or lanthanum hexaboride (LaB6). When the temperature surpasses the filament material's work function, electrons are liberated from its surface. However, thermionic sources exhibit drawbacks such as relatively low brightness, cathode material evaporation, and operational thermal drift. Consequently, achieving high-magnification images (around ×100000) can prove challenging. In contrast, Field Emission offers a solution that mitigates these issues. A Field Emission Source (FES), also known as a cold cathode field emitter, eliminates the need to heat the filament. Instead, electron emission occurs by subjecting the filament to a significant electrical potential gradient. The FES is usually a wire of tungsten (W) fashioned into a sharp point. The significance of the small tip radius (~ 100 nm) is that an electric field can be concentrated to an extreme level, becoming so big that the work function of the material is lowered and electrons can leave the cathode. FESEM uses Field Emission Source producing a cleaner image, less electrostatic distortions, and spatial resolution < 2nm. Imaging by capturing and analyzing secondary electrons, which are ejected from the material under

investigation, is the most common technique used for electron microscopy. An electron-collecting device collects these secondary electrons to produce an electronic signal. The electronic signal is amplified and the image of the sample surface is finally displayed on the screen of a PC. Fig. 2.12 schematically illustrates the basic parts of the operation of SEM.

In the present investigation, the surface morphologies of the films were studied by FESEM (Supra 35 VP) and FESEM (Carl Zeiss).

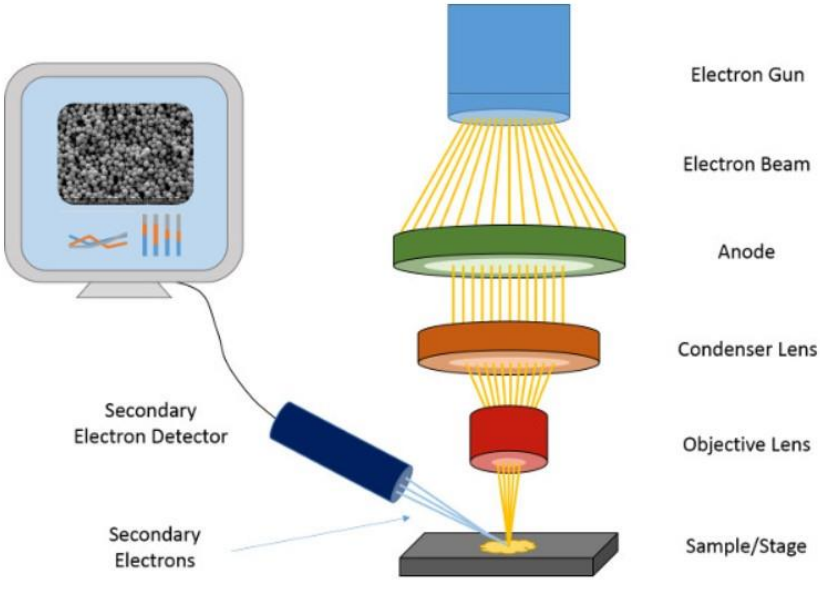

Fig. 2.12 *Schematic of the basic parts of SEM [ref. 11].*

2.6.1.5. Transmission Electron Microscope (TEM):

TEM stands for transmission electron microscope, which was developed to obtain magnification and hence details of a specimen, to a much better level than the conventional optical microscopes. In TEM a beam of electrons is passed through an ultra-thin specimen interacting with the specimen as it passes through. When electrons are accelerated up to high energy levels (a few hundred keV) and focused on a material, they can scatter or backscatter elastically or inelastically, or produce many interactions, source of different signals such as X-rays, Auger electrons or light. Some of them are used in transmission electron microscopy (TEM). An image is formed from the interaction of the electrons transmitted through the specimen; the image is magnified and focused onto an imaging device, such as a fluorescent screen, on a layer of photographic film, or to be detected by a sensor such as a CCD camera. Fig. 2.13 illustrates the schematic of a transmission electron microscope (TEM).

In the present investigation, the structure of the synthesized samples was studied using transmission electron microscopy TEM, and HRTEM images of the filler particles were characterized by Tecnai G2, 30ST instrument (300 kV). To prepare the samples for TEM analysis a pinch of the synthesized filler particle was dispersed in 10 ml of ethanol. After a sonication of 15 min the sample was dropped on the TEM grid using a micropipette and the sample was kept for drying for about 18 to 20 hrs.

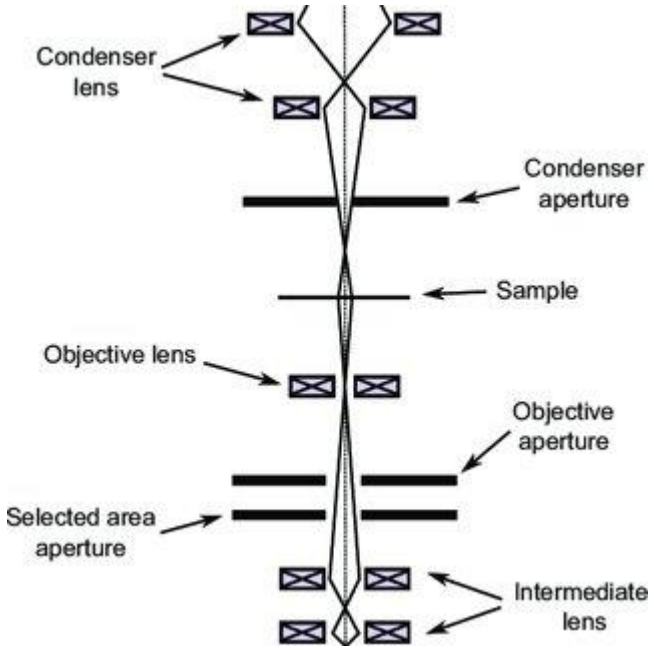

Fig. 2.13 *Schematic of the basic transmission electron microscope (TEM). [ref. 12]*

2.6.2. Elemental Characterization:

Elemental analysis involves the identification and measurement of the kinds and quantities of chemical elements within a given sample. This procedure holds great importance across diverse sectors such as science, and research, encompassing tasks like materials exploration, and stoichiometry assurance in synthesis. A variety of methods exist for elemental analysis, each with its distinct principles and utility.

2.6.2.1. EDX analysis:

Energy-dispersive X-ray Spectroscopy (EDX) is a sophisticated analytical technique employed in conjunction with electron microscopy. It provides insights into the elemental composition of a sample by detecting the X-rays emitted when the sample is bombarded with a focused electron beam.

In EDX, the primary electron beam from the microscope interacts with the atoms in the sample, causing inner-shell electrons to be displaced from their orbits. This creates vacancies in these inner electron shells. To fill these vacancies, electrons from higher energy levels drop down to the lower energy levels, releasing energy in the form of X-rays that are characteristic of the elements involved (Fig. 2.14). These emitted X-rays are then collected by an energy-dispersive detector.

The detector records the energies of the emitted X-rays, and this information is used to generate an energy spectrum. Each element has unique X-ray energies associated with its electron transitions, allowing for the identification of the elements present in the sample. The intensity of the X-ray peaks in the spectrum corresponds to the relative abundance of each element.

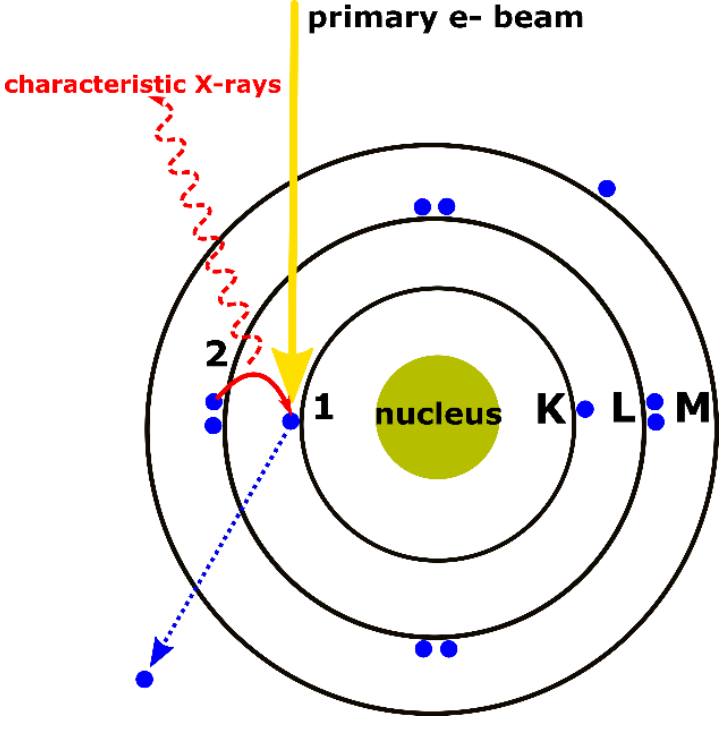

Fig. 2.14 *Schematic of the basic principle of EDX. [ref. 13]*

EDX provides qualitative and semi-quantitative information about the elemental composition of the sample. One of the advantages of EDX is its ability to offer insights at the microscopic scale, providing details about the elemental distribution within the sample.

One of the other characteristics of the EDX is mapping where the recorded X-ray data is processed to generate elemental maps. For each pixel in the SEM image, an energy spectrum is obtained, and the characteristic X-ray peaks of different elements

are identified. By analyzing the intensity of these peaks, the relative abundance of each element is determined. Elemental maps are then created by assigning false colors to each element, allowing to visually see where different elements are distributed across the sample's surface.

In summary, Energy-Dispersive X-ray Spectroscopy is a valuable tool for elemental analysis, particularly when combined with SEM. It enables us to obtain information about the elemental makeup of a sample, contributing to our understanding of material composition, structure, and characteristics on a microscopic level.

2.6.2.2. X-ray Photoelectron Spectroscopy:

X-ray Photoelectron Spectroscopy (XPS) stands as a remarkable cornerstone within the realm of surface science. By employing the fundamental principles of the photoelectric effect, XPS employs X-ray photons to liberate electrons from a material's outermost atomic layers. The kinetic energy of the emitted photoelectrons is related to the binding energy of the electrons in the material. Each element and chemical state have distinct binding energies. By measuring these energies, XPS can identify the elements present on the surface and provide information about their chemical bonding environments. XPS can distinguish between different chemical states of an element. For example, carbon can exist in various chemical environments such as carbon-carbon (C-C) bonds, carbon-oxygen (C-O) bonds, or carbon-nitrogen (C-N) bonds. The specific binding energies of the electrons associated with these different bonds allow researchers to identify the chemical states present. This technique's prowess extends across domains, finding applications in deciphering the mysteries of nanomaterials, catalysts, polymers, and beyond, while allowing scientists and engineers to masterfully engineer and optimize material surfaces for tailored functionalities [14]. Fig. 2.15 shows the typical schematic of the working principle of XPS. In the present work, PHI 5000 VERSA PROBE III ULVAC PHI (Physical Electronics), USA was used for X-ray photoelectron spectroscopy (XPS) characterization.

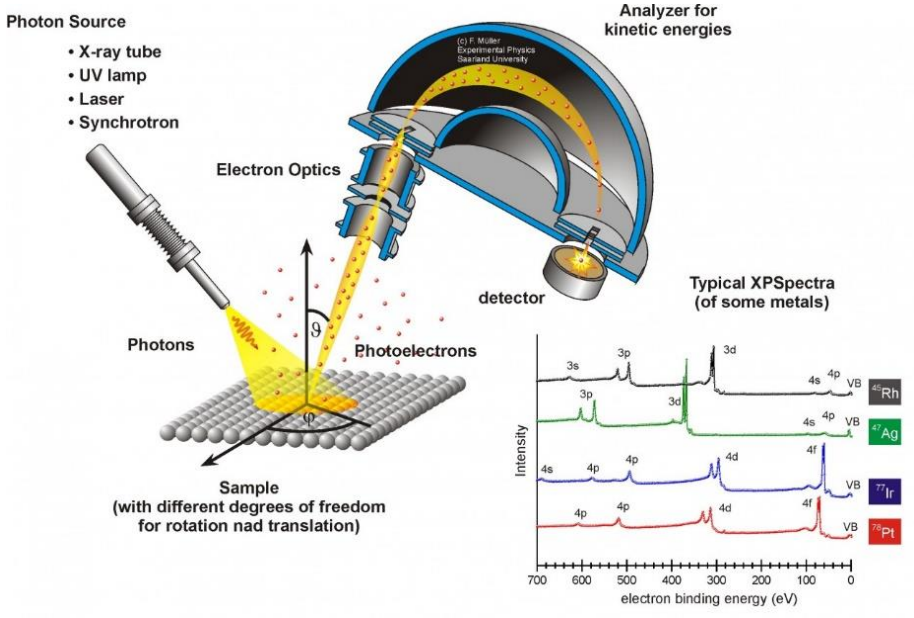

Fig. 2.15 *Schematic of the basic principle of XPS. [ref. 15]*

2.6.3. Thermal Characterisations:

Thermal behavior being one of the physical properties of any material, gives a fair estimation of the constituents and nature of material. In thermal analysis, the physical property of a substance is measured as a function of temperature, while the substance is subjected to a controlled temperature program [16]. Differential Scanning Calorimetry (DSC) is a powerful analytical technique used to study the thermal properties of materials. It provides valuable insights into processes such as phase transitions, melting points, crystallization, and reactions that involve heat changes.

Differential Scanning Calorimetry (DSC):

In addition to the determination of heat and temperature of physical and chemical transitions, DSC is also useful in finding out calorimetric purity and second-order transitions. In this technique, an aluminum pan is used to accommodate the weighted sample powder. The medium used is air and is supplied at the rate of 100 ml/min. The sample is heated at the rate of 10 ^{o}C/min. Here, change in energy, say in mW, is recorded as a function of temperature, which provides either exothermic or endothermic peaks at the time of the DSC curve in fingerprinting in which simple or complex materials can be compared for identification using measurements of peak positions, sizes, or shapes. These methods are widely used in chemical analysis, and for obtaining thermodynamic and kinetic data. By using these DSC curves degree of crystallinity of any sample can be measured by the following relation [17]

$$\text{Degree of crystallinity } (X_c) = \frac{\Delta H_c}{\Delta H_{100\%}} \qquad (2.3)$$

where $\Delta H_{100\%}$=104.6 J/g. The schematic of a differential scanning calorimetry is shown in Fig. 2.16.

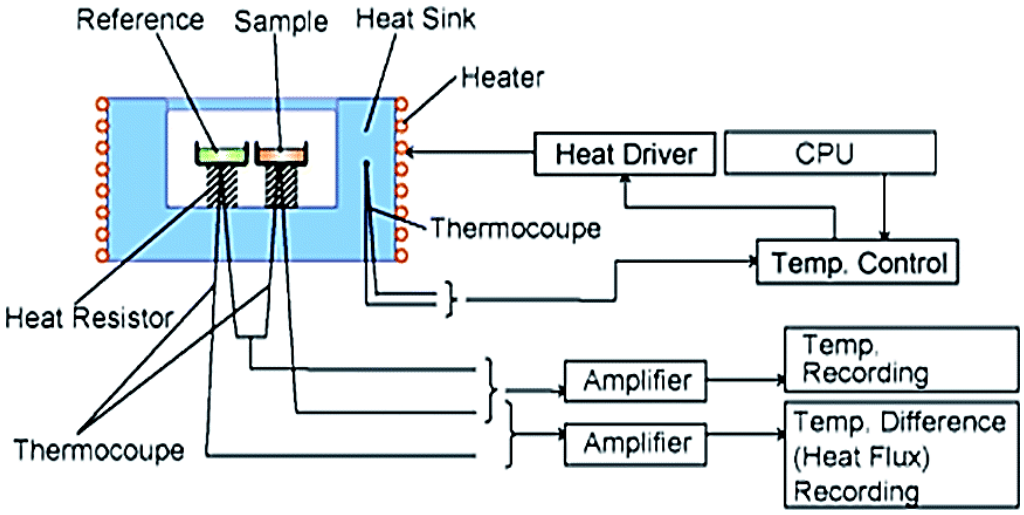

Fig. 2.16 *Schematic of a differential scanning calorimeter (DSC). [ref. 18]*

Differential scanning calorimetry (DSC) (DSC-60, Shimadzu) was also used for further in-depth thermal analyses of the prepared materials.

2.6.4. Optical Measurement:

Ultraviolet-Visible Spectroscopy (UV-Vis):

Ultraviolet-visible spectroscopy (UV-Vis) is an important analytical tool to interpret the optical behavior of a material. It has two different modes, the first is absorption mode and the second is reflectance mode, both are achieved for the ultraviolet-visible range i.e., wavelength region of 200 to 800 nm. The electronic transitions due to absorption of photons (either for ground, or for higher energy or excited state) are obtained, as the absorption versus wavelength is recorded in UV-Vis spectroscopy [19]. The absorbance A is simply expressed as Beer's law:

$$A = \log(\frac{I}{I_0}) \qquad (2.4)$$

Where, the transmittance is denoted by the ratio $\frac{I}{I_0}$, I is the light intensity, and $I_0$is the intensity of light before entering the sample. The absorbance data in the wavelength range 250 – 700 nm were collected for all the samples. The energy difference between

the valence band and the conduction band i.e., the energy band gap (E_g) was calculated by using the Tauc plot method [20] and Equation 2.5.

$$(\alpha h\nu)^2 = A(h\nu - E_g) \quad (2.5)$$

where α is the absorption coefficient, h is the Planck constant, ν is the frequency of the incident light and A is an arbitrary constant. E_g value is calculated by plotting $(\alpha h\nu)^2$ in y-axis, $h\nu$ in x-axis and extrapolating the linear region of the graph. The intersection of this tangent line in the x-axis (where y=0) is the required band gap energy.

In the present work, the measurement of UV-Vis was characterized using a SHIMADZU UV–VIS-NIR spectrometer (UV-3600). Fig. 2.17. shows the schematic diagram of the UV-VIS spectrometer.

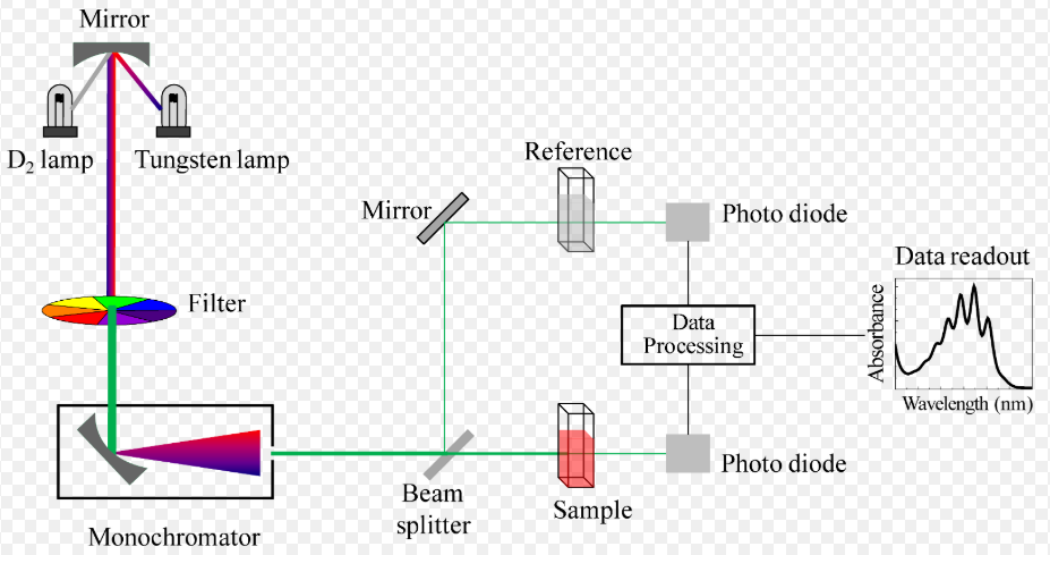

Fig. 2.17 *Schematic of the basic parts of UV-Vis spectrophotometer. [ref. 21]*

2.6.5. Electrical Characterisations

2.6.5.1. Zeta potential analyzer

Zeta potential is a pivotal parameter in the realms of colloidal and surface chemistry, signifying the electrical charge present on the surface of particles within a dispersion. It holds significant importance in ascertaining the stability of colloidal systems and the interactions among particles within a solution. The movement of particles is described by the Stokes-Einstein equation (Equation 2.6).

$$D = kBT/6\pi\eta R \quad (2.6)$$

where, D, k_B, T, η, and R represent the diffusion, Boltzman's constant, temperature, viscosity of the solvent and hydrodynamic radius of the particles, respectively. The zeta potential analyzer measures the electrophoretic mobility of the particles and uses this information to calculate the zeta potential. The zeta potential is typically reported in millivolts (mV).

Fig. 2.18 *Digital image of zeta potential analyzer.*

2.6.5.2. Dielectric properties

Dielectric performance of the pellet samples and composite films was carried out using Wayne Kerr's Precision Impedance Analyzer 6500B within a frequency range of 100 Hz to 1 MHz. a digital image of the impedance analyzer is shown in Fig. 2.19. The value of the dielectric constant (ε') and ac conductivity (σ_{ac}) of the samples were calculated using the following equations [1] :

$$\varepsilon' = \frac{C.d}{\varepsilon_0 A} \qquad (2.7)$$

and

$$\sigma_{ac} = 2\pi f \varepsilon_0 tan\delta \varepsilon' \qquad (2.8)$$

Where *C*, d, A, and $tan\delta$ are the capacitance, thickness, area and dielectric tangent loss of the samples, respectively. f is the frequency of the electric field applied across the samples and ε_0 is the free space permittivity (8.854×10^{-12} F.m^{-1}). In this present work to measure the dielectric properties adhesive aluminium tape/silver paste was used as electrodes.

Fig.2.19 *Digital image of the impedance analyzer.*

2.6.6. Ferroelectric and Piezoelectric characterizations

Ferroelectric measurements by measuring the P-E hysteresis loop were done by using the FE test system (aixact TF Analyser 2000) (Fig. 2.20). The core of your measurement involves applying an electric field to the ferroelectric sample and simultaneously measuring its polarization response. This process generates a P-E hysteresis loop. As we increase the electric field, the material's polarization changes accordingly. With the subsequent reduction in the electric field, the polarization may not return to its original value due to phenomena like domain switching and hysteresis, characteristic of ferroelectric materials.

The aixact TF Analyser 2000 records the changes in polarization as the electric field was swept back and forth. This data was used to create the P-E hysteresis loop, which illustrates the relationship between polarization and electric field strength. Once the data collection is complete, we could analyze the P-E hysteresis loop to extract key parameters such as the remnant polarization, coercive field, and the shape of the loop. These parameters provide insights into the ferroelectric material's behavior, including its ability to retain polarization in the absence of an external field and the energy required to switch its polarization.

Fig. 2.20 *Digital image of the Ceramic Multilayer Actuator Test Bench (aixACCT System GmbH, Germany).*

Piezoelectric Force Microscopy (PFM) is an advanced technique within scanning probe microscopy, focusing on the examination and manipulation of piezoelectric materials with exceptional precision at the nanoscale level (Fig. 2.21). Piezoelectric substances possess the unique property of generating electric charges when subjected to mechanical stress or undergoing deformation due to an applied electric field.

In the PFM process, a pointed tip affixed to a delicate cantilever is employed to precisely interact with the surface of a sample composed of a piezoelectric material. This tip is typically constructed from a conductive material, enabling the application of electric fields and the measurement of electric charges. While the tip traverses the sample's surface, it applies a minute mechanical force, and the ensuing reaction of the material is gauged. This response encompasses both the material's mechanical distortion brought about by the piezoelectric phenomenon and the electric charge generated because of the same phenomenon. Here, Asylum Research AFM (MFP3D Origin) was used for PFM characterizations.

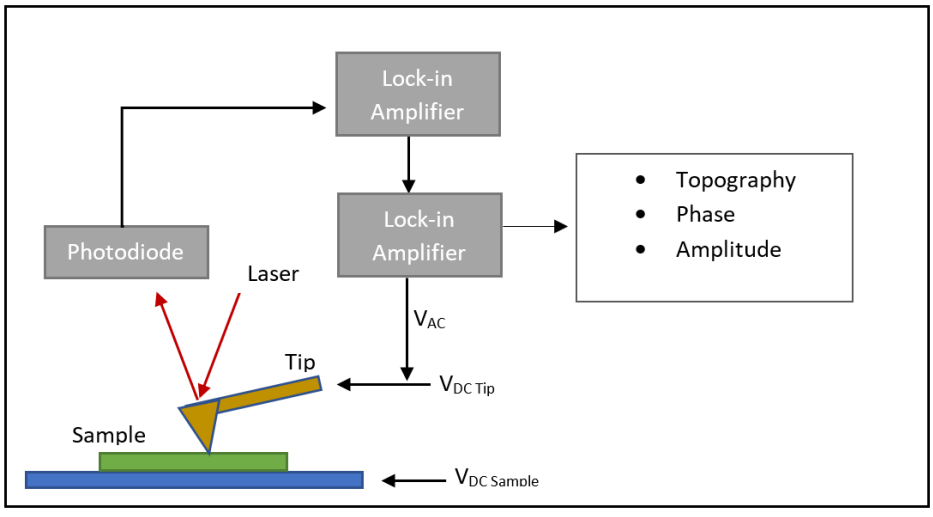

Fig. 2.21 *Schematic of the PFM setup. [ref. 22]*

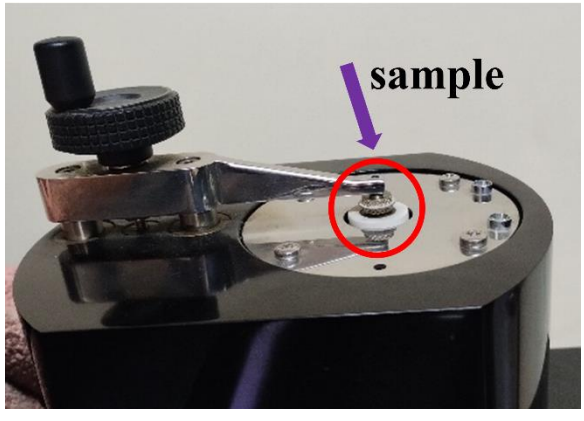

Fig. 2.22*: Digital image of piezoelectric charge coefficient measurement unit (d_{33} meter)*

A d_{33} piezometer is a specialized instrument employed to measure the piezoelectric charge coefficient (d_{33}) of a piezoelectric material. By subjecting the material to a controlled mechanical stress, achieved through methods like mechanical force or piezoelectric actuators, the device collects the charge generated due to the piezoelectric effect via electrodes attached to the sample. This generated charge is directly proportional to the d_{33} coefficient, which quantifies the material's ability to produce charge under stress and is expressed in picocoulombs per newton (pC/N). Here for this specific measurement d_{33} PiezoMeter PIEZOTEST PM300 (Fig. 2.22) was used.

2.6.7. Energy harvesting measurements:

The current work involves generating electrical power from mechanical energy, requiring the use of an electrical signal measurement setup. To measure the output voltage, a Tektronix MDO032 Digital Storage Oscilloscope (DSO) was employed. DSOs are a standard type of digital oscilloscope that presents electrical signals as waveforms

on a screen (Fig. 2.23). One significant advantage of DSOs lies in their capacity to digitally capture and store these waveforms. This capability allows users to examine previous signals, freeze a waveform for closer inspection, or save data for future analysis.

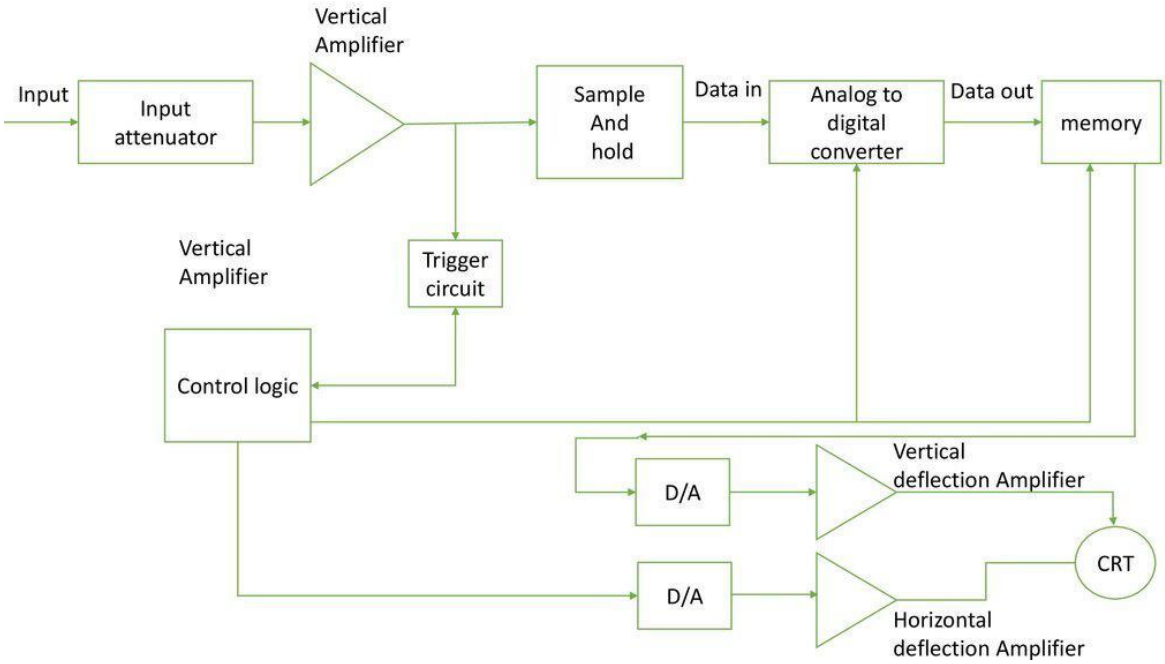

Fig. 2.23 *Schematic of the digital storage oscilloscope [ref. 23].*

For output current measurements a source meter AGILENT B2902A with a connection of Quick IV measurement software was used.

2.6.8. Others characterizations:

Other characterizations and software used throughout the thesis are discussed in each part.

References:

[1] S. Maity, A. Sasmal, S. Sen, Comprehensive characterization of Ba1−xSrxTiO3_ Correlation between structural and multifunctional properties, J Alloys Compd. 884 (2021) 161072. https://doi.org/10.1016/j.jallcom.2021.161072.

[2] P. Christian, D. Hennings, R. Waser. "Progress in the synthesis of nanocrystalline BaTiO3 powders for MLCC." International Journal of Applied Ceramic Technology 2.1 (2005): 1-14.

[3] https://wiki.aalto.fi/display/SSC/Ball+milling+as+a+synthesis+method.

[4] Pechini, M. P. "US Patent No. 3330697, July." (1967).

[5] K. Masato, and M. Yoshimura. "Synthesis and characteristics of complex multicomponent oxides prepared by polymer complex method." Bulletin of the Chemical Society of Japan 72.7 (1999): 1427-1443.

[6] Jr, Rinaldo & Cestari, Marcelo. Effect of crystallization temperature on the crystalline phase content and morphology of poly(vinylidene fluoride). Journal of Polymer Science Part B: Polymer Physics. 32. 859 – 870 (1994) doi: 10.1002/polb.1994.090320509..

[7] https://serc.carleton.edu/research_education/ geochemsheets/BraggsLaw.html.

[8] https://www.list.lu/fileadmin//files/Event/ sites/tudor/files/event/4_Presentation_Dr_Yves_Fleming.

[9] Ojeda, Jesús J., and M. Dittrich. "Fourier transform infrared spectroscopy for molecular analysis of microbial cells." Microbial Systems Biology: Methods and Protocols (2012): 187-211..

[10] https://chem.libretexts.org.

[11] https://www.tribonet.org/wili/scanning-electrone-microscope

[12] M. Naresh. Vision and visual serving for nanomanipulation and nanocharacterization in scanning electron microscope. Diss. Université de Franche-Comté, 2013.

[13] https://www.thermofisher.com/blog/materials/edx-analysis-with-sem-how-does-it-work/.

[14] D. Jean-Charles, et al. "Systematic XPS studies of metal oxides, hydroxides and peroxides." Physical Chemistry Chemical Physics 2.6 (2000): 1319-1324.

[15] https://jacobs.physik.uni-saarland.de.

[16] H. W. Willard; J. A. Dean; Jr. L. L. Merritt; F. A. Sattle; *Instruments Methods of Analysis*, CBS Publishers and Distributore, India, 1986.

[17] P. Thakur, A. Kool, B. Bagchi, S. Das, and P. Nandy. "Enhancement of β phase crystallization and dielectric behavior of kaolinite/halloysite modified poly (vinylidene fluoride) thin films." Applied clay science 99 (2014): 149-159.

[18] https://www.hitachi-hightech.com/global/en/knowledge/analytical systems/thermal-analysis/basics/dsc.html.

[19] C. Zhebo, Huyen N. Dinh, E. Miller, Z. Chen, T. G. Deutsch, H. N. Dinh, K. Domen et al. "UV-vis Spectroscopy." Photoelectrochemical Water Splitting: Standards, Experimental Methods, and Protocols (2013): 49-62.

[20] J. Wang, J. Xiang, S. Duo, W. Li, M. Li, L. Bai, Microstructure, optical and dielectric properties of compositional graded (Ba,Sr)TiO3 thin films derived by RF magnetron sputtering, J. Mater. Sci. Mater. Electron. 20 (2009) 319–322.

[21] https://commons.wikimedia.org/wiki/ File:Schematic_of_UV_visible_spectrophotometer.png

[22] https://wiki.aalto.fi/.

[23] https://www.geeksforgeeks.org/digital-storage-oscilloscope.

Chapter 3

Sr^{2+} doped $BaTiO_3$ incorporated PVDF: an efficient piezoelectric energy harvester and mechanosensor

3.1 Introduction

As mentioned in the previous chapter, for ambient mechanical energy harvesting, piezoelectric and triboelectric nanogenerators are commonly used [1,2]. Researchers are now engaged to develop these devices in a flexible manner so that they can be easily used in various real-life applications. Therefore, polymer-based materials have become the best choice of interest to researchers. The present work is also focused on developing flexible polymer-based composites for energy harvesting and mechanosensing applications. For this purpose, such polymer material is needed to be chosen that, the material exhibits inherent dielectric, ferroelectric and piezoelectric properties. That's why poly(vinylidene fluoride) (PVDF) and its co-polymers are the best choice to fulfill the desired requirements [1]. Therefore, PVDF was chosen as the base polymer matrix in the present study. Inspite of these advantageous properties, it suffers from some limitations including the propensity of exhibiting non-polar α phase in normal conditions and a low value of dielectric permittivity (~ 8-10) which place this material rear side of real life applications.

Ceramic material possesses a pivotal role in the output property (output voltage, output current, and output power density) enhancement of polymer composite based piezo, tribo, and hybrid energy harvesters. In this regard, Barium Titanate ($BaTiO_3$) was chosen as the filler material due to its modifiable dielectric, ferroelectric, and piezoelectric properties, and its lead-free nature [3–6]. This class of materials has a wide range of applications in the development of various technological devices, including energy storage, memory, and switching devices [7,8]. Moreover, the

---

A portion of this chapter appeared as

S. Maity, A. Sasmal, S. Sen, Comprehensive characterization of $Ba_{(1-x)}Sr_xTiO_3$: Correlation between structural and multifunctional properties. **Journal of Alloys and Compounds,** 2021, 884, 161072.

promising dielectric properties of $BaTiO_3$ and $BaTiO_3$-based ceramics make them valuable in diverse fields such as the creation of multilayer and voltage-tunable capacitors, electro-optic devices, infrared sensors, and efficient transducers [9–11]. Due to its exceptional piezoelectric properties, $BaTiO_3$-based materials are now extensively utilized in the fabrication of piezoelectric actuators for energy harvesting [12]. Additionally, this material serves as an environmentally friendly alternative to lead-based piezoelectric materials like lead zirconate titanate (PZT). Therefore, researchers worldwide continue to be intrigued by the study and manipulation of the properties of this material through various techniques. Several methods have been employed to tailor the performance of $BaTiO_3$, including techniques such as alloying with other perovskite oxides, site engineering, and domain engineering [13–15]. Since the perovskite lattice has the ability to accommodate ions of varying sizes, there is significant potential for intentional doping with various ions in this material [16]. In this regard, the process of alloying $BaTiO_3$ with perovskite oxides like, $BiFeO_3$ [17], $KNbO_3$ [15], $BiYbO_3$ [13], $CaTiO_3$ [18], $SrTiO_3$ [19], $Bi_{0.5}Na_{0.5}TiO_3$-$NaNbO_3$ [20], $CaTiO_3$-$BaHfO_3$ [21], $CaTiO_3$-$BaZrO_3$ [22], etc. have already been extensively studied earlier. On the other hand, Ba-site and/or Ti-site doping with Sm^{3+} [23], Sr^{2+} [24], Ca^{2+} [25], Li^{+}-Ho^{3+} [14], Mn^{4+} [26], Ni^{2+} [27], Fe^{2+}-W^{6+} [28], Fe^{3+} [29], Ca^{2+}-Zr^{4+} [16], Ca^{2+}-Zr^{4+}-Mn^{4+} [30], Zr^{4+} [31], Sn^{4+} [31], Hf^{4+} [32], etc. have also been thoroughly studied. Among all these techniques, recent attention has upsurged towards Sr^{2+} doped $BaTiO_3$ owing to its robust non-linear dielectric permittivity, low dielectric loss tangent, high tunability, and thermal stability of dielectric permittivity which are very valuable during the development of tunable microwave devices [9,10]. Additionally, the concentration of Sr^{2+} ions in the Ba^{2+} site profoundly influences the structural properties of $BaTiO_3$, thereby affecting its electrical behavior [33,34]. Notably, Sr^{2+} doping has also led to the emergence of ferroelectricity in $BaTiO_3$ even within the paraelectric centrosymmetric phase, a phenomenon that has sparked significant interest among researchers [35,36].

Despite some prior research on Sr^{2+} doped $BaTiO_3$, there is still a need for in-depth characterization and the establishment of correlations between its different properties. This motivates the choice of investigating this material in the current study. Here, we have fabricated $Ba_{(1-x)}Sr_xTiO_3$ ($0 \leq x \leq 1$) ceramics and thoroughly examined their structural, optical, vibrational, and dielectric properties. Among

them, $Ba_{0.6}Sr_{0.4}TiO_3$ (BST40) was identified as the most favorable composition due to its excellent dielectric properties, including a high permittivity, low loss tangent, and low leakage current density. This composition was subsequently employed as a filler within PVDF for applications in piezoelectric energy harvesting and mechanosensing.

3.2. Experimental

This chapter deals with the fabrication of the piezoelectric energy harvesting device using Barium strontium titanate incorporated PVDF as functional layer. Here, the filler BST particles are synthesized using solid state technique (detail is given in section 2.1.1 of chapter 2). Now to synthesize the composite films which act as the heart of the device simple solution casting technique was utilized (detail of the procedure is discussed in section 2.2.1 of chapter 2). Bare PVDF film was also prepared using the same procedure without adding any filler. The synthesized composites were indexed as 10BST40, 20BST40, 30BST40, 40BST40, 50BST40, and 60BST40 accordingly for 10, 20, 30, 40, 50, 60 wt% BST40 loaded PVDF composite films respectively. The average thickness of the composites and bare PVDF films were found out to be 0.05 mm as measured by the digital slide calipers. The final piezoelectric energy harvesting device was fabricated using the electrode-composite-electrode stack structure (detail of the fabrication procedure is included in section 2.3 of chapter 2)

3.3 Results and Discussions

3.3.1 Characterizations of fillers

3.3.1.1 Structural and Vibrational Characterization

The X-ray diffraction (XRD) patterns presented in Figure 3.1 demonstrate the successful integration of strontium into the perovskite Barium Titanate matrix throughout the entire compositional range, spanning from x = 0 to x = 1. Importantly, these patterns do not exhibit any discernible impurity peaks [37,38]. In the case of pure barium titanate without strontium doping, Figure 3.2 reveals a

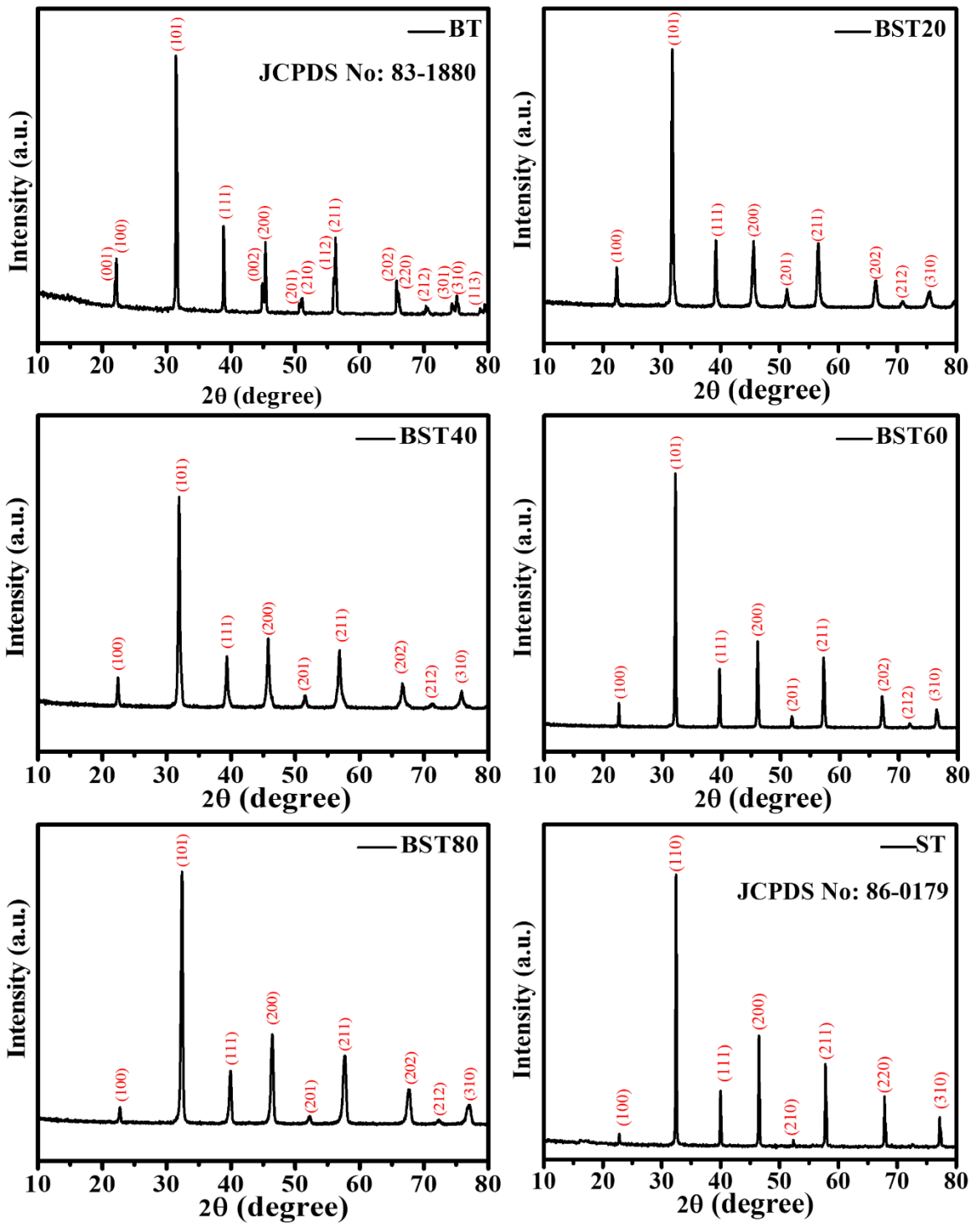

Fig. 3.1 *Indexing of XRD patterns of (a) BT, (b) BST20, (c) BST40, (d) BST60, (e) BST80, and (f) ST powders.*

distinct separation of peaks near the Bragg angle (2θ) of 45⁰, specifically concerning the (200) and (002) peaks. This peak separation becomes apparent when considering the intensity ratio of these two peaks (I_{200}/I_{002}), which measures at approximately 2. This ratio unequivocally validates the tetragonal nature of the

unadulterated Barium Titanate (BT) sample [14,39]. For the composition with x = 0.2, it is worth noting that the two peaks are almost merging. As portrayed in Figure 3.2, there is a gradual shift of diffraction peaks towards higher angles with the increasing concentration of Sr^{2+} doping. This shift signifies a stepwise reduction in the lattice parameters for the respective samples. Moreover, the absence of the (002) peak stands out as an indicator of the gradual structural phase transition from a tetragonal to a cubic configuration [40,41].

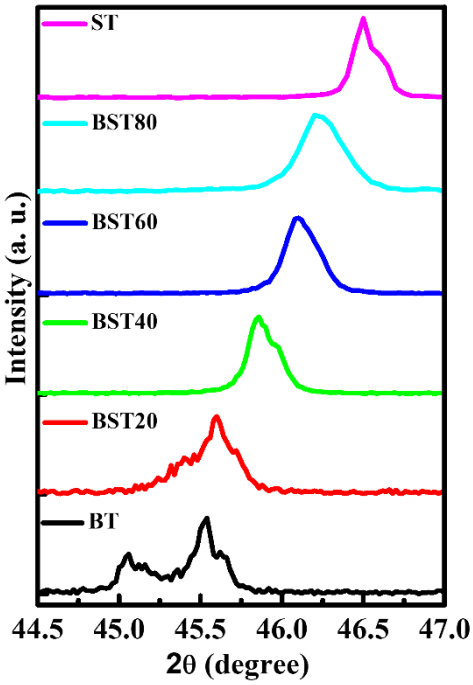

Fig. 3.2 *Zoomed view of the XRD pattern of $Ba_{(1-x)}Sr_xTiO_3$ ceramics of 2θ value from 44.5° - 47°.*

For an in-depth structural analysis, we employed the Rietveld method using the Full prof package to refine the XRD patterns of all synthesized ceramic powders within the $Ba_{(1-x)}Sr_xTiO_3$ series ($0 \leq x \leq 1$). The results of this refinement are presented in Figure 3.3, while the refined lattice parameters and structure fitting factors are summarized in Table 3.1. The Rietveld refinement unequivocally established that the BT and BST20 samples crystallize within the tetragonal P4mm space group. In contrast, BST40, BST60, BST80, and ST samples exhibited a cubic structure with

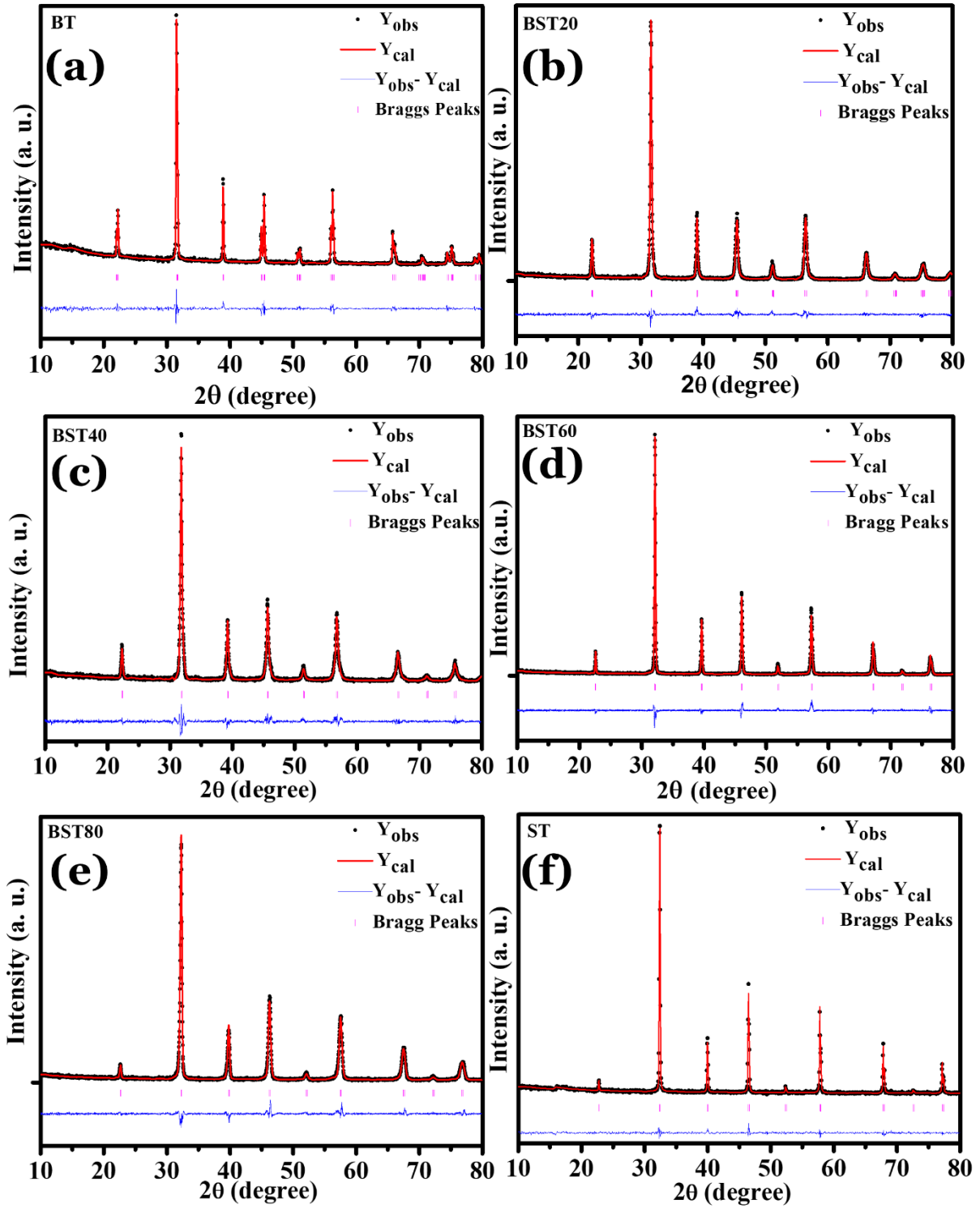

Fig. 3.3 *Rietveld Refined XRD patterns of (a) BT; (b) BST20; (c) BST40; (d) BST60; (e) BST80; (f) ST.*

the Pm-3m space group. An examination of the atomic positions revealed that BT and BST20 adopt a non-symmetrical structure, whereas BST40, BST60, BST80, and ST displayed a symmetrical structure.

Table 3.1 Refined lattice parameters and structure fitting factors of all the samples.

x values and space group	Lattice parameters		c/a	Crystal Volume (Å³)	Atoms	Atomic sites (x,y,z)	Ti-O Bond Length (Å)	Refinement fitting factors
	a (Å)	c (Å)						
BT (P4mm)	3.9937	4.0323	1.0097	64.3134	Ba Ti O1 O2	(0,0,0) (0.5,0.5,0.4820) (0.5,0.5,0.0160) (0.5,0.0,0.5150)	2.15	R_p= 25.7% R_{wp}= 21.3% x^2 = 1.05
BST20 (P4mm)	3.9871	4.0054	1.0046	63.6741	Sr Ba Ti O1 O2	(0,0,0) (0,0,0) (0.5,0.5,0.4850) (0.5,0.5,0.0140) (0.5,0.0,0.5150)	2.12	R_p= 15.1% R_{wp}= 16.9% x^2 = 1.34
BST40 (Pm-3m)	3.9732	3.9732	1.0000	62.7203	Sr Ba Ti O	(0,0,0) (0,0,0) (0.5,0.5,0.5) (0.5,0.5,0)	1.99	R_p= 17.6% R_{wp}= 18.9% x^2 = 1.41
BST60 (Pm-3m)	3.9413	3.9413	1.0000	61.2231	Sr Ba Ti O	(0,0,0) (0,0,0) (0.5,0.5,0.5) (0.5,0.5,0)	1.97	R_p= 18.8% R_{wp}= 18.7% x^2 = 1.57
BST80 (Pm-3m)	3.9242	3.9242	1.0000	60.4294	Sr Ba Ti O	(0,0,0) (0,0,0) (0.5,0.5,0.5) (0.5,0.5,0)	1.96	R_p= 17.2% R_{wp}= 17.3% x^2 = 1.49
ST (Pm-3m)	3.9058	3.9058	1.0000	59.5860	Sr Ti O	(0,0,0) (0.5,0.5,0.5) (0.5,0.5,0)	1.95	R_p= 27.5% R_{wp}= 13.8% x^2 = 1.07

Notably, in BT and BST20, the Ti^{4+} ions are slightly displaced from the crystal's center. The degree of tetragonality, quantified by the c/a ratio (the ratio of lattice parameters along the polar axis to the X-axis), decreased as strontium incorporation increased, maintaining a constant value of 1 for $0.4 \leq x \leq 1.0$. This observation further confirmed a phase transition occurring at x = 0.4, shifting from a tetragonal to a cubic structure [40,42]. The stability of an ionic addition within a perovskite structure relies on the tolerance factor, which falls within a specific range of 0.880 to 1.090 for maintaining stable perovskite structures, as indicated in reference [43].

The Goldschmidt tolerance factor (t) required for this evaluation can be computed using the formula provided in Equation 3.1. [43].

$$t = \frac{r_A + r_O}{\sqrt{2}(r_B + r_O)} \qquad (3.1)$$

where, r_A, r_B, and r_O are the ionic radius of A-site cation, B-site cation, and anionic radius of O^{2-}, respectively. To be precise, r_A represents the ionic radius of either Ba^{2+} or Sr^{2+} ions (1.61Å and 1.44Å, respectively), while r_B corresponds to the ionic radius of Ti^{4+} ions (0.60Å), and r_O symbolizes the ionic radius of O^{2-} ions (1.4Å). These ionic radius values have been sourced from Shannon's ionic radii periodic table, taking into consideration the coordination number [44].

The computed tolerance factor values for all the samples are detailed in Table 3.2. As we can discern from the data presented in Table 3.2, it is evident that the gradual addition of Sr^{2+} results in a decrease in the deviation of tolerance factor (t) values from 1. When t values deviate from 1, it signifies a non-symmetrical structure. Consequently, the transition from a non-symmetrical structure (BT) to a symmetrical one (ST) is confirmed based on the information provided in Table 3.2.

Table 3.2 Calculated tolerance factors of $Ba_{(1-x)}Sr_xTiO_3$($0 \leq x \leq 1$) samples.

x	0	0.2	0.4	0.6	0.8	1
Tolerance factor (t)	1.062	1.050	1.040	1.025	1.010	1.002

The widely recognized Scherrer's Equation (as presented in Equation 3.2) was utilized to determine the crystallite size (D) based on the powder X-ray diffraction patterns of all the samples [45].

$$D = \frac{k\lambda}{\beta \cos\theta} \qquad (3.2)$$

Here, k = 0.9, λ is wavelength (0.154 nm) of incident CuK_α radiation, β is full width at half maximum of a peak, θ is Bragg angle corresponds to the peak position. The

parameter "β" encompasses contributions to peak width originating from both the sample and the instrument. To eliminate the peak broadening attributed to instrumental effects, the following relationship (referred to as Equation 3.3) was employed [46].

$$\beta_c = \sqrt{\beta^2 - \beta_i^2} \qquad (3.3)$$

where β represents measured peak width, β_c is corrected FWHM and β_i is the width of instrument broadening. The peak width component originating from the instrumental effect is measured by keeping Silicon (Si) as the reference material [45]. With this corrected FWHM, we can now calculate the average crystallite size using a modified Scherrer's equation by substituting "β_c" for "β" in Equation 3.1.

The Scherrer equation, which is used to determine crystallite size by analyzing peak broadening, has a limitation because it solely accounts for the broadening caused by crystal size. Another important factor to consider is strain (ε), primarily arising from imperfections within the crystal, which significantly impacts peak broadening [44]. To separate the effects of crystallite size and strain, the Williamson-Hall (W-H) plot method is commonly employed [47]. According to the W-H method, peak broadening due to both crystallite size and strain can be expressed using Equation 3.4 provided below.

$$\beta_{hkl} = \beta_{cry.\ size} + \beta_{strain} \qquad (3.4)$$

Here the 1st term on the right-hand side is reversely proportional to '$\cos\theta$' and 2nd term is proportional to '$\tan\theta$'. The mismatch in size and strain widening is related to the θ dependence [47]. Now Equation 3.4 stands as,

$$\beta_{hkl} = \frac{k\lambda}{D}\left(\frac{1}{\cos\theta}\right) + 4\varepsilon \tan\theta \qquad (3.5)$$

$$\text{or, } \beta_{hkl}\cos\theta = \frac{k\lambda}{D} + 4\varepsilon \sin\theta \qquad (3.6)$$

Equation 3.6 has been visualized in Figure 3.4, where we have plotted βcosθ on the Y-axis against 4sinθ on the X-axis for all the samples. The slope of this linear curve serves as an indicator of the strain, while the intercept value provides information about the crystallite size. It's worth noting that the data points for BT and BST20 exhibit some dispersion, implying an uneven distribution of crystallite sizes and micro-strain values [46]. An examination of the Williamson-Hall (W-H) plot reveals an interesting trend: the introduction of strontium into BT initially decreases the crystallite size within the tetragonal structure. However, at BST40, there's an increase in size before a subsequent decrease with a higher strontium content. This peculiar behavior may be attributed to a sudden structural phase change occurring within the sample, transitioning from a non-symmetric to a symmetric state [24,48]. The micro-strain values obtained from the W-H plot suggest that samples with smaller crystallites tend to have higher strain values, which aligns with previous findings reported by Khirade et al. [29]. Importantly, there's a notable difference in crystallite sizes calculated using the Scherrer method and the W-H plot. This disparity arises because micro-strain within the lattice significantly affects peak broadening.

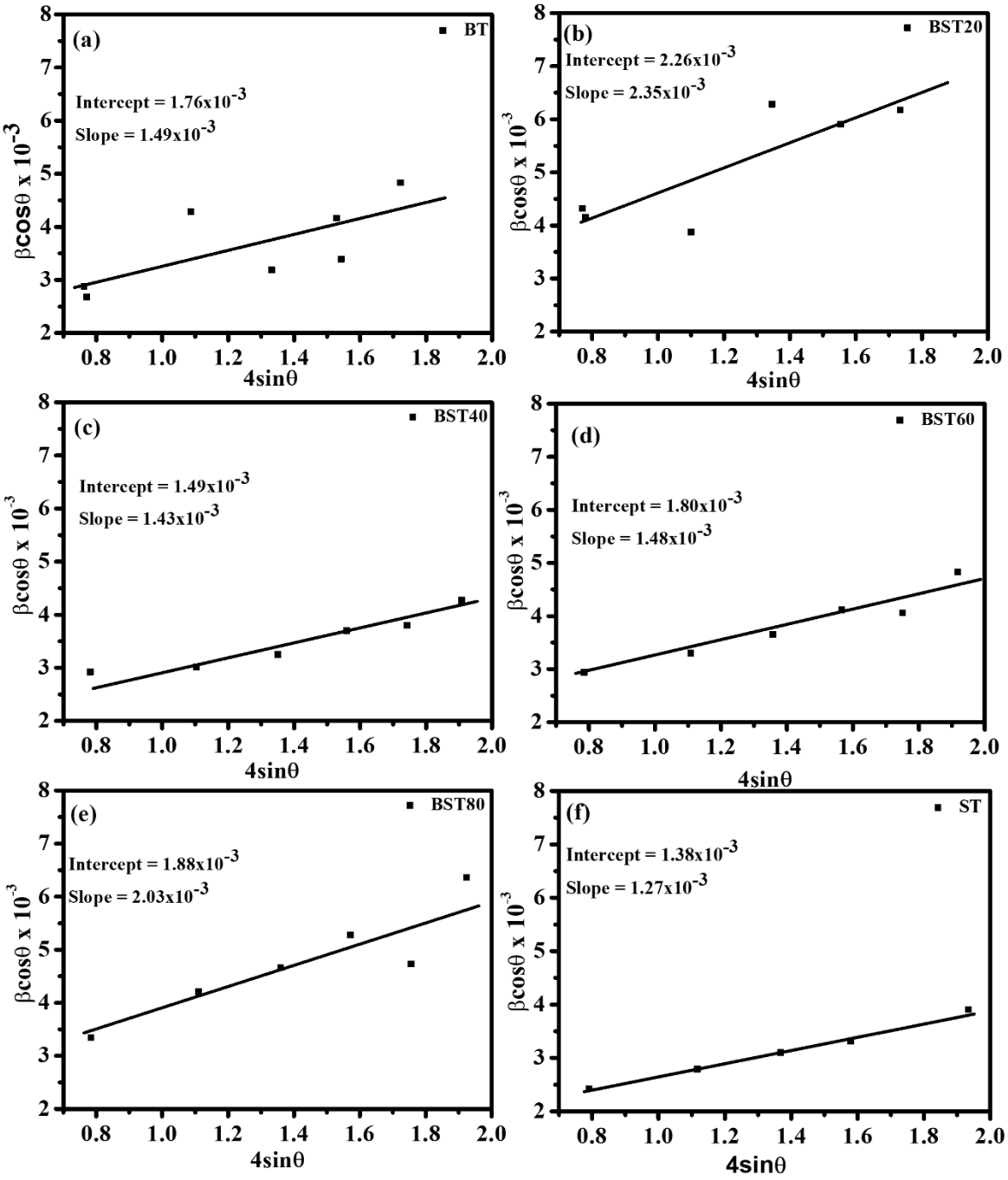

Fig. 3.4 *Williamson – Hall plot of (a) BT, (b) BST20, (c) BST40, (d) BST60, (e) BST80, and (f) ST samples.*

The Scherrer method considers the entire breadth of peak broadening, whereas the W-H plot method separates the two contributing factors to peak broadening [45,49]. Consequently, the full width at half maximum (FWHM) measured by the Scherrer method is greater than that obtained from the W-H method. Crystallite sizes calculated using these different methods for all the samples are tabulated in Table 3.3.

Table 3.3 Calculated crystallite sizes and lattice strains of $Ba_{(1-x)}Sr_xTiO_3$ ($0 \leq x \leq 1$) samples.

x		0	0.2	0.4	0.6	0.8	1
Crystallite size (nm)	Scherrer's method	38	28	40	37	30	45
	Modified Scherrer's method	42	30	45	41	32	53
	W-H plot method	78	61	93	77	73	100
Lattice strain ($\times 10^{-3}$)		1.49	2.35	1.43	1.48	2.03	1.27

Fig. 3.5 shows the room temperature Raman spectra for the prepared samples of $Ba_{(1-x)}Sr_xTiO_3$, where x varies from 0.0 to 1.0. Within this spectrum, when examining BT, there are distinctive features. Specifically, there is a prominent and distinct peak at 268 cm^{-1}, referred to as the $A_1(TO_2)$ mode, and another one at 306 cm^{-1}, denoted as $E(TO_3+LO)$ or B_1 mode. These peaks are a result of the vibrations in the TiO_6 octahedral unit within the perovskite structure of the material [50].

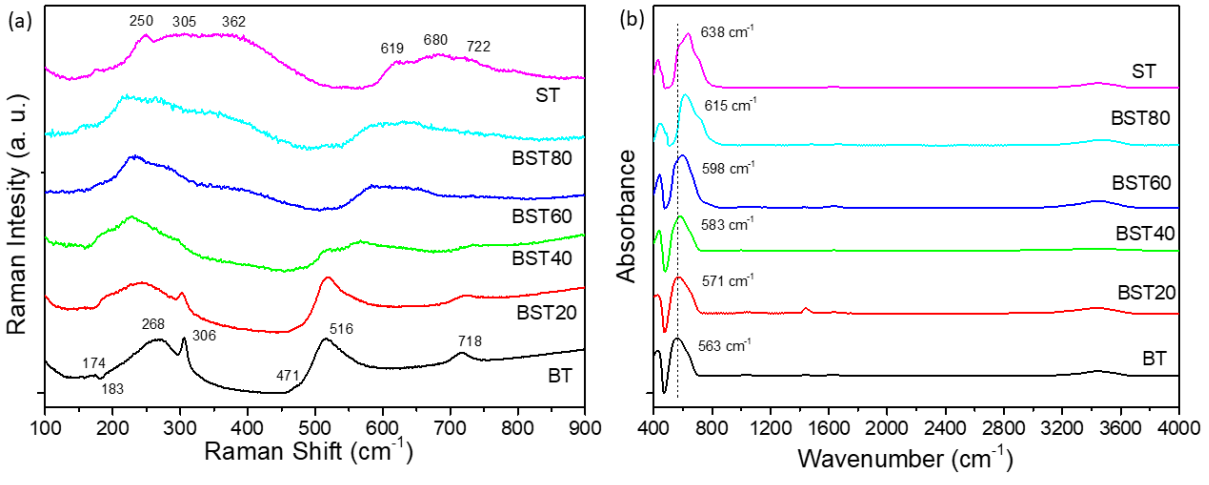

Fig. 3.5 *(a) Raman Scattering Spectra (b) FTIR spectra of* $Ba_{(1-x)}Sr_xTiO_3$ *($0 \leq x \leq 1$) ceramics.*

The presence of a peak at 516 cm^{-1} signifies vibrations resulting from the displacement of an oxygen atom [51]. Additionally, there is a distinct and intense interference dip observed at 183 cm^{-1}, which can be attributed to the coupling between several modes, including $A_1(TO_1)$, $E(TO_2)$, $E(LO_1)$ at 174 cm^{-1}, and the $A_1(TO_2)$ mode at 268 cm^{-1} [50]. Moreover, the scattering peaks at 306 cm^{-1} and 718 cm^{-1} are characteristic features associated with the tetragonal structure of $BaTiO_3$ [52]. In the case of the BST20 sample, it is evident that the intensities of these two

peaks have decreased compared to BT. This decrease suggests that the addition of Sr results in a reduction in both the Curie transition temperature and the degree of tetragonality. At room temperature, ST exhibited a second-order spectrum characterized by peaks primarily resulting from the interaction of transversely polarized phonons [52]. The broadening of bands in the frequency ranges of 200 – 400 cm^{-1} and 550 – 750 cm^{-1} is a clear indicator of the off-center motion of Ti^{4+} ions [53]. Within the first frequency range (200 – 400 cm^{-1}), three peaks were observed. The peak at 250 cm^{-1} corresponds to a combination of 2TA, TO_1 + TA, and $2TO_1$ modes, while the peak at 305 cm^{-1} results from the combination of TO_2 + TA, TO_2 + TO_1, and TO_4 - TO_2 modes [54]. The broad peak centered at 362 cm^{-1} originates from phonon modes associated with TO_4 – TA, TO_4 – TO_1, and $2TO_2$. Due to the identical energy levels of TA and TO_1, the peak at 619 cm^{-1} is attributed to TO_4 combined with them [53]. The two remaining broad peaks at 680 cm^{-1} and 722 cm^{-1} result from the interaction of two phonons in the TO_3 mode and TO_4 + TO_2 modes, respectively [53]. These characteristic patterns of broadened bands are particularly evident for values of x between 0.4 and 1.0. Therefore, it can be inferred that the phase transition from a tetragonal to a cubic structure occurs at x=0.4. Remarkably, BST40 displays a similar band pattern to ST and exhibits polar modes at 300 cm^{-1} and 518 cm^{-1}. Previous studies using powder X-ray diffraction had already confirmed the cubic symmetry of BST40. However, the presence of polar modes in the Raman spectra of BST40 undoubtedly confirms the existence of polar nanoregions [55]. This discrepancy arises from the nature of the scattering processes in X-ray diffraction and Raman spectra. Raman scattering provides insight into short-range order, whereas X-ray diffraction measures the long-range order of the samples [55].

To dig deeper into the vibrational characteristics, FTIR absorption spectra for all the ceramic particles were conducted across a broad wavenumber range spanning from 400 to 4000 cm^{-1}, as illustrated in Figure 3.5(b). Within this spectral range, all the samples exhibited prominent peaks between 450 cm^{-1} and 650 cm^{-1}, which are indicative of the Ti-O stretching vibration, a well-known characteristic [56]. In the case of undoped BT, the most striking peak appeared at 563 cm^{-1}, and this peak can be attributed to the vibrational mode resulting from Ti-O stretching, a phenomenon previously reported [56]. As for the BST20, BST40, BST60, BST80, and ST samples, these modes were observed at 571 cm^{-1}, 583 cm^{-1}, 598 cm^{-1}, 615 cm^{-1}, and 638 cm^{-1},

respectively. The shift of these corresponding peaks towards higher energy values is associated with the reduction in lattice parameters, a characteristic that has been previously validated through XRD analysis.

Vibrational frequency owing to Ti-O bond evaluated by Equation 3.7.

$$\bar{\nu} = \frac{1}{2\pi c}\sqrt{\frac{k}{\mu}} \qquad (3.7)$$

where $\bar{\nu}$ is wavenumber, c represents velocity of light and k is average force constant and expressed by Equation 3.8.

$$k = \frac{17}{r^3} \qquad (3.8)$$

The symbol "r" represents the length of the Ti-O bond, while "μ" signifies the effective mass of the Ti-O bond, as expressed by the following equation (Equation 3.9).

$$\mu = \frac{M_O M_{Ti}}{M_O + M_{Ti}} \qquad (3.9)$$

The table in Table 3.4 displays the calculated values of the average force constant and Ti-O bond length using the equations mentioned above. As the concentration of Sr^{2+} increases, the crystal volume decreases, causing a contraction in the distance between Ti^{4+} and O^{2-}. Consequently, this leads to an increase in bond strength, resulting in a higher average force constant. These measured Ti-O bond length values align closely with the results obtained from the Rietveld Refinement of XRD patterns.

Table 3.4 Calculated average force constant (k) and Ti-O bond lengths of all the samples.

Sample Name	BT	BST20	BST40	BST60	BST80	ST
Average force constant (*k*) (N/cm)	2.24	2.30	2.40	2.53	2.67	2.88
Ti-O bond length (Å)	1.96	1.95	1.92	1.89	1.85	1.81

3.3.1.2 Optical properties

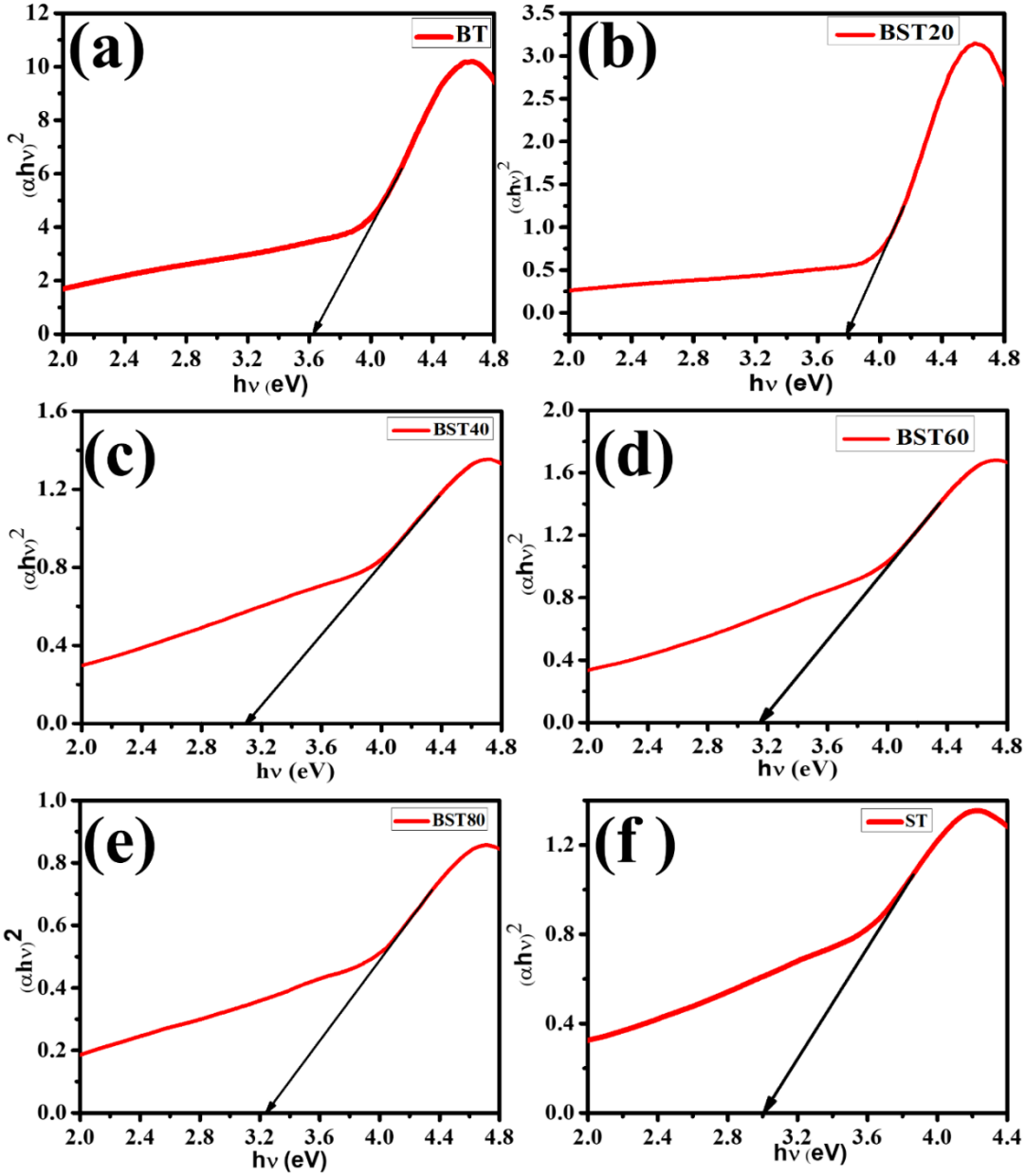

Fig. 3.6 *$(ahv)^2$ vs hν plot of the synthesized $Ba_{(1-x)}Sr_xTiO_3$ $(0\leq x\leq 1)$ ceramics.*

The study investigated the optical properties of $BaTiO_3$ particles with the addition of strontium (Sr) using UV-Vis spectroscopy. Absorption measurements were conducted across the wavelength range of 250 to 700 nm. The calculated energy gap, known as the energy band gap (E_g), between the valence and conduction bands using the Tauc plot method [57] and Equation 3.10.

$$(\alpha h\nu)^2 = A(h\nu - E_g) \qquad (3.10)$$

the energy band gap (E_g) was determined by using certain parameters: α, which represents the absorption coefficient, h (Planck's constant), ν (the frequency of incident light), and A (an arbitrary constant). To obtain the E_g value, a plot was created with $(\alpha h\nu)^2$ on the y-axis and hν on the x-axis, as shown in Figure 3.6. The linear portion of the graph was extrapolated, and the point where the tangent line intersects the x-axis (where y=0) gives the band gap energy. The calculated E_g values for all the samples are presented in Table 3.5.

Table 3.5 Band gap energy (E_g) of $Ba_{(1-x)}Sr_xTiO_3$ ($0 \leq x \leq 1$) samples.

x	0.0	0.2	0.4	0.6	0.8	1.0
E_g (eV)	3.62	3.78	3.10	3.15	3.24	3.01

Undoped $BaTiO_3$ exhibited a band gap of 3.62 eV, consistent with the reported value in the literature [58]. In the case of BST20, the band gap value was found to be higher than that of BT. This increase is primarily attributed to the reduction in crystallite size, as confirmed by XRD analysis, in the BST20 sample compared to BT. As the crystallite size decreases, the atomic distances also shrink, resulting in stronger binding forces between valence electrons and the atoms in the valence band. Consequently, electrons require more energy to transition to the conduction band, explaining the higher E_g value for BST20. On the other hand, the decrease in band gap energy observed in the BST40 sample compared to BST20 may be attributed to a structural phase transition from tetragonal to cubic [59]. In tetragonal BT, the highest valence band state and the lowest conduction band state involve O 2p and Ti 3d states, respectively. However, in cubic BT, the O 2p state shifts slightly upward, and the Ti 3d state shifts downward relative to their tetragonal counterparts [60], resulting in a decrease in the E_g value. This decrease aligns with previous reports [59,60]. In the cubic structured BST60 and BST80 samples, there was an increase in band gap energy to 3.15 eV and 3.24 eV, respectively, compared to the value of 3.10 for BST40. This increase is likely linked to the reduction in crystallite size in the cubic phase of the material.

3.3.1.3 Morphological and elemental characterization of bulk pellets

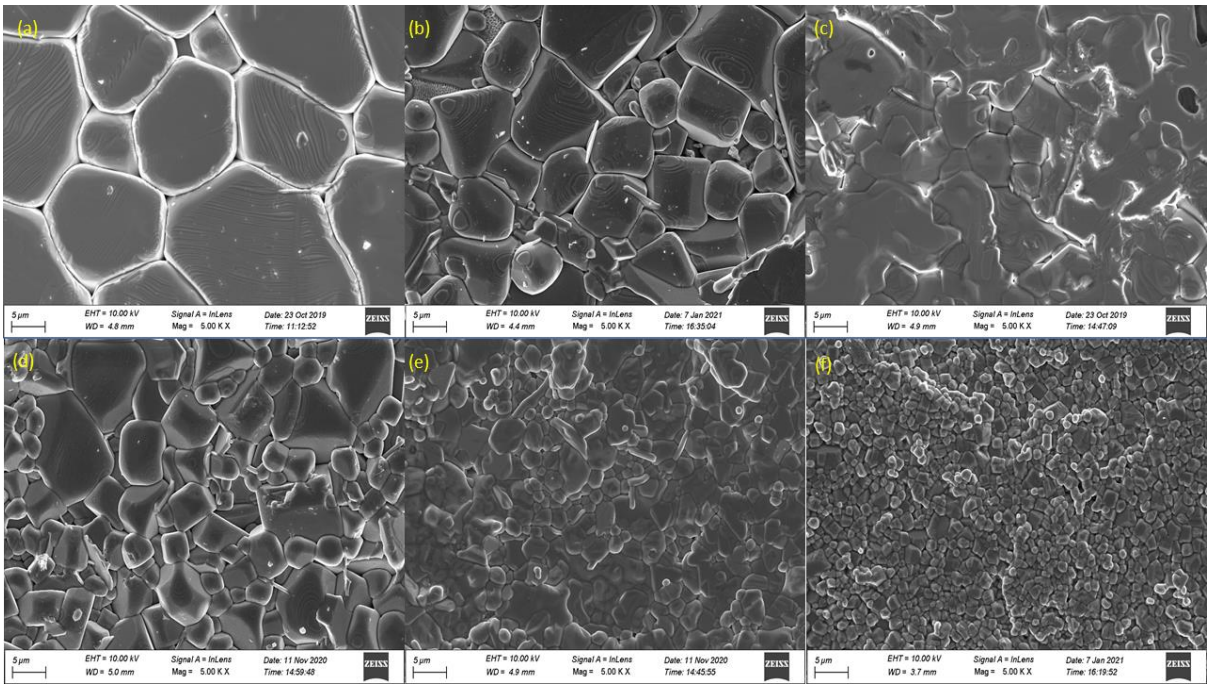

Fig. 3.7 *FESEM image of sintered pellets of (a) BT; (b) BST20; (c) BST40; (d) BST60; (e) BST80; (f) ST.*

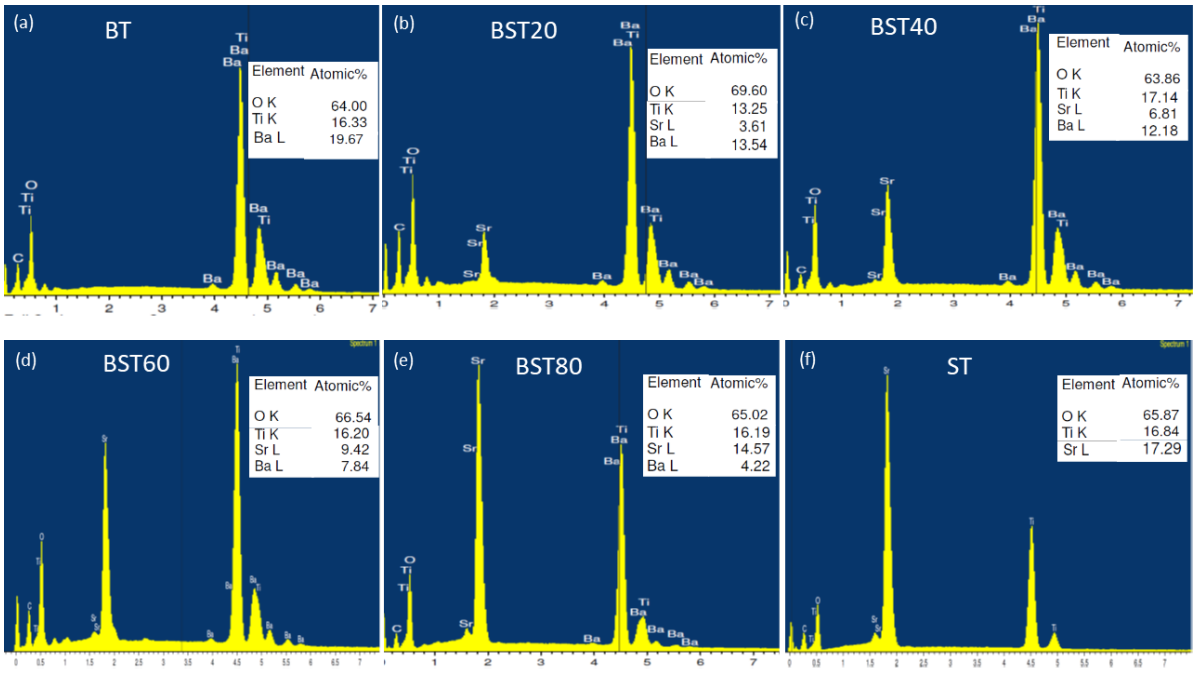

Fig. 3.8 *EDX spectra and elemental composition percentage of (a) BT, (b) BST20, (c) BST40, (d) BST60, (e) BST80, and (f) ST pellets.*

Strontium titanate ($SrTiO_3$) exhibited an E_g value of 3.01 eV, slightly lower than the reported values of around 3.2 eV [37]. It's important to note that band gap values can

also be influenced by lattice defects such as O-vacancies, which could contribute to this variation [61].

As mentioned earlier, to conduct electrical measurements on the synthesized samples, bulk pellets were prepared and subjected to sintering at 1350^{0}C. Since the grain size of these bulk samples significantly influences their electrical properties, the morphology of the sintered pellets was examined using FESEM (Field Emission Scanning Electron Microscopy). Figure 3.7 displays the FESEM images of all the pellets. The average grain size was determined using ImageJ software, employing the linear intercept method. For the Barium Titanate pellet, the measured average grain size was found to be 18.08 µm. This grain size decreases with the increasing strontium content in the samples, a trend consistent with previous research [62,63]. Specifically, for BST20, BST40, BST60, BST80, and ST, the calculated average grain sizes were 13.48 µm, 8.01 µm, 4.67 µm, 3.13 µm, and 1.44 µm, respectively. Quantitative EDAX analysis showed no compositional impurities in the samples, as seen in Figure 3.8.

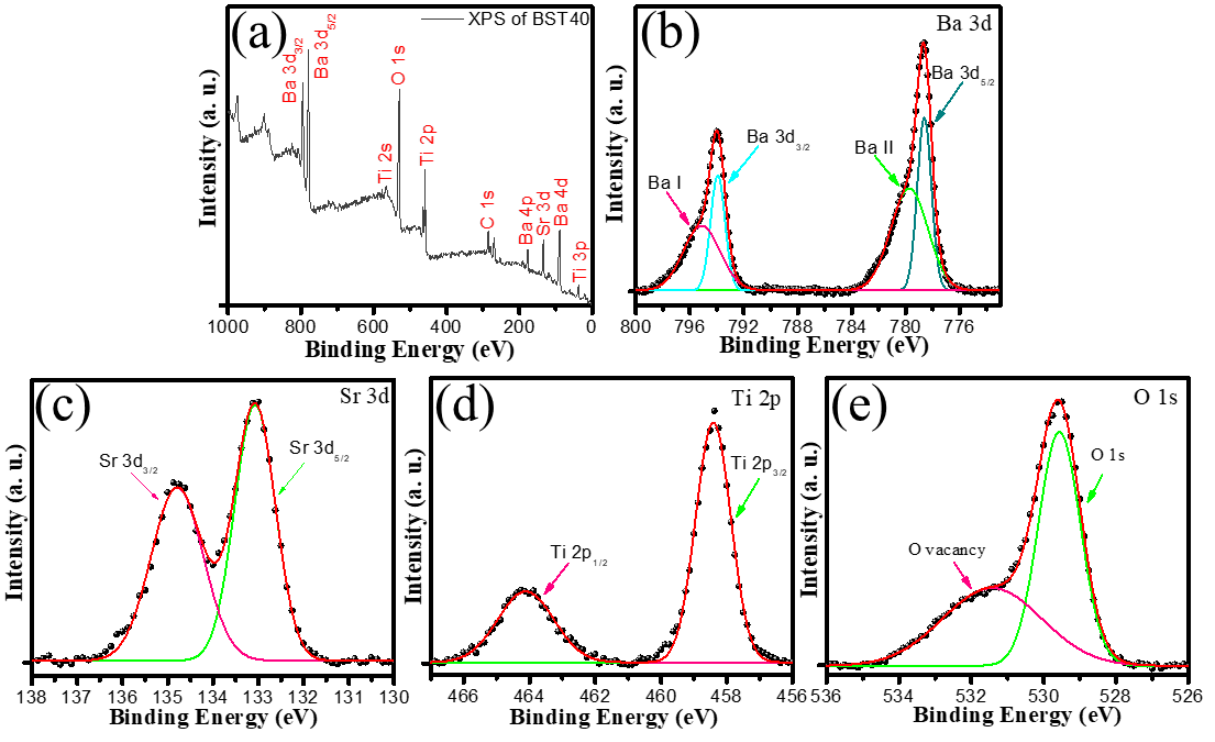

Fig. 3.9 *XPS (a) Survey spectra of BST40; core level spectra of (b) Ba 3d (c) Sr 3d (d) Ti 2p (e) O 1s.*

To gain qualitative compositional insights for BST40, we conducted an XPS (X-ray Photoelectron Spectroscopy) analysis. Figure 3.9(a) illustrates the survey spectra of

the synthesized ceramic powder, and high-resolution XPS spectra were obtained for Ba 3d, Ti 2p, Sr 3d, and O 1s as shown in Figure 3.9(b-e). The Ba 3d spectra exhibited two distinct peaks at binding energy values of 793.5 eV and 778.1 eV, corresponding to the $3d_{5/2}$ and $3d_{3/2}$ states, respectively. These peaks are indicative of the perovskite structure present in the BST40 sample [64]. The Ti 2p peak showed contributions from both Ti 2p1/2 (463.4 eV) and Ti 2p3/2 (457.6 eV), providing information about the titanium states in the material. The Sr 3d peak was split into two peaks at 133.9 eV and 132.3 eV, denoted as $3d_{1/2}$ and $3d_{3/2}$, respectively, providing information about the strontium states in the material. The O 1s peak at a binding energy value of 528.8 eV represented the oxygen states in the sample. Overall, the positions of the XPS peaks for all elements confirmed the presence of Ba in the 2+ state, Sr in the 2+ state, and Ti in the 4+ state in the BST40 material.

3.3.1.4 Leakage characteristics

Leakage current is a critical parameter that significantly influences the electrical

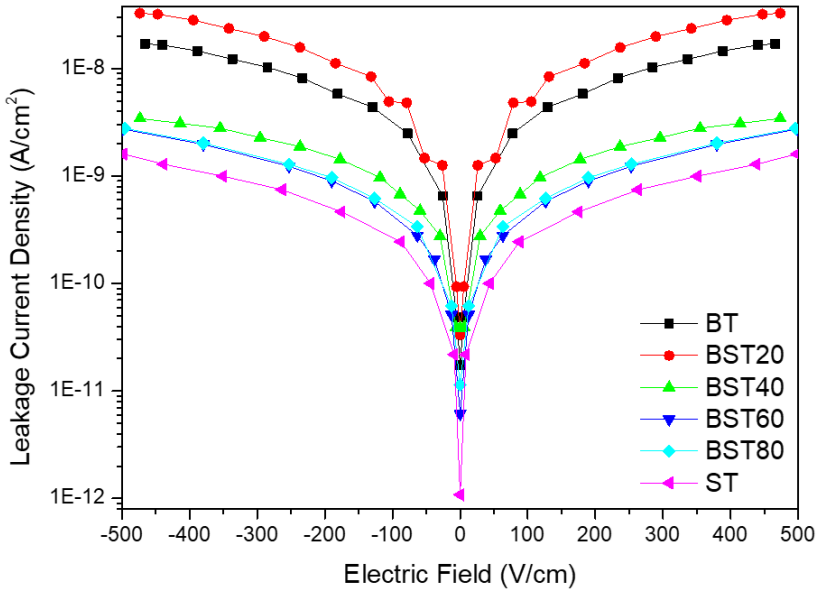

Fig. 3.10 *Leakage current density (J) characteristics of fabricated ceramic pellets with the variation of Electric Field (E).*

characteristics of bulk ceramics. In Figure 3.10, the behavior of leakage current density in response to an electric field ranging from -500 V/cm to 500 V/cm is depicted for all $Ba_{(1-x)}Sr_xTiO_3$ ceramics. At very low electric fields, the leakage current increases sharply as the electric field strength rises for all the samples. This sudden

increase in mobility, caused by the externally applied electric field and the subsequent rise in electron density, leads to the observed increase in leakage current [65]. This trend saturates at electric fields above 100 V/cm. Interestingly, the addition of strontium initially increases the leakage current, which then decreases as the strontium content approaches $SrTiO_3$ (ST). At an electric field of 450 V/cm, the leakage current density values for BT, BST20, BST40, BST60, BST80, and ST are 16.86 nA/cm², 31.95 nA/cm², 3.29 nA/cm², 2.39 nA/cm², 2.38 nA/cm², and 1.35 nA/cm², respectively.

3.3.1.5 Dielectric and impedance characteristics

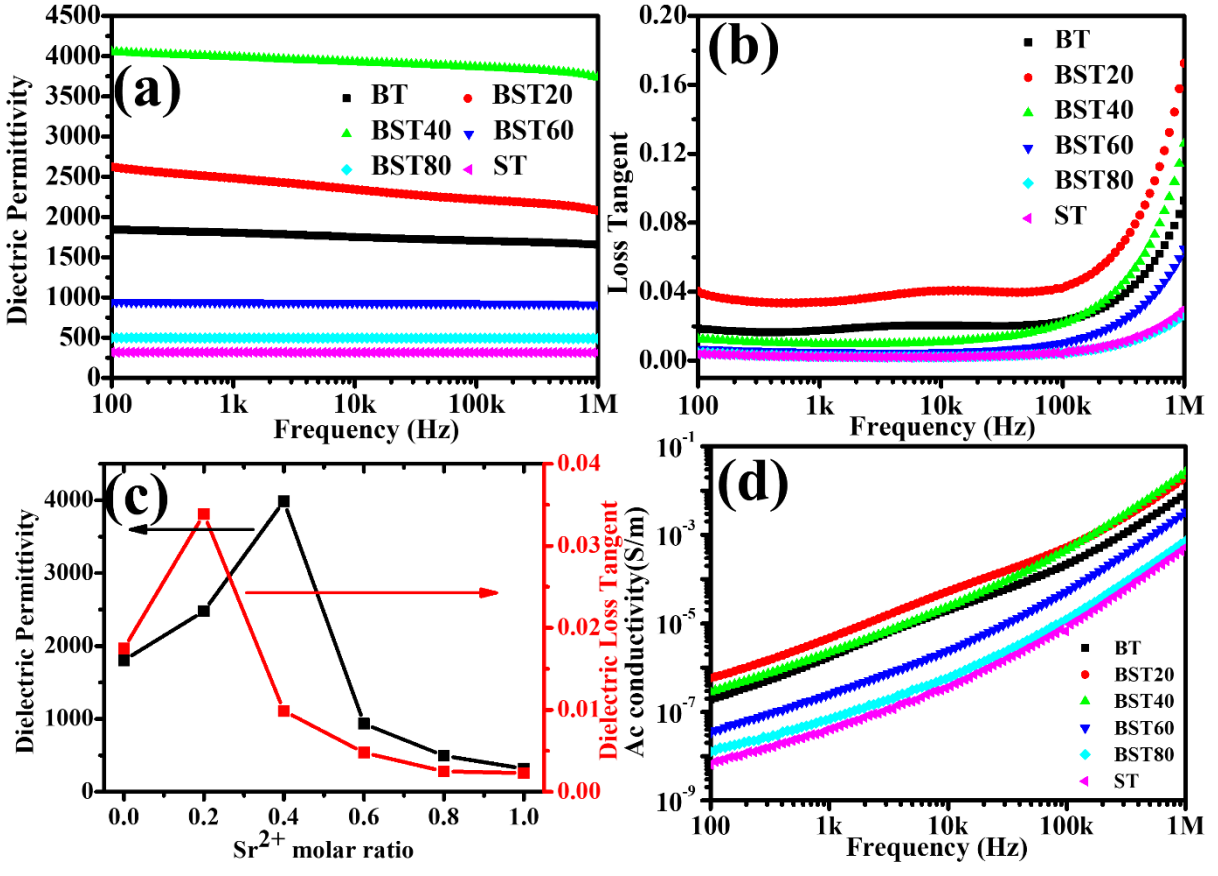

Fig. 3.11 *Frequency dependency of (a) Dielectric Permittivity (b) Dielectric loss tangent of the $Ba_{(1-x)}Sr_xTiO_3$ pellets; (c) Dielectric Permittivity and Dielectric loss tangent at 1 KHz frequency with the variation of Strontium molar ratio; (d) AC conductivity vs Frequency of the fabricated pellets.*

Barium titanate (BaTiO3) is a well-studied material known for its ferroelectric and dielectric applications, characterized by its exceptionally high dielectric permittivity. In our study, we conducted a thorough examination of the dielectric properties of all

the ceramic samples produced. Figure 3.11(a) displays the frequency-dependent relative dielectric permittivity (ϵ_r) of all the samples at room temperature, spanning a wide frequency range from 100 Hz to 1 MHz. Notably, all the samples exhibit consistent dielectric permittivity across this frequency range, demonstrating excellent frequency independence. However, a subtle decline in permittivity as the frequency increases is observed around 10^6 Hz which can be attributed to the dipole relaxation mechanism [66]. Figure 3.11(b) illustrates the frequency-dependent dielectric loss tangent (tanδ) for all the samples. The tanδ values remain stable from 100 Hz to 100 kHz and then experience a sudden increase. This observed behavior aligns with the Debye relaxation formula outlined in Equation 3.11 [67].

$$tan\,\delta = \frac{(\epsilon_{rs}-\epsilon_{r\infty})\omega\tau}{\epsilon_{rs}+\epsilon_{r\infty}\omega^2\tau^2} \qquad (3.11)$$

The static dielectric permittivity (ϵ_{rs}) represents the permittivity of the material at zero frequency, while $\epsilon_{r\infty}$ is the permittivity where dielectric polarization comprises solely electronic and ionic contributions. The angular frequency is represented by ω and relaxation time is represented by τ. Dielectric loss in materials typically arises from two main factors: leakage current and polarization loss. At low frequencies, dipoles within the material have sufficient time to align themselves in response to the applied electric field. Consequently, in the low-frequency range, the tanδ, which primarily comes from leakage current, remains relatively small. However, as the frequency increases beyond 10^5 Hz, the dipoles in the material cannot keep up with the rapidly changing electric field, resulting in a sharp increase in the tanδ value. This behavior is attributed to the limitations in dipole alignment at higher frequencies [66]. Fig. 3.11(c) presents the variation of room temperature ϵ_r and tanδ values at 1 KHz frequency with the variation of strontium concentration in $BaTiO_3$. In $Ba_{(1-x)}Sr_xTiO_3$ (x = 0, 0.2, 0.4, 0.6, 0.8, 1), permittivity upsurged at first up to x = 0.4. A decrease in grain size leads to a reduction in the number of domains, which in turn increases the stress within the material. According to Devonshire's phenomenological theory, an increase in stress values correlates with higher permittivity [68].

Among all the samples tested, BST40 exhibited the highest dielectric permittivity of ~ 3986, which is nearly twice that of undoped barium titanate (BT). However, when

the strontium content in BT exceeded 40%, resulting in smaller grain sizes, no further increase in permittivity was observed. Instead, there was a reduction in permittivity. This decrease in permittivity after x = 0.4 is likely associated with a stronger effect than just stress, possibly related to the cubic crystal structure where no polar direction is present. The dielectric loss tangent value reached its maximum for the BST20 sample and then gradually decreased with increasing Sr2+ concentration. The high dielectric loss observed is primarily due to increased leakage current [67]. For instance, at room temperature and a frequency of 1 kHz, BT exhibited a dielectric loss tangent of 0.0175, which increased to a maximum value of 0.0338 for the BST20 sample. The lowest loss tangent value of 0.0023 was observed in strontium titanate. Notably, the BST40 sample exhibited a tanδ value of 0.0098 (at room temperature and 1 kHz frequency), which is even lower than that of BT. Consequently, the BST40 sample demonstrated both a high dielectric permittivity and a relatively lower dielectric loss tangent.

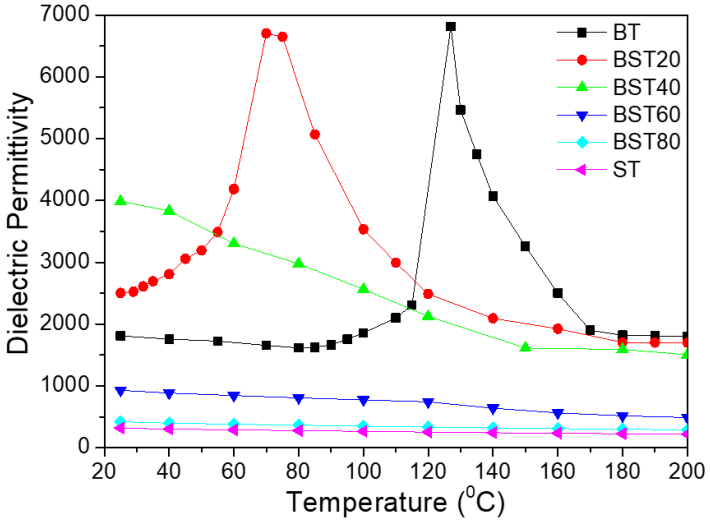

Fig. 3.12 *Temperature-dependent Dielectric Permittivity of* $Ba_{(1-x)}Sr_xTiO_3$ *pellets.*

The temperature-dependent dielectric permittivity at a frequency of 1 kHz for all the pellet samples is illustrated in Figure 3.12. As the temperature increases towards the Curie temperature (T_c), which is the transition temperature in ferroelectric materials, domains within the material separate into smaller polar nanoregions. This leads to the highest dielectric permittivity at T_c [69]. Above this transition temperature, the samples enter a paraelectric phase where spontaneous polarization diminishes, resulting in a decrease in ϵ_r [69]. For BT and BST20, the ferroelectric-to-paraelectric

transition peaks were observed at 127^{0}C and 70^{0}C, respectively. Notably, the curve for BST20 exhibited a broader nature compared to BT. According to previous reports, as the concentration of Sr^{2+} increases, the ϵ_r vs. T curve tends to show more diffuse characteristics, and the ferroelectric-to-paraelectric transition temperature (T_c) linearly decreases with a relation expressed as T_c (K) = 400 - 330x [70]. For values of x≥0.4, the transition temperature falls below room temperature, but this cannot be shown in the current study due to experimental limitations (lack of lower temperature availability). Previous reports indicate that T_c for BST40 is approximately 0^{0}C [71]. The notably high dielectric permittivity observed for BST40 can be attributed to the diffuse phase transition occurring near room temperature. The broadened nature of the ϵ_r vs. T curve for BST40 indicates that the dielectric permittivity remains high over a wide temperature range. This diffuse phase transition phenomenon mainly arises from compositional inhomogeneity and the irregular distribution of the strain field [72]. The combination of this dielectric anomaly with low dielectric loss in BST40 positions it as a valuable material for various applications, particularly in the field of microwave devices [73].

The conduction mechanisms of the synthesized samples were investigated through the AC conductivity study. The AC conductivity was determined at a specific frequency using the formula provided in Equation 3.12:

$$\sigma_{ac}=2\pi f \epsilon_0 \epsilon_r \tan\delta \qquad (3.12)$$

In this equation, σ_{ac} represents the AC conductivity, f is the linear frequency, ϵ_0 is the free space permittivity (equal to 8.854e-12 F/m), and ϵ_r denotes the relative dielectric permittivity. As depicted in Figure 3.11(d), the conductivity at room temperature increases as the frequency rises. Strontium titanate (ST) exhibits the lowest conductivity, while BST20 displays the highest conductivity due to its elevated dielectric loss tangent. This conductivity study suggests that the conductivity mechanism is predominantly influenced by the tanδ value.

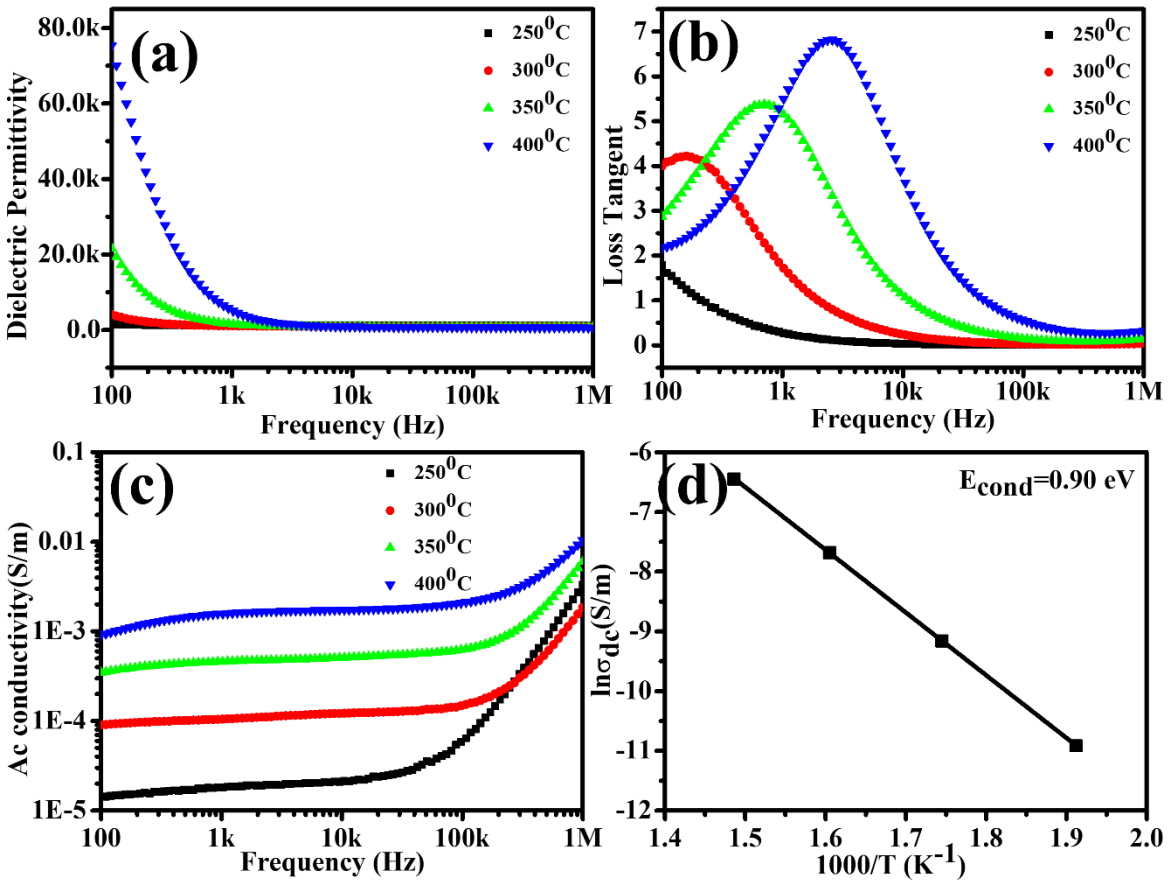

Fig. 3.13 *(a) Dielectric Permittivity (b) Loss tangent (c) AC conductivity with the variation of frequency at 250°C, 300°C, 350°C, and 400°C temperature of BST40 pellet; (d) Activation Energy for the conduction process from Plot of $ln\sigma_{dc}$ vs (1000/T) for BST40.*

Considering our earlier experiments, which indicated that the BST40 sample exhibited favorable dielectric performance, we decided to further investigate its dielectric properties at elevated temperatures beyond room temperature. Figure 3.13(a) illustrates the variation in dielectric permittivity (ϵ_r) of BST40 as a function of frequency within the temperature range of 250⁰C to 400⁰C. This graph highlights the dependency of ϵ_r on both frequency and temperature. In the low-frequency range, there is a significant decrease in dielectric permittivity as the frequency increases, followed by saturation to a constant value above 4 kHz. This decline in dielectric permittivity with increasing frequency, particularly at lower frequencies, is attributed to the Maxwell-Wagner effect [74]. This phenomenon arises from charge accumulation at interfaces due to differing relaxation times between charge carriers

in the grains and those at grain boundaries [75]. The accumulation of charges at the highly resistive grain boundaries leads to net polarization, initially increasing permittivity. In the high-frequency range, the reduction in dielectric permittivity is linked to the suppression of space charge polarization [76]. Moreover, in the low-frequency range, there is a notable increase in ϵ_r with rising temperature. This enhancement is attributed to increased ion mobility and imperfections within the material [76]. Figure 3.13(b) provides insight into the frequency-dependent tanδ (loss tangent) of BST40 at the specified temperatures. At 250^{0}C, the loss tangent decreases with increasing frequency across the entire frequency range. However, at temperatures ≥ 300˚C, a peak emerges in the tanδ vs. frequency graph. This distinctive relaxation peak is a result of polarization caused by space charge, contributing to both dielectric permittivity and loss tangent in the material [77]. The observed peak in the tanδ vs. frequency graph exhibits a shifting nature as the temperature increases. Specifically, this peak shifts from 159 Hz at 300^{0}C to 705 Hz at 350˚C and further to 2595 Hz at 400˚C. This shift towards higher frequencies is attributed to relaxation phenomena stimulated by thermal effects. Along with this shifting trend, the intensity of the loss tangent peak also increases, indicating a larger accumulation of charge carriers [78].

To gain insight into the charge carriers and the conduction process, we investigated the frequency-dependent AC conductivity (σ_{ac}) of BST40 at selected temperatures. Figure 3.13(c) illustrates the variation of σ_{ac} with frequency at four specific temperatures (250˚C, 300˚C, 350˚C, 400˚C) in a log-log scale. These plots can be divided into two distinct regions. In one region, conductivity remains unaffected by an increase in frequency, known as the DC conductivity. In the other region, conductivity is highly dependent on frequency. According to the Jump Relaxation Model proposed by Funke [78], the DC conductivity at low frequencies can be attributed to the successful hopping of charged species to the nearest unfilled state [79]. The transition frequency at which the plateau region transforms to the steep

region is referred to as the hopping frequency [79]. This hopping frequency gradually shifts to higher values with increasing temperature. The conductivity component highly dependent on frequency progressively decreases with increasing temperature, indicating an accelerated hopping rate due to thermal activation. In accordance with Jonscher's power law, the AC conductivity in the frequency-dependent dispersive region can be described by the relationship given in Equation 3.13 [80].

$$\sigma_{ac} = \sigma_{dc} + P(2\pi f)^n \qquad (3.13)$$

where σ_{dc} is the dc conductivity, P is the pre-exponential constant, f is frequency and n is the frequency exponent varies in between 0 and 1. The increase in DC conductivity with rising temperature signifies the Negative Temperature Coefficient of Resistance (NTCR) behavior exhibited by the material [76]. Figure 3.13(d) illustrates a linear fitting of the logarithm of the DC conductivity ($\ln(\sigma_{dc})$) against the inverse of temperature at 1 kHz. This linear relationship provides empirical support for the Arrhenius equation (Equation 3.14).

$$\sigma_{dc} = \sigma_0 \, exp(-\frac{E_{cond}}{kT}) \qquad (3.14)$$

Here, σ_0 represents a constant, k is the Boltzmann constant, T represents the absolute temperature and E_{cond} stands for the activation energy associated with the conduction mechanism. It is a well-established fact that the activation energy, which measures the energy barrier for involvement in a DC conduction process, is temperature-dependent [28]. The measured activation energy at a frequency of 1 kHz, calculated from the slope of the linear fit of $\ln(\sigma_{dc})$ vs. 1000/T for BST40 within the experimental temperature range, was determined to be 0.90 eV.

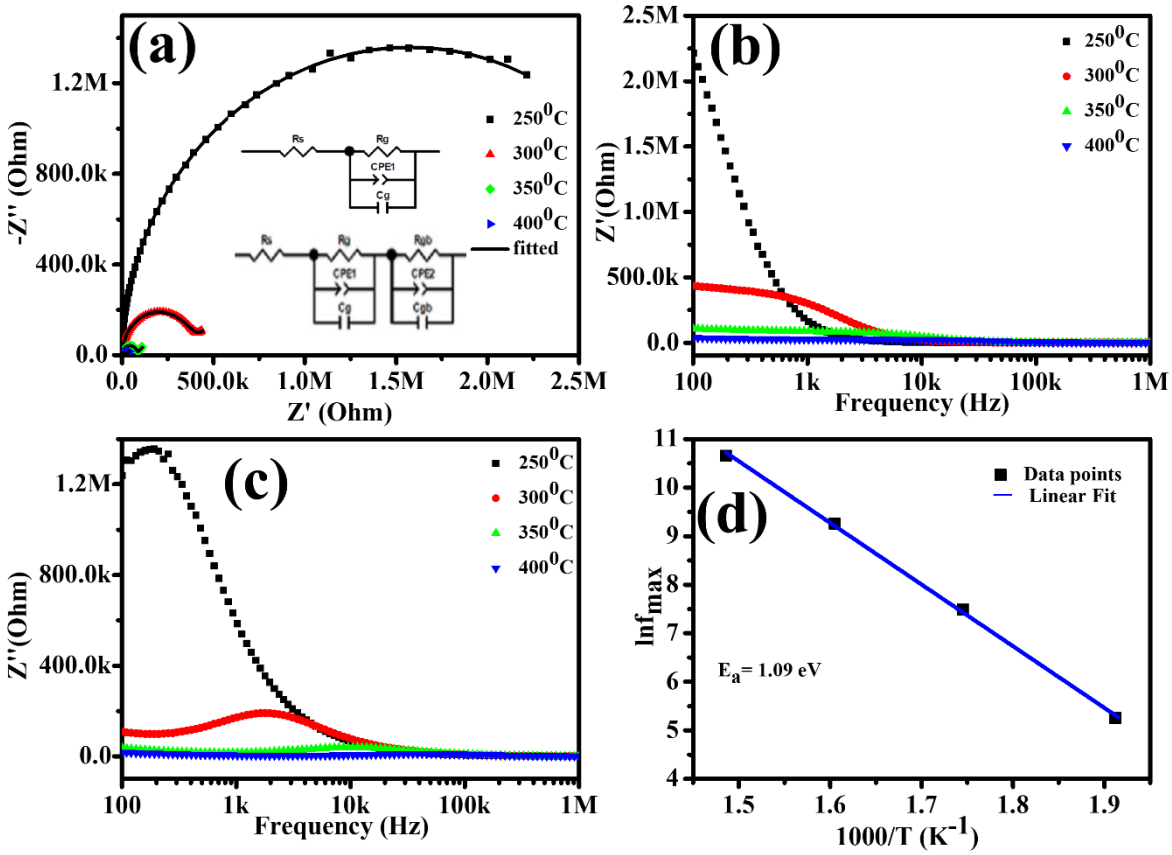

Fig. 3.14*(a) Nyquist Plot (−Z''vs Z'); variation of (b) real part of impedance (Z') (c) imaginary part of impedance (Z'') with the alteration of frequency; (d) activation energy from lnf$_{max}$ vs (1000/T) graph for the relaxation process for BST40.*

To gain a more comprehensive understanding of the electrical properties related to the grain, grain boundary, and electrode interfaces of the BST40 pellet, impedance spectroscopy was done. This technique is valuable for distinguishing the contributions of the bulk material, inter-grain regions, and electrode interfaces. Impedance, represented by Z, consists of two components: the resistive real part (Z′) and the reactive imaginary part (Z″). To analyze the electrical properties of the active region within the ceramic, we utilized the Nyquist plot, a powerful tool in which Z″ is plotted against Z′. In an ideal defect-free and homogeneous ceramic, the Nyquist plot typically exhibits a semicircle with its center positioned along the real axis [81]. The number of semicircles observed in the plot corresponds to the number of active regions within the ceramic [81]. A single semicircle can be modeled using a parallel RC circuit, which is characteristic of perfect Debye-type relaxation [81]. The total number of semicircles reflects the presence of multiple parallel RC circuits connected in series [81]. Within the Nyquist plot, the first semicircle in the high-frequency

region is associated with the grain's contribution, while the second semicircle corresponds to the inter-grain boundary [81]. The mathematical relationships describing these semi-circular arcs are provided by Equation 3.15 and Equation 3.16.

$$Z' = \frac{R_g}{(1+R_g\omega_g C_g)^2} + \frac{R_{gb}}{(1+R_{gb}\omega_{gb} C_{gb})^2} \quad (3.15)$$

$$Z'' = \frac{R_g^2}{1+(R_g\omega_g C_g)^2} + \frac{R_{gb}^2}{1+(R_{gb}\omega_{gb} C_{gb})^2} \quad (3.16)$$

In those equations, the symbols "g" and "gb" represent the grain and grain boundary, respectively, while the other symbols have their conventional meanings [76]. The intersections of the Nyquist plot with the Z′ axis (X-axis) occur at points (0, 0), (Rg, 0), and (Rg + Rgb, 0). These points allow for the determination of the grain and grain boundary resistance values [76].

To describe these contributions, we analyzed the Z′ and Z″ impedance data over a wide range of frequencies (100 Hz – 1 MHz) and temperatures (250˚C – 400˚C). The Nyquist plots at all the experimental temperatures are presented in Figure 3.14(a). At 250˚C, the Nyquist plot displays only one semicircle, indicating the presence of grain contribution exclusively. However, for temperatures ≥ 300˚C, the appearance of two semi-circular arcs are observed, which is attributed to grain boundary activation above 300˚C (as discussed earlier in the dielectric section). The radii of these semi-circular arcs decrease as the temperature increases. It is a well-established phenomenon that the mobility of charged species increases with temperature [82]. Consequently, the space charge that accumulates at the grain boundary gains enough energy to overcome the barrier potential, leading to an increase in conductivity [82]. To fit the curves, we implemented a circuit model (previously used by Purohit et al. [83]). Alongside the parallel RC circuit, we added a constant phase element (CPE) in parallel. This addition ascribes to the fact that the plotted semicircles in Figure 3.14(a) are not perfect circles, and the centers of the arcs lie below the Z′ axis. This behavior is characteristic of non-ideal Debye-type relaxation [75]. This polydispersive relaxation arises from the inhomogeneity on the surface of the sample. All the temperature-related plots were fitted using the nearly brick layer model with the assistance of ZView2 software. The Z′ vs. Z″ plot at 250˚C closely matches the (RQC) model, where Q represents a constant phase element. For

temperatures ≥ 300˚C, the Nyquist plots are fitted with the (RQC)(RQC) model. The obtained values of electrical parameters such as R_g, R_{gb}, C_g, and C_{gb} are tabulated in Table 3.6. The results from Table 3.6 reveal that the resistance due to the grain is lower than the grain boundary resistance. This finding suggests that the grain is more conductive than its barrier region [28]. Both grain and grain boundary resistance decrease with increasing temperature, following the Arrhenius-type equation (Equation 3.17).

$$R = R_0 T \exp\left(-\frac{E_a}{kT}\right) \qquad (3.17)$$

where E_a stands for the activation energy and from the slope of ln(R/T) vs (1/kT) graph it can be calculated (Fig. 3.15). Calculated values of activation energy for grain and grain boundary are measured from Fig. 3.15, measured values are 1.16 and 1.43 eV, respectively.

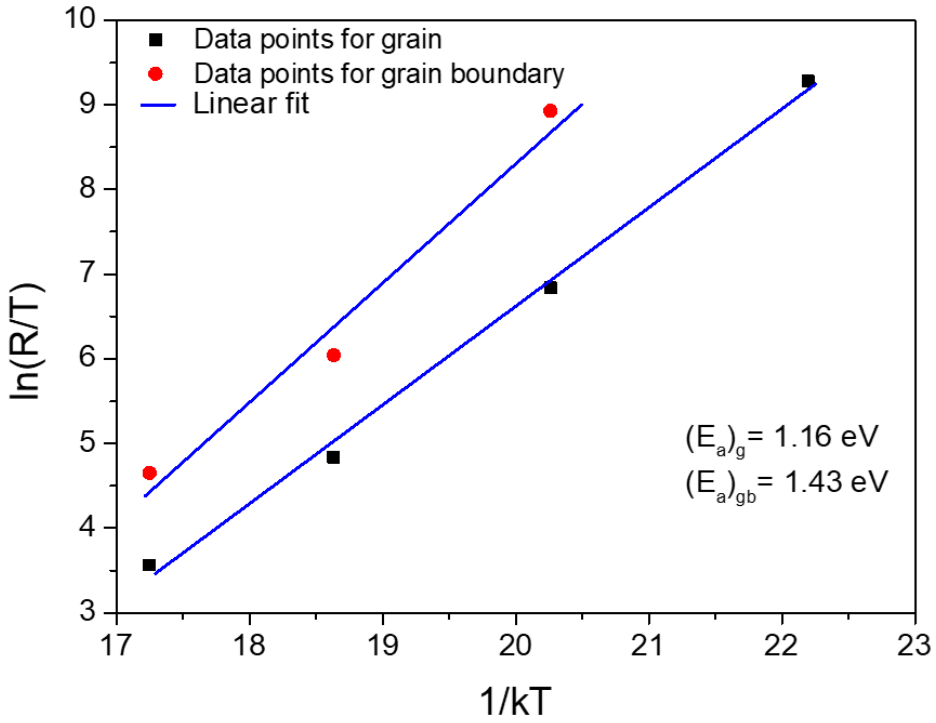

Fig. 3.15 *Activation Energy from ln(R/T) vs (1/kT) graph for grain and grain boundary for bulk BST40 ceramic.*

Table 3.6 Different electrical parameters obtained from Nyquist Plot fitting

Temp (°C)	R_g (Ohm)	CPE1	C_g (F)	R_{gb} (Ohm)	CPE2	C_{gb} (F)
250	5.60×10^{6}	5.79×10^{-8}	2.37×10^{-10}	-	-	-
300	5.35×10^{5}	1.10×10^{-7}	7.12×10^{-9}	4.32×10^{6}	1.56×10^{-6}	1.94×10^{-10}
350	7.86×10^{4}	1.00×10^{-18}	1.74×10^{-10}	2.62×10^{5}	4.23×10^{-7}	8.46×10^{-10}
400	2.37×10^{4}	3.36×10^{-10}	1.00×10^{-10}	7.05×10^{4}	3.21×10^{-7}	9.08×10^{-9}

Additionally, we conducted analyses of Z′ and Z″ variations with frequency. The resistive impedance (Z′), exhibits some dispersion within the frequency range of 100 Hz to 10 KHz across the entire temperature range from 250°C (as shown in Figure 3.14(b)). This dispersion phenomenon is believed to be a result of the presence of space charge effects [83]. At high frequencies, the convergence of Z′ into a single line indicates the liberation of space charges [83]. Conversely, at low frequencies, Z′ decreases with increasing temperature, confirming the Negative Temperature Coefficient of Resistance (NTCR) behavior displayed by BST40 within the experimental temperature range.

Figure 3.14(c) provides insight into the changes in Z″ concerning frequency variations. In this graph, associated with each specific temperature, there is a peak indicating dipole relaxation. This peak arises when the frequency of the applied electric field matches with the hopping frequency of charge carriers [79]. This frequency is known as the relaxation frequency (f_{max}). The figure demonstrates that as the temperature increases, this relaxation frequency shifts to higher values. Moreover, the peaks become more dispersed in nature at higher temperatures. Each peak corresponds to a specific relaxation time, and the broadening of peaks at elevated temperatures suggests a flattening of the relaxation times. Within the experimental frequency and temperature range, the Z″ vs. frequency graph in Figure 3.14(c) displays only one peak, corresponding to the grain component. The relaxation frequency follows the relationship $f_{max} = f_o \exp(-E_{rel}/kT)$, where E_{rel} represents the

activation energy associated with the relaxation process. Figure 3.14(d) displays the plot of ln(f_{max}) as a function of (1000/T). A linear fit of these data points allows us to determine the activation energy of the relaxation process. The measured activation energy is 1.09 eV, slightly higher than the activation energy related to the conduction mechanism (0.90 eV).

It is noteworthy to mention that within perovskite-structured lattices, the primary conducting entities are typically singly and doubly ionized oxygen vacancies. According to the Kroger-Vink notation, these oxygen vacancies lead to the generation of conducting electrons, as described by Equations 3.18 through 3.20 [84].

$$O_O^x \rightarrow V_O + \frac{1}{2}O_2 \qquad (3.18)$$

$$V_O \rightarrow V_O^{\cdot} + e' \qquad (3.19)$$

$$V_O^{\cdot} \rightarrow V_O^{\cdot\cdot} + e' \qquad (3.20)$$

During the low-temperature sintering process, singly ionized oxygen vacancies are generated, whereas at higher sintering temperatures, these singly ionized vacancies transform into doubly ionized oxygen vacancies. These conducting electrons facilitate the hopping process between Ti^{4+} and Ti^{3+} ions. During the cooling phase, re-oxidation, predominantly occurs at the grain boundary region indicated in Equation 3.21.

$$2V_O^{\cdot} + O_2 + 2e' \rightarrow 2O_O^x \qquad (3.21)$$

Consequently, oxygen vacancies have a detrimental impact on permittivity and impedance, leading to changes in grain boundary resistance. This disparity between the grain and grain boundary creates a potential barrier [84]. The movement of oxygen vacancies is not confined to the lattice but contributes to the development of conductivity in the sample [85]. The high conductivity observed at elevated temperatures primarily arises from conducting electrons generated through the ionization processes described in Equations (3.19) and (3.20). In perovskite crystal structures, the activation energy is closely linked to deviations from the stoichiometric ABO_3 composition. For example, it is 2 eV for a vacancy-free ABO_3, 1 eV for $ABO_{2.95}$, and 0.5 eV for $ABO_{2.90}$ [86]. The calculated values of oxygen vacancy, obtained from the conduction mechanism and relaxation phenomena, indicate that

oxygen vacancies are responsible for both processes. Previous reports suggest that singly ionized oxygen vacancies have activation energies in the range of 0.3-0.5 eV, while doubly ionized oxygen vacancies exhibit activation energies close to 1 eV [85]. The calculated activation energies for BST40 from the dielectric and impedance characteristics are nearly 1 eV, suggesting that both the conduction and relaxation processes are governed by doubly ionized oxygen vacancies [85]. There is a slight difference in the activation energy values obtained from conductivity and relaxation mechanisms. The activation energy from the relaxation mechanism is associated with the short-range migration of charge carriers from one site to another, maintaining a barrier potential between them. In contrast, the activation energy for the conduction process is a combined phenomenon involving charge carrier generation and long-range hopping, resulting in a smoother path for dc conductivity. This accounts for the lower activation energy in the conduction process compared to the relaxation mechanism [87,88].

In the light of the above discussion, it can be concluded that doping 40 wt% of Sr^{2+} at the Ba site of $BaTiO_3$ leads to the preparation of $Ba_{0.6}S_{0.4}TiO_3$ (BST40), which exhibited a considerably high value of dielectric permittivity (~4000 at 1 kHz), low dielectric loss, low leakage current at ambient temperature and pressure. These improved intrinsic characteristic of the BST40 enables it as a good filler candidate to prepare the flexible PVDF based functional layer in order to develop the flexible piezoelectric energy harvesting device. In this respect it is worthwhile to be mentioned here that development of sufficient electroactive phase inside the PVDF polymer acts as the prerequisite for developing energy efficient PVDF based energy harvesters. Thus, before incorporation of such fillers inside the polymer matrix the type of surface charges should be examined as they play the pivotal role in the alignment of the polymer chain in the electroactive phase configuration [89]. Keeping this in mind the zeta potential measurement of the filler particles was carried out as illustrated in Fig. 3.16. It can be seen from the graph that the surface of

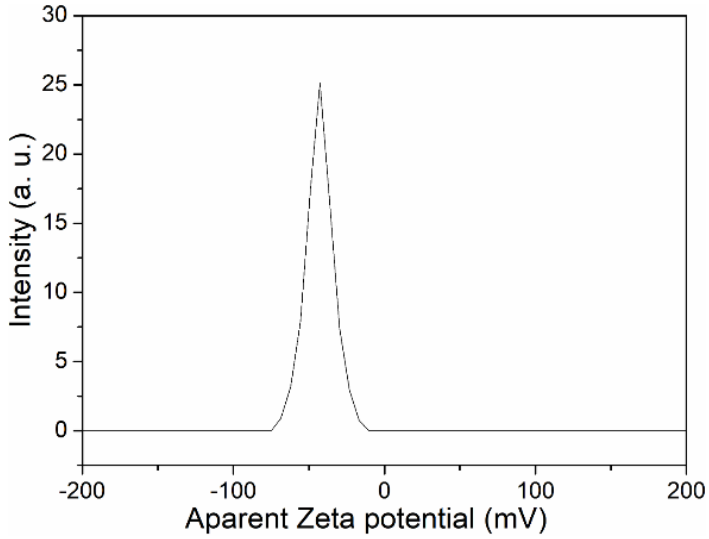

Fig. 3.16 Zeta Potential of the synthesized BST40 particle.

the filler particles are negatively charged. Interestingly, this negatively charged surface of the filler particles will help the polymer chains of PVDF to be aligned in the all-trans conformation which is the desirable electroactive β phase.

3.3.2. Characterizations of the BST/PVDF composites:

3.3.2.1. Phase analysis of the bare PVDF and BST/PVDF composite:

The prerequisite for creating an efficient energy harvesting device with strong power generation capabilities is the development of the essential electroactive phase within the polymer. Thus, an in-depth phase analysis of the synthesized composites is required to optimize the best suitable functional layer to fabricate the final energy harvesting device. For this purpose, the Fourier transform infrared microscopy (FTIR) and X-ray diffraction (XRD) analysis of the bare PVDF and BST/PVDF composite films were carried out. FTIR analysis is considered to be beneficial in this aspect as it gives a quantitative investigation of the crystalline phases in PVDF in addition to the qualitative analysis. Though PVDF can exists in several phases, among all the of the possible crystalline phases, TGTG' structure (α) exhibits minimum free energy [90]. Consequently, the bare PVDF film exhibits the maximum α-crystalline phase fraction at ambient temperature and pressure. Fig. 3.17(a) reveals

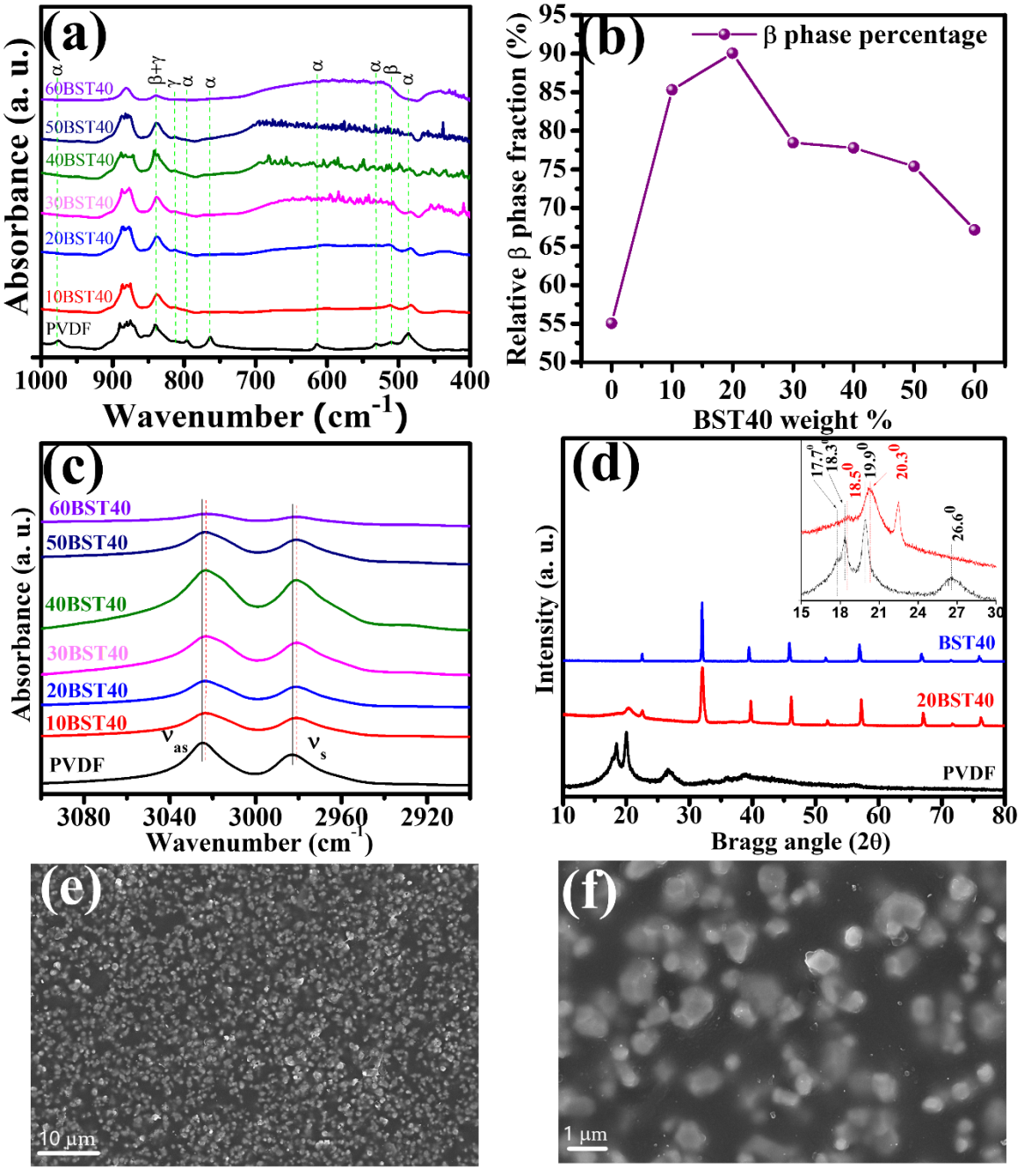

Fig. 3.17 *(a) FTIR spectra of all the fabricated composite films in the wavenumber range of 1000 - 400 cm^{-1}. (b) Relative β phase fraction of composite films with respect to BST40 weight%. (c) Extended view of the absorbance spectra of the composite films in between the wavenumber range 3100 cm^{-1} - 2900 cm^{-1}. (d) X-Ray Diffraction patterns of PVDF and 20BST40 sample. Inset shows the extended XRD patterns of both the samples in the Bragg Angle (2θ) range of 15^{o} – 30^{o}. (e) FESEM image (f) enlarged FESEM image of the 20BST40 composite film.*

the FTIR spectra of the neat PVDF and composite films within the wavenumber range of 1000 cm^{-1} - 400 cm^{-1}. The well recognizable peaks positioned at 976, 795, 763, 613, 532 and 488 cm^{-1} for pure PVDF film are typically responsible to the α

phase conformation whereas the peaks positioned at 812, 510 and 840 cm^{-1} represents the presence of the γ, β and β+γ phase, respectively [91]. Interestingly, the FTIR spectra reveals that the relative intensity of the peaks related to the α phase of PVDF decreases where the intensity of the peaks related to the β phase increases with the increasing filler concentration, upto a certain critical limit. Thus, the FTIR analysis infers a successful transformation of the non-polar α phase to the polar β phase with the impregnation of the filler particles. Now, in order to draw a comparative analysis of the electroactive β phase content inside PVDF characteristic α and β bands situated at 763 and 840 cm^{-1} were examined. The electroactive β phase content of all the composite films can be calculated keeping in mind that the infrared absorbance follows the Lambert-Beer Law [92]. According to the law, percentage of β phase can be derived from the following relation given by Equation (3.22).

$$F(\beta) = \frac{A_\beta}{\left(\frac{k_\beta}{k_\alpha}A_\alpha + A_\beta\right)} \times 100\% \qquad (3.22)$$

where, A_β and A_α are the intensity in arbitrary unit of the peak at 840 and 763 cm^{-1} respectively. k_α and k_β are absorption coefficients valued as 6.1 x 10^4 and 7.7 x 10^4 cm^2/mol, respectively. It can be seen from Fig. 3.17(b) that, the maximum electroactive β phase fraction (~90 %) can be achieved with the loading of 20 wt% of the filler. Whereas the β phase fraction for bare PVDF was found out to be ~ 55%. Thus, with the incorporation of fillers upto a certain concentration can significantly enhance the electroactive β phase fraction inside the polymer matrix. However, the decrease in β phase fraction after 20 wt% BST40 loading in PVDF can be readily attributed to the agglomeration of the BST40 particles inside polymer matrix [93,94]. Such a significant enhancement of the β phase fraction with the filler loading can be assigned to the efficient interaction between the filler particles and PVDF matrix. In order to confirm, the possible electrostatic interaction between the filler and polymer matrix, the FTIR absorption spectra within the wavenumber region of 3100-2900 cm^{-1} (Fig. 3.17(c)), where the characteristic bands for symmetric (ν_s) and asymmetric stretching (ν_{as}) vibration of -CH_2 dipoles are situated, was explored [93]. As depicted by the figure, there is a ssuccessive shifting of the vibrational bands towards lower wavenumber region with the increment of filler concentration validates the interaction between -CH_2 dipole of PVDF and BST40 particle surface. Negative surface charge of the fillers as depicted in Fig. 3.16 leads to this electrostatic

interaction with the positive $-CH_2$ dipole of the polymer chain, which results in the alignment of the polymer in all trans (TTTT) conformation.

As concluded from the FTIR analysis that the maximum β phase fraction was obtained with 20 wt% loading of BST in PVDF, therefore to have a further analysis of the phase fraction as well as crystallinity of the 20BST40, XRD analysis was carried out. Fig. 3.17(d) shows the XRD diffraction patterns of neat PVDF and 20BST40 composite films. The presence of the characteristic peaks related to BST40 in the XRD pattern of the 20BST40 composite confirms the successful inclusion of fillers in the polymer matrix. The inset of Fig. 3.17(a) shows the extended view of the XRD patterns with 2θ ranging from 15° to 30° which confirms the presence of distinctive peaks of PVDF around 2θ = 20°. The peaks positioned at 17.7°, 18.3°, 19.9° and 26.6° for neat PVDF confirms the abundance of non-polar α phase in the bare polymer [91]. However, incorporation of the fillers results in the appearance of a prominent peak positioned at 20.3° with a complete disappearance of the peak centered at 26.6° and 17.7°, which readily confirms the presence of polar β phase in the composite [91]. Thus, the XRD results also confirm that the incorporation of BST40 leads to the transformation of the non-polar α phase to electroactive orthorhombic β phase. Also, uniform mixing and distribution of BST40 filler within PVDF matrix was also confirmed from the FESEM characterization of 20BST40 film presented in Fig. 3.17(e and f).

3.3.2.2. Dielectric properties

The mechanical energy harvesting performance of composite films based on PVDF is significantly influenced by the dielectric permittivity. Therefore, it is essential to study the dielectric properties of the fabricated composite films, which will act as the heart of the piezoelectric energy harvesting device. The room temperature frequency variation of the dielectric properties over a wide frequency range of 100 Hz – 1 MHz of the neat PVDF and the composite films are shown in Fig. 3.18(a). The figure shows a significant increment in the value of the dielectric permittivity with the increment

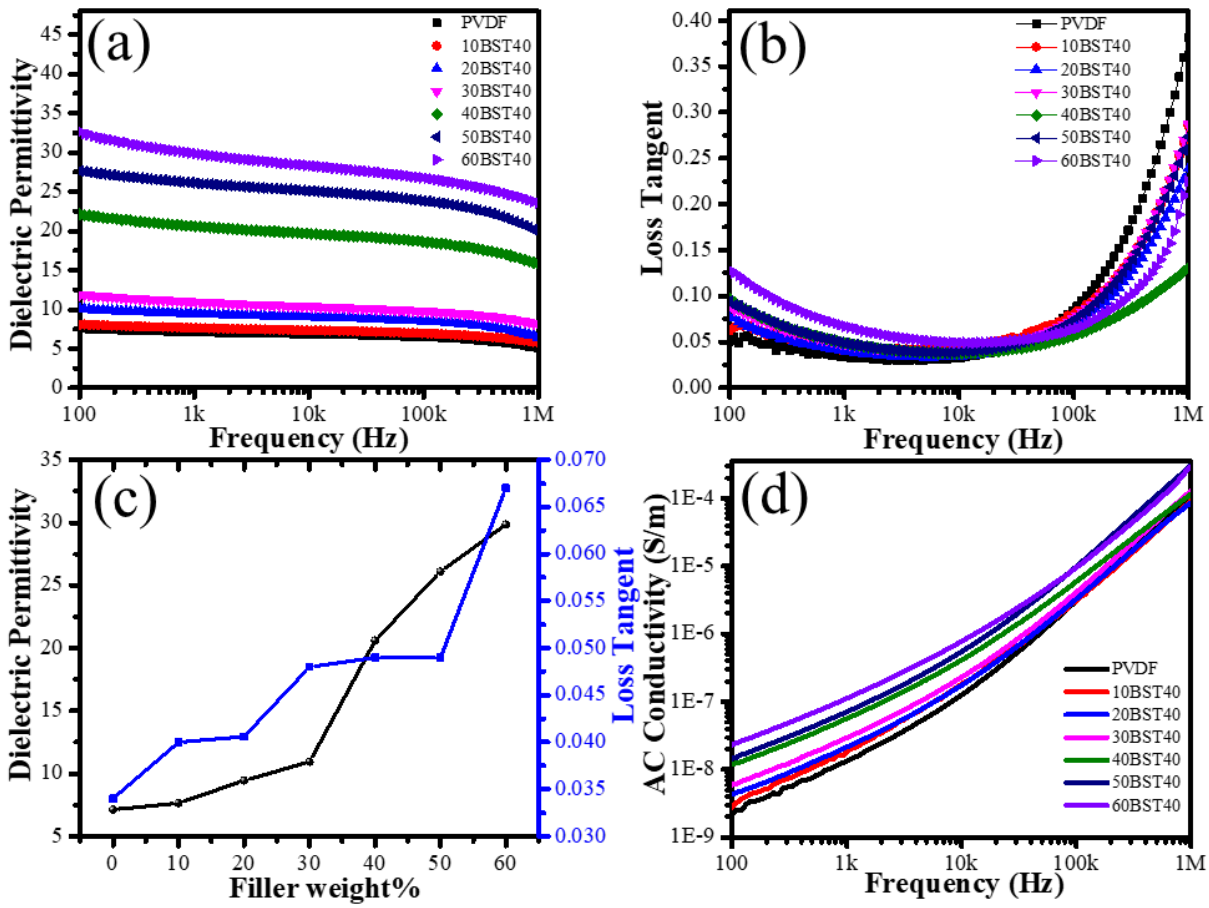

Fig. 3.18 *Variation of (a) dielectric permittivity (b) dielectric loss tangent with a function of frequency (100 Hz – 1 MHz) at RT. (c) Dielectric permittivity and dielectric loss tangent values with the variation in BST40 filler weight % at 1 KHz frequency. (d) AC conductivity of all the composite films with the change in frequency.*

in the filler loading for the entire frequency range. According to Lewis's model [95], as a particle infiltrates a polymer matrix, the surface of the particle becomes charged because of the chemical potential disparity. Subsequently, the polymer responds to neutralize the charge accumulation on the particle surface by generating opposing charges in the vicinity of the filler's surface, and this region is referred to as the Stern layer. Whereas, the rest portion of the polymer matrix is known as the diffusion layer. Since the Stern layer acquires an opposite charge in comparison to the particle surface, the charges within the diffusion layer reorganize themselves due to the influence of Coulomb interaction [96,97]. Due to this rearrangement of charges, the dielectric permittivity of the polymer composites increases with the increase in filler loading in polymer matrix. Whereas, as per the Tanaka's model [98], the filler incorporation in PVDF is described as the formation of three layers over the particle

named as bonded layer, bound layer and loose layer. The presence of a bound layer adversely affects the alignment of dipoles within ceramic particles, while the loose layer reduces the available space within the PVDF matrix. These combined effects result in a lower dielectric permittivity for the polymer composite compared to the ceramic material [99]. Conversely, Lichtenecker's model suggests that the dielectric permittivity of a PVDF composite system is determined by the intrinsic permittivity of each component and their overall interaction [100]. These theories help us to understand the obtained values of the dielectric permittivity of the composites, which are still lower than the dielectric permittivity of the ceramic fillers. Another important feature of the frequency variation of the dielectric permittivity from Fig. 3.18(a), reveals a decrease in dielectric permittivity with the increasing frequency. This can be explained as, at lower frequency, due to the presence of all four varieties of polarization (space charge, dipolar, electronic and ionic polarization) the dielectric permittivity is higher whereas at higher frequency (~10^6 Hz) the polarization contribution from space charge diminishes, which results in a decrement in the overall permittivity value [101]. Again, the sudden decrement in ε_r at nearly 1 MHz frequency can be attributed to the dipolar relaxation phenomenon occurring at this frequency.

Along with dielectric permittivity, dielectric loss tangent (tanδ) is also a significant parameter, which plays a key role to finalise the output performance of the energy harvesting device. Dielectric loss tangent mainly originates due to the absorption of absorbed energy by the respective material on the application of a certain electric field. Thus, in order to fabricate an efficient energy harvesting device with adequate power density it is desirable to choose a functional layer with a loss tangent loss. Fig. 3.18(b) shows that though the value of tanδ is low at lower frequency level, however an increment in the value can be observed with the incorporation of BST40 filler in the PVDF matrix. Such an increment can be readily attributed to the space charge polarization gained from the filler materials. A closer observation to the Fig. 3.18(b) reveals a sudden increment in tanδ for all the composite films after 100 kHz. Now, this is due to the fact that, at high frequency, dipoles are incapable of orienting themselves along the applied field direction due to short time span. As a result, some polarisation loss arises which causes this spike in the loss tangent graph and also the

sudden decrement in dielectric permittivity value. This spike represents the glass transition relaxation of PVDF [102].

As observed in Fig. 3.18(c), the room temperature dielectric permittivity and dielectric loss tangent values, at a frequency of 1 kHz, exhibit a clear dependence on composition. These values show a notable increase, with the dielectric permittivity rising from 7.13 to 29.85 and the loss tangent increasing from 0.034 to 0.067 as we transition from bare PVDF to the 60BST40 sample. Therefore, it can be considered that the BST40 is an efficient filler material to manipulate the dielectric nature of the PVDF. Fig. 3.18(d) shows the ac conductivity of the composite films as a function of frequency. It can be observed from the figure that, with the increment in frequency, ac conductivity also increases. With the increase in the filler concentration BST40 inside PVDF matrix, there is an increase in conduction network which simultaneously augments the ac conductivity values [103]. The enhancement of PVDF's dielectric properties through the addition of BST40 to its matrix implies that the energy storage capability is likely to see improvement as well.

3.3.2.3 Ferroelectric and energy storage performance

For real life capacitor application of any material, energy storage density is a vital parameter. As the dielectric permittivity value of the PVDF based composite films continuously increased in the present work with the increase in ceramic filler incorporation, it is expected that the energy storage density will also be increased. [103,104] To explore the energy storage capacity and ferroelectricity of BST40/PVDF composite films, the electric displacement (D) vs electric field (E) loops were assessed. Fig. 3.19(a) reveals the room temperature D vs E loops of the fabricated composite films upon the application of 1 Hz triangular waveform. Due to the limitation of experimental setup (unavailability of higher applied field) the saturation in D vs E curves could not be achieved in the present work. On the application of same electric field, the composite films showed the increasing nature of maximum electric displacement (D_m) and remnant electric displacement (D_r) with the enhancement in filler loading (Fig. 3.19(b)). These enhancements in D_r and D_m attribute to the improvement of ferroelectric properties. From the study of ac conductivity, it was proven that there is enhancement of conduction pathway which also has a simultaneous contribution in increasing the leakage current. This leakage

current along with displacement current promoted improved ferroelectricity in BST40 incorporated PVDF composite films [103]. Another interesting feature of the obtained ferroelectric hysteresis loop is that, for all the composite films there is a "gap" in the hysteresis curve at zero electric field. This ascribes to the statement that the dipoles were not able to return to its original position after the elimination of the applied field. This disparity in displacement between initial and finishing electric field got enlarged with the increased BST40 inclusion in PVDF. This type of nature is a clear manifestation of high conduction loss [105,106].

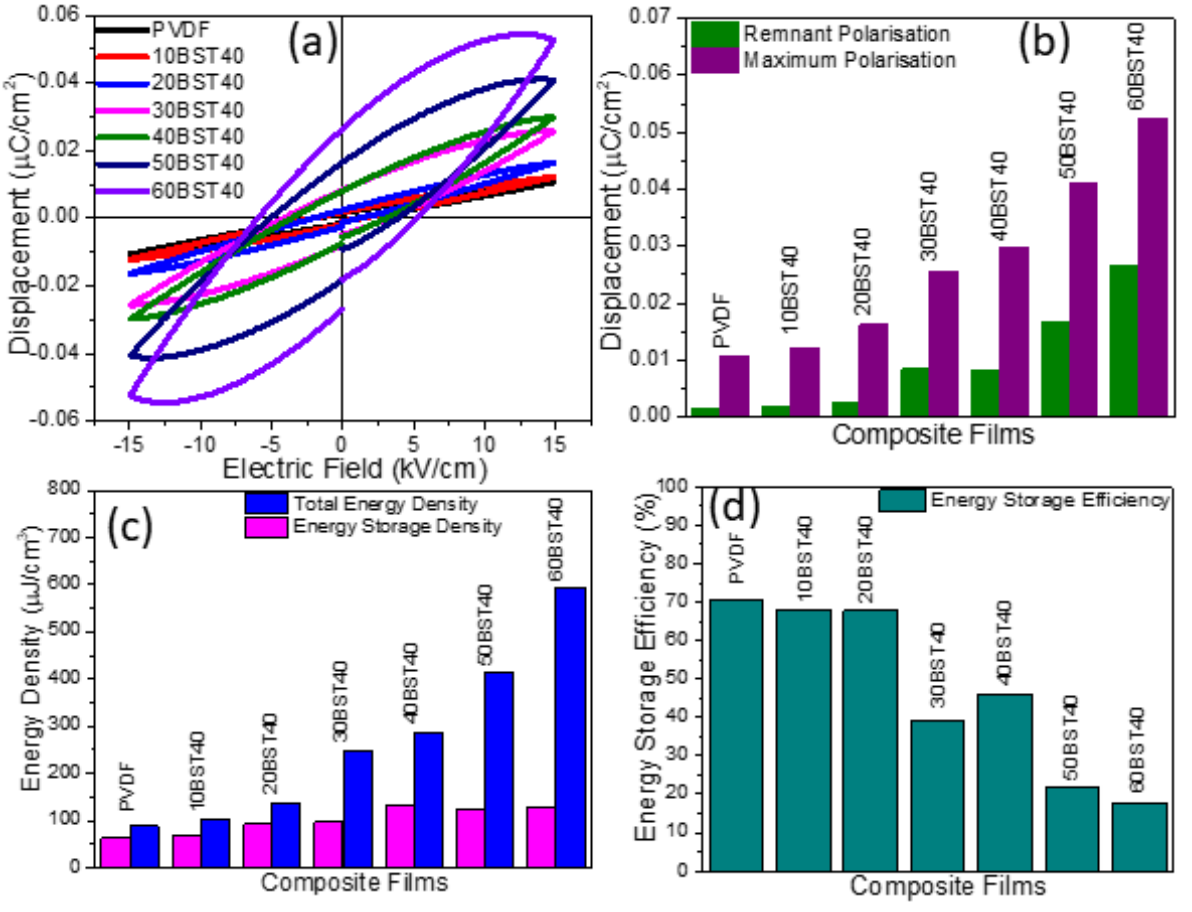

Fig. 3.19 *(a) Ferroelectric Displacement vs. Electric field (D vs E) curve, bar chart of (b) Remnant and maximum polarization (c) Energy density and energy storage density (d) Energy storage efficiency of all the composite films.*

As PVDF is not a linear dielectric material, the energy storage density of the PVDF based composite films can be evaluated from their ferroelectric hysteresis loops (through desired loop area calculation) by employing the following relation given by Equation 3.23.

$$U_s = \int_{D_r}^{D_m} E\, dD \qquad (3.23).$$

Calculated values of the total energy density and stored energy density are shown in Fig. 3.19(c). Energy storage density increased from 62.08 μJ/cm^3 for bare PVDF to a value of 131.6 μJ/cm^3 for 40BST40 film at 15 kV/cm. From this result, it is clear that the dielectric energy storage density increased with the BST40 filler incorporation in PVDF matrix. For the application of the PVDF based composite films as energy storage materials, energy storage efficiency plays a dominant role. Energy storage efficiency (η) can be deduced utilizing the Equation 3.24 [107].

$$\eta = \frac{U_S}{U_S + U_L} \times 100\% \qquad (3.24)$$

where, U_S and U_L are energy storage density and energy loss density, respectively. Fig. 3.19(d) represents the bar graph of η for all the composite films. Though the energy storage density increased with the increase in the amount of filler loading, the energy storage efficiency got reduced. Measured η for neat PVDF film was 70.4% and for 10BST40 and 20BST40 the values decreased to 68% and 67.8% respectively. Declining nature of η usually happens for every filler material.

3.3.2.4 Leakage characteristics

Energy storage properties of a material are highly dependent on the current leaking through the sample in between two electrodes. Fig. 3.20 shows the voltage dependent leakage current density of the fabricated composite films. The gradual increase in leakage current density with the successive increase in filler loading was observed from this figure. Incorporation of BST40 filler inside PVDF caused higher conductive pathway which simultaneously increased the leakage current [104]. From all the curves, it is clear that the leakage current is also dependent on the applied voltage. This leakage current behavior also authenticates the increment in conductivity which is already described during explanation of ac conductivity and ferroelectric properties.

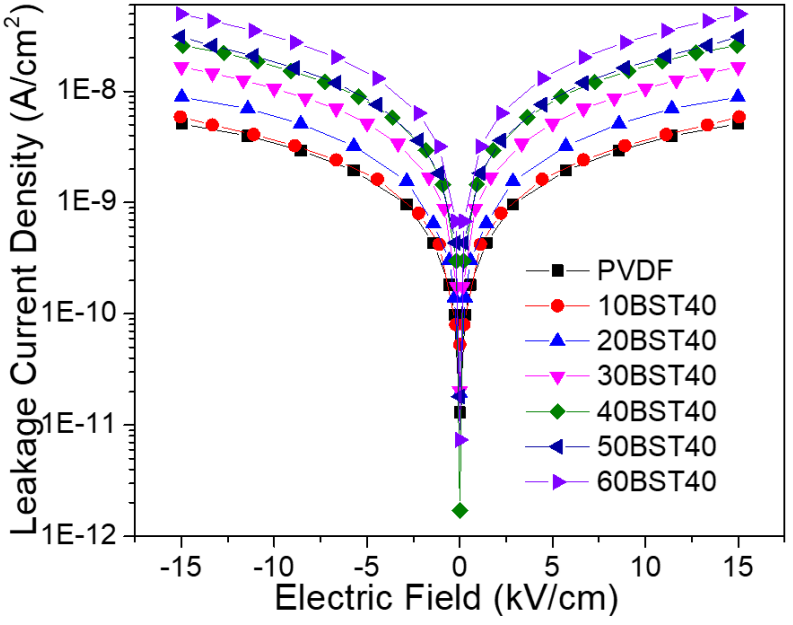

Fig. 3.20 *Leakage current behavior of all the composite films on the application of electric field.*

3.3.2.5. Piezoelectric behaviour

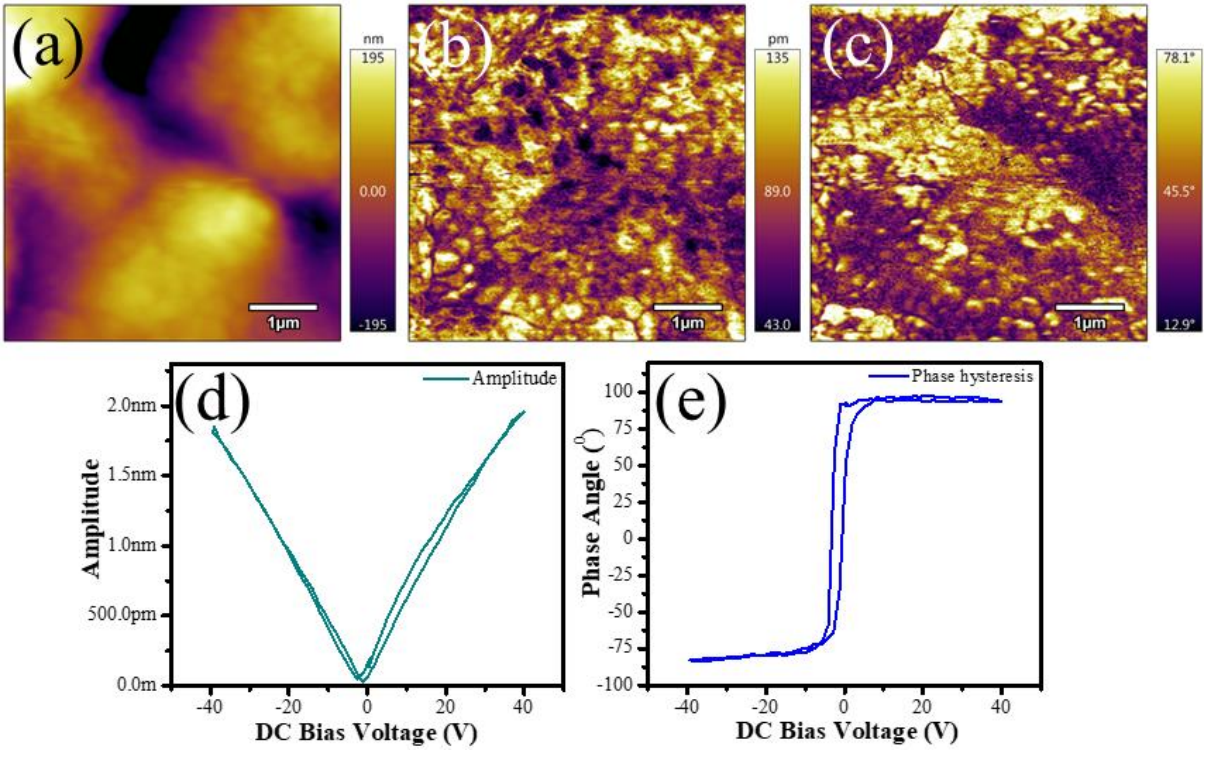

Fig. 3.21 *(a-c) topography image, amplitude image and corresponding phase image of the 20BST40 sample on a surface area of 5 x 5 µm². (d) Obtained amplitude vs applied dc bias voltage of ± 40 V. (e) Corresponding produced phase hysteresis loop on the application of ± 40 V dc bias voltage.*

To investigate the piezoelectric characteristics of the manufactured composite films for potential mechanical energy harvesting applications, it is crucial to conduct a study. The most commonly employed technique to elucidate the ferroelectric and piezoelectric properties of a sample is Piezoelectric Force Microscopy (PFM). In PFM measurements, a domain image is acquired by utilizing the principle of the inverse piezoelectric effect, where a low AC voltage is applied to the probe to detect nanoscale piezoelectric strain on the sample's surface [108]. From the FTIR analysis it was observed that the composite with 20 wt % loading of BST40 exhibits the maximum electroactive phase fraction, thus to have a more in-depth analysis, PFM characterization of the sample was carried out. Electroactive response produced by the applied electric field by the tip was thoroughly investigated in a surface area of 5 x 5 μm^2 of the 20BST40 sample and the topography image is shown in Fig. 3.21(a). Whereas, the amplitude response and the polarization phase images are displayed in Fig. 3.21(b) and Fig. 3.21(c), respectively. The contrast difference between dark and bright areas on the images clearly demonstrates the presence of oppositely polarized domains [109,110]. Such bright and dark spots formation is related to the positive and negative domains, respectively [111]. The piezoelectric amplitude loop, as depicted in Figure 3.21(d), exhibits a butterfly-like shape when subjected to a direct current bias voltage ranging from -40 V to +40 V. This observation provides evidence for the piezoelectric properties of the 20BST40 sample to some extent [109]. In order to authenticate the ferroelectric attributes, phase response was also studied as shown in Fig. 3.21(e). The polarisation phase behaviour exhibits a 180^0 phase difference, which clearly demonstrates the presence of 180^0 domains [112]. A careful observation of the phase loop, shows that the hysteresis loop has slightly moved to the negative X axis. This movement may be a plausible contribution from the pinning effect originated from the internal bias, oxygen vacancies, etc [112]. The hysteresis loop is relatively narrow indicates that the sample can be easily switched by applying a low electric field [113]. Therefore, the findings from the Piezoelectric Force Microscopy (PFM) study suggest that the composite films that were fabricated are well-suited for applications in piezoelectric mechanical energy harvesting.

3.3.2.6. Piezoelectric energy harvesting performance

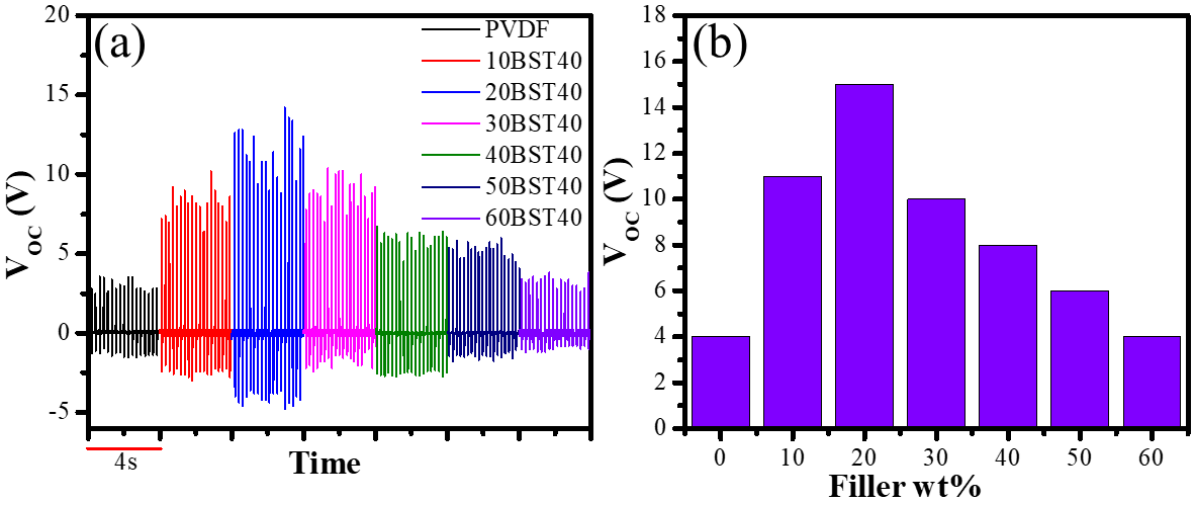

Fig. 3.22 *(a) Open circuit output voltages (b) Bar chart of average open circuit voltages of all the fabricated film samples on the application of ~10 N at a rate of 5 Hz.*

In order to investigate the effectiveness of the functional layers (containing varying filler concentration) to fabricate energy efficient piezoelectric energy harvesting devices (PEH), the energy generation capability of all the fabricated PEH devices (using composite films with varying filler concentration) were studied. It is well known that human motion-based bio-mechanical energy is considered to be the most abundant source of mechanical energy. Thus, in order to utilise the efficacy of the fabricated PEH devices to scavenge human motion-based bio-mechanical energies the electrical output generated from the PEH devices upon the application of periodic tapping force of ~ 10 N at a rate of nearly 5 Hz was analysed. The effective area of all the composite films was 6 cm^2 (2 cm x 3 cm). The open circuit voltage (V_{OC}) patterns obtained from different PEH devices are shown in Fig. 3.22(a). In this context it is worthwhile to be mentioned here that no external poling process has been applied in the present case thus stress induced polarization of the functional layers of the device act as the sole contributor towards the generation of the output signals [114]. Fig. 3.22(b) shows the comparative study of the average output voltage V_{OC} obtained from the fabricated energy harvesters. Pristine PVDF shows an average output voltage of ~ 4 V whereas the V_{OC} increased up to ~ 15 V for 20BST40. However, there is a decrement in the output voltages beyond 20 Wt% percent loading of the fillers, which is in a well agreement with the results obtained from the FTIR analysis of the composite films. This can be attributed to the presence of a less

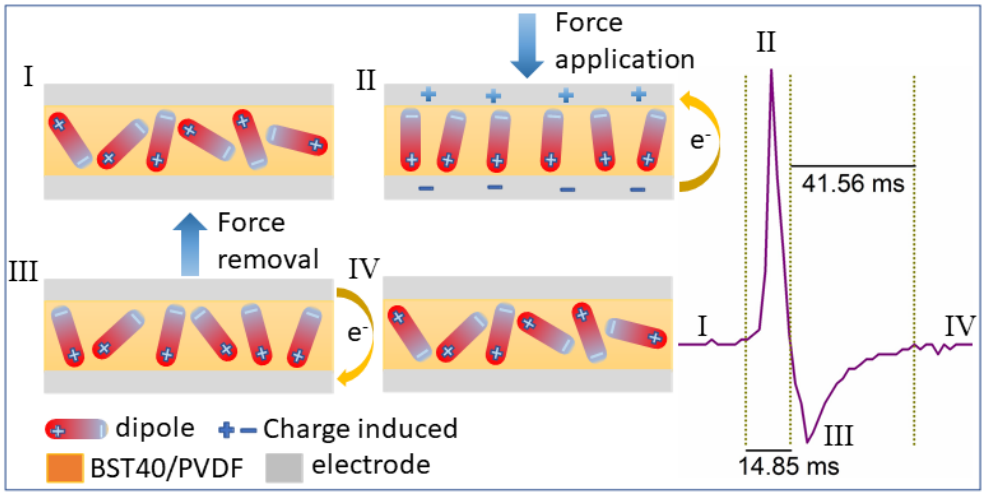

Fig. 3.23 *Possible piezoelectric voltage generation mechanism*

dominant dipole alignment in composites with a low β phase, as the energetically stable α phase is prevalent. In contrast, a higher β phase ensures more pronounced dipole arrangements when subjected to external stress [114]. The filler particles inside PVDF act as the stress concentration centres which enhance the inner deformation and augment the piezoelectric outputs [115,116]. The degradation in the value of V_{OC} for higher concentration of the fillers may be assigned to the higher agglomeration of the BST40 particles inside PVDF. Therefore, in light of the above discussion, PEH device fabricated using 20BST40 composite was considered as the optimized PEH, and was used for further analysis. Feasible perception about piezoelectric voltage generation can be elucidated by sketched mechanism as illustrated in Fig. 3.23. Initially, due to the abrupt arrangement of the dipoles the generated piezo potential is zero. However, on the application of perpendicular compressive stress, the dipoles arrange themselves along the force direction and as a result of this high directionality of the dipoles due to stress induced polarisation, there is certain induced charge generation across the electrodes [109,117]. Therefore, the generation of positive peak is a consequence of created positive piezo-potential. Afterwards, on the removal of applied stress, potential diminishes, as a result of the proceeding of gathered electrons along the opposite direction, which in turn produces the negative pulse [109]. Fig. 3.23 also displays the piezoelectricity generated single waveform pattern.

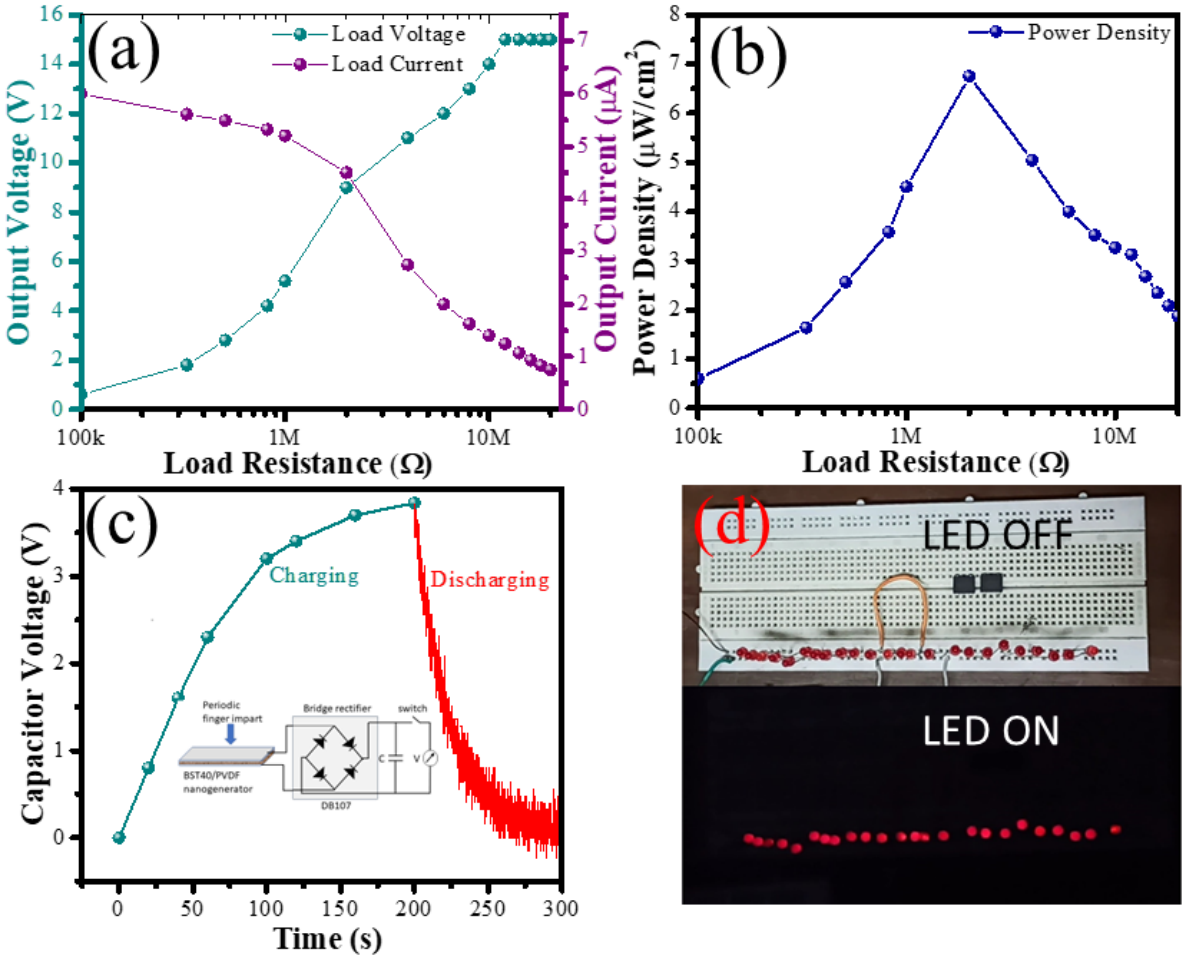

Fig. 3.24 *(a) Average piezoelectric output voltage and output current values with the variation in load resistances (100 kΩ – 20 MΩ) for 20BST40 sample. (b) Calculated corresponding output power density for the sample. (c) Charging and discharging of a capacitor of capacitance 2.2 μF under repeated finger tapping for 200 s. Inset displays the bridge rectifier circuit used for the charging and discharging. (d) LED off condition and during the discharging through the capacitor, it was capable to light up some red LEDs connected parallel.*

Real life application of any energy harvesting device depends upon the output power generation capabilities of the fabricated PEH. Therefore, the voltage generation capability of the optimised PEH using external load resistance (10^5 – 2 x 10^7 Ω) was studied. Fig. 3.24(a) shows the load voltage (V_L) and the load current (I_L) at some specific load resistances. The load current was calculated by dividing the load voltage

by corresponding resistance values. As seen from the figures that the voltage (V_L) across the load resistance increases with the increment in load resistance whereas I_L shows a opposite behaviour. The output power density (P_L) of the device can be calculated using the formula, $P_L = (I_L \times V_L) / A$, where, A is the active area of the energy harvester device. Fig. 3.24(b) presents the output power density at different load resistances which exhibits the clear demonstration of the enhancement of power density with load resistance up to 2 MΩ and after that P_L decreased. Obtained optimum power density was 6.75 μW/cm² at 2 MΩ (the internal impedance of the fabricated energy harvester is also ~ 2 MΩ). This is a transparent corroboration of the fact that the maximum power can be procured when there is a match between internal and external impedance values. Further, the output ac voltage obtained from the device under finger tapping was converted to dc signal using bridge rectifier IC (DB107) and the obtained voltage was used to charge a commercial capacitor with a capacitance value of 2.2 μF (Fig. 3.24(c)). Circuit diagram utilised to convert ac voltage to dc voltage is displayed in Fig. 3.24(c). In the case of capacitor charging, we deliberately avoided connecting the oscilloscope to prevent any potential discharge through it. After tapping the capacitor repeatedly for 200 seconds, the capacitor reached a charge level of approximately 3.8 V. The discharge data was obtained by connecting the oscilloscope after this initial 200-second charging period. Figure 3.24(c) demonstrates the visualization of the charging and discharging curves. During the discharging of the capacitor, the energy stored in the capacitor was utilised to instantly light up some commercial red light emitting diodes (LED) as shown in Fig. 3.24(d).

A portion of this chapter appeared as

S. Maity, A. Sasmal, S. Sen, "Barium Titanate based paraelectric material incorporated Poly(vinylidene fluoride) for Biomechanical Energy Harvesting and Self-Powered Mechanosensing", **Materials Science in Semiconductor Processing**, 2023, 153, 107128.

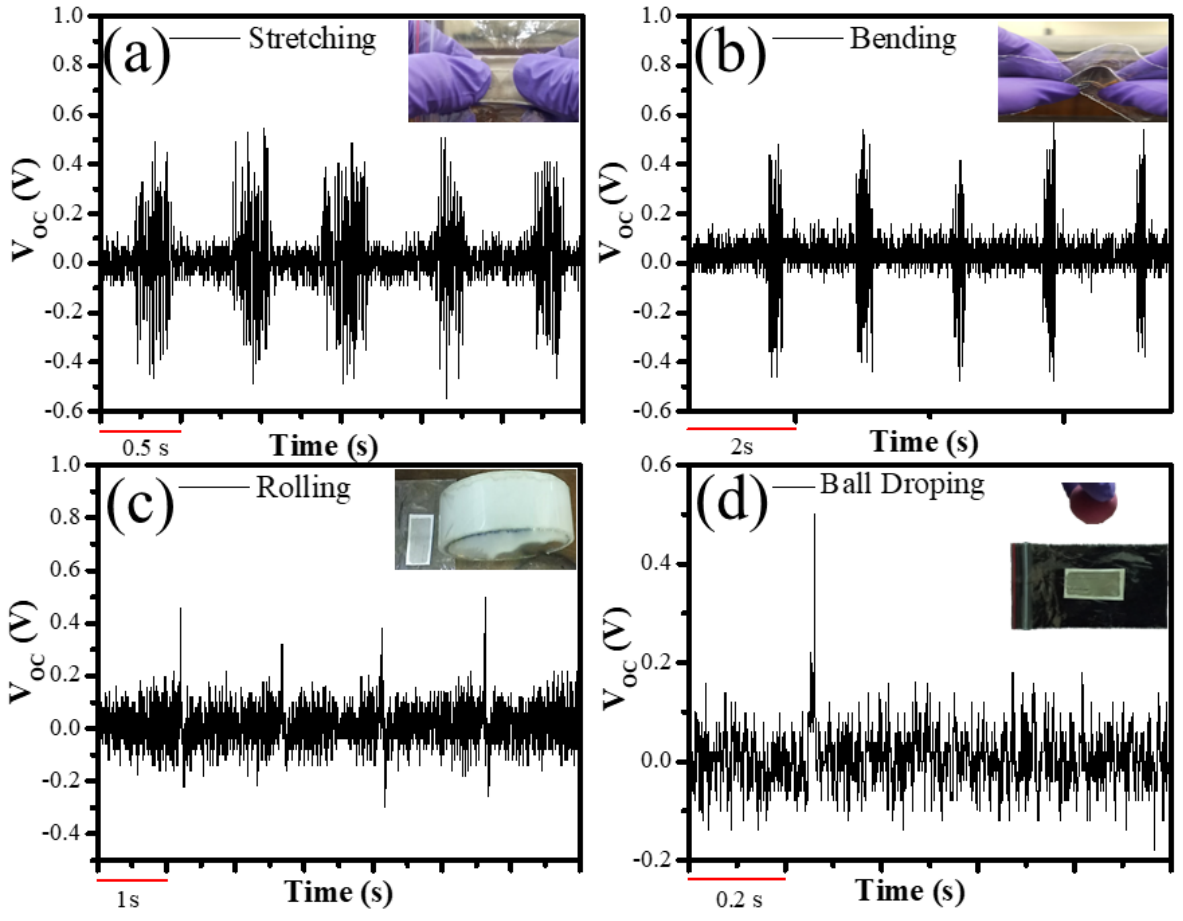

Fig. 3.25 *generated open circuit voltage patterns under the mechanical stimuli like (a) stretching of the film, (b) bending of the film, (c) rolling a cylindrical sample above the composite film and (d) dropping of a free-falling rubber ball.*

Further, the capability of the optimised PEH to harvest energy from the different motions such as stretching, bending, rolling and dropping of ball, were also studied as shown in Fig. 3.25(a-d). Owing to the flexibility as well as stretchability of the fabricated energy harvester, the energy harvester was capable enough to generate voltage output from such fine motions. Thus, the output generated from the device under bio-mechanical motion such as finger tapping and other fine motions confirms its applicability as a potential piezoelectric energy harvester.

3.3.2.7. Performance of the optimised piezoelectric energy harvester as a static pressure sensor

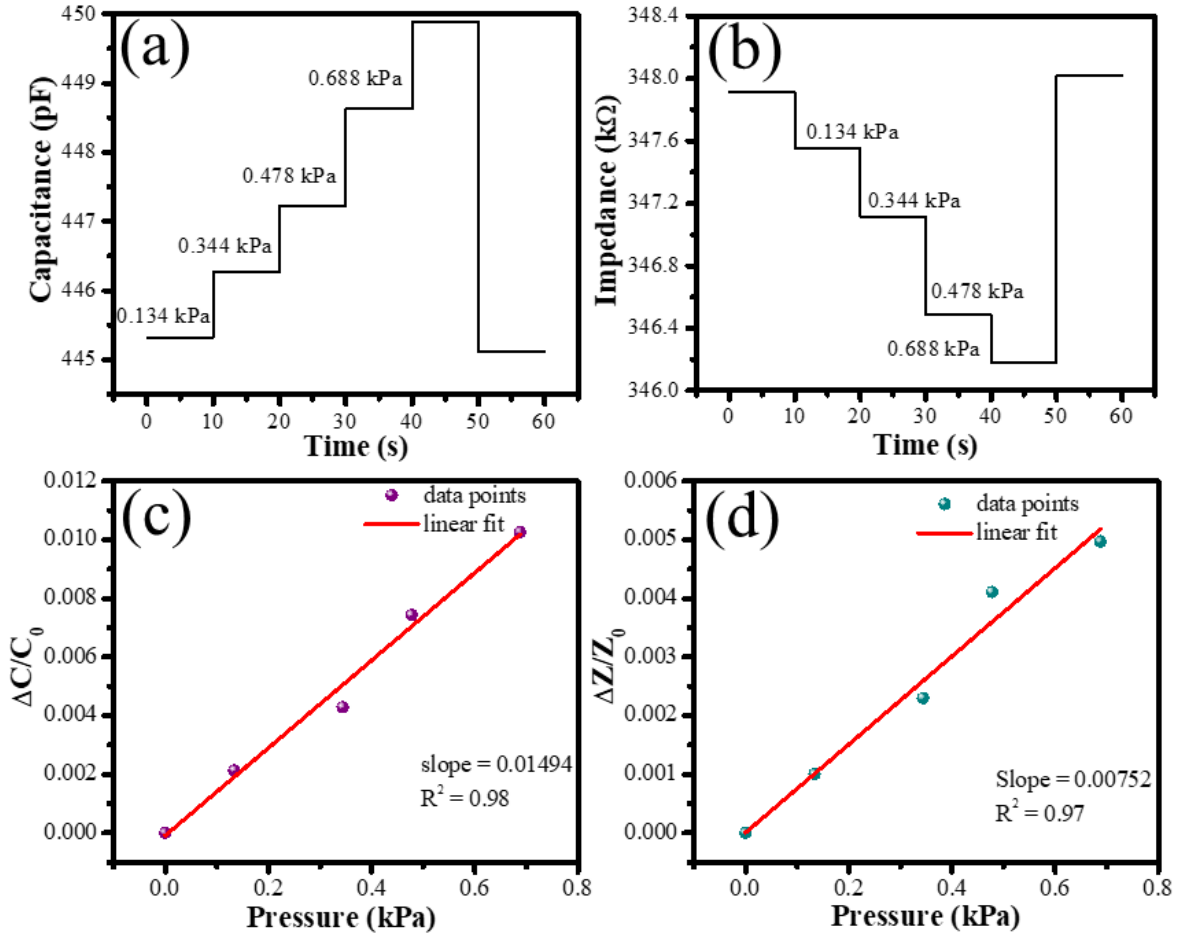

Fig. 3.26 *Time dependent static pressure tracking by changing the applied pressure in the form of computing (a) capacitance and (b) impedance. Linear fitting of (c) relative change in capacitance and (d) relative change in impedance with a function of applied static pressure.*

The fabricated energy harvesters were further utilised as static pressure sensor to monitor pressure variation. Fig. 3.26(a) and Fig. 3.26(b) show the variation of capacitance (C) and impedance (Z) value with the application of an increasing amount of static pressure upon the optimised PEH. From these plots, it can be seen that the value of the capacitance increases whereas the impedance decreases with the increment in pressure from 0.14 to 0.69 kPa. This variation can be typically due to the fact that upon the application of an external static pressure, minor compressive contractions occur inside the sample, which augments the connection path resulting in the change of the capacitance or impedance value [118,119]. Now, it is well known that real life applicability of any pressure sensor depends upon its linearity. Thus, as a static linear pressure sensor the relative change in capacitance ($\Delta C / C_0$) (where, ΔC

= (C - C_0) and C_0 = capacitance without applied pressure) and the relative change in impedance ($\Delta Z/Z_0$) (where, ΔZ = (Z - Z_0) and Z_0 = impedance without applied pressure) must change linearly with the static applied pressure. From the Fig. 3.26(c) and Fig. 3.26(d) it is clear that the relative change in capacitance and impedance with a function of static pressure follows a linear trend with the fitting factor R^2>0.96 [118]. From the slope of these fitting curves, sensitivity of the sample towards pressure can be calculated. Here in the experimental pressure range, the sensitivity of the 20BST40 energy harvester device was found out to be 14.94 MPa^{-1} which supports that the device can be comfortably used as an efficient static pressure sensor.

3.4. Conclusion

In summary, this chapter demonstrates the promise of utilizing $Ba_{0.6}Sr_{0.4}TiO_3$ (BST40) particles, synthesized through the traditional solid-state reaction method, as effective fillers for the creation of efficient piezoelectric energy harvesting devices. The filler underwent structural analysis, confirming its pure phase with a centrosymmetric space group, indicating its non-ferroelectric nature. Elemental analysis of the filler verified the presence of the desired elements, free from impurities. Moreover, the effective integration of the filler into the matrix was confirmed through XRD characterization of the composite film. The FTIR analysis demonstrated a notable enhancement in the polar phase of PVDF after the addition of BST40 filler to the matrix. Through the incorporation of various concentrations of BST40 filler particles, the composite films' phase formation, dielectric and ferroelectric properties, energy storage capabilities, and energy harvesting performance were effectively tailored. The composite film that exhibited the most efficient mechanical energy harvesting performance was further applied for energy harvesting from different motions such as bending, stretching etc and effective static pressure sensing. Thus, the effective use of specific filler at a critical weight percentage can significantly augment different physiochemical properties of the flexible polymer substrate thereby paving the way towards effective flexible bio-mechanical energy harvesters with adequate power density.

References

[1] L. Lu, W. Ding, J. Liu, B. Yang, Flexible PVDF based piezoelectric nanogenerators, Nano Energy. 78 (2020). https://doi.org/10.1016/j.nanoen.2020.105251.

[2] M. Sahu, V. Vivekananthan, S. Hajra, K.S. Abisegapriyan, N.P. Maria Joseph Raj, S.J. Kim, Synergetic enhancement of energy harvesting performance in triboelectric nanogenerator using ferroelectric polarization for self-powered IR signaling and body activity monitoring, J Mater Chem A Mater. 8 (2020) 22257–22268. https://doi.org/10.1039/d0ta06215d.

[3] X. Wang, H. Yamada, C.N. Xu, Large electrostriction near the solubility limit in BaTi O3 -CaTi O3 ceramics, Appl Phys Lett. 86 (2005) 2012–2015. https://doi.org/10.1063/1.1850598.

[4] H. JAFFE, Piezoelectric Ceramics, Journal of the American Ceramic Society. 41 (1958) 494–498. https://doi.org/10.1111/j.1151-2916.1958.tb12903.x.

[5] X. Ren, Large electric-field-induced strain in ferroelectric crystals by point-defect-mediated reversible domain switching, Nat Mater. 3 (2004) 91–94. https://doi.org/10.1038/nmat1051.

[6] E. Burcsu, G. Ravichandran, K. Bhattacharya, Large strain electrostrictive actuation in barium titanate, Appl Phys Lett. 77 (2000) 1698–1700. https://doi.org/10.1063/1.1308533.

[7] S.S. Parizi, A. Mellinger, G. Caruntu, Ferroelectric barium titanate nanocubes as capacitive building blocks for energy storage applications, ACS Appl Mater Interfaces. 6 (2014) 17506–17517. https://doi.org/10.1021/am502547h.

[8] B.J.J. Urban, J.E. Spanier, L. Ouyang, W.S. Yun, H. Park, Urban, Jeffrey J., et al. Single-Crystalline Barium Titanate Nanowires. Advanced Materials 15.5 (2003) 423-426..pdf, (2003) 423–426.

[9] D. Zhang, W. Hu, C. Meggs, B. Su, T. Price, D. Iddles, M.J. Lancaster, T.W. Button, Fabrication and characterisation of barium strontium titanate thick film device structures for microwave applications, J Eur Ceram Soc. 27 (2007) 1047–1051. https://doi.org/10.1016/j.jeurceramsoc.2006.05.051.

[10] P. Bao, T.J. Jackson, X. Wang, M.J. Lancaster, Barium strontium titanate thin film varactors for room-temperature microwave device applications, J Phys D Appl Phys. 41 (2008). https://doi.org/10.1088/0022-3727/41/6/063001.

[11] T. Zhang, H. Ni, Pyroelectric and dielectric properties of sol-gel derived barium-strontium-titanate (Ba0.64Sr0.36TiO3) thin films, Sens Actuators A Phys. 100 (2002) 252–256. https://doi.org/10.1016/S0924-4247(02)00139-5.

[12] G. Suo, Y. Yu, Z. Zhang, S. Wang, P. Zhao, J. Li, X. Wang, Piezoelectric and Triboelectric Dual Effects in Mechanical-Energy Harvesting Using BaTiO3/Polydimethylsiloxane Composite Film, ACS Appl Mater Interfaces. 8 (2016) 34335–34341. https://doi.org/10.1021/acsami.6b11108.

[13] Z. Shen, X. Wang, B. Luo, L. Li, BaTiO3-BiYbO3 perovskite materials for energy storage applications, J Mater Chem A Mater. 3 (2015) 18146–18153. https://doi.org/10.1039/c5ta03614c.

[14] Y. Huang, C. Zhao, J. Yin, X. Lv, J. Ma, J. Wu, Giant electrostrictive effect in lead-free barium titanate-based ceramics: Via A-site ion-pairs engineering, J Mater Chem A Mater. 7 (2019) 17366–17375. https://doi.org/10.1039/c9ta05681e.

[15] Y. Lin, D. Li, M. Zhang, S. Zhan, Y. Yang, H. Yang, Q. Yuan, Excellent Energy-Storage Properties Achieved in BaTiO3-Based Lead-Free Relaxor Ferroelectric Ceramics via Domain Engineering on the Nanoscale, ACS Appl Mater Interfaces. 11 (2019) 36824–36830. https://doi.org/10.1021/acsami.9b10819.

[16] M. Acosta, N. Novak, V. Rojas, S. Patel, R. Vaish, J. Koruza, G.A. Rossetti, BaTiO3-based piezoelectrics: Fundamentals, current status, and perspectives, 041305 (2017).

[17] L.F. Zhu, X.W. Lei, L. Zhao, M.I. Hussain, G.Z. Zhao, B.P. Zhang, Phase structure and energy storage performance for BiFeO3–BaTiO3 based lead-free ferroelectric ceramics, Ceram Int. 45 (2019) 20266–20275. https://doi.org/10.1016/j.ceramint.2019.06.300.

[18] D. Fu, M. Itoh, S.Y. Koshihara, Invariant lattice strain and polarization in BaTiO3-CaTiO 3 ferroelectric alloys, Journal of Physics Condensed Matter. 22 (2010). https://doi.org/10.1088/0953-8984/22/5/052204.

[19] H. Muta, K. Kurosaki, S. Yamanaka, Thermoelectric properties of doped BaTiO3-SrTiO3 solid solution, J Alloys Compd. 368 (2004) 22–24. https://doi.org/10.1016/j.jallcom.2003.07.016.

[20] W. Bai, X. Zhao, Y. Ding, L. Wang, P. Zheng, J. Hao, J. Zhai, Giant Field-Induced Strain with Low Hysteresis and Boosted Energy Storage Performance under Low Electric Field in (Bi0.5Na0.5)TiO3-Based Grain Orientation-Controlled Ceramics, Adv Electron Mater. 6 (2020) 1–11. https://doi.org/10.1002/aelm.202000332.

[21] D. Wang, Z. Jiang, B. Yang, S. Zhang, M. Zhang, F. Guo, W. Cao, Phase Diagram and Enhanced Piezoelectric Response of Lead-Free BaTiO 3 - CaTiO 3 -BaHfO 3 System , Journal of the American Ceramic Society. 97 (2014) 3244–3251. https://doi.org/10.1111/jace.13137.

[22] C. Liu, X. Liu, D. Wang, Z. Chen, B. Fang, J. Ding, X. Zhao, H. Xu, H. Luo, Improving piezoelectric property of BaTiO3-CaTiO 3-BaZrO3 lead-free ceramics by doping, Ceram Int. 40 (2014) 9881–9887. https://doi.org/10.1016/j.ceramint.2014.02.082.

[23] V.P. Mirjana M, R. Grigalaitis, N. Ilic, J.D. Bobić, A. Dzunuzovic, J. Banys, B.D. Stojanović, Interdependence between structure and electrical characteristics in Sm-doped barium titanate, J Alloys Compd. 724 (2017) 959–968. https://doi.org/10.1016/j.jallcom.2017.07.099.

[24] M. Arshad, H. Du, M.S. Javed, A. Maqsood, I. Ashraf, S. Hussain, W. Ma, H. Ran, Fabrication, structure, and frequency-dependent electrical and dielectric properties of Sr-doped BaTiO3 ceramics, Ceram Int. 46 (2020) 2238–2246. https://doi.org/10.1016/j.ceramint.2019.09.208.

[25] M.H. Khedhri, N. Abdelmoula, H. Khemakhem, R. Douali, F. Dubois, Structural, spectroscopic and dielectric properties of Ca-doped BaTiO 3, Appl Phys A Mater Sci Process. 125 (2019) 1–13. https://doi.org/10.1007/s00339-019-2487-y.

[26] S.P. More, M. V. Khedkar, D.D. Andhare, A. V. Humbe, K.M. Jadhav, Influence of manganese (Mn) substitution on structural, infrared and dielectric properties of BaTiO3 nanoceramics, Journal of Materials Science: Materials in Electronics. 31 (2020) 19756–19763. https://doi.org/10.1007/s10854-020-04500-6.

[27] A. Rani, J. Kolte, P. Gopalan, Investigation on the structural, multiferroic and magnetoelectric properties of BaTi1-xNixO3 ceramics, Ceram Int. 45 (2019) 5312–5320. https://doi.org/10.1016/j.ceramint.2018.11.229.

[28] P. Gupta, P.K. Mahapatra, R.N.P. Choudhary, Investigations on structural and electrical characteristics of Fe and W modified BaTiO3 ceramic, Physica B Condens Matter. 572 (2019) 203–213. https://doi.org/10.1016/j.physb.2019.08.002.

[29] P.P. Khirade, S.D. Birajdar, A. V. Raut, K.M. Jadhav, Multiferroic iron doped BaTiO3 nanoceramics synthesized by sol-gel auto combustion: Influence of iron on physical properties, Ceram Int. 42 (2016) 12441–12451. https://doi.org/10.1016/j.ceramint.2016.05.021.

[30] K.M. Sangwan, N. Ahlawat, R.S. Kundu, S. Rani, S. Rani, N. Ahlawat, S. Murugavel, Improved dielectric and ferroelectric properties of Mn doped barium zirconium titanate (BZT) ceramics for energy storage applications, Journal of Physics and Chemistry of Solids. 117 (2018) 158–166. https://doi.org/10.1016/j.jpcs.2018.01.051.

[31] A.K. Kalyani, K. Brajesh, A. Senyshyn, R. Ranjan, Orthorhombic-tetragonal phase coexistence and enhanced piezo-response at room temperature in Zr, Sn, and Hf modified BaTiO3, Appl Phys Lett. 104 (2014) 252906. https://doi.org/10.1063/1.4885516.

[32] J. Gao, Y. Liu, Y. Wang, X. Hu, W. Yan, X. Ke, L. Zhong, Y. He, X. Ren, Designing High Dielectric Permittivity Material in Barium Titanate, Journal of Physical Chemistry C. 121 (2017) 13106–13113. https://doi.org/10.1021/acs.jpcc.7b04636.

[33] S. Sasikumar, S. Saravanakumar, S. Asath Bahadur, D. Sivaganesh, Electronic structure, optical and chemical bonding properties of strontium doped Barium Titanate, Optik (Stuttg). 206 (2020) 163752. https://doi.org/10.1016/j.ijleo.2019.163752.

[34] M. Ben Chamekh, Z. Ben Achour, A. Thamri, R. Chtourou, E. Dhahri, O. Touayar, Structural and electrical characterization of strontium doped barium titanate for radiometric measurement, Chem Phys Lett. 761 (2020) 138008. https://doi.org/10.1016/j.cplett.2020.138008.

[35] W. Ma, L.E. Cross, Flexoelectric polarization of barium strontium titanate in the paraelectric state, Appl Phys Lett. 81 (2002) 3440–3442. https://doi.org/10.1063/1.1518559.

[36] L.M. Garten, S. Trolier-Mckinstry, Enhanced flexoelectricity through residual ferroelectricity in barium strontium titanate, J Appl Phys. 117 (2015). https://doi.org/10.1063/1.4913858.

[37] L.F. Da Silva, W. Avansi, M.L. Moreira, A. Mesquita, L.J.Q. Maia, J. Andrés, E. Longo, V.R. Mastelaro, Relationship between crystal shape, photoluminescence, and local structure in SrTiO 3 synthesized by microwave-assisted hydrothermal method, J Nanomater. 2012 (2012). https://doi.org/10.1155/2012/890397.

[38] H.W. Lee, S. Moon, C.H. Choi, D.K. Kim, Synthesis and size control of tetragonal barium titanate nanopowders by facile solvothermal method,

Journal of the American Ceramic Society. 95 (2012) 2429–2434. https://doi.org/10.1111/j.1551-2916.2012.05085.x.

[39] A.M. Gonzalez, L. Pardo, M.E. Montero-Cabrera, L.E. Fuentes-Cobas, Analysis of the rhombohedral-tetragonal symmetries coexistence in lead-free 0.94 (Bi0.5Na0.5)TiO3-0.06BaTiO3 ceramics from nanopowders, Advances in Applied Ceramics. 115 (2016) 96–105. https://doi.org/10.1080/17436753.2015.1131906.

[40] B. Vigneshwaran, P. Kuppusami, S. Ajithkumar, H. Sreemoolanadhan, Study of low temperature - dependent structural , dielectric , 3 (2020).

[41] R.E. Patru, C.P. Ganea, C.A. Stanciu, V.A. Surdu, R. Trusca, A.C. Ianculescu, I. Pintilie, L. Pintilie, (Ba,Sr)TiO3 solid solutions sintered from sol-gel derived powders: An insight into the composition and temperature dependent dielectric behavior, Ceram Int. 46 (2020) 4180–4190. https://doi.org/10.1016/j.ceramint.2019.10.136.

[42] Y. Yu, H. Zou, Q.F. Cao, X.S. Wang, Y.X. Li, X. Yao, Phase Transitions and Relaxation Behaviors in Barium Strontium Titanate Ceramics Determined by Dynamic Mechanical and Dielectric Analysis, Ferroelectrics. 487 (2015) 77–85. https://doi.org/10.1080/00150193.2015.1070641.

[43] W.C. Lee, C.Y. Huang, L.K. Tsao, Y.C. Wu, Chemical composition and tolerance factor at the morphotropic phase boundary in (Bi0.5Na0.5)TiO3-based piezoelectric ceramics, J Eur Ceram Soc. 29 (2009) 1443–1448. https://doi.org/10.1016/j.jeurceramsoc.2008.08.028.

[44] R.D. Shannon, Revised Effective Ionic Radii and Systematic Studies of Interatomie Distances in Halides and Chaleogenides, 1976.

[45] R. Yogamalar, R. Srinivasan, A. Vinu, K. Ariga, A.C. Bose, X-ray peak broadening analysis in ZnO nanoparticles, Solid State Commun. 149 (2009) 1919–1923. https://doi.org/10.1016/j.ssc.2009.07.043.

[46] A. Khorsand Zak, W.H. Abd. Majid, M.E. Abrishami, R. Yousefi, X-ray analysis of ZnO nanoparticles by Williamson-Hall and size-strain plot methods, Solid State Sci. 13 (2011) 251–256. https://doi.org/10.1016/j.solidstatesciences.2010.11.024.

[47] D. Nath, F. Singh, R. Das, X-ray diffraction analysis by Williamson-Hall, Halder-Wagner and size-strain plot methods of CdSe nanoparticles- a comparative study, Mater Chem Phys. 239 (2020) 122021. https://doi.org/10.1016/j.matchemphys.2019.122021.

[48] T. Zaman, K. Islam, A. Rahman, A. Hussain, A. Matin, Mono and co-substitution of Sr 2 + and Ca 2 + on the structural , electrical and optical properties of barium titanate ceramics, Ceram Int. 45 (2019) 10154–10162. https://doi.org/10.1016/j.ceramint.2019.02.064.

[49] N.S. Gonçalves, J.A. Carvalho, Z.M. Lima, J.M. Sasaki, Size-strain study of NiO nanoparticles by X-ray powder diffraction line broadening, Mater Lett. 72 (2012) 36–38. https://doi.org/10.1016/j.matlet.2011.12.046.

[50] S.Y. Kuo, W.Y. Liao, W.F. Hsieh, Structural ordering transition and repulsion of the giant LO-TO splitting in polycrystalline (formula presented), Phys Rev B Condens Matter Mater Phys. 64 (2001) 1–7. https://doi.org/10.1103/PhysRevB.64.224103.

[51] A.K. Sood, N. Chandrabhas, D.V.S. Muthu, A. Jayaraman, Phonon interference in BaTi03. High-pressure Raman study, 1995.

[52] S. Li, Y. Yao, Y.I. Yuzyuk, Y. Jia, X. Wang, S. Xie, Y. Jing, Investigations of BaxSr1-xTiO3 ceramics and powders prepared by direct current arc discharge technique, Appl Phys Lett. 105 (2014). https://doi.org/10.1063/1.4894456.

[53] M. Banas, R.D. Duhamel, U. Balachandran, N.G. Eror, The assistance of C Raman Spectra of Strontium Titanate, 1982.

[54] W.G. Nilsen, J.G. Skinner, Raman spectrum of strontium titanate, J Chem Phys. 48 (1968) 2240–2248. https://doi.org/10.1063/1.1669418.

[55] Y.I. Yuzyuk, P. Simon, Comment on “Structural ordering transition and repulsion of the giant LO-TO splitting in polycrystalline BaxSr1–xTiO3,” Phys Rev B Condens Matter Mater Phys. 68 (2003) 1–2. https://doi.org/10.1103/PhysRevB.68.216101.

[56] X. Jin, D. Sun, M. Zhang, Y. Zhu, J. Qian, Investigation on FTIR spectra of barium calcium titanate ceramics, J Electroceram. 22 (2009) 285–290. https://doi.org/10.1007/s10832-007-9402-1.

[57] J. Wang, J. Xiang, S. Duo, W. Li, M. Li, L. Bai, Microstructure, optical and dielectric properties of compositional graded (Ba,Sr)TiO 3 thin films derived by RF magnetron sputtering, Journal of Materials Science: Materials in Electronics. 20 (2009) 319–322. https://doi.org/10.1007/s10854-008-9727-9.

[58] W. Jiang, W. Cai, Z. Lin, C. Fu, Effects of Nd-doping on optical and photovoltaic properties of barium titanate thin films prepared by sol-gel method, Mater Res Bull. 48 (2013) 3092–3097. https://doi.org/10.1016/j.materresbull.2013.04.048.

[59] R.A.P. Ribeiro, S.R. De Lázaro, Theoretical investigations of the bulk modulus in the tetra-cubic transition of PbTiO3material, Quim Nova. 37 (2014) 1165–1170. https://doi.org/10.5935/0100-4042.20140190.

[60] S. Sanna, C. Thierfelder, S. Wippermann, T.P. Sinha, W.G. Schmidt, Barium titanate ground- and excited-state properties from first-principles calculations, Phys Rev B Condens Matter Mater Phys. 83 (2011) 1–9. https://doi.org/10.1103/PhysRevB.83.054112.

[61] N. Oshime, J. Kano, N. Ikeda, T. Teranishi, T. Fujii, T. Ueda, T. Ohkubo, Quantitative study of band structure in BaTiO3 particles with vacant ionic sites, J Appl Phys. 120 (2016). https://doi.org/10.1063/1.4964803.

[62] J.H. Jeon, Y.D. Hahn, H.D. Kim, Microstructure and dielectric properties of barium-strontium titanate with a functionally graded structure, J Eur Ceram Soc. 21 (2001) 1653–1656. https://doi.org/10.1016/S0955-2219(01)00085-1.

[63] J.W. Liou, B.S. Chiou, Effect of direct-current biasing on the dielectric properties of barium strontium titanate, Journal of the American Ceramic Society. 80 (1997) 3093–3099. https://doi.org/10.1111/j.1151-2916.1997.tb03237.x.

[64] M. Wang, X. Zuo, K. Li, K. Wang, G. Zhang, Growth characteristics of BaxSr(1-x)TiO3thin films produced by micro-arc oxidation, J Mater Res. 35 (2020) 1703–1714. https://doi.org/10.1557/jmr.2020.66.

[65] H.Y. Lee, K.C. Lee, J.N. Schunke, L.C. Burton, Leakage Currents in Multilayer Ceramic Capacitors, IEEE Transactions on Components, Hybrids, and Manufacturing Technology. 7 (1984) 443–453. https://doi.org/10.1109/TCHMT.1984.1136375.

[66] S. Dupuis, S. Sulekar, J.H. Kim, H. Han, P. Dufour, C. Tenailleau, J.C. Nino, S. Guillemet-Fritsch, Colossal permittivity and low losses in Ba1-xSrxTiO3-δ reduced nanoceramics, J Eur Ceram Soc. 36 (2016) 567–575. https://doi.org/10.1016/j.jeurceramsoc.2015.10.017.

[67] D. Xu, X. Yue, Y. Zhang, J. Song, X. Chen, S. Zhong, J. Ma, L. Ba, L. Zhang, S. Du, Enhanced dielectric properties and electrical responses of cobalt-doped CaCu3Ti4O12 thin films, J Alloys Compd. 773 (2019) 853–859. https://doi.org/10.1016/j.jallcom.2018.09.340.

[68] S. Edition, Electroceramics, in: 2003.

[69] X. Wei, X. Yao, Nonlinear dielectric properties of barium strontium titanate ceramics, Mater Sci Eng B Solid State Mater Adv Technol. 99 (2003) 74–78. https://doi.org/10.1016/S0921-5107(02)00423-3.

[70] A. Elbasset, S. Sayouri, F. Abdi, T. Lamcharfi, L. Mrharrab, Effect of Sr addition on piezoelectric properties and the transition temperature of BaTiO3, Glass Physics and Chemistry. 43 (2017) 91–97. https://doi.org/10.1134/S1087659617010059.

[71] Y. Bai, X. Han, K. Ding, L.J. Qiao, Combined effects of diffuse phase transition and microstructure on the electrocaloric effect in Ba1-

xSrxTiO3 ceramics, Appl Phys Lett. 103 (2013) 16–20. https://doi.org/10.1063/1.4825266.

[72] T. Badapanda, V. Senthil, S. Panigrahi, S. Anwar, Diffuse phase transition behavior of dysprosium doped barium titanate ceramic, J Electroceram. 31 (2013) 55–60. https://doi.org/10.1007/s10832-013-9808-x.

[73] M.W. Cole, C. V. Weiss, E. Ngo, S. Hirsch, L.A. Coryell, S.P. Alpay, Microwave dielectric properties of graded barium strontium titanate films, Appl Phys Lett. 92 (2008). https://doi.org/10.1063/1.2919080.

[74] T. Prodromakis, C. Papavassiliou, Engineering the Maxwell-Wagner polarization effect, Appl Surf Sci. 255 (2009) 6989–6994. https://doi.org/10.1016/j.apsusc.2009.03.030.

[75] P. Gupta, P.K. Mahapatra, R.N.P. Choudhary, Investigation on structural and electrical properties of Co and W modified BaTiO3, Ceram Int. 45 (2019) 22862–22871. https://doi.org/10.1016/j.ceramint.2019.07.329.

[76] A. Kaur, L. Singh, K. Asokan, Electrical relaxation and conduction mechanisms in iron doped barium strontium titanate, Ceram Int. 44 (2018) 3751–3759. https://doi.org/10.1016/j.ceramint.2017.11.158.

[77] S. Chao, V. Petrovsky, F. Dogan, Effects of sintering temperature on the microstructure and dielectric properties of titanium dioxide ceramics, J Mater Sci. 45 (2010) 6685–6693. https://doi.org/10.1007/s10853-010-4761-4.

[78] P.S. Solid, S. Chem, JUMP R E L A X A T I O N IN SOLID ELECTROLYTES, 22 (1993) 111–195.

[79] T. Badapanda, S. Sarangi, S. Parida, B. Behera, B. Ojha, S. Anwar, Frequency and temperature dependence dielectric study of strontium modified Barium Zirconium Titanate ceramics obtained by mechanochemical synthesis, Journal of Materials Science: Materials in Electronics. 26 (2015) 3069–3082. https://doi.org/10.1007/s10854-015-2799-4.

[80] 267673a0, (n.d.).

[81] P. Gupta, P.K. Mahapatra, R.N.P. Choudhary, Structural and electrical characteristics of rare-earth modified bismuth layer structured compounds, J Alloys Compd. 863 (2021). https://doi.org/10.1016/j.jallcom.2020.158457.

[82] Z. Li, H. Fan, Polaron relaxation associated with the localized oxygen vacancies in Ba0.85Sr0.15TiO3 ceramics at high temperatures, J Appl Phys. 106 (2009) 0–5. https://doi.org/10.1063/1.3211308.

[83] V. Purohit, R.N.P. Choudhary, M. Sahu, Structural and Electrical Properties of Lead-Free Perovskite: Bi(Sr0.25Ti0.25Fe0.5)O3, J Inorg Organomet Polym Mater. 30 (2020) 3026–3035. https://doi.org/10.1007/s10904-020-01459-z.

[84] Q. Ke, X. Lou, Y. Wang, J. Wang, Oxygen-vacancy-related relaxation and scaling behaviors of Bi 0.9La0.1Fe0.98Mg0.02O3 ferroelectric thin films, Phys Rev B Condens Matter Mater Phys. 82 (2010). https://doi.org/10.1103/PhysRevB.82.024102.

[85] T.F. Zhang, X.G. Tang, Q.X. Liu, S.G. Lu, Y.P. Jiang, X.X. Huang, Q.F. Zhou, Oxygen-vacancy-related relaxation and conduction behavior in (Pb1-xBax)(Zr0.95Ti0.05)O3 ceramics, AIP Adv. 4 (2014) 0–11. https://doi.org/10.1063/1.4900610.

[86] M.D. Li, X.G. Tang, S.M. Zeng, Y.P. Jiang, Q.X. Liu, T.F. Zhang, W.H. Li, Oxygen-vacancy-related dielectric relaxation behaviours and impedance spectroscopy of Bi(Mg1/2Ti1/2)O3 modified BaTiO3 ferroelectric ceramics, Journal of Materiomics. 4 (2018) 194–201. https://doi.org/10.1016/j.jmat.2018.03.001.

[87] I.W. Kim, C.W. Ahn, J.S. Kim, T.K. Song, J.S. Bae, B.C. Choi, J.H. Jeong, J.S. Lee, Low-frequency dielectric relaxation and ac conduction of SrBi 2Ta2O9 thin film grown by pulsed laser deposition, Appl Phys Lett. 80 (2002) 4006–4008. https://doi.org/10.1063/1.1482138.

[88] Q. Li, H. Wang, H. Fan, M. Xu, B. Peng, C. Long, X. Liu, Dielectric properties and electrical conduction of La2O 3-doped (Bi0.5Na0.5)0.94Ba 0.06TiO3 ceramics, Appl Phys A Mater Sci Process. 114 (2014) 551–558. https://doi.org/10.1007/s00339-013-7613-7.

[89] E. Kar, N. Bose, B. Dutta, N. Mukherjee, S. Mukherjee, MWCNT@SiO2 Heterogeneous Nanofiller-Based Polymer Composites: A Single Key to the High-Performance Piezoelectric Nanogenerator and X-band Microwave Shield, ACS Appl Nano Mater. 1 (2018) 4005–4018. https://doi.org/10.1021/acsanm.8b00770.

[90] H.J. Ye, W.Z. Shao, L. Zhen, Crystallization kinetics and phase transformation of poly(vinylidene fluoride) films incorporated with functionalized baTiO3 nanoparticles, J Appl Polym Sci. 129 (2013) 2940–2949. https://doi.org/10.1002/app.38949.

[91] P. Martins, A.C. Lopes, S. Lanceros-Mendez, Electroactive phases of poly(vinylidene fluoride): Determination, processing and applications, Prog Polym Sci. 39 (2014) 683–706. https://doi.org/10.1016/j.progpolymsci.2013.07.006.

[92] N.A. Hoque, P. Thakur, P. Biswas, M. Saikh, based superior piezoelectric nanogenerator †, Journal of Materials Chemistry A: Materials for Energy and Sustainability. 6 (2018) 13848–13858. https://doi.org/10.1039/C8TA04074E.

[93] E. Kar, N. Bose, B. Dutta, S. Banerjee, N. Mukherjee, S. Mukherjee, 2D SnO2 nanosheet/PVDF composite based flexible, self-cleaning piezoelectric energy harvester, Energy Convers Manag. 184 (2019) 600–608. https://doi.org/10.1016/j.enconman.2019.01.073.

[94] J. Liu, B. Yang, L. Lu, X. Wang, X. Li, X. Chen, J. Liu, Flexible and lead-free piezoelectric nanogenerator as self-powered sensor based on electrospinning BZT-BCT/P(VDF-TrFE) nanofibers, Sens Actuators A Phys. 303 (2020). https://doi.org/10.1016/j.sna.2019.111796.

[95] T.J. Lewis, Nanometric Dielectrics, IEEE Transactions on Dielectrics and Electrical Insulation. 1 (1994) 812–825. https://doi.org/10.1109/94.326653.

[96] Prateek, V.K. Thakur, R.K. Gupta, Recent Progress on Ferroelectric Polymer-Based Nanocomposites for High Energy Density Capacitors: Synthesis, Dielectric Properties, and Future Aspects, Chem Rev. 116 (2016) 4260–4317. https://doi.org/10.1021/acs.chemrev.5b00495.

[97] H. Hu, F. Zhang, S. Luo, W. Chang, J. Yue, C.-H. Wang, Recent advances in rational design of polymer nanocomposite dielectrics for energy storage, Nano Energy. 74 (2020) 104844. https://doi.org/10.1016/j.nanoen.2020.104844.

[98] T. Tanaka, M. Kozako, N. Fuse, Y. Ohki, Proposal of a multi-core model for polymer nanocomposite dielectrics, IEEE Transactions on Dielectrics and Electrical Insulation. 12 (2005) 669–681. https://doi.org/10.1109/TDEI.2005.1511092.

[99] Prateek, V.K. Thakur, R.K. Gupta, Recent Progress on Ferroelectric Polymer-Based Nanocomposites for High Energy Density Capacitors: Synthesis, Dielectric Properties, and Future Aspects, Chem Rev. 116 (2016) 4260–4317. https://doi.org/10.1021/acs.chemrev.5b00495.

[100] I. Chinya, S. Sen, Improved dielectric and touch sensing performance of surface modified zinc ferrite (ZF)/Polyvinylidene fluoride (PVDF) composite, Sens Actuators A Phys. 267 (2017) 301–309. https://doi.org/10.1016/j.sna.2017.10.031.

[101] S. Pratihar, A. Patra, A. Sasmal, S.K. Medda, S. Sen, Enhanced dielectric, ferroelectric, energy storage and mechanical energy harvesting performance of ZnO-PVDF composites induced by MWCNTs as an additive third phase, Soft Matter. 17 (2021) 8483–8495. https://doi.org/10.1039/d1sm00854d.

[102] J. Fu, Y. Hou, M. Zheng, Q. Wei, M. Zhu, H. Yan, Improving Dielectric Properties of PVDF Composites by Employing Surface Modified Strong

Polarized BaTiO3 Particles Derived by Molten Salt Method, ACS Appl Mater Interfaces. 7 (2015) 24480–24491. https://doi.org/10.1021/acsami.5b05344.

[103] A. Sasmal, S. Sen, P.S. Devi, Frequency dependent energy storage and dielectric performance of Ba-Zr Co-doped BiFeO3loaded PVDF based mechanical energy harvesters: Effect of corona poling, Soft Matter. 16 (2020) 8492–8505. https://doi.org/10.1039/d0sm01031f.

[104] A. Sasmal, S. Sen, P.S. Devi, Role of suppressed oxygen vacancies in the BiFeO3 nanofiller to improve the polar phase and multifunctional performance of poly(vinylidene fluoride), Physical Chemistry Chemical Physics. 21 (2019) 5974–5988. https://doi.org/10.1039/c8cp07281g.

[105] X. Hu, Y. Zhou, J. Liu, B. Chu, Improved flexoelectricity in PVDF/barium strontium titanate (BST) nanocomposites, J Appl Phys. 123 (2018). https://doi.org/10.1063/1.5022650.

[106] L. Jin, F. Li, S. Zhang, Decoding the fingerprint of ferroelectric loops: Comprehension of the material properties and structures, Journal of the American Ceramic Society. 97 (2014) 1–27. https://doi.org/10.1111/jace.12773.

[107] A. Sasmal, A. Patra, P.S. Devi, S. Sen, Space charge induced augmented dielectric permittivity and improved energy harvesting ability of nano-Ag decorated ZnSnO3 filled PVDF based flexible nanogenerator, Compos Sci Technol. 213 (2021). https://doi.org/10.1016/j.compscitech.2021.108916.

[108] A. Gruverman, M. Alexe, D. Meier, Piezoresponse force microscopy and nanoferroic phenomena, Nat Commun. 10 (2019) 1–9. https://doi.org/10.1038/s41467-019-09650-8.

[109] C. Zhang, Y. Fan, H. Li, Y. Li, L. Zhang, S. Cao, S. Kuang, Y. Zhao, A. Chen, G. Zhu, Z.L. Wang, Fully Rollable Lead-Free Poly(vinylidene fluoride)-Niobate-Based Nanogenerator with Ultra-Flexible Nano-

Network Electrodes, ACS Nano. 12 (2018) 4803–4811. https://doi.org/10.1021/acsnano.8b01534.

[110] S. Pratihar, S.K. Medda, S. Sen, P.S. Devi, Tailored piezoelectric performance of self-polarized PVDF-ZnO composites by optimization of aspect ratio of ZnO nanorods, Polym Compos. 41 (2020) 3351–3363. https://doi.org/10.1002/pc.25624.

[111] Prateek, R. Bhunia, A. Garg, R.K. Gupta, Poly(vinylpyrrolidone)/Poly(vinylidene fluoride) as Guest/Host Polymer Blends: Understanding the Role of Compositional Transformation on Nanoscale Dielectric Behavior through a Simple Solution-Process Route, ACS Appl Energy Mater. 2 (2019) 6146–6152. https://doi.org/10.1021/acsaem.9b01092.

[112] R. Bhimireddi, B. Ponraj, K.B.R. Varma, Structural, Optical, and Piezoelectric Response of Lead-Free Ba0.95Mg0.05Zr0.1Ti0.9O3 Nanocrystalline Powder, Journal of the American Ceramic Society. 99 (2016) 896–904. https://doi.org/10.1111/jace.14018.

[113] C. Zhang, Y. Fan, H. Li, Y. Li, L. Zhang, S. Cao, S. Kuang, Y. Zhao, A. Chen, G. Zhu, Z.L. Wang, Fully Rollable Lead-Free Poly(vinylidene fluoride)-Niobate-Based Nanogenerator with Ultra-Flexible Nano-Network Electrodes, ACS Nano. 12 (2018) 4803–4811. https://doi.org/10.1021/acsnano.8b01534.

[114] S. Mondal, T. Paul, S. Maiti, B.K. Das, K.K. Chattopadhyay, Human motion interactive mechanical energy harvester based on all inorganic perovskite-PVDF, Nano Energy. 74 (2020). https://doi.org/10.1016/j.nanoen.2020.104870.

[115] L. Lu, W. Ding, J. Liu, B. Yang, Flexible PVDF based piezoelectric nanogenerators, Nano Energy. 78 (2020). https://doi.org/10.1016/j.nanoen.2020.105251.

[116] X. Hu, X. Yan, L. Gong, F. Wang, Y. Xu, L. Feng, D. Zhang, Y. Jiang, Improved Piezoelectric Sensing Performance of P(VDF-TrFE) Nanofibers by Utilizing BTO Nanoparticles and Penetrated Electrodes, ACS Appl Mater Interfaces. 11 (2019) 7379–7386. https://doi.org/10.1021/acsami.8b19824.

[117] R. Pandey, G. Sb, S. Grover, S.K. Singh, A. Kadam, S. Ogale, U. V. Waghmare, V.R. Rao, D. Kabra, Microscopic Origin of Piezoelectricity in Lead-Free Halide Perovskite: Application in Nanogenerator Design, ACS Energy Lett. 4 (2019) 1004–1011. https://doi.org/10.1021/acsenergylett.9b00323.

[118] Q. Wang, M. Jian, C. Wang, Y. Zhang, Carbonized Silk Nanofiber Membrane for Transparent and Sensitive Electronic Skin, Adv Funct Mater. 27 (2017). https://doi.org/10.1002/adfm.201605657.

[119] E. Kar, N. Bose, B. Dutta, N. Mukherjee, S. Mukherjee, Ultraviolet-and Microwave-Protecting, Self-Cleaning e-Skin for Efficient Energy Harvesting and Tactile Mechanosensing, ACS Appl Mater Interfaces. 11 (2019) 17501–17512. https://doi.org/10.1021/acsami.9b06452.

Chapter 4

Multiphase Coexisted Perovskite/PVDF-based Piezo-Tribo Hybrid Energy Harvester: A Wearable Flexi-Electronic for Real-Time Wireless Smart Applications

4.1 Introduction

From the previous chapter, we have seen that the incorporation of BST40 inside PVDF augmented piezoelectric energy generation performance to some extent. As BST40 has a centrosymmetric crystal structure, it shows no piezoelectricity. Though BST40/PVDF composite-based piezoelectric energy harvester showed greater power production capability than the mere PVDF-based piezoelectric energy harvester. It was mainly due to the enhancement in the polar phase of the PVDF polymer part. That is why it was not able to generate enough power as far as application purposes are concerned. As per the scientific community's consensus, the incorporation of piezoelectric ceramic fillers is expected to significantly enhance the efficiency of piezoelectric energy harvesting in PVDF composite films [1,2]. That is why in this specific work we have synthesized barium titanate based piezoelectric material with high piezoelectricity. In this regard, it is worthwhile to mention that this PEH device faces some limitations in output generation performances. Meanwhile, TEH devices have outperformed the PEH devices in energy generation efficiency. In this chapter, we have taken advantage of these two energy generation procedures (piezoelectric energy harvesting and the triboelectric energy harvesting) by hybridizing these two approaches in a single device.

4.2 Experimental

The modified Pechini method was used to synthesize $(Ba_{0.85}Ca_{0.15})(Ti_{0.90}Hf_{0.10})O_3$ (BCHT) particles (details are described in Chapter 2). The synthesized BCHT

Portion of this chapter appeared as

S. Maity, E. Kar, A. Kar, and S. Sen. “Multiphase Coexisted Perovskite/PVDF Composite Derived Wearable Piezo-Tribo Hybrid Energy Harvester for Wireless Smart Applications”. Chemical Engineering Journal, 2023, 474, 145959.

particles were then employed as a filler to fabricate flexible PVDF-based composite films using a straightforward solution casting method (details are mentioned in Chapter 2). As per the loaded BCHT wt% inside PVDF, the composite films are named 5BCHT, 10BCHT, and 15BCHT for 5, 10, and 15 wt% loaded BCHT respectively. Piezoelectric energy harvesting device, Triboelectric energy harvesting device, and piezoelectric assisted triboelectric hybrid energy harvesting device were fabricated and the output properties in terms of output voltage and output current were studied. The details methods and techniques are elaborated in Chapter 2.

4.3 Results & Discussions

4.3.1 Characterization of fillers

4.3.1.1 Structural characterizations

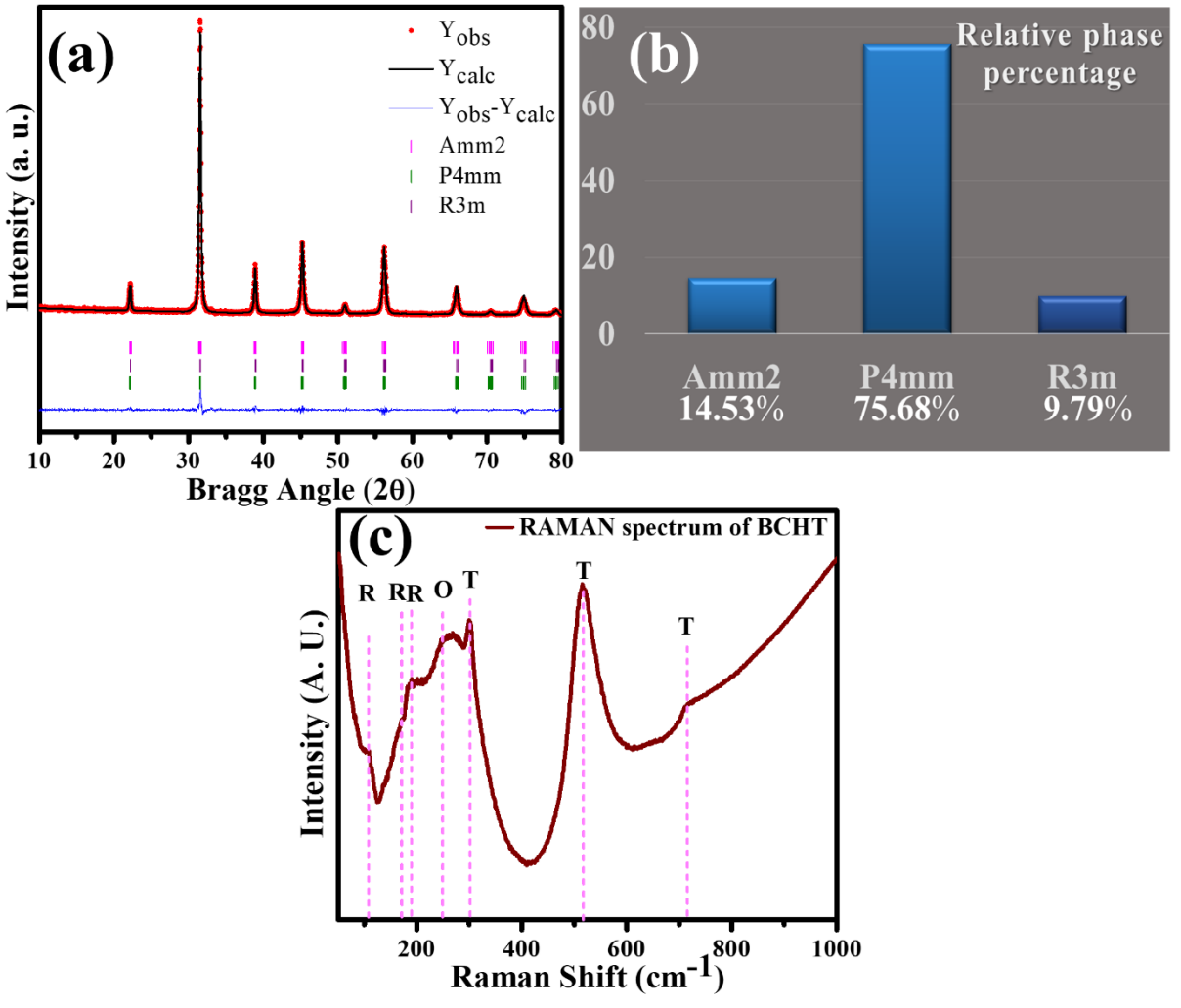

Fig. 4.1*(a) Rietveld refined XRD pattern of synthesized BCHT particles, (b) relative phase percentage from the Rietveld refined XRD result, (c) Raman spectrum of the synthesized BCHT particles.*

X-ray Diffraction (XRD) analysis was conducted on the synthesized BCHT powder sample to investigate both its crystalline phases and purity. The presence of well-defined peaks in the XRD pattern of the BCHT particles confirms that they have a crystalline structure (as shown in Fig. 4.1(a)). Furthermore, the absence of any unwanted impurity-related peaks in the XRD pattern confirms that the synthesized BCHT is pure. To gain a more detailed understanding of the various phases present in the synthesized BCHT powder, Rietveld refinement of the XRD data was conducted using the Fullprof software package. A careful examination of Fig. 4.1(a) reveals that the XRD data closely matched a model featuring the coexistence of three phases: Orthorhombic (O) Amm2, Rhombohedral (R) R3m (with a hexagonal axis), and Tetragonal (T) P4mm. This model had an excellent goodness of fit (χ^2) value of 1.23. The Rietveld analysis provided phase fractions (measured) for the Amm2, R3m, and P4mm phases, which were determined to be 14.53%, 9.79%, and 74.68%, respectively (as shown in Fig. 4.1(b)). The relevant parameters obtained from the fitting process, along with fitting factors, are presented in Table 4.1. In summary, the XRD pattern of the synthesized BCHT particles indicates the presence of three distinct phases (Amm2, R3m, and P4mm) due to the formation of a morphotropic phase boundary. It is noteworthy that the creation of a morphotropic phase boundary in ceramic fillers can significantly enhance their piezoelectric properties, leading to a higher piezoelectric charge coefficient (d_{33}). The Raman spectrum displayed in Fig. 4.1(c) shows the presence of key bands associated with the tetragonal nature of $BaTiO_3$. Peaks centered at 301 cm^{-1}, 517 cm^{-1}, and 715 cm^{-1} can be attributed to the distinctive bands of the tetragonal (P4mm) structure [3,4] present in BCHT. Again, the presence of peaks at 109 cm^{-1}, 169 cm^{-1}, and 187 cm^{-1}, along with interference dips at 125 cm^{-1} and 176 cm^{-1}, clearly indicate the distinct Rhombohedral distortion of the BCHT sample [5,6]. Additionally, the emergence of an additional phonon vibration mode at approximately 249 cm^{-1} can be assigned to the Orthorhombic phase of $BaTiO_3$ [7]. Therefore, the Raman vibration spectrum provides strong evidence for the coexistence of multiple phases at room temperature.

Table 4.1. Rietveld Refinement fitted lattice parameters and fitting factors of BCHT particles

Space Group	Lattice Parameters			Atoms	Atomic sites	Relative phase percentage	Refinement fitting factors
	a	b	c				
Amm2	3.9988	4.6503	4.6982	Ba	0.0, 0.0, 0.0	14.53%	R_p =17.9% R_{wp} =17.6% R_{exp} =14.93% x^2 = 1.23
				Ca	0.0, 0.0, 0.0		
				Ti	0.5, 0.0, 0.518		
				Hf	0.5, 0.0, 0.518		
				O1	0.0, 0.0, 0.496		
				O2	0.5, 0.266, 0.207		
R3m (H)	4.6657	4.6657	6.9334	Ba	0.0, 0.0, 0.0	9.79%	
				Ca	0.0, 0.0, 0.0		
				Ti	0.5, 0.0, 0.479		
				Hf	0.5, 0.0, 0.479		
				O	0.124, 0.351, 0.397		
P4mm	4.0450	4.0450	4.0211	Ba	0.0, 0.0, 0.0	74.68%	
				Ca	0.0, 0.0, 0.0		
				Ti	0.5, 0.5, 0.482		
				Hf	0.5, 0.5, 0.482		
				O1	0.5, 0.5, 0.016		
				O2	0.5, 0.0, 0.465		

4.3.1.2 Morphological characterizations

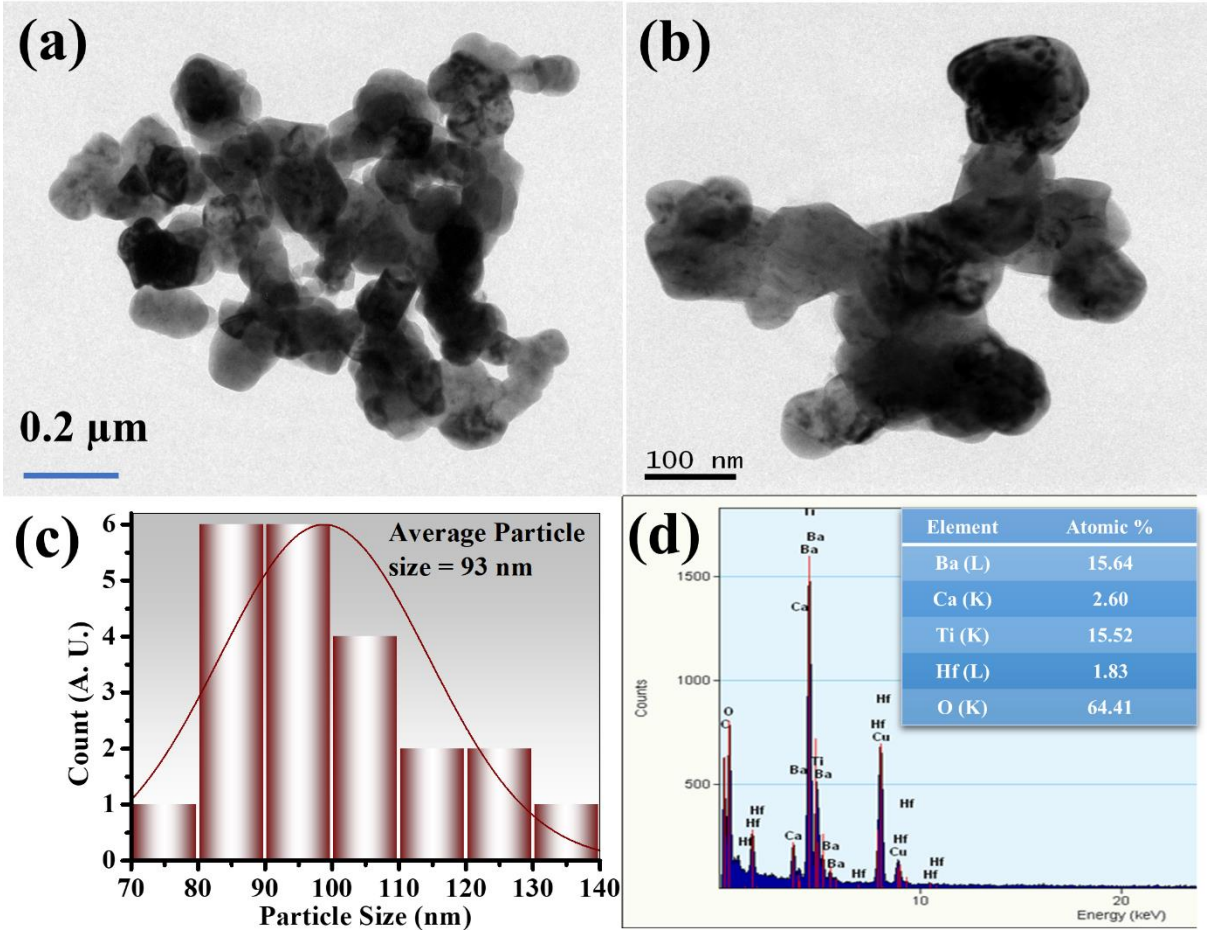

Fig. 4.2*(a,b) TEM micrograph of BCHT particles (c) the particle size variation histogram, (d) EDX spectra and quantitative elemental composition of BCHT.*

Transmission Electron Microscopy (TEM) bright field images of the BCHT particles are presented in Fig. 4.2(a,b). The TEM image in Fig. 4.2(a) reveals the irregularly shaped synthesized BSHT particles. The size distribution curve of these synthesized BCHT particles Fig. 4.2(c) illustrates that their size ranges from 70 nm to 140 nm, with an average size of approximately 93 nm. To perform an elemental composition analysis, Energy Dispersive X-ray (EDAX) was carried out, as shown in Fig. 4.2(d), confirming the presence of Ba, Ca, Ti, Hf, and O in the synthesized BCHT particles. The inset of Fig. 4.2(d) provides the localized quantitative elemental percentages (from the EDAX analysis) of Ba, Ca, Ti, Hf, and O in the as-synthesized BCHT.

4.3.1.3 Electrical characterizations

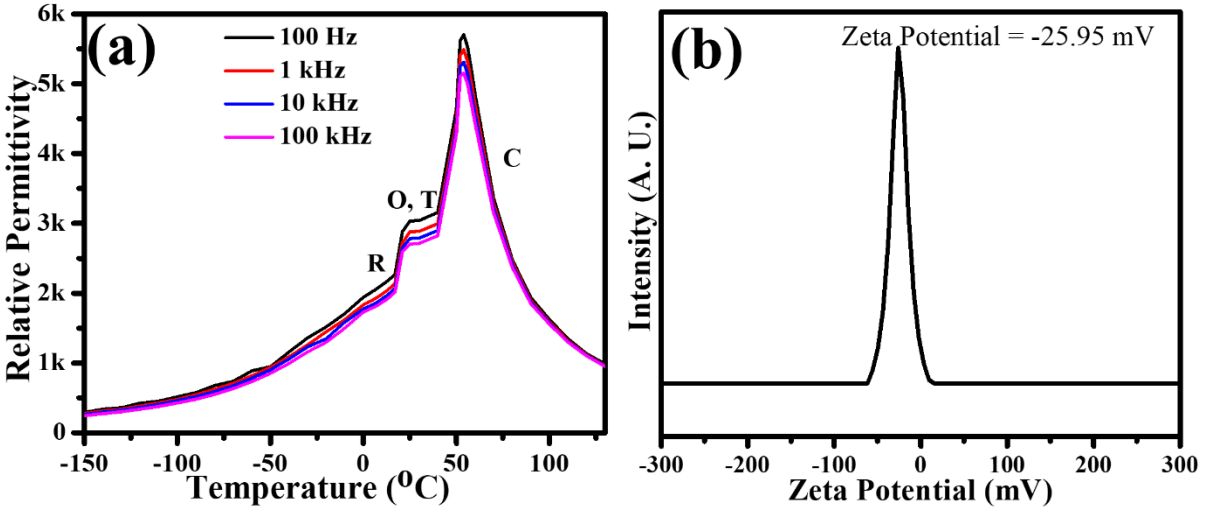

Fig. 4.3*(a) Temperature-dependent dielectric property (relative permittivity vs temperature) of the BCHT pellet, (b) Zeta potential of BCHT particles.*

To validate the formation of a morphotropic phase boundary in the prepared BCHT particles, dielectric analyses were also conducted. To further confirm the presence of these three coexisting phases, temperature-dependent relative permittivity of the BCHT particles was carried out. Figure 4.3(a) shows the variation in relative permittivity of the BCHT pellet across a temperature range spanning from -150°C to 130°C [5,6]. It is well-established that $BaTiO_3$ undergoes three distinct phase transitions as temperature changes. Typically, R-O phase transition of $BaTiO_3$ takes place at approximately -90°C to an O phase, which in turn stabilizes into a T phase at around 5°C. Subsequently, the ferroelectric T phase transforms into a paraelectric Cubic (C) phase at a temperature of approximately 120°C [8]. However, here, the introduction of both Ca^{2+} and Hf^{4+} ions has altered the phase transition behavior of $BaTiO_3$. The presence of a dielectric anomaly (as depicted in Fig. 4.3(a)) around 55°C corresponds to the transition from the ferroelectric (T) phase to the Cubic (C) phase. Furthermore, the appearance of a peak at approximately 25°C in the dielectric permittivity-temperature curve serves as conclusive evidence of the coexistence of multiple phases, namely the R-O/O-T phases. These findings align with results reported by other researchers for this specific BCHT composition [4,9]. The coexistence of multiple phases in the BCHT filler effectively reduces the inherent energy barrier. Consequently, the dipoles within the sample increased freedom of

movement for polarization rotation when subjected to mechanical forces such as pressure. Therefore, the significantly high d_{33} value observed in the synthesized BCHT particles can be attributed to the R-O/O-T phase transition. Now, the zeta potential of a material plays a key role in gaining knowledge about the interaction between the material and its polymer matrix. So, for better understanding and to get details about the surface charge of the particles we have examined the zeta potential study. Fig. 4.3 (b) shows that, BCHT particles have a negative surface charge with a value of -24.95 mV. How this negative surface charge can be corroborated to the enhanced interaction between polymer and BCHT is depicted in the next section.

4.3.2 Characterization of BCHT/PVDF composite films

4.3.2.1 Structural characterizations

X-ray Diffraction (XRD) plays a pivotal role in identifying the presence of various crystalline phases in PVDF-based films. Fig. 4(a) illustrates the room temperature XRD patterns for both bare PVDF and BCHT/PVDF composite films, covering a Bragg Angle (2θ) range from 15° to 30°. In the XRD patterns of the bare PVDF film, four distinct peaks are evident at 17.7°, 18.3°, 19.9°, and 26.54°, corresponding to the (100), (020), (110), and (021) diffraction planes of the non-polar α phase of PVDF [10]. As BCHT particles are progressively incorporated into PVDF, the relative intensity of the peaks centered at 17.7°, 18.3°, and 26.54° (associated with the non-polar α phase of PVDF) gradually diminishes. A closer examination of the XRD patterns of the composite reveals a notable shift of the peak originally positioned at 19.91° to a new location at 20.23°, corresponding to the electroactive β phase (110)(200). This shift clearly confirms that the inclusion of BCHT within PVDF has facilitated the transition from the non-polar α phase to the polar β phase [10]. The presence of the peak at a Bragg angle of 22.21° in all the composite films confirms the successful integration of BCHT filler into the PVDF matrix. Consequently, the XRD results provide compelling evidence for the successful conversion of the non-polar α phase to the polar β phase of PVDF through the incorporation of filler particles.

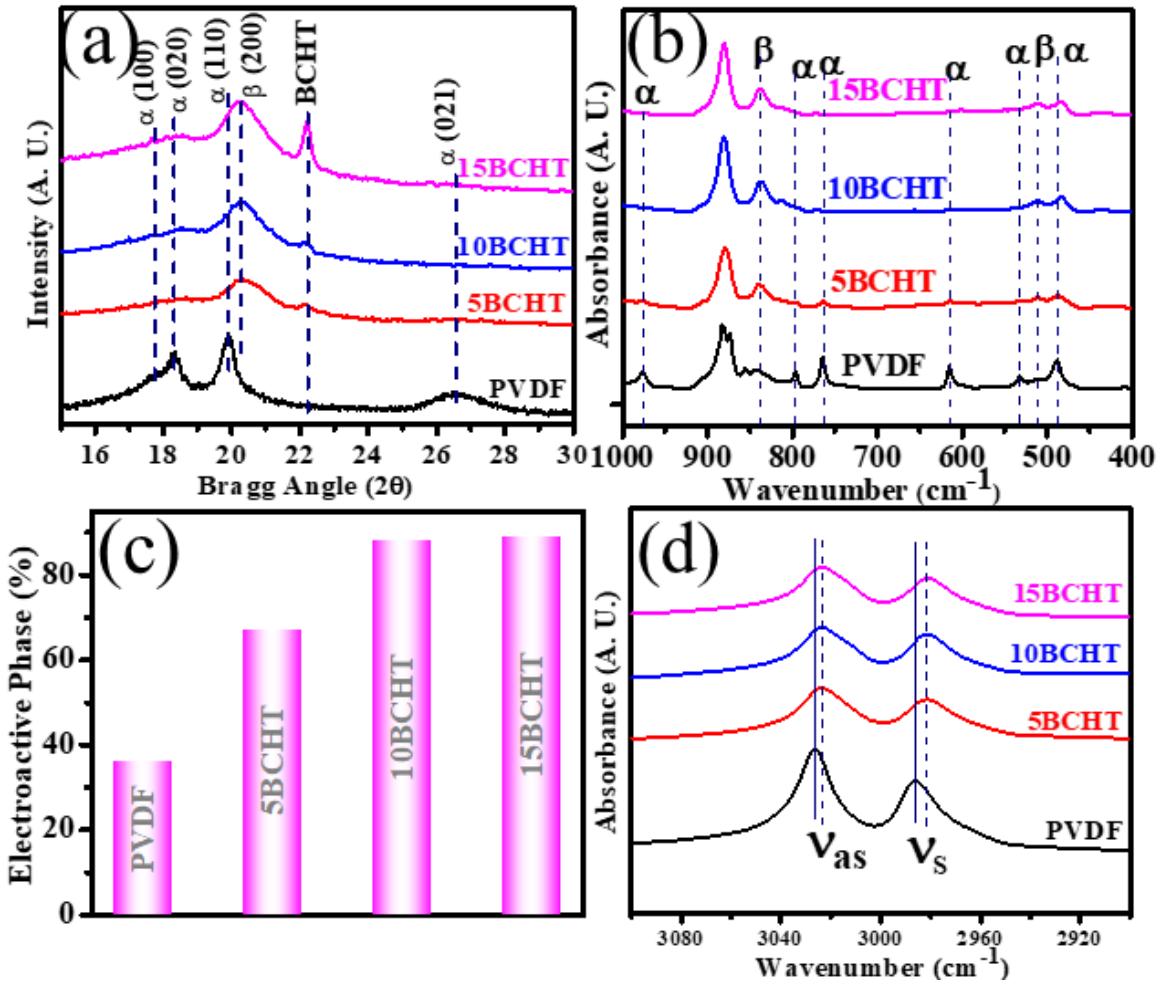

Fig. 4.4*(a) XRD pattern of neat PVDF and BCHT loaded PVDF composites (5 wt%, 10 wt%, 15 wt%) (b) FTIR spectra for neat PVDF and BCHT loaded PVDF composites (5 wt%, 10 wt%, 15 wt%) in the range 400 cm⁻¹ to 1000 cm⁻¹ (c) Variation of electroactive β phase fraction with filler percentage (d) FTIR spectra for neat PVDF and BCHT loaded PVDF composites (5 wt%, 10 wt%, 15 wt%) in the range 3100 cm⁻¹ to 2900 cm⁻¹.*

To further confirm the transformation of PVDF's non-polar α phase into the polar β phase, as evidenced by the XRD patterns, Fourier Transform Infrared Spectroscopy (FTIR) was performed. FTIR is a highly effective method for quantifying the phase fractions in PVDF before and after the incorporation of BCHT fillers. By analyzing the IR active vibrational bands in bare PVDF and BCHT/PVDF films, we gain valuable insights into the interaction between the filler and the polymer matrix. The corresponding Infrared Spectroscopy plots of the composite films within a selected wavenumber range of 1000 cm^{-1} to 400 cm^{-1} are depicted in Fig. 4.4(b). In the absorbance spectrum of PVDF, we observe prominent absorbance bands centered at 487, 532, 613, 764, 796, and 976 cm^{-1}, which are characteristic of the stable α phase. Additionally, two bands associated with the β phase of PVDF are also present,

positioned at 510 and 840 cm^{-1} with comparatively lower intensity [10,11]. Typically, when PVDF is crystallized from a solution casting process, it predominantly crystallizes in the α phase due to its TGTG' conformation, which possesses minimal free energy [12]. Upon closer examination of the FTIR spectra of composite films, we observe that the relative intensity of the peaks associated with the α phase has either completely diminished or significantly weakened. In contrast, the relative intensity of the peaks corresponding to the preferred β phase has increased. This observation clearly indicates that BCHT particles functioned as local nucleating agents and successfully facilitated the transformation of the α phase into the β phase of PVDF.

Variation of electroactive β phase fraction in bare PVDF, as well as BCHT/PVDF composite films as a function of filler weight percentage, is shown in Fig. 4.4(c). The quantitative determination of the polar β phase fraction was carried out using Lambert Beer's law, as expressed by the following equation [1]:

$$F(\beta) = \frac{A_{840}}{\frac{k_{840}}{k_{764}}A_{764}+A_{840}} X\ 100\% \qquad (4.1)$$

- F(β) represents the percentage of the β phase.
- A_{840} and A_{764} are the intensity values in arbitrary units obtained from the absorbance spectra at wavenumber values of 840 cm^{-1} and 764 cm^{-1}, respectively.
- k_{840} and k_{764} are the absorbance coefficients corresponding to their respective wavenumbers, with values of 7.7 x 10^4 cm^2 mol^{-1} and 6.1 x 10^4 cm^2 mol^{-1}, respectively.

Notably, a loading of 5 wt% BCHT in PVDF (~66%) is shown to nearly double the β phase fraction compared to pure PVDF (~36%). The continuous incorporation of the filler within the PVDF matrix further enhances the β phase fraction, with a peak value of approximately 89% achieved for 15BCHT. This high electroactive phase fraction is attributed to the uniform distribution of BCHT particles within the PVDF matrix, as evident from the FESEM image of the 15BCHT [11]. The negative surface potential of BCHT, as seen in the zeta potential curve (Fig. 4.3(b)), facilitates interaction between BCHT particles and the positive -CH_2 dipole of PVDF. This interaction results in the alignment of PVDF chains in the all-trans (TTTT) conformation [13,14]. This interfacial interaction between the filler and the polymer matrix enhances the β phase percentage in the composite films, subsequently boosting their electron transfer capability [11,15]. Confirmation of the interfacial interaction between the positive -CH_2 dipole of PVDF and BCHT particles is further evident in the absorbance spectra of the

composites within the wavenumber range of 3100 cm^{-1} to 2900 cm^{-1}. This range is significant because it only contains characteristic bands related to the -CH_2 stretching vibration of PVDF films, which play a pivotal role in probing interfacial interactions. Specifically, absorbance bands at approximately 3026 cm^{-1} and 2985 cm^{-1} correspond to the asymmetric and symmetric stretching vibrations of the -CH_2 band of PVDF [11,16]. In Fig. 4.4(d), the absorbance spectra of the BCHT/PVDF composite films in this wavenumber range are displayed. Remarkably, the IR spectra in the aforementioned range (Fig. 4.4(d)) reveal a gradual shift of absorbance bands toward lower wavenumber values with increasing BCHT loading. This band shifting towards lower wavenumber values can be attributed to the increased effective mass of the -CH_2 dipole due to its interaction with the negative surface of BCHT [13,14,17].

4.3.2.2 Morphological characterizations

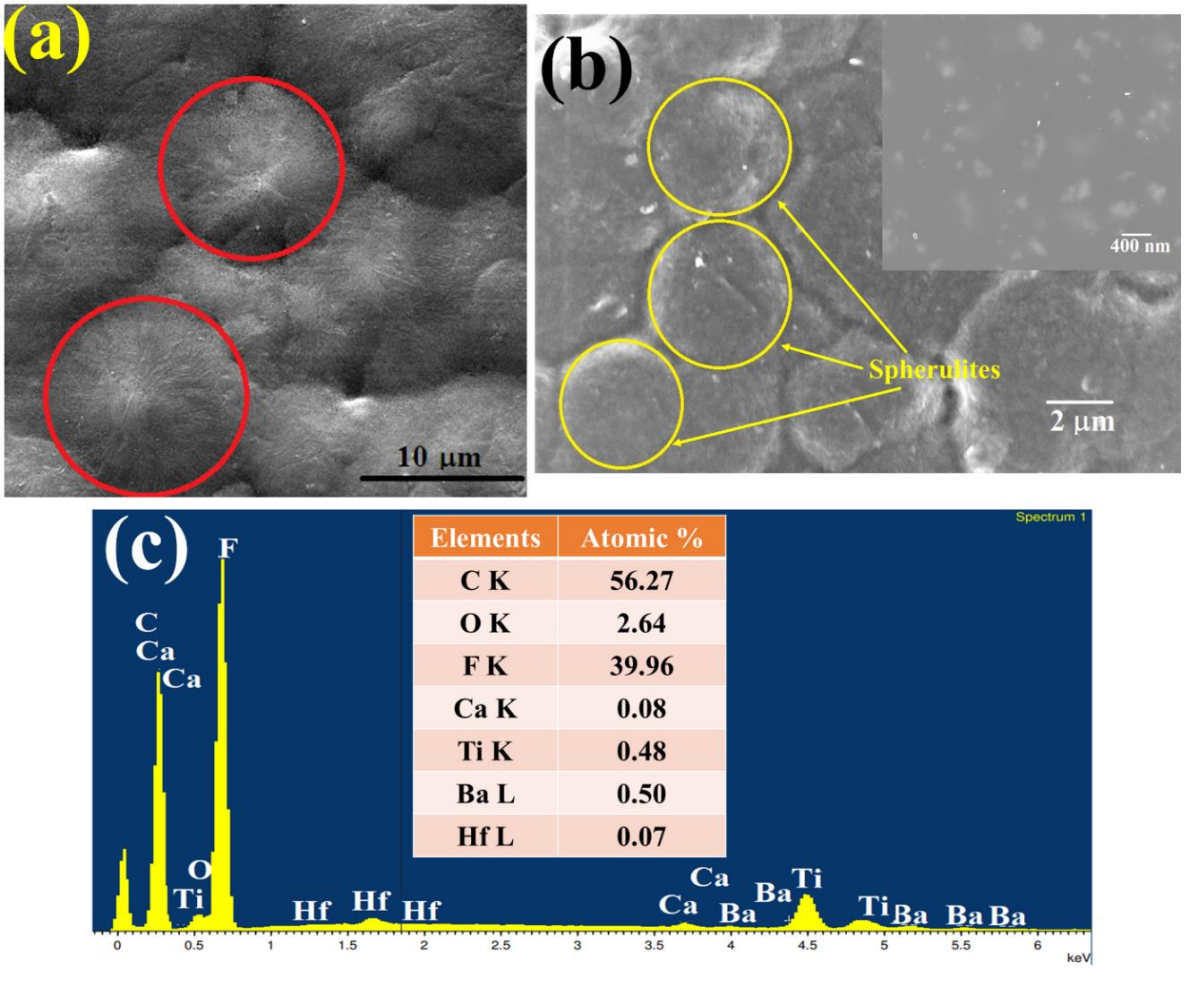

Elements	Atomic %
C K	56.27
O K	2.64
F K	39.96
Ca K	0.08
Ti K	0.48
Ba L	0.50
Hf L	0.07

Fig. 4.5*(a) FESEM image of pure PVDF film, (b) FESEM image of 15BCHT showing the uniform distribution of spherulites, inset shows the presence of BCHT in PVDF matrix (c) EDAX spectrum of 15BCHT composite with the elemental atomic weight percentage.*

The effectiveness of the interaction between the filler and the PVDF matrix is supported by reduction in the size of the spherulites (highlighted in yellow and approximately 4 μm in size in Fig. 4(b)) in comparison to pure PVDF (~10 μm, as shown in Fig. 4.5(a)) [11]. This reduction in spherulite size is a critical parameter for enhancing the performance of the hybrid device. The uniform distribution of spherulites across the entire surface of the composite material, as depicted in Fig. 4.5(b) additionally establishes improved interaction. This consistent distribution of spherulites can be attributed to the even dispersion of the filler particles within the polymer matrix. Furthermore, the FESEM image of the 15BCHT composite reveals a compact surface without any noticeable cracks. A closer examination of the inset in Fig. 4.5(b) clearly shows the presence of BCHT particles within the polymer matrix. To further confirm the successful incorporation of BCHT particles into the PVDF matrix, an elemental analysis of the 15BCHT composite was conducted through EDAX analysis, as illustrated in Fig. 4.5(c). This analysis provides additional evidence of the effective inclusion of BCHT particles in the PVDF matrix. The uniform distribution of fillers within the polymer matrix offers several advantages in enhancing the physicochemical properties of the composite material.

4.3.2.3 Electrical characterizations

The charge storage capacity of the functional layer used in constructing the hybrid energy harvester (HEH) device is a critical factor influencing the device's output performance [18,19]. To assess this, we conducted measurements of the relative permittivity (ϵ_r) of the BCHT/PVDF composite films across a frequency range spanning from 100 Hz to 1 MHz, all at room temperature (30°C). The results are presented graphically in Fig. 4.6(a). Notably, the considerable difference in dielectric constant between the base PVDF matrix and the filler material leads to substantial changes in the relative permittivity of the composite system. As evident from Fig. 4.6(a), there is a clear trend of increasing relative permittivity with a higher loading of the filler material in the PVDF matrix. Remarkably, these elevated dielectric constant values in the composite films remain consistent across the entire frequency range, spanning from 100 Hz to 1 MHz. The enhancement in dielectric permittivity can be understood through the microcapacitor model. According to this model, the inclusion

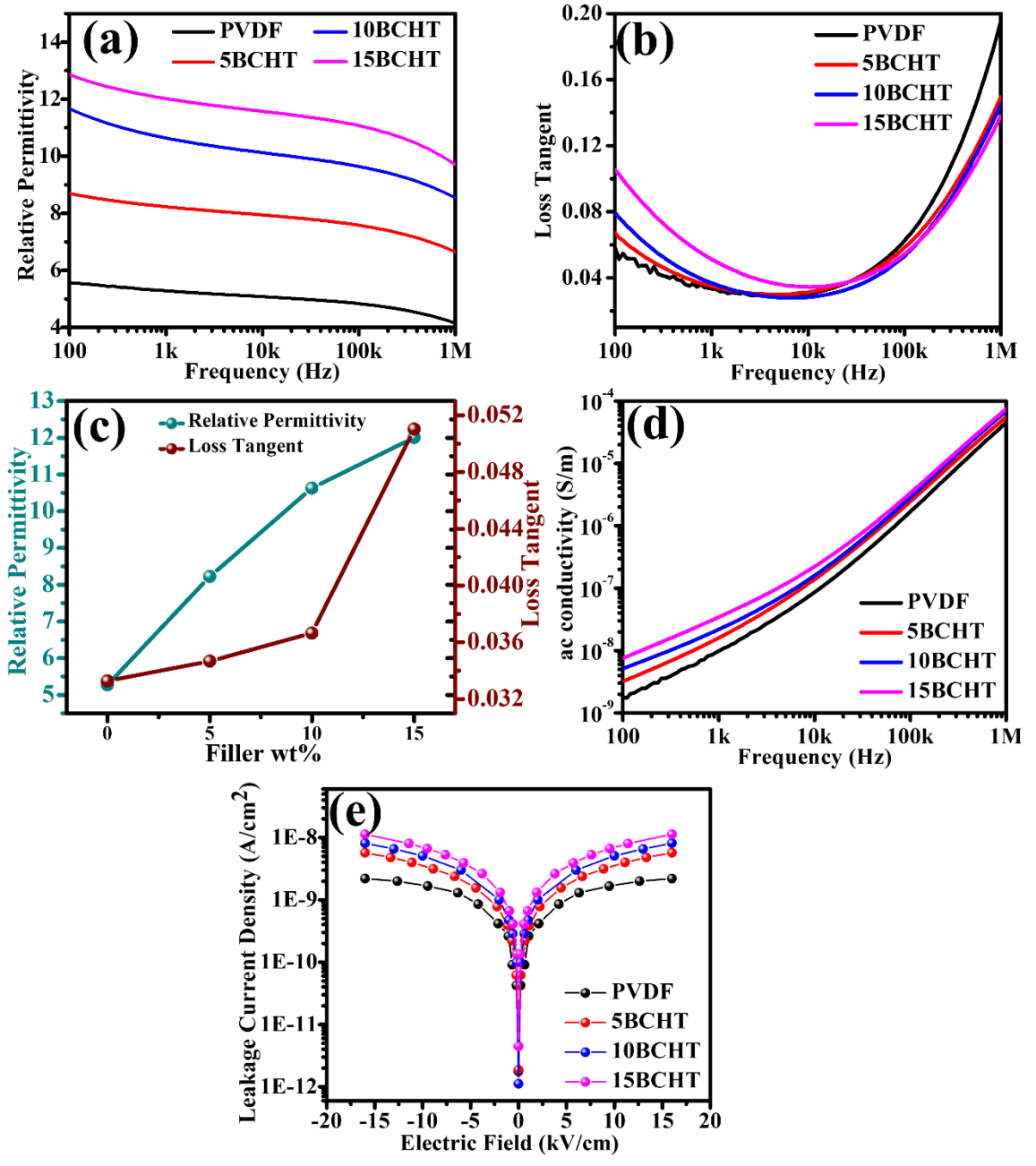

Fig. 4.6*(a) Variation of dielectric permittivity with frequency (100 Hz to 1 MHz) for neat PVDF, BCHT loaded PVDF composites (5 wt%, 10 wt%, 15 wt%). (b) Variation of tangent loss (tanδ) with frequency (100 Hz to 1 MHz) for neat PVDF, BCHT loaded PVDF composites (5 wt%, 10 wt%, 15 wt%). (c) Variation of relative permittivity and loss tangent of PVDF composite with filler wt% variation (d) Variation of ac conductivity with frequency (100 Hz to 1 MHz) for neat PVDF, BCHT loaded PVDF composites (5 wt%, 10 wt%, 15 wt%) (e) Variation of leakage current density with applied electric field (-16 kV/cm to 16 kV/cm) for neat PVDF, BCHT loaded PVDF composites (5 wt%, 10 wt%, 15 wt%).*

of ceramic particles in the PVDF matrix results in the creation of an insulating layer situated between two adjacent ceramic particles, effectively forming a configuration resembling a capacitor. As the concentration of BCHT fillers increases, these

capacitors establish parallel connections, thereby collectively amplifying the relative permittivity of the BCHT/PVDF composites [16]. Furthermore, following Lewi's model, when a particle is introduced into a polymer matrix, a layer of charges with an opposite polarity form on the surface of the particle, driven by differences in work function [20]. In addition to this, Coulombic interactions lead to the alignment of charges in the remaining areas of the polymer, forming what is referred to as the diffusion layer [21,22]. These charge-related mechanisms collectively contribute to the overall augmentation of dielectric properties observed in the composite materials. The incorporation of ceramics into the PVDF polymer leads to the alignment of charges within the material, resulting in an increase in the relative permittivity of the composite films. Upon closer examination of Fig. 4.6(a), it is evident that there is a slight decline in relative permittivity in the higher frequency region. This behavior can be attributed to the presence of space charge polarization at lower frequencies, which contributes to the high relative permittivity observed in this region. Conversely, in the higher frequency range, the dipoles in the material do not have enough time to align themselves with the applied electric field, leading to a reduction in relative permittivity [13,16]. It is noteworthy to mention that, the increased incorporation of filler particles creates discrete conductive pathways within the material, diminishing its insulating properties. Consequently, the composite begins to show degradation in its ability to retain stored charges and starts to exhibit a leaky nature. To address this limitation in charge retention, we measured the dielectric loss tangents (tanδ) for both pure PVDF and BCHT/PVDF composites as a function of frequency, as depicted in Fig. 4.6(b). The tanδ values increase with higher loading of BCHT particles, particularly in the low applied electric field region. This increase is attributed to the presence of high space charge polarization in this region [16,23]. However, in the high applied electric field region, the dipoles within the material do not have sufficient time to align themselves with the applied electric field, resulting in polarization loss and a subsequent increase in tanδ [24]. Notably, the 15BCHT composite exhibits the highest relative permittivity (ϵ_r) at approximately 12.01 at 1 kHz, which is more than twice the value obtained for pure PVDF (approximately 4.27 at 1 kHz). However, there is a slight increase in tanδ, from 0.03 for bare PVDF to 0.05 for the 15BCHT composite. Importantly, this slight

increase in tanδ remains within acceptable limits [17]. Fig. 4.6(c) displays the variation of ϵ_r and tanδ with filler percentage at room temperature (at 1 kHz).

The assessment of conducting pathways formation within PVDF due to the incorporation of BCHT fillers can be examined through AC conductivity measurements. AC conductivity was calculated using the following equation

$$\sigma_{ac} = 2\pi f . \epsilon_0 . \epsilon_r . \tan\delta \qquad (4.2)$$

Where all the notations denote their usual meaning [25].

In Fig. 4.6(d), the AC conductivity results for the composite films are presented, covering a broad frequency range from 100 Hz to 1 MHz. The figure clearly illustrates that the introduction of BCHT particles into the base PVDF matrix leads to an enhancement in AC conductivity across the entire frequency spectrum (100 Hz – 1 MHz). As the concentration of fillers increased, discrete electron pathways are formed within PVDF, resulting in the augmentation of AC conductivity [26]. This phenomenon allows some stored charges to bypass the material, contributing to leakage current, which is subsequently absorbed by the composite material [13,16]. To validate the points discussed above, we measured the leakage current density of the prepared composite films as a function of electric field strength at room temperature (30°C), as shown in Fig. 4.6(e). Fig. 4.6(e) indicate that the gradual increase in filler loading within PVDF leads to a corresponding increase in the leakage current density. At an applied electric field of 16 kV/cm, the 15BCHT/PVDF film exhibited a leakage current density of approximately 1.12 x 10^{-8} A/cm², while pure PVDF displayed a value of around 2.18 x 10^{-9} A/cm². This observed rise in leakage current density serves as strong confirmation that the incorporation of fillers within the polymer matrix indeed results in the formation of discrete conducting pathways [13,16,26]. Taking all the aforementioned factors into account, it can be confidently concluded that the 15BCHT composite, characterized by a high electroactive phase content (89%), relative permittivity of approximately 12.01, a relatively low loss tangent (0.05), and a manageable leakage current density, is a highly promising candidate for the final assembly of the hybrid energy harvesting device.

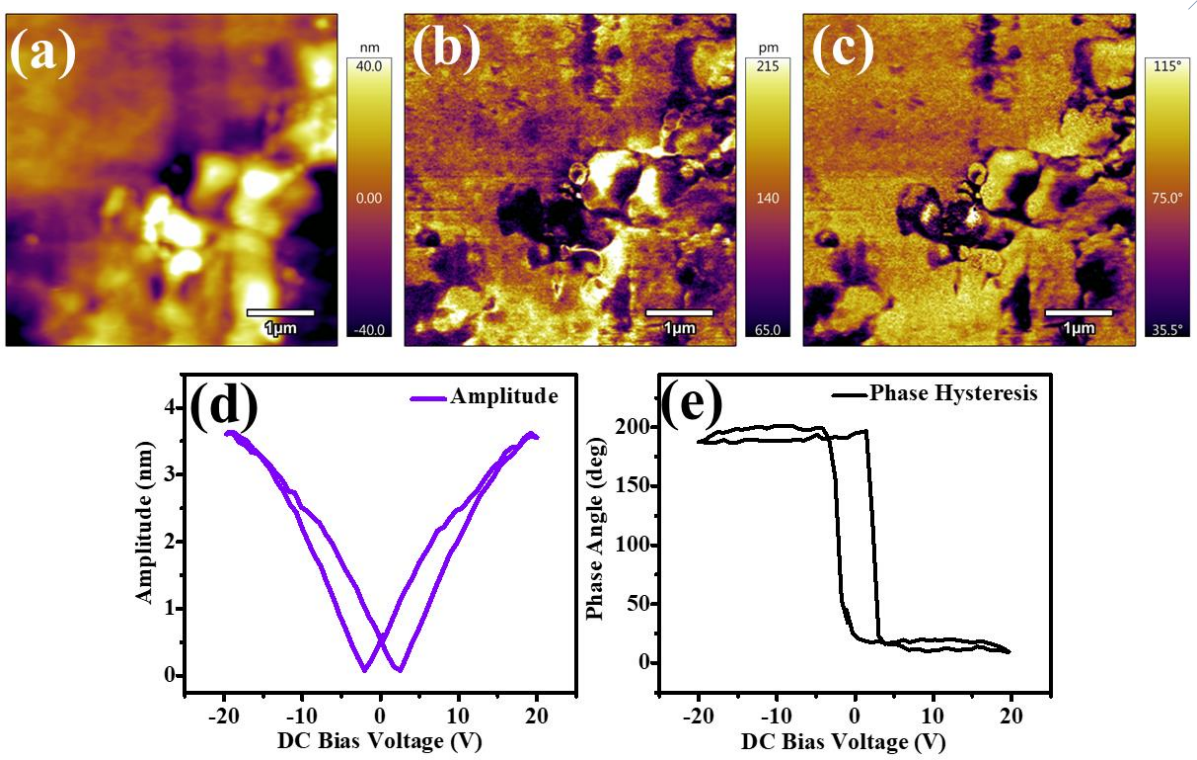

Fig. 4.7*(a-c) PFM topography, amplitude, and phase digital images; (d) amplitude response and (e) phase hysteresis with applied dc bias voltage from -20 V to 20 V.*

In our pursuit to create a high-performance hybrid energy harvester device that combines piezoelectric and triboelectric properties, it is imperative to confirm the piezoelectric characteristics of the composite film used as the device's functional layer. For this purpose, we turned to Piezoresponse Force Microscopy (PFM), widely regarded as the most suitable method for assessing the piezoelectricity of composite films [27,28]. As the 15BCHT composite emerged as the prime candidate for the final hybrid energy harvester (HEH), we conducted PFM analysis specifically on this composite. In the PFM analysis, we applied a direct current (dc) bias voltage spanning from -20 V to 20 V to the composite in order to determine its polarization switching angle. Fig. 4.7(a-c) showcases the topography image, amplitude behavior, and hysteresis phase response of the composite, captured within a 5 x 5 μm^2 area. The clear variation in color contrast observed in the amplitude image (Fig. 4.7(b)) provides compelling evidence of the piezoelectric nature inherent in the 15BCHT film [28,29]. Furthermore, the presence of contrasting spots in the phase hysteresis image (Fig. 4.7(c)), featuring both bright and dark areas, confirms the ferroelectric characteristics of the film. These contrasts can be attributed to the presence of distinct polarized

domains within the composite [28–30]. The amplitude variation of the piezoresponse signal, which was extracted from the PFM measurements and recorded across the applied DC bias voltage range (-20 V to 20 V), exhibits a butterfly loop pattern (Fig. 4.7(d)). This distinct butterfly loop is a hallmark of strong piezoelectric properties and signifies the material's response to a periodic external electric field. The name "butterfly loop" derives from its shape, which resembles the unfolded wings of a butterfly [31]. Additionally, as depicted in Fig. 4.7(e), the 15BCHT film demonstrates a hysteresis loop with a phase difference of approximately 180°, providing further confirmation of the film's ferroelectric nature [13]. These enhanced piezoelectric properties observed in the composite can be ascribed to the presence of a substantial electroactive β phase fraction in PVDF, an effect induced by the inclusion of BCHT fillers.

4.3.3 Energy harvesting performance of HEH

At first, confirmation of the piezoelectricity enhancement through BCHT loading was confirmed by piezoelectric energy harvesting characteristics under a uniform force applying setup of force 5 N at a rate of 2 Hz. With the increasing filler loading piezoelectric voltage got increased and we got a maximum voltage (~6.5 V) for 15BCHT film (Fig. 4.8(a)). As a biomechanical energy source, we have also applied finger imparting upon the device. On the application of finger flapping (force ~ 100 N and frequency ~4 Hz), the PEH device where 15BCHT film was utilized, generated the maximum peak to peak output voltage of 40 V ± 2 V (Fig. 4.8(b)). As indicated by both the XRD analysis (Fig. 4.4(a)) and FTIR analysis (Fig. 4.4(b)) of the composite films, it becomes evident that an increase in the filler loading percentage has the effect of augmenting the interactions occurring at the interface between the filler and the polymer matrix. This, in turn, leads to the alignment of a greater number of Polyvinylidene Fluoride (PVDF) chains in an all-trans conformation (TTT). Consequently, there is an enhancement in the polar β phase fraction within the composite, resulting in a higher number of dipoles being generated. Additionally, the exceptional piezoelectric property of the filler also plays a role in contributing to the improvement of the piezoelectric output performance of the devices.

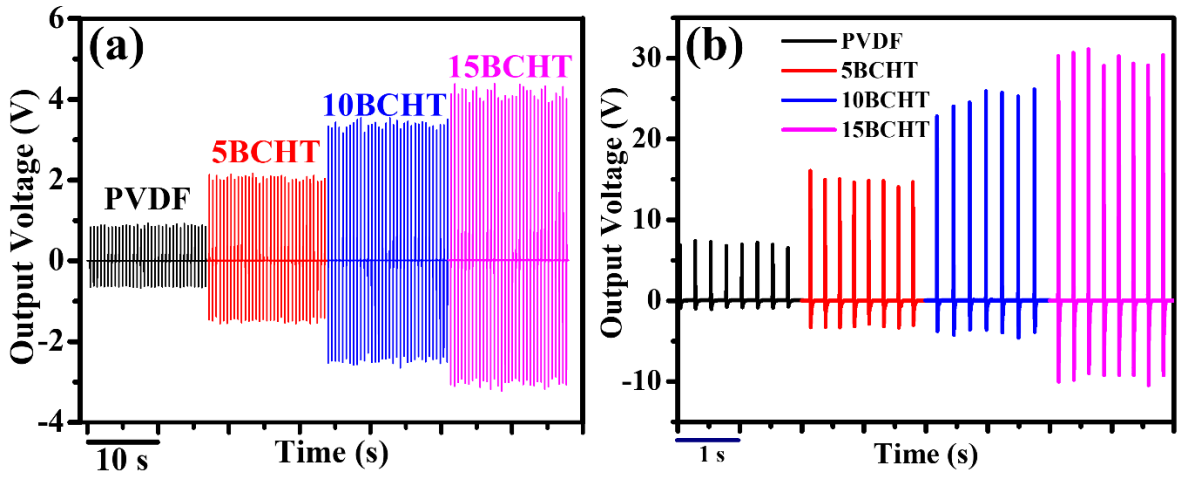

Fig. 4.8 *Generated output voltage patterns from PEH devices (a) using constant force application setup (5 N, 2 Hz), (b) using finger imparting (100 N, 4 Hz).*

Therefore, from the previous results we can validate that the optimization of the composite layer in the HEH device plays a pivotal role in acquiring in-depth insights into its energy harvesting performance. To get the most favorable composite film as far as energy harvesting is concerned, the filler loading percentage inside PVDF was varied from 5 wt% to 15 wt%. As the main objective of our work here is to efficiently harvest mechanical energy using a flexible hybrid energy harvester device, the flexibility of the device plays a major significance. In this regard, the composite film should also be flexible. That is why we have limited the filler loading inside PVDF up to 15 wt%. Beyond that, the films got wavy and were not straight for application purposes.

Now, to evaluate the electromechanical conversion capabilities, HEH devices with varying filler concentrations were fabricated. All the devices were applied by the same mechanical stress with the help of a constant force-applying setup (shown in Fig. 4.9(a)) of force ~ 5 N and frequency of ~ 2 Hz. From Fig. 4.9(b) we can confirm that the generated peak to peak output voltage reached a maximum value of ~60 V for the HEH device consisting of the 15BCHT film from a value of ~20 V for that of the bare PVDF-based energy harvester.

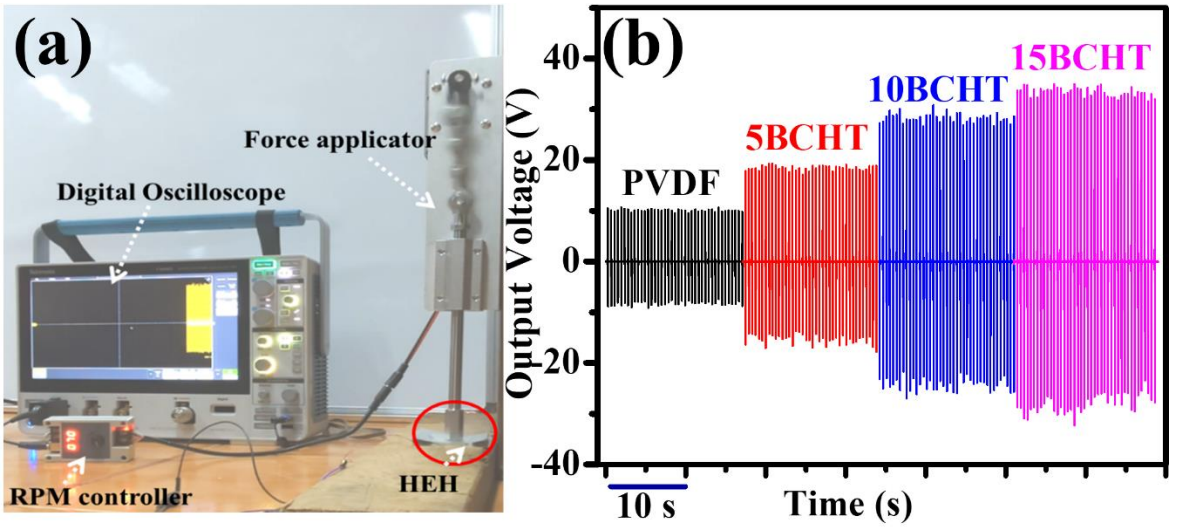

Fig. 4.9*(a) Constant force applying setup, (b) output voltage patterns on the application of a force ~ 5 N at a rate of ~2 Hz.*

Figure 4.10(a) and Figure 4.10(b) clearly exhibit a significant improvement in output performance for HEH5 when compared to a device made solely with PVDF. However, as the filler concentration increased, there was a continuous improvement in both output voltage and current. HEH15, as depicted in Figure 4.10(a) and Figure 4.10(b), could generate the highest peak-to-peak output voltage and current. The measured values for output voltage and current were 396 V ± 10 V and 30 µA ± 2 µA, respectively. Upon closer examination of Figure 4.10(a) and Figure 4.10(b), it is evident that there are two peaks in voltage and current on both the positive and negative sides, corresponding to the compression and release phases of the device. Based on these results, it can be concluded that the device with 15BCHT as the functional layer exhibited the best output performance. The output of the HEH was a result of a synergetic effect between the piezoelectric and triboelectric phenomena occurring inside the device during each cycle of pressure application [32,33]. Therefore, to gain a deeper understanding of the output performance of HEH15, it was essential to investigate the output performance of the 15BCHT-based piezoelectric device (PEH15, which exhibited the best piezoelectric output performance among the options, as shown in Figure 4.8) and the triboelectric energy harvester (TEH). To visually compare the outputs obtained from HEH15, PEH15, and TEH, the output voltage and current from these devices are presented in Figure 4.10(c) and Figure 4.10(d). Both figures (Figure 4.10(c) and Figure 4.10(d)) clearly demonstrate that the output performance of HEH15 surpasses the individual performances of PEH15 and TEH, providing further evidence of the synergistic phenomenon occurring inside HEH14.

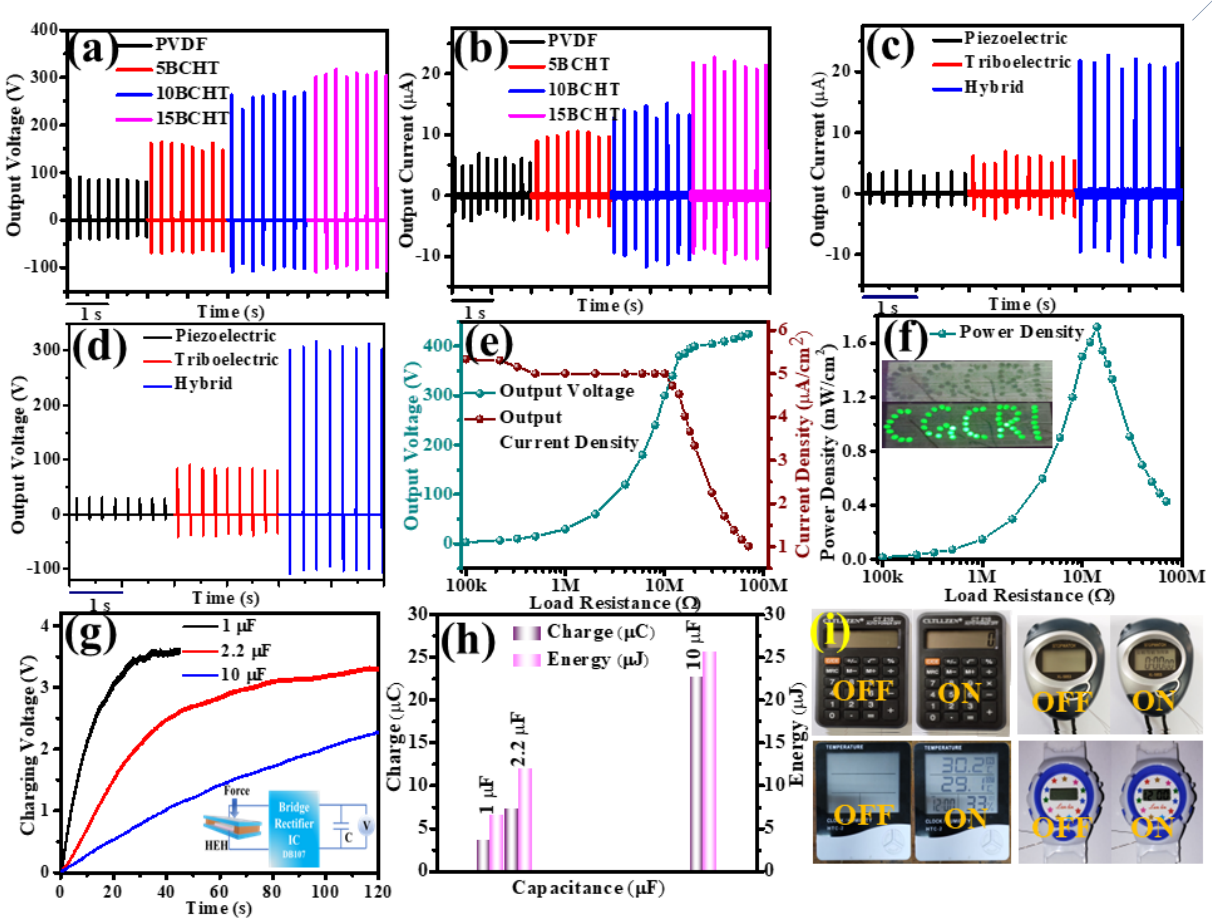

Fig. 4.10*(a) & (b) Variation of output voltage and output current generated from HEH under finger imparting with different filler concentrations. (c) & (d) Generated output voltage and current from piezoelectric, triboelectric, and hybrid energy harvesting device (e) Variation of output voltage and current density with load resistance from HEH15 (f) Variation of output power density with load resistance obtained from HEH15 under finger imparting, inset showing 52 LEDs connected in series forming 'CGCRI' glowing on each impart on the device, (g) Charging of commercial capacitors (1, 2.2 and 10 μF) by the voltage generated from HEH15 (using a bridge rectifier circuit) (h) Stored energy and charge in the commercial capacitors 1, 2.2 and 10 μF. (i) Powering up small electronic devices (electronic calculator, stopwatch, hygrometer, and digital watch) using HEH15 device. All the measurements were done by finger imparting of force ~ 100 N and frequency of ~ 4 Hz (measured by flexi force sensor).*

Moreover, the improved output performance of HEH15, as demonstrated in Figure 4.10(a) and Figure 4.10(b), can also be ascribed to the enhanced dielectric properties of the composites when BCHT is added, reaching its peak with 15BCHT (with a dielectric constant ϵ_r~ 12.01 at 1 kHz) as shown in Figure 4.6(a). This increase in dielectric properties for the 15BCHT composite, compared to the other composites, results in a greater accumulation of charges on the surface of 15BCHT. Additionally, the lower values of leakage current density (as shown in Figure 4.6(e)) and dissipation

factor for 15BCHT further confirm the excellent insulating properties of the composite, contributing to higher output performance [34]. Surface roughness is another critical factor influencing the output performance of HEH15 [35]. The enhanced triboelectrification between the positive and negative triboelectric layers of the device due to the inclusion of fillers amplifies the overall output performance of the optimized device, HEH15 [35]. It's worth noting that when external pressure is applied, the alignment of dipoles in the composite film significantly increases the presence of triboelectric charges generated by friction between the positive and negative triboelectric layers of HEH14. This accumulation of triboelectric charges further intensifies the dipolar polarization of the functional layer, leading to the buildup of more negative surface charges on the composite film's surface. Consequently, a synergistic effect between the piezoelectric and triboelectric phenomena occurs, resulting in an overall enhanced output from the HEH15 device.

The practical utility of any energy harvesting device is heavily reliant on the power output and current density it can generate. As such, we examined how the output voltage and current density (calculated by squaring the voltage and then dividing it by the load resistance, and the electrode area, $V^2/R.A$) from HEH15 varied with different load resistances, as depicted in Figure 4.10(e). In Figure 4.10(e), it's evident that the output voltage reaches its maximum at approximately 396 V and becomes nearly constant beyond a load resistance of 20 MΩ. Correspondingly, the maximum instantaneous power density (computed by multiplying voltage with current density) achieved by the device was 1.72 mW/cm^2, observed at a load resistance of 14 MΩ, as shown in Figure 4.10(f). With each application of finger flapping, the HEH15 device can generate enough power to illuminate 52 LEDs connected in series (wavelength of 515-520 nm, DC voltage of 3-3.2 V, and a current of 20 mA). This series arrangement of LEDs is designed in a 'CGCRI' pattern, as illustrated in Figure 4.10(f). When an external force is applied, the LEDs blink in synchrony. It is worth emphasizing that the maximum voltage output of HEH15 is nearly ten times higher than that of PEH15 and approximately 3.5 times higher than that of TEH. Furthermore, the generated output current by HEH15 is significantly greater than that of the respective piezoelectric and triboelectric devices approximately eight times higher than the PEH15 device and

about four times higher than the TEH device. This substantial improvement in the output performance of HEH15 compared to PEH15 and TEH can be attributed to the effective coupling of the piezoelectric and triboelectric phenomena during each operational cycle. In this context, it's worth noting that the output performance of HEH15, including voltage, current, and power density, is quite competitive when compared to recently reported PVDF-based energy harvesting devices, as highlighted in Table 4.2.

The rectified output signal generated by HEH15, using a DB107 bridge rectifier IC, was utilized to charge various commercial capacitors during hand flapping. The charging capability of HEH15 proved to be quite fast, as depicted in Figure 4.10(g). The quantity of charge and energy stored in the capacitors during charging via HEH15, with finger pressure applied, were quantified using the relationships $W=1/2\ CV^2$ and $Q=CV$. Here, W represents the energy stored, C is the capacitance of the capacitors used, V signifies the saturation voltages of the charged capacitors, and Q stands for the charge stored in the capacitors. The stored charge in 1 μF, 2.2 μF, and 10 μF capacitors was calculated to be 3.6 μC, 7.26 μC, and 22.6 μC, respectively. Simultaneously, the energy stored in these capacitors amounted to 6.48 μJ, 11.98 μJ, and 24.54 μJ, respectively, as depicted in Figure 4.10(h). Additionally, during the discharging process, these capacitors were able to power low-powered devices such as an electronic calculator, stopwatch, hygrometer, and digital watch, as demonstrated in Figure 4.10(i).

Therefore, based on the results mentioned above, it can be concluded that the output performance of the device is notably stable. However, the practical application of an energy harvesting device necessitates long-term durability, stability, and robustness. To confirm the stability of the output generated by HEH15, the device underwent a continuous operation for a large number of cycles (more than 10,000 cycles) using the systematic setup with a force of approximately 5 N and a frequency of approximately

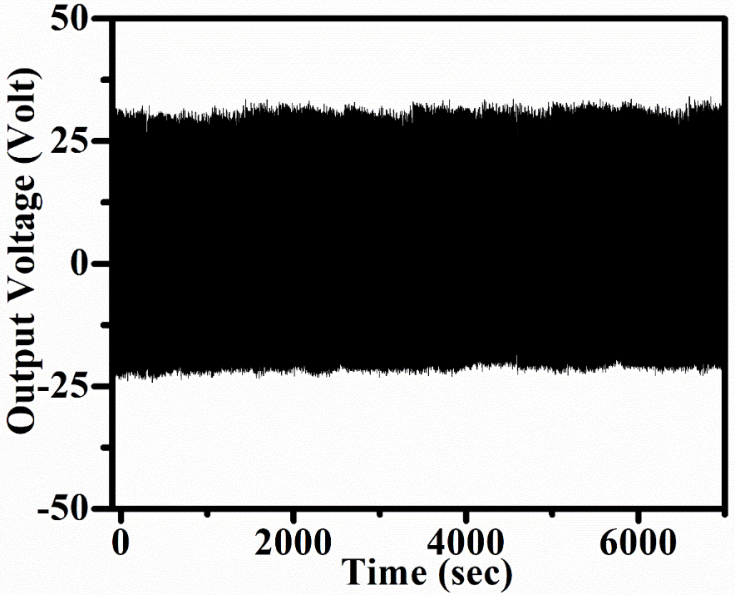

Fig. 4.11 *Output voltage obtained from HEH15 under continuous operation for more than fourteen thousand cycles.*

2 Hz, as shown in Figure 4.11. Importantly, no significant degradation of the output was observed, affirming the durability of the fabricated device. Consequently, the output performance of this sustainable HEH15 suggests that this hybrid device can be effectively utilized as a portable, next-generation green energy source.

Table 4.2 Comparison of the output performance of the fabricated HEH with the recently reported PVDF-based energy harvesters.

-ve Tribo material	+ve Tribo material	electrode	Voltage (V)	Current/Current density (I)	Power/Power density	Ref.
PVDF	Polymide 6	Cu	14.2	3.9 µA	--	[36]
poly(3-hexylthiophene) (P3HT)/PVDF-HFP	Kapton	Al	78.0	7.0 µA	0.55 mW	[37]
$CoFe_2O_4$/PVDF	ITO	ITO	17.2	2.27 µA	90.3 mW/m^2	[38]
ZnO/PVDF	PTFE	Al	78.0	0.46 µA/cm^2	24.5 µW/cm^2	[39]
KNN/MWCNT/PVDF	Cu	Cu	54.1	29.4 µA	164.74 µW/cm^2	[40]
$(Ba_{0.85}Ca_{0.15})(Zr_{0.1}Ti_{0.9})O_3$/PVDF-HFP	Silicone Rubber	Ag/Ni	34 .0	1.12 mA/m^2	161.7 mW/m^2	[33]
MXene/PVDF-TrFE	Nylon-11	Conductive Fabric	270.0	140 mA/m^2	4.02 W/m^2	[41]
$Cs_3Bi_2Br_9$/PVDF-HFP/SEBS	Al	Ag/Al	400.0	1.63 µA/cm^2	2.34 W/m^2	[42]
Nafion functionalized $BaTiO_3$/PVDF	Cu	Cu	307	1.8 µA/cm^2	1.12 mW/cm^2	[43]
$(Ba_{0.85}Ca_{0.15})(Ti_{0.90}Hf_{0.10})O_3$ (BCHT)/PVDF	Al	Al	396	5 µA/cm^2	1.72 mW/cm^2	**This Work**

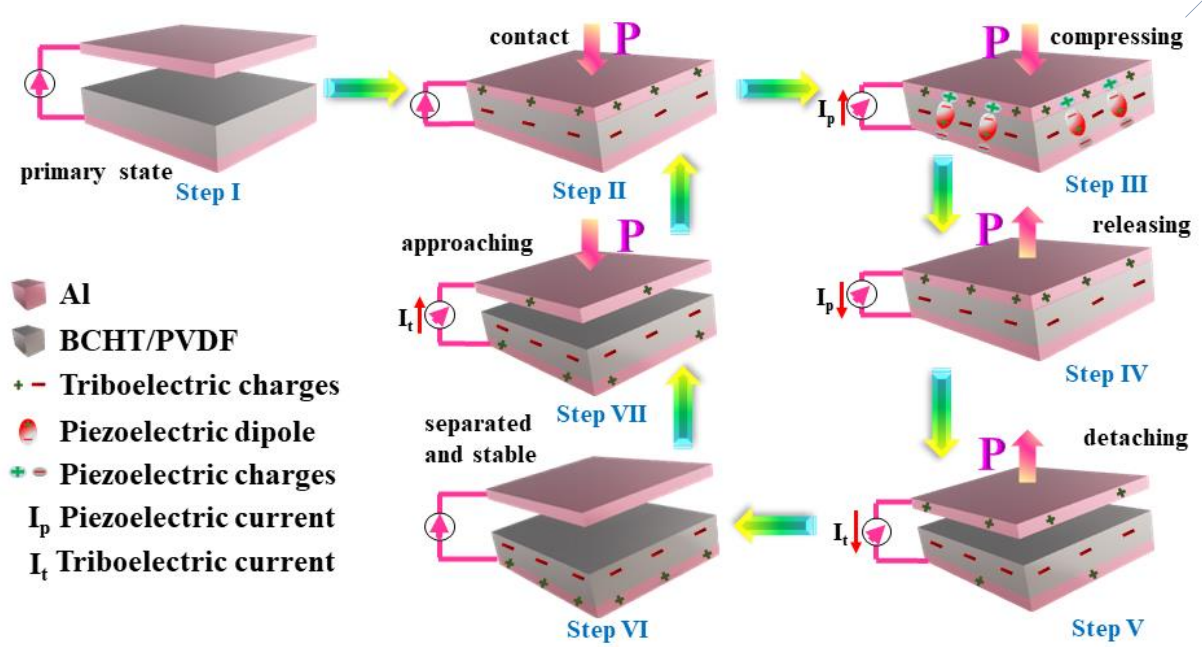

Fig. 4.12 *Schematic behind the working mechanism of the hybrid energy harvesting device.*

Now, the operational mechanism of the Hybrid Energy Harvester (HEH) based on the combined effects of piezoelectric and triboelectric phenomena in BCHT/PVDF-based composite films is schematically illustrated in Figure 4.12. In this representation, there is a separation between the BCHT/PVDF composite film and the aluminum (Al) electrode inside the device. The Al electrode, attached to the PET sheet, serves as the top layer, while the BCHT/PVDF composite/Al/PET constitutes the bottom part of the device. The Al electrode functions as the positive triboelectric layer, while the BCHT/PVDF composite serves as the negative triboelectric layer of the device. The entire mechanism can be elaborated into several steps:

Step-I: Initially, without any external pressure, there is no charge on the electrodes, resulting in zero output voltage.

Step-II: Upon the application of external pressure, both the top (PET/Al) and bottom (PET/Al/BCHT/PVDF) parts of the device come into contact, leading to the generation of equal and opposite charges depending on their respective triboelectric affinities. Following the triboelectric series, Al acquires a positive triboelectric charge, while the BCHT/PVDF composite obtains a negative triboelectric charge.

Step-III: In addition to triboelectrification, the application of external pressure causes the inherent dipoles within the composite to align themselves along the direction of pressure, inducing charges in the upper and bottom electrodes of the device due to piezoelectricity. Electrons move from the upper electrode to the lower electrode, resulting in a piezoelectric current (I_p).

Step-IV: When the applied stress is released, the pressure on the device is relieved. This leads to the reorientation of the aligned dipoles back to their original positions, generating I_p in the opposite direction.

Step-V: Further releasing the pressure causes electrons to flow from the bottom to the upper Al electrode, generating a triboelectric current (I_t) in the opposite direction.

Step-VI: The BCHT/PVDF composite layer and the upper Al electrode reach their stable positions, causing no movement of electrons.

Step-VII: Again, if we apply pressure, the equilibrium condition is disrupted, resulting in a triboelectric current in the opposite direction, from the bottom electrode to the upper electrode through the load. This completes one cycle of operation.

In this way, HEH device generates alternating output through these stages, and the periodic application and release of pressure produce an alternating output voltage that can be detected in the external load circuit. The key feature of this mechanism is the coupling of the piezoelectric and triboelectric effects, leading to the synergetic generation of output voltage in the HEH device. It is important to highlight that the alignment of dipoles in the composite film under applied pressure is significantly enhanced by the presence of triboelectric charges. This enhances dipolar polarization and leads to the accumulation of more negative surface charges on the composite film's surface, ultimately resulting in an enhanced final output voltage of the typical HEH device.

4.3.3.1. Biomechanical energy harvesting

Furthermore, HEH15 was employed to harness biomechanical energy generated by different movements of the human body, including finger movements, heel tapping,

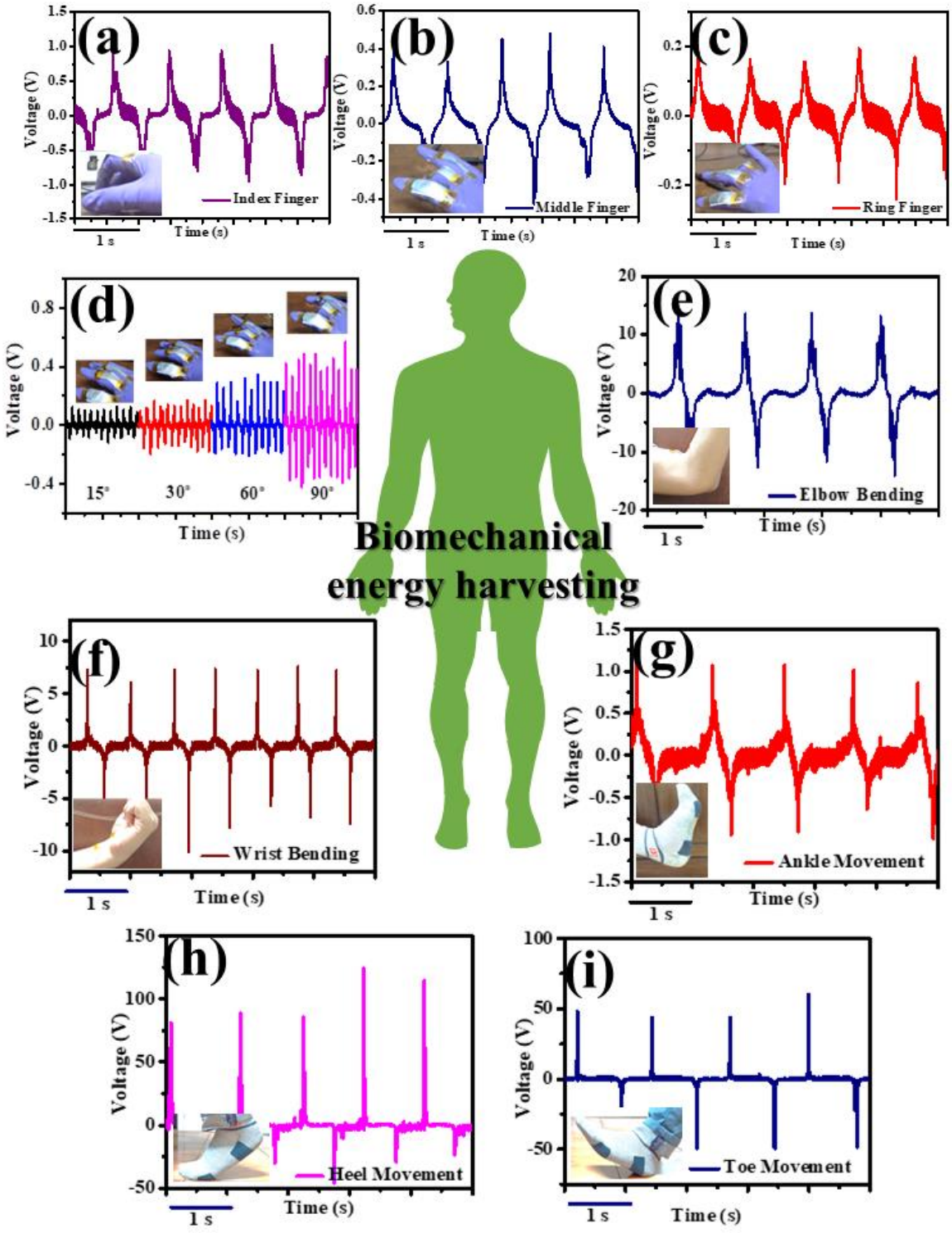

Fig. 4.13 *Output voltage generation from the movement of (a) index finger (b) middle finger (c) ring finger (d) fine movement of middle finger with varying angles (e) elbow (f) wrist (g) ankle (h) heel and (i) toe movement.*

toe movement, wrist movement, and elbow movement. To achieve this, HEH15 was attached to the respective body parts using double-sided adhesive tapes. The resulting output voltage generated from these diverse body movements is visually represented in Figure 4.13. An intriguing observation is that the fabricated HEH15 possesses the capability to capture energy not only from the subtle and intricate movements of various fingers, such as the index, middle, and ring fingers, as portrayed in Figure 4.13(a), Figure 4.13(b), and Figure 4.13(c), respectively, but it can also produce distinct output patterns corresponding to these movements. Moreover, the device exhibits remarkable sensitivity, as evident in Figure 4.13(d), where it efficiently detects and distinguishes variations in the degree of bending of the index finger. This demonstrates the HEH's proficiency in detecting and discerning fine motions of different fingers, as well as variations in the bending angles of a specific finger. The device could generate significant output voltage levels, producing approximately ~95 V ± 10 V during heel tapping, ~50 V ± 5 V during toe movement, ~1 V ± 0.1 V during ankle motion, ~7 V ± 0.5 V during wrist movements, and ~15 V ± 0.5 V during elbow motion. It is worth noting that the relatively lower output values observed during these movements, compared to finger movements, can be attributed to differences in the frequency and amplitude of the applied pressure. Consequently, the fabricated HEH15 not only excels in harvesting energy from various body movements, including fine finger motions but also exhibits the ability to differentiate between them. These findings signify the extensive potential of HEH, not only for bio-motion-based energy generation but also as a self-powered dynamic pressure sensor with promising applications in healthcare monitoring, particularly for patients who are confined to bed [44].

4.3.3.2. Application as smart switch

The growing popularity of portable electronic devices has led to an increased demand for modern smart home systems. Today's smart homes incorporate a variety of electronic devices and sensors, making it highly desirable to control and monitor these devices from both inside and outside a building. To address this need, researchers have explored the use of energy-harvesting devices to create smart switches for monitoring and controlling smart home applications a tribo [41,45]. However, previous smart switches had limitations, such as using a single energy harvesting device to individually control different home appliances. In real-life scenarios, it is often

necessary to control multiple household appliances simultaneously. Consequently, a 2×2 array of switches, created using Co-based nanoporous carbon-based Triboelectric Nanogenerators (TENG), was reported by M.T. Rahman et al. for smart home applications [46]. However, using multiple smart switches within a single platform can lead to interference during external triggers, complicating the overall operation. It is essential to analyze whether an array of self-powered smart switches can generate distinguishable signals under individual triggers.

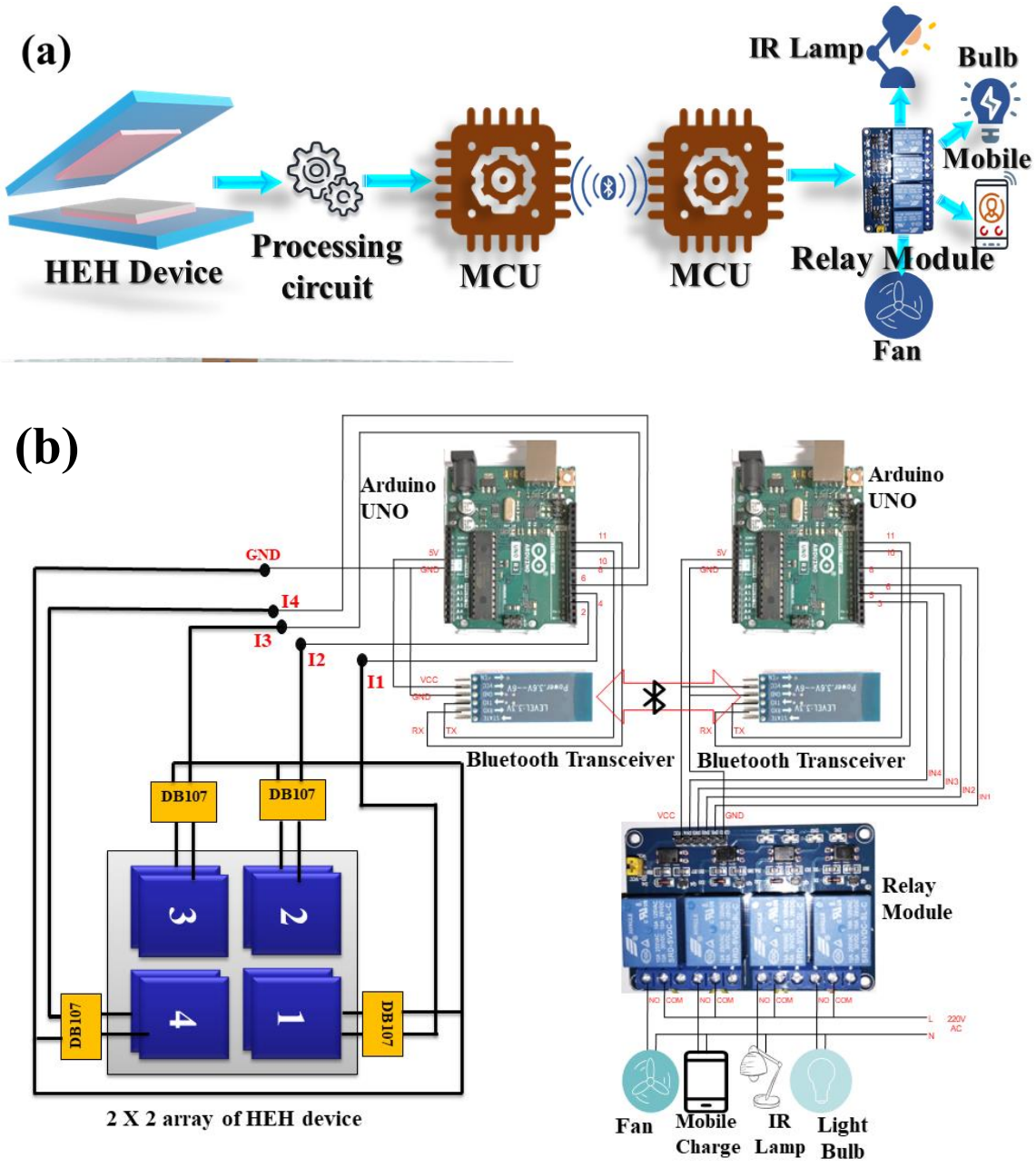

Fig. 4.13*(a) Graphical illustration of fabricated HEH device acting as the switch for wireless control of home appliances through Bluetooth, (b) circuit diagram for the wireless controlling of home appliances.*

In addition to these challenges, previous works relied on wired systems to transmit signals generated by the smart switches. This limitation hindered the convenience of using self-powered switches from both inside and outside a specific room in a house, making them like commercial switches. To address these issues, this work utilized the fabricated HEH15 device as a self-powered triggering sensor for smart home applications. Figure 4.13(a) illustrates a schematic diagram showing how the device was employed to remotely control and monitor household electronic appliances in a smart home setup. As a proof of concept, a 2×2 matrix array was created, comprising four HEH15 devices, each with dimensions of 1×1 cm^2. Each pixel in this array functions as a smart switch for operating appliances. To implement the smart home concept, microcontroller units (Arduino UNO R3 (ATmega328P)), Bluetooth IC chips (HC05), and a 4-channel Relay module were used. The entire circuit diagram of the system is provided in Figure 4.13(b).

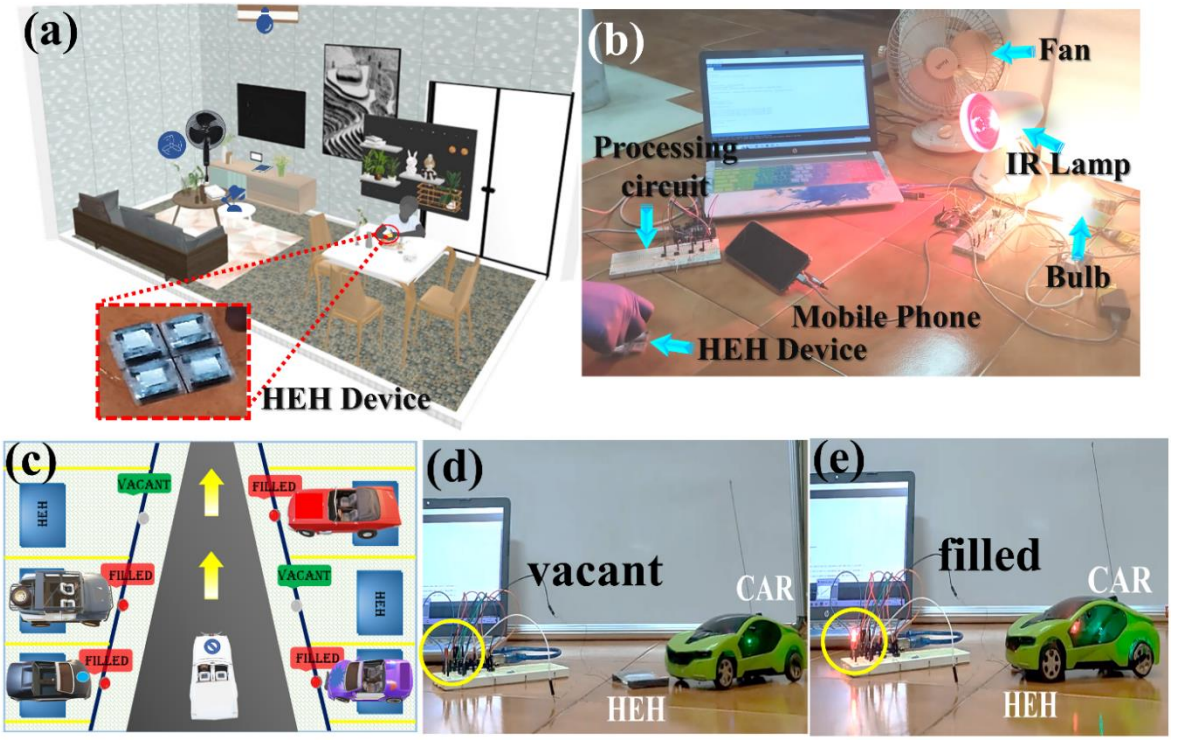

Fig. 4.14*(a) A schematic of the smart home comprising of HEH device with home appliances, (b) Digital image of the experimental setup, (c) schematic illustration of smart parking system using HEH, digital photograph of the demonstration of the vacant and filled state of a parking slot (d) when the slot is vacant (led not glowing) (e) occupied state (red led glowing).*

Figure 4.14(a) showcases the smart home setup incorporating HEH devices for controlling various home appliances. In the digital image (Figure 4.14(b)), the four

smart switches were wirelessly connected to four different appliances: a fan, an IR lamp, a mobile charger, and a bulb. These wireless connections enable the user to control the respective appliances without needing to be physically present in the room. When a specific switch (made with HEH15) in the matrix array is pressed, it generates a triggering signal specific to the corresponding device. This signal is processed by the first microcontroller unit and then transferred to the second microcontroller unit through the Bluetooth IC chips, forming the wireless circuit. The signal processing by the second microcontroller unit operates the relay, turning on or off the respective appliance.

Even though the four smart switches are connected in a matrix array, they can generate distinguishable signals with each operation, allowing them to switch the assigned devices on or off. Further, the device was employed as a sensor in a smart parking system, efficiently providing information to the driver about the availability or occupancy of a parking spot (Figure 4.14(c), Figure 4.14(d), Figure 4.14(e). The signal generated by the device due to pressure applied by a parked car is processed through a processing circuit, and the signal is then transmitted to a control system MCU (Arduino UNO R3 (ATmega328P)). The MCU processes the signal and provides instructions accordingly. When the parking slot is occupied, the signal from the device activates the Red LED, conveying this information to the driver. Conversely, when the parking slot is empty, the LED remains off. These demonstrations of smart applications using HEH15 confirm its feasibility in meeting the demands of IoT technologies, virtual reality, and artificial intelligence.

4.4. Conclusion

BCHT with a high piezoelectric charge constant of 333 pC/N was used as filler to synthesize flexible BCHT/PVDF composite, which acts as the heart of the fabricated hybrid energy harvesting (HEH) device. The impregnation of piezoelectric BCHT fillers enhanced the piezoelectric as well dielectric properties of the composite films. Such perovskite BCHT particles acted as the nucleation centers for the alignment of the PVDF polymer chains in all trans conformation which elevated its electroactive phases fraction as well as the electron trapping capabilities. These augmented piezoelectric properties of the composites further enhanced the output performance of the HEH device by coupling with the triboelectric phenomenon occurring inside the

system. The fabricated optimized HEH device is capable of generating a maximum output voltage and current of ~ 396 V ± 10 V, ~ 30 μA ± 2 μA with an instantaneous power density of 1.72 mW/cm^2. This significantly enhanced output performance of the fabricated HEH is attributed to the efficient coupling between piezoelectric and triboelectric effects. Further, the fabricated HEH shows efficient electromechanical convertibility in scavenging energy from different body part's motions including heel, toe, wrist, and elbow as well as fine finger movement. Finally, the fabricated HEH device was utilized as self-powered sensor in designing smart home and smart parking systems. Due to its exceptional power generation capacity and a strong emphasis on wireless technology, the designed HEH device has become an incredibly versatile portable energy source for flexible smart electronics.

References

[1] G. Tian, W. Deng, Y. Gao, D. Xiong, C. Yan, X. He, T. Yang, L. Jin, X. Chu, H. Zhang, W. Yan, W. Yang, Rich lamellar crystal baklava-structured PZT/PVDF piezoelectric sensor toward individual table tennis training, Nano Energy. 59 (2019) 574–581. https://doi.org/10.1016/j.nanoen.2019.03.013.

[2] S. Ye, C. Cheng, X. Chen, X. Chen, J. Shao, J. Zhang, H. Hu, H. Tian, X. Li, L. Ma, W. Jia, High-performance piezoelectric nanogenerator based on microstructured P(VDF-TrFE)/BNNTs composite for energy harvesting and radiation protection in space, Nano Energy. 60 (2019) 701–714. https://doi.org/10.1016/j.nanoen.2019.03.096.

[3] D. Wang, Z. Jiang, B. Yang, S. Zhang, M. Zhang, F. Guo, W. Cao, Phase transition behavior and high piezoelectric properties in lead-free BaTiO3-CaTiO3-BaHfO3 ceramics, J Mater Sci. 49 (2014) 62–69. https://doi.org/10.1007/s10853-013-7650-9.

[4] C. Zhao, W. Wu, H. Wang, J. Wu, Site engineering and polarization characteristics in (Ba1-yCay)(Ti1-xHfx)O3 lead-free ceramics, J Appl Phys. 119 (2016). https://doi.org/10.1063/1.4939762.

[5] N.P. Maria Joseph Raj, N.R. Alluri, G. Khandelwal, S.J. Kim, Ferroelectric flexible composite films based on morphotropic phase boundary for self-powered multisensors, Chemical Engineering Journal. 414 (2021). https://doi.org/10.1016/j.cej.2021.128840.

[6] A.C. Ianculescu, C.A. Vasilescu, L. Trupina, B.S. Vasile, R. Trusca, M. Cernea, L. Pintilie, A. Nicoară, Characteristics of Ce3+-doped barium titanate nanoshell tubes prepared by template-mediated colloidal chemistry, J Eur Ceram Soc. 36 (2016) 1633–1642. https://doi.org/10.1016/j.jeurceramsoc.2016.01.044.

[7] L. Zhang, X. Lou, D. Wang, Y. Zhou, Y. Yang, M. Kuball, M.A. Carpenter, X. Ren, Glass-Glass Transitions by Means of an Acceptor-Donor Percolating Electric-Dipole Network, Phys Rev Appl. 8 (2017). https://doi.org/10.1103/PhysRevApplied.8.054018.

[8] M.M. Vijatović, J.D. Bobić, B.D. Stojanović, History and challenges of barium titanate: Part I, Science of Sintering. 40 (2008) 155–164. https://doi.org/10.2298/SOS0802155V.

[9] M. Acosta, N. Novak, V. Rojas, S. Patel, R. Vaish, J. Koruza, G.A. Rossetti, J. Rödel, BaTiO3-based piezoelectrics: Fundamentals, current status, and perspectives, Appl Phys Rev. 4 (2017). https://doi.org/10.1063/1.4990046.

[10] P. Martins, A.C. Lopes, S. Lanceros-Mendez, Electroactive phases of poly(vinylidene fluoride): Determination, processing and applications, Prog Polym Sci. 39 (2014) 683–706. https://doi.org/10.1016/j.progpolymsci.2013.07.006.

[11] E. Kar, N. Bose, B. Dutta, N. Mukherjee, S. Mukherjee, Poly(vinylidene fluoride)/submicron graphite platelet compositeA smart, lightweight flexible material with significantly enhanced β polymorphism, dielectric and microwave shielding properties, Eur Polym J. 90 (2017) 442–454. https://doi.org/10.1016/j.eurpolymj.2017.03.030.

[12] Q. Li, J. Zhao, B. He, Z. Hu, Solution processable poly(vinylidene fluoride)-based ferroelectric polymers for flexible electronics, APL Mater. 9 (2021) 010902. https://doi.org/10.1063/4.0035539.

[13] S. Maity, A. Sasmal, S. Sen, Barium titanate based paraelectric material incorporated Poly(vinylidene fluoride) for biomechanical energy harvesting and self-powered mechanosensing, Mater Sci Semicond Process. 153 (2023). https://doi.org/10.1016/j.mssp.2022.107128.

[14] S. Mondal, T. Paul, S. Maiti, B.K. Das, K.K. Chattopadhyay, Human motion interactive mechanical energy harvester based on all inorganic perovskite-PVDF, Nano Energy. 74 (2020). https://doi.org/10.1016/j.nanoen.2020.104870.

[15] N.A. Hoque, P. Thakur, P. Biswas, M.M. Saikh, S. Roy, B. Bagchi, S. Das, P.P. Ray, Biowaste crab shell-extracted chitin nanofiber-based superior piezoelectric nanogenerator, J Mater Chem A Mater. 6 (2018) 13848–13858. https://doi.org/10.1039/c8ta04074e.

[16] A. Sasmal, S. Sen, P.S. Devi, Frequency dependent energy storage and dielectric performance of Ba-Zr Co-doped BiFeO3loaded PVDF based mechanical energy

harvesters: Effect of corona poling, Soft Matter. 16 (2020) 8492–8504. https://doi.org/10.1039/d0sm01031f.

[17] S. Ippili, V. Jella, A.M. Thomas, C. Yoon, J.S. Jung, S.G. Yoon, ZnAl-LDH-induced electroactive β-phase and controlled dielectrics of PVDF for a high-performance triboelectric nanogenerator for humidity and pressure sensing applications, J Mater Chem A Mater. 9 (2021) 15993–16004. https://doi.org/10.1039/d1ta02966e.

[18] L. Jin, X. Xiao, W. Deng, A. Nashalian, D. He, V. Raveendran, C. Yan, H. Su, X. Chu, T. Yang, W. Li, W. Yang, J. Chen, Manipulating Relative Permittivity for High-Performance Wearable Triboelectric Nanogenerators, Nano Lett. 20 (2020) 6404–6411. https://doi.org/10.1021/acs.nanolett.0c01987.

[19] Z. Peng, X. Xiao, J. Song, A. Libanori, C. Lee, K. Chen, Y. Gao, Y. Fang, J. Wang, Z. Wang, J. Chen, M.K.H. Leung, Improving Relative Permittivity and Suppressing Dielectric Loss of Triboelectric Layers for High-Performance Wearable Electricity Generation, ACS Nano. 16 (2022) 20251–20262. https://doi.org/10.1021/acsnano.2c05820.

[20] T.J. Lewis, Nanometric Dielectrics, IEEE Transactions on Dielectrics and Electrical Insulation. 1 (1994) 812–824. https://doi.org/10.1109/94.326653.

[21] H. Hu, F. Zhang, S. Luo, W. Chang, J. Yue, C.-H. Wang, Recent advances in rational design of polymer nanocomposite dielectrics for energy storage, Nano Energy. 74 (2020) 104844. https://doi.org/10.1016/j.nanoen.2020.104844.

[22] Prateek, V.K. Thakur, R.K. Gupta, Recent Progress on Ferroelectric Polymer-Based Nanocomposites for High Energy Density Capacitors: Synthesis, Dielectric Properties, and Future Aspects, Chem Rev. 116 (2016) 4260–4317. https://doi.org/10.1021/acs.chemrev.5b00494.

[23] A. Sasmal, A. Patra, P.S. Devi, S. Sen, Space charge induced augmented dielectric permittivity and improved energy harvesting ability of nano-Ag decorated $ZnSnO_3$ filled PVDF based flexible nanogenerator, Compos Sci Technol. 213 (2021). https://doi.org/10.1016/j.compscitech.2021.108916.

[24] S. Maity, A. Sasmal, S. Sen, Comprehensive characterization of Ba1−xSrxTiO3: Correlation between structural and multifunctional properties, J Alloys Compd. 884 (2021). https://doi.org/10.1016/j.jallcom.2021.161072.

[25] Y.C. Lai, J. Deng, S.L. Zhang, S. Niu, H. Guo, Z.L. Wang, Single-Thread-Based Wearable and Highly Stretchable Triboelectric Nanogenerators and Their Applications in Cloth-Based Self-Powered Human-Interactive and Biomedical Sensing, Adv Funct Mater. 27 (2017). https://doi.org/10.1002/adfm.201604462.

[26] S. Pratihar, A. Patra, A. Sasmal, S.K. Medda, S. Sen, Enhanced dielectric, ferroelectric, energy storage and mechanical energy harvesting performance of ZnO-PVDF composites induced by MWCNTs as an additive third phase, Soft Matter. 17 (2021) 8483–8494. https://doi.org/10.1039/d1sm00854d.

[27] Prateek, R. Bhunia, A. Garg, R.K. Gupta, Poly(vinylpyrrolidone)/Poly(vinylidene fluoride) as Guest/Host Polymer Blends: Understanding the Role of Compositional Transformation on Nanoscale Dielectric Behavior through a Simple Solution-Process Route, ACS Appl Energy Mater. 2 (2019) 6146–6152. https://doi.org/10.1021/acsaem.9b01092.

[28] A. Ferri, S. Barrau, R. Bourez, A. Da Costa, M.H. Chambrier, A. Marin, J. Defebvin, J.M. Lefebvre, R. Desfeux, Probing the local piezoelectric behavior in stretched barium titanate/poly(vinylidene fluoride) nanocomposites, Compos Sci Technol. 186 (2020). https://doi.org/10.1016/j.compscitech.2019.107914.

[29] R. Bhimireddi, B. Ponraj, K.B.R. Varma, Structural, Optical, and Piezoelectric Response of Lead-Free Ba0.95Mg0.05Zr0.1Ti0.9O3 Nanocrystalline Powder, Journal of the American Ceramic Society. 99 (2016) 896–904. https://doi.org/10.1111/jace.14018.

[30] J. Anthoniappen, W.S. Chang, A.K. Soh, C.S. Tu, P. Vashan, F.S. Lim, Electric field induced nanoscale polarization switching and piezoresponse in Sm and Mn co-doped BiFeO3 multiferroic ceramics by using piezoresponse force microscopy, Acta Mater. 132 (2017) 174–181. https://doi.org/10.1016/j.actamat.2017.04.034.

[31] H.Y. Ye, J.Z. Ge, Y.Y. Tang, P.F. Li, Y. Zhang, Y.M. You, R.G. Xiong, Molecular Ferroelectric with Most Equivalent Polarization Directions Induced by the Plastic Phase Transition, J Am Chem Soc. 138 (2016) 13175–13178. https://doi.org/10.1021/jacs.6b08817.

[32] M. Sahu, V. Vivekananthan, S. Hajra, K.S. Abisegapriyan, N.P. Maria Joseph Raj, S.J. Kim, Synergetic enhancement of energy harvesting performance in triboelectric nanogenerator using ferroelectric polarization for self-powered IR signaling and body activity monitoring, J Mater Chem A Mater. 8 (2020) 22257–22268. https://doi.org/10.1039/d0ta06215d.

[33] Y. Wu, J. Qu, W.A. Daoud, L. Wang, T. Qi, Flexible composite-nanofiber based piezo-triboelectric nanogenerators for wearable electronics, J Mater Chem A Mater. 7 (2019) 13347–13354. https://doi.org/10.1039/c9ta02345c.

[34] B. Shi, Z. Liu, Q. Zheng, J. Meng, H. Ouyang, Y. Zou, D. Jiang, X. Qu, M. Yu, L. Zhao, Y. Fan, Z.L. Wang, Z. Li, Body-Integrated Self-Powered System for Wearable and Implantable Applications, ACS Nano. 13 (2019) 6017–6024. https://doi.org/10.1021/acsnano.9b02233.

[35] S. Hajra, A.M. Padhan, M. Sahu, P. Alagarsamy, K. Lee, H.J. Kim, Lead-free flexible Bismuth Titanate-PDMS composites: A multifunctional colossal dielectric material for hybrid piezo-triboelectric nanogenerator to sustainably power portable electronics, Nano Energy. 89 (2021). https://doi.org/10.1016/j.nanoen.2021.106316.

[36] P. Tofel, K. Částková, D. Říha, D. Sobola, N. Papež, J. Kaštyl, Ş. Ţălu, Z. Hadaš, Triboelectric Response of Electrospun Stratified PVDF and PA Structures, Nanomaterials. 12 (2022). https://doi.org/10.3390/nano12030349.

[37] M.F. Lin, K.W. Chang, C.H. Lee, X.X. Wu, Y.C. Huang, Electrospun P3HT/PVDF-HFP semiconductive nanofibers for triboelectric nanogenerators, Sci Rep. 12 (2022). https://doi.org/10.1038/s41598-022-19306-1.

[38] D.L. Vu, K.K. Ahn, Triboelectric Enhancement of Polyvinylidene Fluoride Membrane Using Magnetic Nanoparticle for Water-Based Energy Harvesting, Polymers (Basel). 14 (2022). https://doi.org/10.3390/polym14081547.

[39] H.H. Singh, N. Khare, Flexible ZnO-PVDF/PTFE based piezo-tribo hybrid nanogenerator, Nano Energy. 51 (2018) 216–222. https://doi.org/10.1016/j.nanoen.2018.06.054.

[40] A.M. Abdullah, M.U.K. Sadaf, F. Tasnim, H. Vasquez, K. Lozano, M.J. Uddin, KNN based piezo-triboelectric lead-free hybrid energy films, Nano Energy. 86 (2021). https://doi.org/10.1016/j.nanoen.2021.106133.

[41] S.M.S. Rana, M.T. Rahman, M. Salauddin, S. Sharma, P. Maharjan, T. Bhatta, H. Cho, C. Park, J.Y. Park, Electrospun PVDF-TrFE/MXene Nanofiber Mat-Based Triboelectric Nanogenerator for Smart Home Appliances, ACS Appl Mater Interfaces. 13 (2021) 4955–4967. https://doi.org/10.1021/acsami.0c17512.

[42] F. Jiang, X. Zhou, J. Lv, J. Chen, J. Chen, H. Kongcharoen, Y. Zhang, P.S. Lee, Stretchable, Breathable, and Stable Lead-Free Perovskite/Polymer Nanofiber Composite for Hybrid Triboelectric and Piezoelectric Energy Harvesting, Advanced Materials. 34 (2022). https://doi.org/10.1002/adma.202200042.

[43] P. Pandey, D.H. Jung, G.J. Choi, M.K. Seo, S. Lee, J.M. Kim, I.K. Park, J.I. Sohn, Nafion-mediated barium titanate-polymer composite nanofibers-based triboelectric nanogenerator for self-powered smart street and home control system, Nano Energy. 107 (2023). https://doi.org/10.1016/j.nanoen.2022.108134.

[44] E. Kar, P. Ghosh, S. Pratihar, M. Tavakoli, S. Sen, Nature-Driven Biocompatible Epidermal Electronic Skin for Real-Time Wireless Monitoring of Human Physiological Signals, ACS Appl Mater Interfaces. (2023). https://doi.org/10.1021/acsami.3c00509.

[45] K. Shrestha, S. Sharma, G.B. Pradhan, T. Bhatta, S.S. Rana, S. Lee, S. Seonu, Y. Shin, J.Y. Park, A triboelectric driven rectification free self-charging supercapacitor for smart IoT applications, Nano Energy. 102 (2022). https://doi.org/10.1016/j.nanoen.2022.107713.

[46] M.T. Rahman, S.S. Rana, M.A. Zahed, S. Lee, E.S. Yoon, J.Y. Park, Metal-organic framework-derived nanoporous carbon incorporated nanofibers for high-performance triboelectric nanogenerators and self-powered sensors, Nano Energy. 94 (2022). https://doi.org/10.1016/j.nanoen.2022.106921.

Related video file links

LED GLOWING

https://ars.els-cdn.com/content/image/1-s2.0-S1385894723046909-mmc2.mp4

FINGER MOVEMENT

https://ars.els-cdn.com/content/image/1-s2.0-S1385894723046909-mmc3.mp4

SMART HOME

https://ars.els-cdn.com/content/image/1-s2.0-S1385894723046909-mmc4.mp4

SMART PARKING

https://ars.els-cdn.com/content/image/1-s2.0-S1385894723046909-mmc5.mp4

Chapter 5

Morphotropic Phase Boundary-Assisted Lead-Free $BaTiO_3$/PDMS Based Hybrid Energy Harvester: A Portable Power Source for Wireless Power Transmission

5.1. Introduction

As discussed in the previous chapter, hybridization of piezoelectric and triboelectric energy harvesting technologies has gained tremendous attention to fabricate mechanical energy harvesting devices with adequate power generation capabilities. In terms of materials choice, along with PVDF, PDMS is also considered as a favorable candidate to design energy efficient hybrid devices due to its high electron affinity and flexibility [1]. However, in terms of energy generation capabilities bare PDMS-based energy harvesters are unable to cop up with the ever-increasing energy demands of the modern world. Therefore, suitable modifications of the bare PDMS have been considered as an effective pathway in a means to increase the power generation capacity of the PDMS based hybrid energy harvesting devices. One such way is to impregnate efficient piezoelectric materials inside the PDMS matrix to effectively nurture its intrinsic properties. Now, the responsibility goes on to the various filler materials which can be effectively used to increase the power generation capability of the ultimate fabricated hybrid device. In this aspect, perovskite materials are considered as one of the most favorable candidates due to the presence of local charge defects which inherently act as efficient charge acceptors [2]. Consequently, owing to the good dielectric permittivity as well as piezoelectricity Barium Titanate ($BaTiO_3$), is one of the most favorable choices of material in terms of lead-free perovskite piezoelectric materials. This results in the successful utilization of $BaTiO_3$ in order to tailor the intrinsic properties of the PDMS by a large number of researchers worldwide. Zhang et. al has recently reported the development of a triboelectric nanogenerator

---

A portion of this chapter appeared as

S. Maity, A. Sasmal, E. Kar, S. Sen, Morphotropic Phase Boundary-Assisted Lead-Free $BaTiO_3$ /PDMS Composite-Based Hybrid Energy Harvester: A Portable Power Source for Wireless Power Transmission, **ACS Appl. Energy Mater.** 2023, 6, 13, 7052–7064.

based on $BaTiO_3$/PDMS composite, which can generate an output voltage of 72 V and power 5.5 μW/cm² [3]. Again, a use of Barium Titanate/PDMS composite for the fabrication of hybrid energy harvesting device with an output voltage of 10 V was reported by Suo et al. [4]. Interestingly, suitable modifications in order to achieve preferred characteristics from Barium Titanate can be achieved using common approaches like domain engineering, elemental doping, etc. [5,6]. Such an approach was utilized successfully by Dudem et al., where Al was used to modify the properties of $BaTiO_3$ before using it as a filler in the PDMS matrix to fabricate an efficient hybrid energy harvesting device [7]. $BaTiO_3$/MWCNT has also been used as filler to fabricate a hybrid energy harvester with a power generating capacity of 4.61 mW/m² [8]. As already discussed in the last chapter, the formation of morphotropic phase boundaries within the ceramic fillers through specific cation doping can effectively enhance the piezoelectric properties [9–12]. Driven by the concept, Sn^{4+} has been doped in the Ti site of $BaTiO_3$ to successfully enhance the piezoelectric properties of the ceramic filler [13,14]. Such elemental doping can significantly enhance the piezoelectric coefficient of the ceramic filler due to its four-phase coexistence [13,14]. Therefore, this chapter includes an insight analysis of the detailed pathway starting from the modifications of the intrinsic properties of PDMS by BTS fillers to the fabrication of an effective flexible piezo-triboelectric hybrid energy harvesting device with adequate power density.

5.2. Experimental

$BaTi_{0.89}Sn_{0.11}O_3$ (BTS) powders were successfully synthesized using the modified Pechini method and incorporated inside PDMS. To maintain the flexibility of PDMS and also to get advantageous prospects of BTS, BTS loading inside PDMS was limited upto 20 wt% (5 wt%, 10 wt%, 15 wt% and 20 wt%) (details are elaborated in chapter 2). These composites were used for the fabrication of piezoelectric and hybrid energy harvester. To fabricate a triboelectric energy harvester only PDMS film was used as the negative layer and normal printer paper was used as the positive triboelectric layer (details are described in Chapter 2). For wireless power transfer induction-based resonance coupling method was utilized.

5.3. Results and discussions

5.3.1 Filler characteristics

5.3.1.1 Structural characteristics

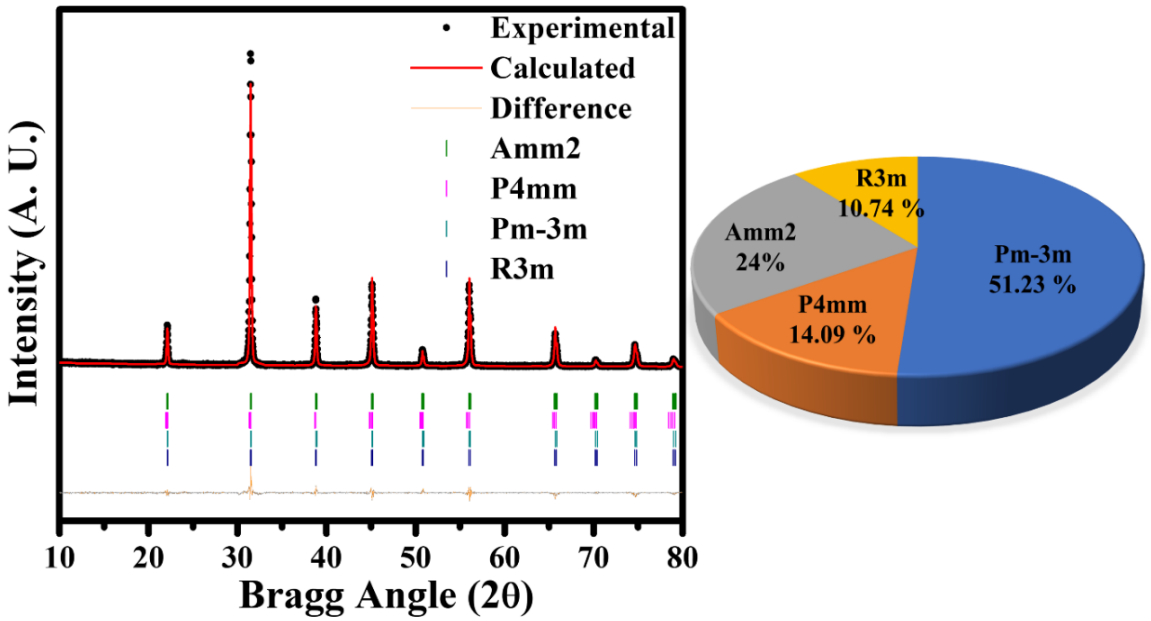

Fig. 5.1 *Rietveld Refined X-ray Diffraction pattern of as-prepared BTS powders illustrating the coexistence of Amm2, P4mm, R3m, and Pm-3m phases of BTS along with respective phase percentage.*

BTS was included in this study because of its exceptional piezoelectric properties, resulting from the simultaneous presence of various phases. Therefore, it was crucial to investigate the structural and elemental characteristics of the synthesized BTS particles. Figure 5.1 shows the X-ray diffraction pattern of the produced BTS particles. To gain a deeper understanding of the phase structure, Rietveld refinement was done. The refinement process revealed the best match when considering a combination of non-centrosymmetric Orthorhombic (Amm2), Tetragonal (P4mm), and Rhombohedral (Hexagonal axis) (R3m) phases, as well as a centrosymmetric Cubic (Pm-3m) phase within Barium Titanate. This fitting yielded a satisfactory parameter (χ^2) value of 1.46. The quantitative analysis indicated that the fractions of these phases, Amm2, P4mm, Pm-3m, and R3m, were 23.94%, 14.09%, 51.23%, and 10.74%, respectively, confirming the presence of multiple phases (Fig. 5.1). Additional information on unit cell parameters and profile fitting factors can be found in Table 5.1. In this context, it's important to note that the coexistence of multiple phases within

nanodomains reduces the energy barrier at phase boundaries. This phenomenon promotes polarization rotation and contributes to a high piezoelectric coefficient [15,16]. This is supported by the optimal d_{33} value of 412 pC/N observed in the poled sintered BTS pellet.

Table 5.1 Rietveld Refined lattice parameters and fitting factors of synthesized BTS.

Space Group	Lattice Parameters			Atoms	Atomic sites	Relative phase percentage	Refinement fitting factors
	a	b	c				
Amm2	4.0148	5.6795	5.6885	Ba	0.0, 0.0, 0.0	23.94%	R_p =17.8% R_{wp}=18.3% R_{exp}=15.21% x^2 = 1.46
				Ti	0.5, 0.0, 0.517		
				O1	0.0, 0.0, 0.489		
				O2	0.5, 0.256, 0.248		
				Sn	0.5, 0.0, 0.517		
P4mm	4.0209	4.0209	4.0440	Ba	0.0, 0.0, 0.0	14.09%	
				Ti	0.5, 0.5, 0.486		
				O1	0.5, 0.5, 0.016		
				O2	0.5, 0.0, 0.474		
				Sn	0.5, 0.5, 0.486		
Pm-3m	4.0173	4.0173	4.0173	Ba	0.5, 0.5, 0.5	51.23%	
				Ti	0.0, 0.0, 0.0		
				O	0.5, 0.0, 0.0		
				Sn	0.0,0.0, 0.0		
R3m	5.6828	5.6828	6.9631	Ba	0.0, 0.0, 0.0	10.74%	
				Ti	0.0, 0.0, 0.488		
				O	0.162, 0.333, 0.425		
				Sn	0.0, 0.0, 0.488		

5.3.1.2 Morphological and Elemental Characteristics

Fig. 5.2(a) reveals the SEM image of the synthesized BTS particles showing their morphology to be irregular (quasi-spherical). Energy Dispersive X-ray Spectra (EDS) in Fig. 5.2(b) clearly demonstrates the presence of required elements with nearly the prerequisite ratio prohibiting the effect of any type of chemical segregation. To clarify the homogeneous distribution of all the elements EDS mapping was carried out. EDS mapping presented in Fig. 5.2(c) proves the uniform spreading of Barium (Ba), Titanium (Ti), Tin (Sn), and Oxygen (O) throughout the sample. Further analysis of the elements and their charge state was carried out with the help of X-ray Photoelectron Spectroscopy (XPS) shown in Fig. 5.2(d-h). Fig. 5.2(d) shows the XPS survey spectrum of BTS, which exhibits the existence of Barium, Tin, Titanium, and Oxygen. High resolution core level spectrum of the Ba 3d can be seen in the Fig. 5.2(e).

From Gaussian peak fitting it can be noticed that both the Ba $3d_{3/2}$ and Ba $3d_{5/2}$ peaks are composed of two peaks. Ba $3d_{3/2}$ has two components situated at binding energy values of 796.6 eV (Ba I) and 794.9 eV (Ba $3d_{3/2}$). The binding energy values

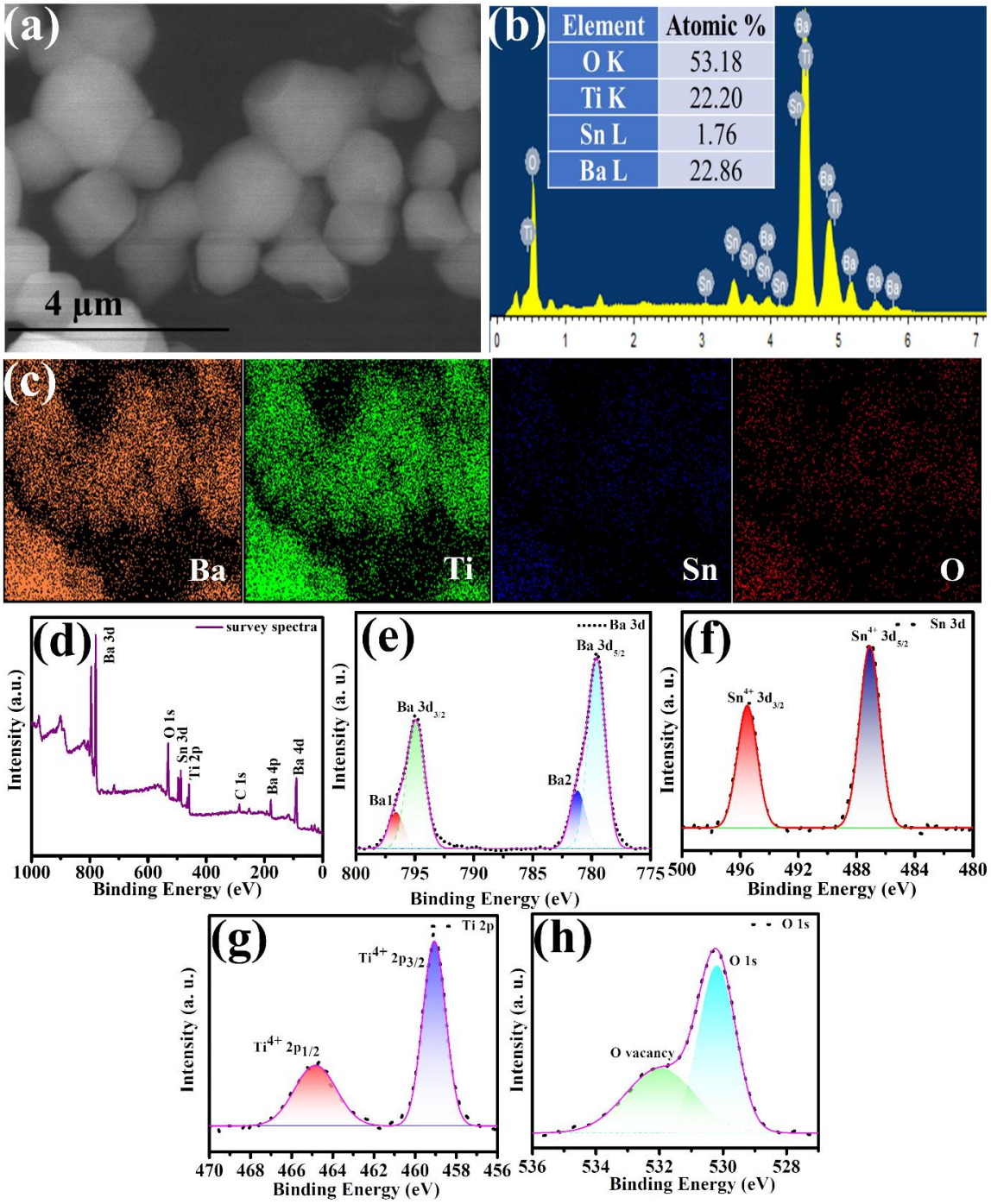

Fig. 5.2 *(a) SEM image of the synthesized BTS particles. (b) EDS spectra along with the percentage elemental composition of BTS reveal the presence of Ba, Sn, Ti, and O in BTS particles. (c) EDS mapping of all elements of BTS. XPS (d) survey spectra, (e) Ba 3d, (f) Sn 3d, (g) Ti 2p and (h) O 1s spectra of BTS.*

for the components of Ba $3d_{5/2}$ are 781.18 eV (Ba II) and 779.55 eV ($3d_{5/2}$). According to previous reports [17–19], Ba I and Ba II are associated with the surface of the material whereas the $3d_{3/2}$ and $3d_{5/2}$ are corresponding to the perovskite structure of the BTS particles. There are two peaks at binding energy values of 495.51 eV and 487.09 eV, which are corresponding to Sn $3d_{3/2}$ and Sn $3d_{5/2}$, respectively. These energy values are related to the peaks of Sn^{4+} [20]. Fig. 5.2(g) shows the binding energy gap of 5.7 eV between Ti $2p_{1/2}$ (464.84 eV) and Ti $2p_{3/2}$ (459.07 eV) which manifests the presence of only Ti^{4+} ion [21]. Fig. 5.2(h) displays the high-resolution O 1s spectra of BST40 sample which is fitted into two peaks. The low energy peak at 530.19 eV is due to the contribution from lattice oxygen those bonds with Ba, Sn and Ti atoms whereas; the peak at high energy (531.98 eV) comes from the hydroxylation of surface due to air contamination [19]. This part shows the presence of oxygen vacancy in the sample [18].

5.3.1.3 Thermal characteristics

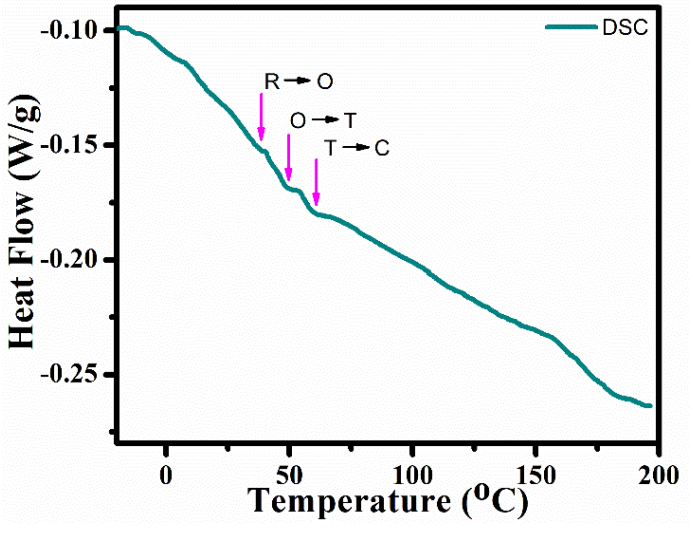

Fig. 5.3 *DSC study of synthesized BTS particles within a temperature range of -20°C to 200°C.*

To further confirm the coexistence of phases in BTS, Differential Scanning Calorimetry (DSC) was carried out (as given In Fig. 5.3). Fig. 5.3 displays the DSC thermograph of the BTS particles between -20 °C to 200 °C. DSC thermograph shows the presence of three endothermic peaks situated at ~ 40 °C, ~ 50 °C and ~ 60 °C. This particular nature of the DSC thermograph further confirms that the synthesized BTS particles contain different phases of Barium Titanate. These endothermic peaks correspond to

the R-O, O-T and T-C phase transition of Barium Titanate, respectively. Therefore, the coexistence of multiple phases is confirmed through the DSC study.

5.3.1.4 Electrical characteristics

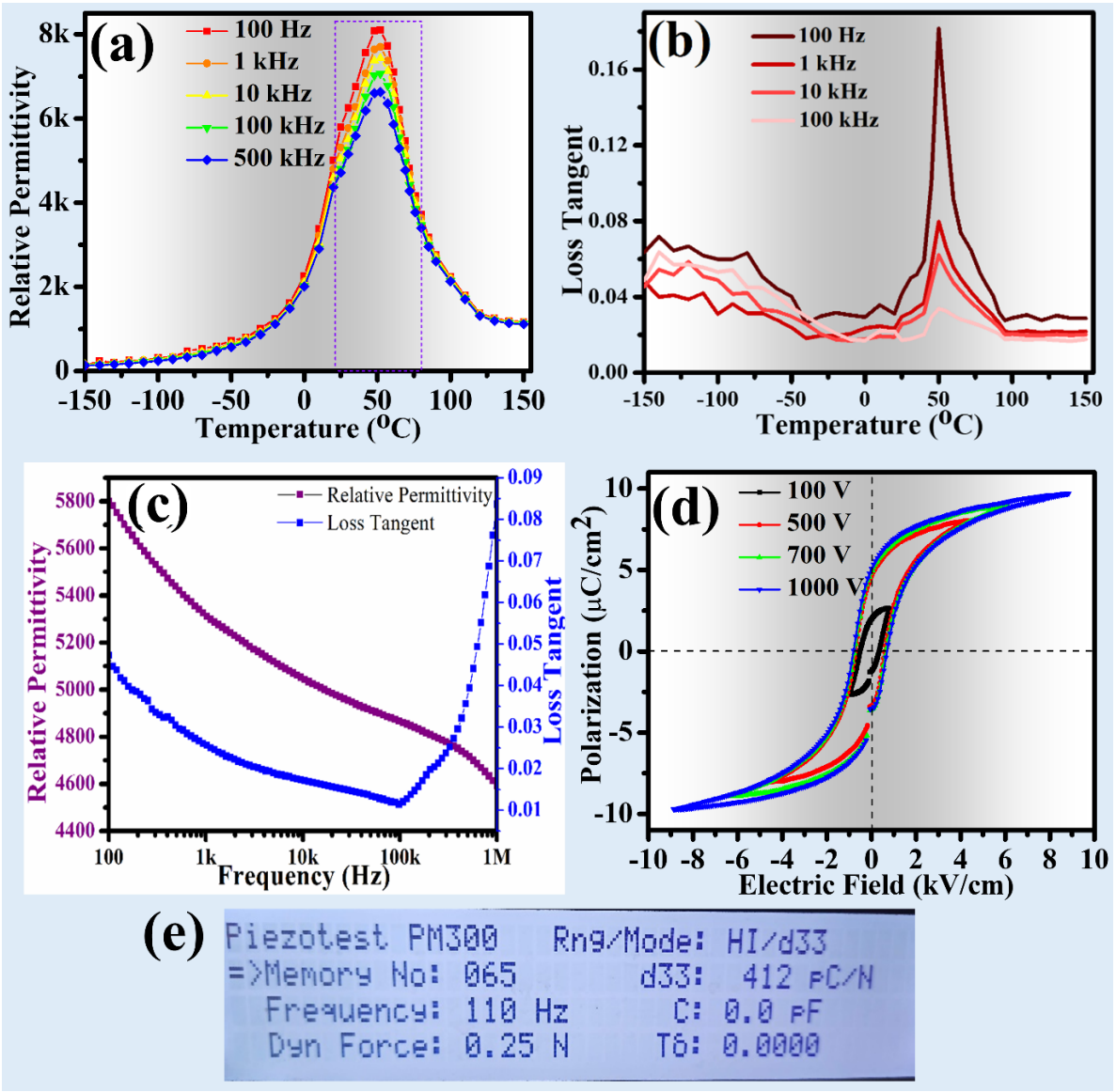

Fig. 5.4*(a) Relative Permittivity, (b) dielectric loss tangent with a variation in temperature (-150°C to 150°C) at some certain frequencies (100 Hz, 1 kHz, 10 kHz, 100 kHz, and 500 kHz) revealing the peak positioned at ~ 50°C, (c) relative permittivity and loss tangent of BTS at RT(25°C) within a frequency range from 100 Hz to 1 MHz, (d) Ferroelectric polarization vs electric field (P-E loop) of the BTS pellet on the application of external electric field at frequency 1 Hz, (e) measured d_{33} value of BTS pellet.*

For the sake of confirmation of the multiple phase coexistence in BTS particles temperature dependent dielectric properties were performed (Fig. 5.4(a) and Fig. 5.4(b)) in the temperature range of -150°C to 150°C. It should be highlighted here that

the presence of any peak in the temperature variation of dielectric permittivity and tangent loss can be attributed to the phase transition temperature of that material. A closer observation of both the curves reveals the presence of a phase transition temperature at ~ 50°C, which is in fair agreement with the results reported earlier for the given composition [22,23]. This temperature variation of loss tangent of BTS is in well agreement with the temperature variation of relative permittivity. In case of $BaTiO_3$, three distinguishable peaks are observed in the temperature variation of relative permittivity and loss tangent [24]. However, these three peaks merge in a single one at around 50°C with 11 wt% doping of Sn at the Ti site of $BaTiO_3$. This is due to the formation of morphotropic phase boundary in BTS. In this context, it should be highlighted here that, the observed temperature range in Fig. 5.3 is in well agreement with the temperature variation of dielectric properties of BTS. Again, the frequency dependence of the dielectric permittivity of BTS (Fig. 5.4(c)) reveals a sustainable high value in the entire frequency range (100 Hz to 1 MHz, dielectric permittivity ~ 5312, 1 kHz, 25°C) (Fig. 5.4(c)) with a considerable low tangent loss (0.0256, 1 kHz, 25°C) (Fig. 5.4(c)). In addition to that, BTS also possesses good ferroelectric properties as evident from Fig. 5.4(d), with a saturation polarization value of 9.7 $\mu C/cm^2$ at an electric field of 8.84 kV/cm. To confirm its good piezoelectric nature, sintered BTS pellets were poled to 1 kV/mm for 1 h. Direct measurement of piezoelectric charge coefficient (d_{33}) measures its value to be 412 pC/N (Fig. 5.4(e)). These excellent physicochemical properties confirm the suitability of BTS as a filler material in PDMS, beneficial for the output properties of a hybrid energy harvester.

5.3.2 Mechanism for Hybrid Energy harvesting

The fundamental operational mechanism of the fabricated contact separation mode-based hybrid energy harvester is illustrated in Fig. 5.5(i-vii). In the primary state (step i), under no external pressure, the two functional layers (paper and BTS/PDMS surface) are in stable mode and hence there is no charge generation. With the application of compressive stress, the two layers come in close contact (step ii) with each other. When these two layers are just in contact with each other, the triboelectric effect (contact electrification) appears. Due to their contrast in charge affinity, the paper gets the positive surface charge, and the negative surface charge is induced on

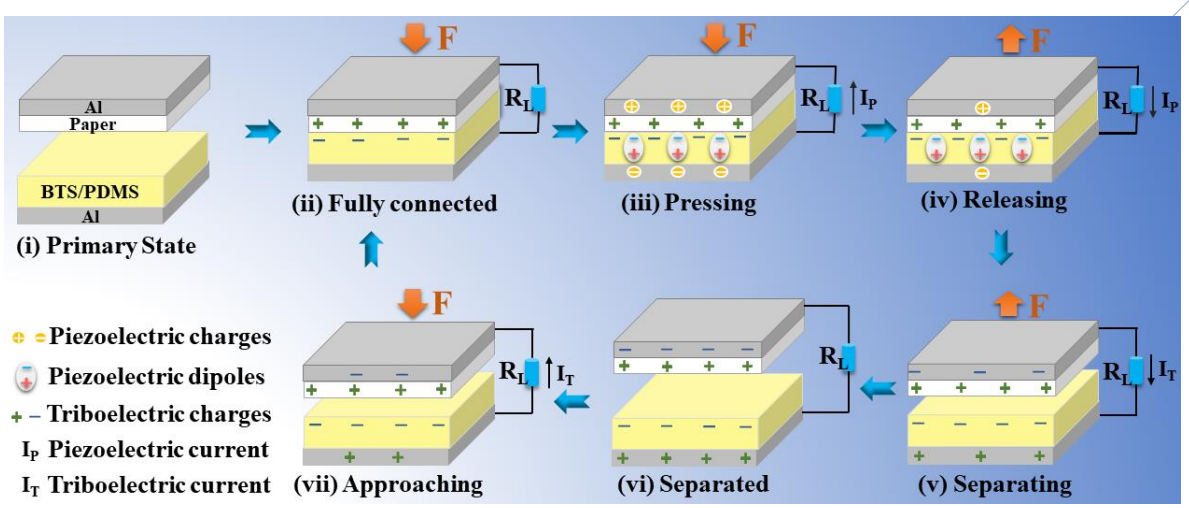

Fig. 5.5 *Fundamental working mechanism of hybrid energy harvester device.*

BTS/PDMS surface. At the same time, the applied force also compresses the BTS/PDMS layer (step iii) which results in the generation of piezoelectric effect due to the inherent piezoelectric nature of BTS particles. As the BTS/PDMS layer was not poled before this device fabrication, the piezoelectric effect that appeared here may be considered to be due to the stress-induced poling effect [25–27]. (Here it can be noted that polarization in piezoelectric materials can be induced in two ways one by applying an external electric field and another one by applying external mechanical stimuli.) Due to this effect, a piezoelectric potential is generated across the thickness of the BTS/PDMS layer when it is acted upon by external mechanical stimuli in the same direction [25–27]. To balance this potential, opposite free charges (opposite to the charges of aligned BTS dipoles residing just below the respective surfaces of the BTS/PDMS layer) are induced in the lower and upper Al electrodes resulting in the flow of piezoelectric current through the external circuit. (Here it is worth mentioning that the piezoelectric free charges are developed on both the electrodes by the method of electrostatic induction driven by the generated piezoelectric potential across the active layer. The induction process may appear even without direct contact with materials which justifies the development of piezoelectric charges in the upper electrode even though a paper layer is there in between this electrode and the active layer [28]. With the removal of the external pressure (step iv), the decompression of BTS/PDMS layer occurs and the opposite piezoelectric potential (compared to that of

the earlier one) is generated which results in the generation of piezoelectric current in the opposite direction. As soon as the complete decompression is achieved, the upper paper layer starts separating from the lower BTS/PDMS layer during this removal of force (step v). As a result of this fact, the formation of the positive charge takes place on the bottom Al electrode due to electrostatic induction from the negatively charged BTS/PDMS surface. As a result, an electric current start flowing from the top to bottom Al electrode due to the unidirectional movement of electrons in the opposite direction. As soon as the electrodes move back to their stable state (step vi), the electrostatic equilibrium condition is achieved. Again, when there is an application of external stimuli (step vii) the equilibrium condition is terminated and electrons start to flow in the opposite direction leading to the opposite peak of the output signal [25–27]. The output performance of the fabricated HEH device comes from the synergistic effect between the piezoelectric and triboelectric phenomena. When, a piezoelectric active material such as BTS is incorporated in PDMS for the fabrication of such a HEH device, the piezo-active material undergoes a mechanical deformation due to the applied strain. Consequently, the dipoles present in the active material (BTS/PDMS) try to align along the direction of applied stress under stress-induced polarization. Again, due to the presence of the field generated due to the triboelectrification, the alignment of the dipoles will be considerably augmented resulting in the enhancement of dipolar polarization. Thereby, more negative charges are generated on the negative triboelectric surface, resulting in further enhancement in the triboelectric performance of the device during the operation of HEH. In this way, the overall output performance of HEH increases due to the coupling of triboelectric and piezoelectric effects inside the device [29]. With the application of repeated mechanical stimuli, this cycle continues periodically resulting in the generation of alternating electrical output signal.

5.3.3 Energy harvesting performance of the fabricated energy harvester devices

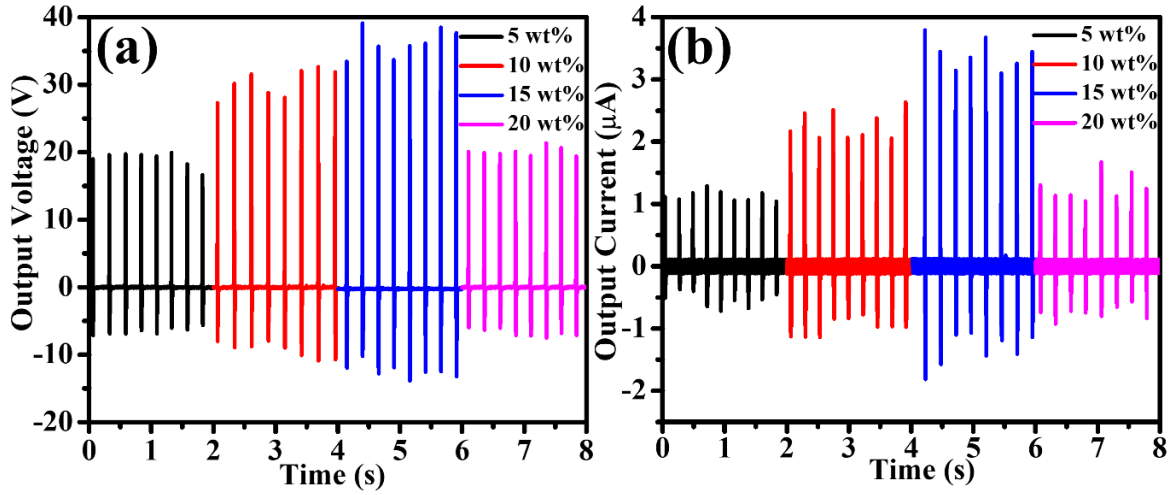

Fig. 5.6*(a) Piezoelectric voltage output, (b) current output of BTS/PDMS based piezoelectric energy harvester.*

As discussed in the previous section, the output generated from a hybrid energy harvesting device can be considered as a synergistic effect of both piezoelectric and triboelectric outcomes. Therefore, it is now essential to investigate the effect of BTS particles in PDMS matrix in enhancing the output energy harvesting performance. For this purpose, the piezoelectric output signals from BTS/PDMS based composite films were recorded under repeated human finger tapping. To fabricate a piezoelectric energy harvester, the 5 wt%, 10 wt%, 15 wt%, and 20 wt% BTS particles incorporated PDMS composite films were sandwiched between two Aluminium (Al) electrodes and encapsulated using PET sheet. Two copper wires were connected to the Al electrodes for output performance measurements. The peak-to-peak output voltage (V) and output current (I) obtained from the piezoelectric energy harvesters on the application of a finger flapping force of ~100 N at a rate of 4 Hz is presented in Fig. 5.6(a) and Fig. 5.6(b), respectively. With the increment in BTS wt% inside PDMS the generated peak to peak piezoelectric output at first increased and then decreased after the BTS doping exceeds the 15 wt% limit. At first incorporation of BTS inside the PDMS matrix increased the piezoelectric voltage due to the high intrinsic piezoelectric voltage coefficient of BTS. Due to the inhomogeneity and agglomeration, after 15 wt% BTS doping results in a decreased piezoelectric output. It can be seen from both the figures that the film with 15 wt% loading of BTS (indexed as PEH15) showed the maximum output voltage and current confirming its superiority for piezoelectric power

generation. Table 5.2 tabulates the output voltage and output current generated from the respective piezoelectric energy harvesters.

Table 5.2 Piezoelectric output from the BTS/PDMS composites with the variation of BTS concentration

BTS doping wt% inside PDMS	Average peak to peak Piezoelectric Voltage Output (V)	Average peak to peak Piezoelectric Current Output (μA)
5	26	1.5
10	40	3.0
15	46	4.4
20	25	1.6

Further, a comparative study of the output voltage and current generated from the hybrid energy harvesters (based on 5, 10, 15, and 20 wt% loaded BTS/PDMS composite) was performed (Fig. 5.7(a) and 5.7(b)). A closer observation of both Fig. 5.7(a) and Fig. 5.7(b) demonstrates that the incorporation of BTS inside the PDMS matrix increased the output voltage and current of the resulting hybrid energy harvester, with a maximum value obtained for 15 wt% loading of BTS. In this context, it should be highlighted that as mentioned earlier the maximum piezo output was obtained for the same loading fraction of BTS in PDMS (15 wt%). 15 wt% BTS loaded PDMS and paper-based HEH was able to generate the output voltage of ~358 V and output current of 36 μA, respectively under the tapping force of 100 N at a rate of 4 Hz, which is nearly 8-fold than that of the 15 wt% BTS/PDMS PEH (~ 46 V) and nearly 3-fold than that of the bare PDMS and paper-based TEH (~ 125 V) under same force condition (Fig. 5.7(d) and Fig. 5.7(e)). This enhancement in the output performance of the hybrid energy harvesters can be explained by the dielectric permittivity parameters of the functional layers as it plays a crucial role in determining the output energy harvesting performance of the final device [5,30]. The frequency dependent (100 Hz – 1 MHz) dielectric permittivity graphs of all the BTS/PDMS based composite films as

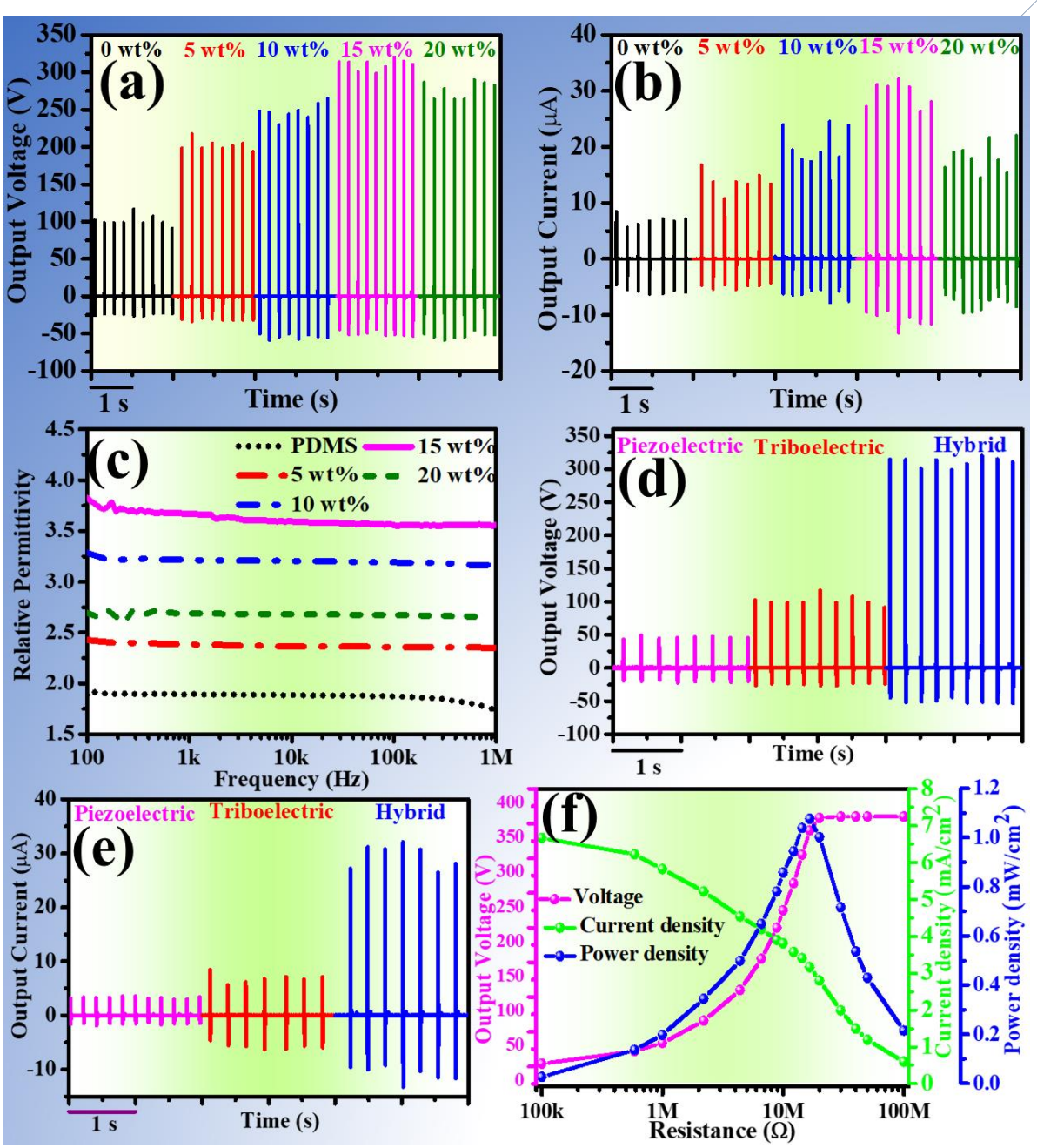

Fig. 5.7*(a) Output voltage and (b) Output current with the variation in BTS doping weight% inside PDMS for HEH devices. (c) Relative Permittivity of the BTS/PDMS composite films with a variation in frequency (100 Hz – 1 MHz). Generated (d) Output voltage and (e) Output current from different device structures (PEH15, TEH, and HEH15). (f) Generated voltage, measured current density, and power density of the hybrid energy harvester made of 15 wt% BTS doped PDMS composite film with a function of load resistance (100 kΩ – 100 MΩ). Electrical output measurements were done using finger tapping.*

presented in Fig. 5.7(c) suggested almost 1-fold increment of the dielectric permittivity of 15 wt% BTS/PDMS film compared to that of bare PDMS. This gradual enhancement of dielectric permittivity of the BTS/PDMS films with the increase in BTS filler wt%

(up to 15 wt%) was directly associated with the intrinsic high polarization of BTS particles. This enhancement of dielectric permittivity of the used functional layer (BTS/PDMS composite film) improved their charge storage capacity which in turn augmented the output performance of the HEH device via an enriched triboelectrification process [31]. But, as there was only a ~ 1-fold increase in dielectric permittivity which was comparatively less than the increase in output voltage (~ 2-fold) of the HEH for 15 wt% BTS/PDMS based film compared to that of bare PDMS, it is obvious that there were some other additional effects which played a significant role in the performance enhancement of the HEH. Due to the poor frictional force between PDMS and paper surface, the produced triboelectric charge was small and the output performance was comparatively low. The enhancement in the surface roughness of the composite films due to ceramic filler inclusion helped in enhancing the frictional force between the two layers of the HEH along with the increase in surface charge density of the composite film [5,32]. Enhancement of these parameters played a positive role in augmenting the HEH output. On the other hand, the enhanced piezoelectric properties of the BTS/PDMS films (as described earlier) caused by the highly piezoelectric BTS fillers also helped to couple the piezoelectric output electricity with triboelectric output which in turn, improved the final output performance. All these factors, as mentioned above, acted synergistically in improving the output performance of the fabricated HEH. Additional doping of BTS into PDMS beyond 15 wt% weakened the output (for 20 wt% filler loading) which is attributed to the formation of agglomerates of BTS particles inside the PDMS matrix [2,25,27]. This agglomeration of BTS particles beyond 15 wt% can also be confirmed from the decrement of the dielectric permittivity (Fig. 5.7(c)) beyond 15 wt% loading inside PDMS matrix [25]. Here, it is to be mentioned that the PET sheet, which has been used as a support structure during the device fabrication in the present work, is also a well-known triboelectric material that has been very often used as a negative triboelectric layer in triboelectric nanogenerators [33,34]. Thus, the use of this material in the present type of hybrid devices may always lead to a possibility of friction charge generation either from contact electrification from other active layers or from contact

electrification from ambient air. So, to decrease any effects due to the substrate (PET), all the HEH devices were fabricated using the same fabrication technique, including the device fabricated with bare PDMS. So, during comparison, the net effect of PET on the performance of the hybrid devices can be avoided. In addition to that, as observed from the present experiments, the devices showed a significant variation in their output performances with several inherent properties of the active BTS/PDMS layer despite the presence of a PET support structure for all of them. This proves that the effect of contact electrification of PET with ambient air (which might be present here in small amounts) is negligible compared to the effect of various physiochemical parameters of BTS/PDMS films. (If PET could render a strong effect on the output performance of the devices fabricated here, much variation of output electrical signal with the inherent properties of BTS/PDMS composites could not be observed.) Thus, it can be concluded that the output properties of the fabricated HEHs mainly depend on the properties of the used active layers and can be effectively modified with piezoelectric BTS filler loading within the PDMS matrix. As the 15 wt% BTS doped PDMS was observed as the optimal composite in the viewpoint of HEH output, it was employed for further analysis and experiments regarding real-life applications and indexed as HEH15.

In order to clarify the fundamental mechanism of output performance of the HEH15 device, in the synergistic mode consisting of both piezoelectric and triboelectric part, a systematic study where the electrical output of both the individual parts were scrutinized. The output performance of the piezoelectric (PEH15), triboelectric (TEH) (fabricated via replacing the BTS/PDMS film of the hybrid device structure), and piezo-tribo hybrid device HEH15 was observed separately. To elucidate the output electricity generation from the above three devices (PEH15, TEH, HEH15), the same force was applied to all of them. Under these mechanical stimuli, the generated peak to peak maximum output voltage and current for PEH15, TEH, and HEH15 was found to be ~ 46 V, 125 V, and 358 V (Fig. 5.7(d)) and 4.4 μA, 11 μA and 36 μA (Fig. 5.7(e)), respectively. It is worthwhile to mention here that the generated current for the

piezoelectric devices compared to the triboelectric devices are smaller. The lower value of current is quite obvious for any kind of piezoelectric energy harvesting device as the output current for such devices is directly related to the Maxwell displacement current [35,36]. Such displacement current depends upon the cross-sectional area of the device, surface polarization as well as the corresponding surface boundary. Such polarization charges only exist at the boundary surfaces. In the present case as we have used a common sandwich structure to fabricate the piezoelectric energy harvester the polarization charges utilized to generate output current only exist in the two interfaces between the positive and negative electrode and the BTS/PDMS composite. Again, the polarization charges which appear at the boundary surfaces are solely due to the presence of BTS in PDMS (which acts as the filler in the non-piezoelectric PDMS matrix). Thus, the amount of polarization charges generated is also limited as it depends upon the percentage of filler loading. This results in a lower output current of the piezoelectric device. On the other hand, the output current obtained from the triboelectric energy harvesting device can also be related to the Maxwell displacement current [37]. Thus, the output current generated from the triboelectric energy harvester depends upon the surface charge density of the triboelectric layers. Now, when the two triboelectric surfaces touch each other due to contact electrification positive and negative charges get accumulated at the positive tribo (paper) and negative triboelectric layer (PDMS). As PDMS acts as a good triboelectric material so the generated charged density on the entire surface of the PDMS and paper will be quite higher. This results in a higher triboelectric output current in comparison to the piezoelectric device. Similar, results are also obtained for other HEH devices [2,7,38]. To further check the sustainability of the fabricated device the HEH15 was subjected to continuous operation after several weeks and it does not show any considerable degradation in output performance as displayed in Fig. 5.8. These results are a clear demonstration of the fact that the incorporation of piezoelectric material inside triboelectric layer can significantly enhance the electrical output of the resulting HEH15 device.

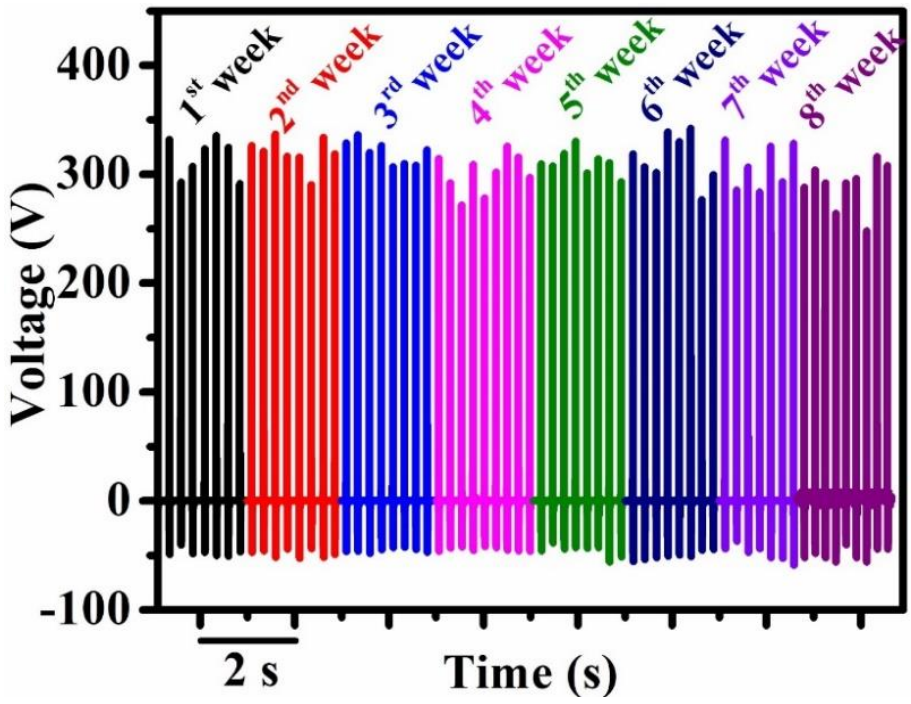

Fig. 5.8 *Output performance of HEH15 device over eight weeks.*

To investigate the maximum power generation capability of the fabricated HEH15, the external load (resistance 100 kΩ – 100 MΩ) dependent output voltage (V) (Fig. 5.7(f)) was measured. Output voltage followed the increasing nature with external load resistance and got saturated after 20 MΩ resistance. The variation of current density, as well as instantaneous power density with varying load resistance is illustrated in Fig. 5.7(f) (Current density (I/A) was simply calculated by dividing the output voltage (V) by the corresponding resistance (R) and the essential device area (A). The instantaneous power density (P) was computed using the relation $P = V^2/(R \cdot A)$. The fabricated HEH15 was able to produce a maximum instantaneous power density of 1.08 mW/cm^2 at an external resistance of 16.7 MΩ. In this regard it is worthwhile to mention here that the output performance of the fabricated HEH15 is quite comparable with the recently reported lead free $BaTiO_3$/PDMS based and energy harvesting devices where paper is used as the positive triboelectric layer as illustrated in Table 5.3 and Table 5.4, respectively.

Table 5.3 Comparison of output performance of lead-free $BaTiO_3$ impregnated PDMS based energy harvesters

Materials used	Voltage (V)		Current		Power density		Ref
	Without filler	**With filler**	**Without filler**	**With filler**	**Without filler**	**With filler**	
$BaTiO_3$/PDMS	22	72.2	0.65 µA	1.82 µA	-----	5.5 µW/cm²	[20]
$BaTiO_3$/PDMS	4	10	----	---	----	----	[21]
$BaTiO_3$ - MWCNT-PVDF/PDMS	15.23	19.26	0.54 mA/m²	0.84 mA/m²	6.23 mW/m²	4.61 mW/m²	[24]
$BaTiO_3$/PDMS	150	380	12 µA/cm²	30 µA/cm²	--	2.5 mW/cm²	[53]
$BaTiO_3$/PDMS	40	60	0.5 µA	1 µA	48.1 mW/cm²	97.41 mW/m²	[54]
Al doped $BaTiO_3$/PDMS	252	580	22.6 µA	44 µA	6.08 W/m²	28.1 W/m²	[55]
$BaTiO_3$/PDMS	120	280	0.8 µA	5.6 µA	--	0.040 mW/cm²	[56]
$BaTi_{0.89}Sn_{0.11}O_3$ /PDMS	**125**	**358**	**11 µA**	**36 µA**	**--**	**1.08 mW/cm²**	**This work**

Table 5.4 Comparison of output performance of energy harvesting devices where paper is used as a triboelectric layer.

+ve Tribo material	-ve Tribo material	electrode	Voltage (V)	Current / Current density	Power density (mW/ cm²)	Ref
Printer Paper	PTFE	Al	20	2 µA	0.0140	[32]
Printer Paper	FEP	ITO	90	0.6 µA/cm²	0.0285	[33]
Cellulose Paper	Poly(caprolactone) / GO	Au	120	2.5 mA/cm²	0.0072	[57]
Crepe Cellulose Paper	Nitrocellulose Paper	Cu	196.8	31.5 µA	1.6100	[58]
Polypyrrole / Cellulose paper	Nitrocellulose Membrane	Polypyrrole / Cellulose paper	60	-	0.0830	[59]
Paper	PTFE	Graphite	85	3.75 µA	0.0398	[60]
Cellulose nano paper	Polylactic Acid	PEDOT: PSS		0.92 µA	0.0211	[37]
Paper	Teflon Tape	Conductive ink	119	29.75 µA	0.2950	[61]
Printer Paper	**BTS/PDMS**	**Al**	**358**	**36 µA**	**1.0800**	**This work**

5.3.3.1 Feasibility of the fabricated HEH15 in real-life applications

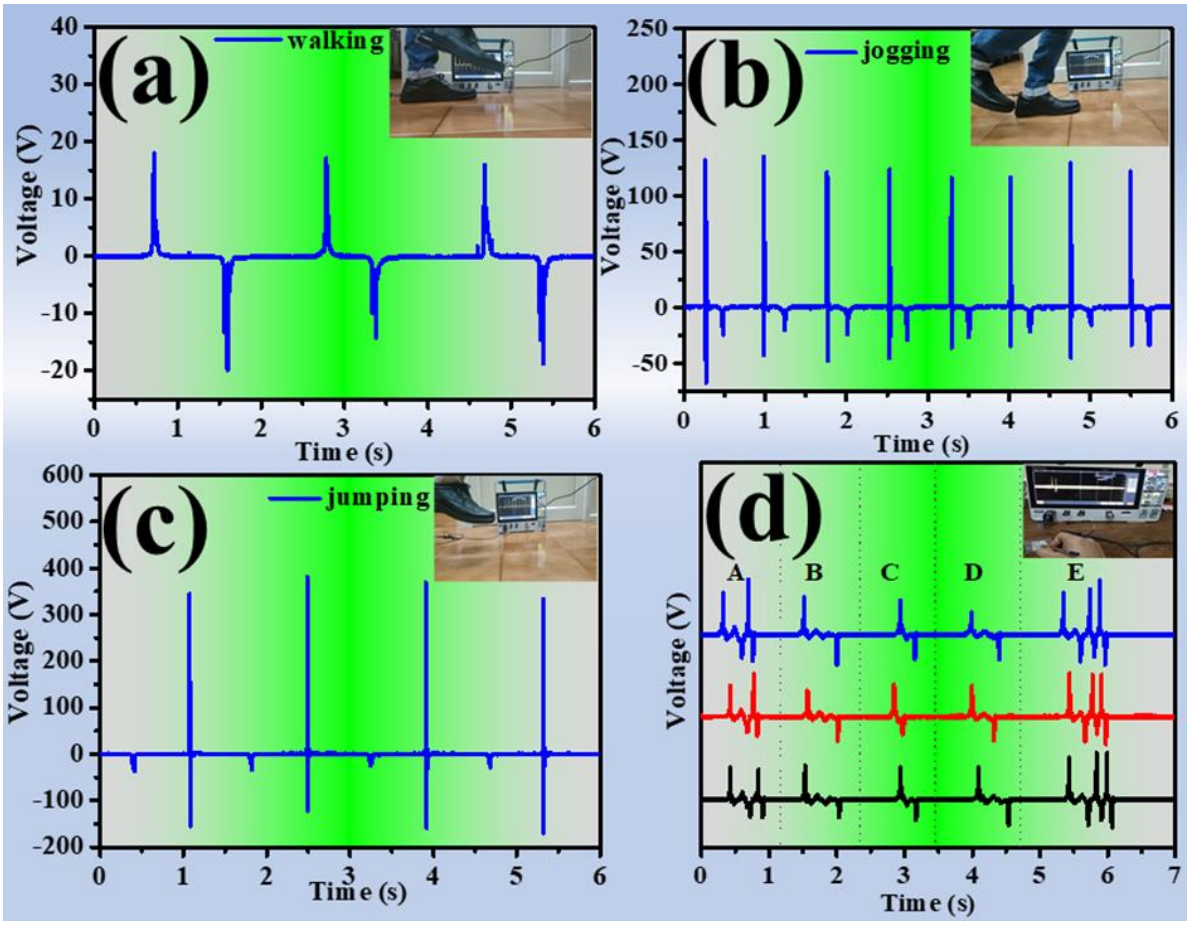

Fig. 5.9 *Measured output voltage patterns attaching the HEH device beneath the shoe from different activities (a) walking, (b)jogging, (c) jumping. (d) Generated output voltage patterns by writing English alphabet capital letters (A – E) on the HEH15 device using a pencil.*

Utilization of the human body's motion-based energy in order to generate electrical energy can revolutionize the power solutions required for modern-day flexible smart electronics. Thus, to check the real-life applicability of the fabricated device, HEH15 was further investigated to scavenge human body motion-based energy. For the sake of the presentation of harnessing mechanical energy from human body movements, the fabricated HEH15 device was affixed beneath a shoe. The appearance of a negative pulse in the voltage pattern of walking was due to the compression of the device by our foot and when the foot was removed from the device it generated a positive pulse. For jogging and jumping activity (Fig. 5.9(b) and Fig. 5.9(c)), small output signals related to the damping phenomenon occurred. This may correspond to the damping nature of the applied pressure during jogging and jumping, which was absent for walking or

finger imparting. Interestingly, this typical nature of the device can be utilized to differentiate and analyze the complications related to foot and joint movements of different human beings by collecting the output electrical signals which in turn may be very beneficial in various healthcare monitoring [51]. Therefore, the device shows a promising aspect in the field of rehabilitation purposes in the medical field.

Besides the biomechanical energy harvesting and usage of the device in the medical rehabilitation field, it can also be used to harvest and/or sense different other ambient mechanical stimuli too. To demonstrate this, the device was utilized to analyze patterns of writing and harvesting energy from this mechanical stimulus. Writing is a widely used method of communication and representative of a language. So, to harvest energy from this ever-wasted energy source we have utilized the fabricated HEH15 device as a writing pad. For demonstration purposes, only the letters 'A', 'B', 'C', 'D', and 'E' were written, and the characteristic output voltage patterns are shown in Fig. 5.9(d). The output patterns obtained via writing these letters on the device showed a significant difference between them in terms of intensity and periodicity. To observe the repeatability, the above-mentioned letters were written several times (3 times illustrated in Fig. 5.9(d)) and the generated output patterns were the same in all the cases. Thus, along with energy harvesting from writing, the device can be suitably used for code language communication for security purposes, recognition of letters in smart robotics, and smart sensing of writing. This applicability of the device can also be utilized for communication between patients and doctors for medical purposes which can improve the field of medical diagnosis. Not only in energy harvesting from writing, the fabricated device thus can be applied in energy harvesting from various other ambient mechanical stimuli if coupled suitably with the corresponding source. Thus, it is worth mentioning that the device is very effective to be applied in several real-life applications.

5.3.3.2 Wireless power transfer using HEH15 via inductor based resonant coupling technique

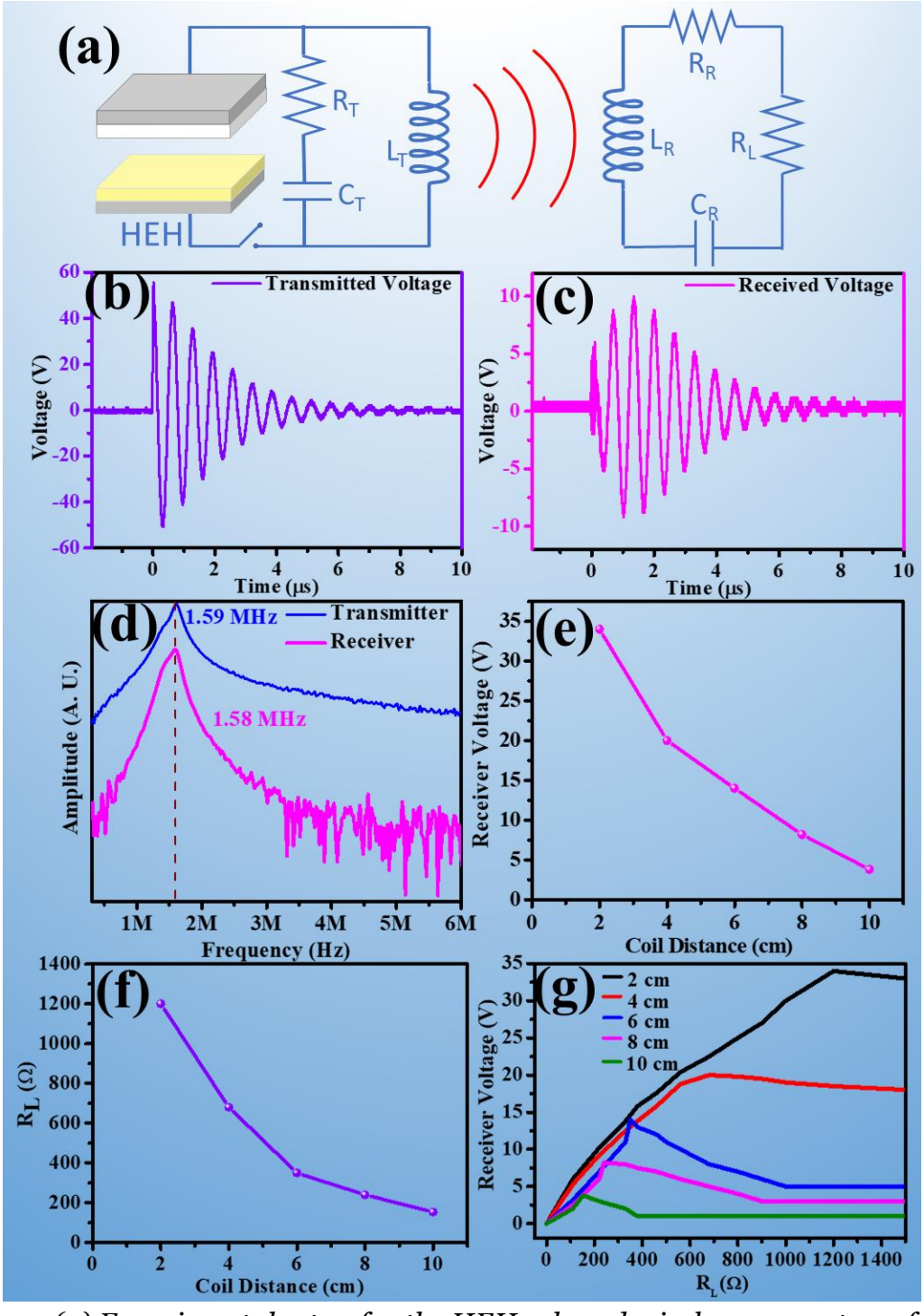

Fig. 5.10 *(a) Experimental setup for the HEH15 based wireless power transfer. The (b) transmitted and (c) received waveform patterns (voltage) when the coil distance is 4 cm and the system functions on the resonance coupled state. (d) Fast Fourier Transformation (FFT) spectra of the waveform patterns from the transmitter and the receiver. (e) Voltage at the receiver ends with the variation in coil distance. (f) Variation in load resistance (R_L) to achieve resonance coupled state with the change in coil distance. (g) Dependency in receiver voltage with the variation in load resistance (R_L) at various coil distances (2, 4, 6, 8, 10 cm).*

It is observed that portable and low-power consuming electronic devices are very often required to be applied in wireless mode, especially in bio-medical applications during diagnosis and treatments [52–55]. Therefore, in order to demonstrate the usability of the fabricated HEH15 device in a wireless power transmission system, it was utilized as the power source of the wireless power transmission system. Inductor based resonant coupling circuit was utilized here in this work for the desired wireless transmission of energy. A schematic presentation of the HEH15-powered wireless induction-based power transfer system used in the present work is shown in Fig. 5.10(a). This induction-based wireless HEH15 (IWHEH) consists of two parts, a transmitter, and a receiver. In the transmitter portion, there is the HEH15 device attached with a single contact micro switch, a tank circuit comprising of an inductor (L_T) and a capacitor (C_T), and parasitic resistance R_T [52]. Whereas, at the receiver side there is another inductor (L_R) and a capacitor (C_R) in series connection along with a parasitic resistance (R_R) and the load resistance (R_L) connected in series. Fig. 5.10(b) and 5.10(c) show the transmitter and receiver voltage signal which is measured across the inductor (L_T) and load resistance (R_L) respectively. When an alternating current generated from the HEH15 device comes to the tank circuit, it first charges the capacitor. After the capacitor gets fully charged then it starts charging the inductor. With the increment in charging current inside the inductor, it instantly produces a circular magnetic field (according to Ampere's law) around the inductor which is made by bending the copper wire into a coil. After reaching a maximum value, when the current starts decreasing, the inductor starts to supply energy back to the capacitor in the reverse direction. That is why ceramic capacitor which has both chargeable terminals have been used rather than the electrolyte capacitor. As the energy flows back and forth between the capacitor and inductor loss of energy occurs. Therefore, the produced voltage output from the transmitter part is a damped oscillating signal. As a result of this fact, the nature of the output signal collected directly from the device (Figure 5.7(a)) has been observed to be significantly different from the output signal collected from the transmitter inductor under similar input mechanical stimuli. Now, due to the presence of the receiver inductor within the created magnetic field of the transmitter inductor, electromotive force (emf) is induced which simultaneously generates an ac current in the receiver circuit [56,57]. To get the maximum output at the receiver circuit, two inductor coils were placed coaxially to each other. For a perfect coupling setup between the transmitter and the receiver, the resonant frequency of the

receiver part was modulated to the resonant frequency of the L_TC_T tank circuit. For matching the resonance frequency, primarily C_R was varied by keeping all other parameters fixed. The diameter and inductance of the coils were also fixed throughout the experiment. The resonant coupled state was achieved by varying the C_R to a value of 100 pF. The matching of the resonance frequency of the transmitter and receiver section was confirmed from the Fast Fourier Transform (FFT) of the transmitter and receiver voltage signal for the mentioned values (Table 5.5) of the components of the circuit. At this resonance condition, the measured peak to peak voltage was ~ 117 V at the transmitter part and ~ 20 V at the receiver part.

Table 5.5. Values of all the components of the IWHEH system.

Distance between two coils	**4 cm**
Diameter of the coils (L_T, L_R)	**14 cm**
Inductance (L_T, L_R)	**100 μ*H***
Resistances (R_T, R_R)	**1 *Ω*, 1 *Ω***
Capacitance (C_T + intrinsic capacitance of HEH)	**100 pF**
Capacitance (C_R)	**100 pF**
Load resistance (R_L)	**680 *Ω***

The output signal largely depends on the values of the components used to design the circuit and the resonant coupling between the transmitter and receiver. Therefore, the output receiver voltage was measured as a function of the distance between two coils keeping all other parameters the same as that mentioned in Table 5.5. Fig. 5.10(e) shows the variation in receiver voltage as a function of coil distance, which is a very common phenomenon in WPT. The peak to peak output voltage changed from ~34 V to ~20 V when the distance between the two inductor coils was changed from 2 cm to 4 cm. This decrease in receiver voltage with the increase in the distance between two coils is a very common phenomenon in WPT and is directly associated with the disturbance of resonance condition and reduction in induced electromotive force. The

resonance condition can be restored by changing the R_L value along with the variation of coil distance which are shown in Fig. 5.10(f-g). Fig. 5.10(f) shows the values of R_L required to maintain the resonance condition at a specific coil distance and Fig. 5.10(g) presents the receiver voltage as a function of both R_L and the coil distance. The occurrence of different receiver voltage at the resonance condition associated with different coil distances is directly governed by the variation of emf with the variation of coil distance. The ability of the HEH15 device to transfer power in different conditions, especially in different coil distances, thus confirmed its superiority in various real-life applications which specifically require the portable wireless power transfer technology.

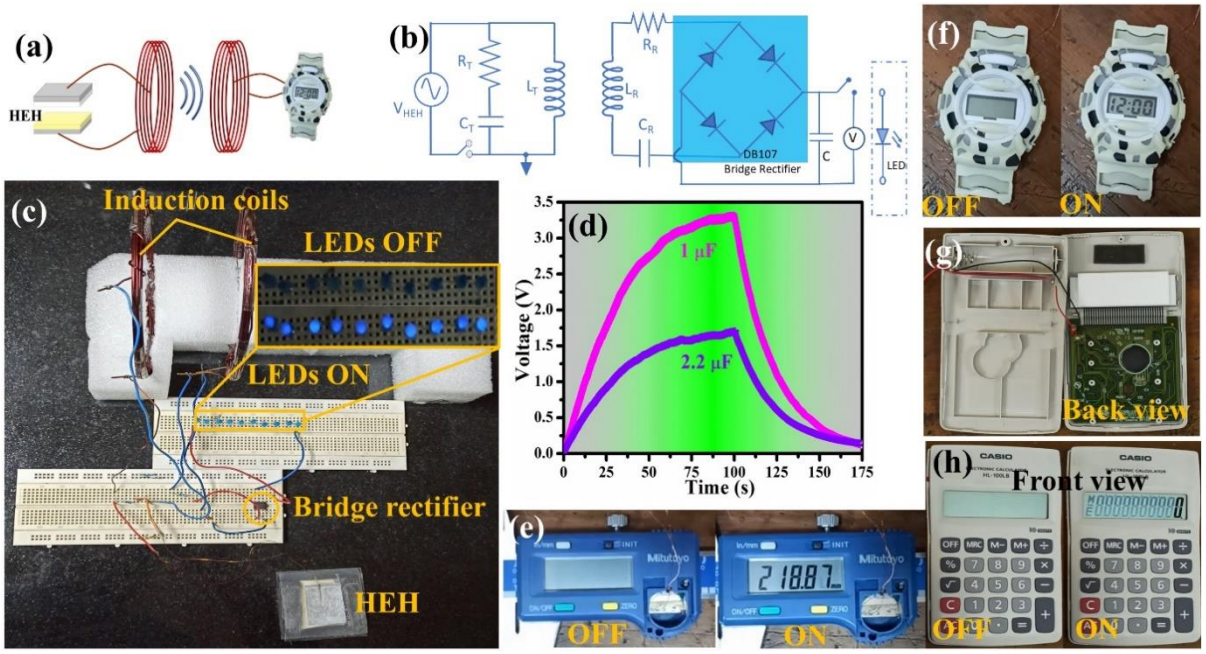

Fig. 5.11 *(a) Schematic of the wireless power transfer mechanism. (b) Circuit diagram of the wireless power transfer setup for application purposes. (c) A digital image of the used wireless power transfer system with the coil distance at 4 cm, enlarged image of the LEDs connected in series in OFF condition and ON condition. (d) Charging and discharging curves of 1 µF and 2.2 µF commercial capacitor from the voltage of rectified receiver output (transmitter coil and receiver coil are in the resonant state at a distance of 4 cm). Digital image of the corresponding OFF and ON state of wirelessly powered (e) slide callipers, (f) digital watch, (g) backside view of the batteryless connection of digital calculator, (h) front view of the calculator representing OFF and ON state of powered by wirelessly transmitted power.*

Now, to authenticate the wireless power transfer capability of the IWHEH system, some real-life applications were tested. For this purpose, the device structure was kept the same and similar mechanical stimuli were applied to the device while the coil

distance was kept constant at 4 cm. The schematic diagram of the HEH powered induction based wireless power transfer is shown in Fig. 5.11(a). The generated alternating signal from the receiver circuit, upon continuous mechanical impact on the HEH device connected to the transmitter, was rectified using a DB107 bridge rectifier IC (Fig. 5.11(b)). This generated output upon each mechanical impact was high enough to light up 10 blue LEDs connected in series which can be clearly viewed from the digital image of Fig. 5.11(c). This wirelessly transferred power was also efficient to charge several commercial capacitors. Fig. 5.11(d) clearly shows that the 1 μF and 2.2 μF capacitors were charged up to 3.3 V and 1.7 V, respectively under repeated mechanical impacting for 100 s. This stored electrical energy was capable of powering low powered electronic gadgets like electronic calculator, digital watch, and digital slide callipers (Fig. 5.11(d-f)). Despite various damping in the wireless power transfer circuit, the fabricated HEH device was able to transfer sufficient power to power up the electronic devices which proved its potentiality and high efficacy. Thus, it can be inferred that the fabricated optimized HEH is quite capable of powering up various small and portable electronic devices via a wireless power transfer mechanism. This technology may therefore be very useful for various purposes, especially in biomedical applications such as wireless charging of batteries used in pacemakers and other implanted devices.

5.4. Conclusions

Lead-free morphotropic phase boundary composition $BaTi_{0.89}Sn_{0.11}O_3$ (BTS) was synthesized via the modified Pechini method. Due to four phase coexistence, BTS showed piezoelectric charge coefficient (d_{33}) of ~ 412 pC/N. BTS incorporated PDMS based composite films were further arranged suitably with normal printer paper to fabricate a piezo tribo hybrid energy harvester device. The coupling of high piezoelectricity along with high relative permittivity of BTS fillers inside PDMS augmented the output voltage by 200 %. The generated optimized output voltage, output current, and instantaneous power density by the HEH device were 358 V, 36 μA, and 1.08 mW/cm^2, respectively. Moreover, the optimized device was used for different biomechanical energy harvesting. It was found to be very suitable for analyzing writing patterns which could be suitably used in smart robotics and code-

language communication for security purposes. Furthermore, the device was successfully utilized as a power source for induction based real time wireless power transmission. The real-life application of wirelessly transmitted output power was experimentally confirmed through charging capacitors, powering low-powered electronic gadgets such as a digital watch, electronic calculator, slide callipers, and lighting up LEDs. Thus, the present technology paves the way for different real-life applications including biomedical fields.

Chapter 5

References

[1] A. Chen, C. Zhang, G. Zhu, Z.L. Wang, Polymer Materials for High-Performance Triboelectric Nanogenerators, Advanced Science. 7 (2020). https://doi.org/10.1002/advs.202000186.

[2] F. Jiang, X. Zhou, J. Lv, J. Chen, J. Chen, H. Kongcharoen, Y. Zhang, P.S. Lee, Stretchable, Breathable, and Stable Lead-Free Perovskite/Polymer Nanofiber Composite for Hybrid Triboelectric and Piezoelectric Energy Harvesting, Advanced Materials. 34 (2022). https://doi.org/10.1002/adma.202200042.

[3] P. Zhang, W. Zhang, L. Deng, H. Zhang, A triboelectric nanogenerator based on temperature-stable high dielectric BaTiO3-based ceramic powder for energy harvesting, Nano Energy. 87 (2021). https://doi.org/10.1016/j.nanoen.2021.106176.

[4] G. Suo, Y. Yu, Z. Zhang, S. Wang, P. Zhao, J. Li, X. Wang, Piezoelectric and Triboelectric Dual Effects in Mechanical-Energy Harvesting Using BaTiO3/Polydimethylsiloxane Composite Film, ACS Appl Mater Interfaces. 8 (2016) 34335–34341. https://doi.org/10.1021/acsami.6b11108.

[5] H. Patnam, B. Dudem, N.R. Alluri, A.R. Mule, S.A. Graham, S.J. Kim, J.S. Yu, Piezo/triboelectric hybrid nanogenerators based on Ca-doped barium zirconate titanate embedded composite polymers for wearable electronics, Compos Sci Technol. 188 (2020). https://doi.org/10.1016/j.compscitech.2019.107963.

[6] S. Maity, A. Sasmal, S. Sen, Comprehensive characterization of Ba1−xSrxTiO3: Correlation between structural and multifunctional properties, J Alloys Compd. 884 (2021). https://doi.org/10.1016/j.jallcom.2021.161072.

[7] B. Dudem, L.K. Bharat, H. Patnam, A.R. Mule, J.S. Yu, Enhancing the output performance of hybrid nanogenerators based on Al-doped BaTiO3 composite films: A self-powered utility system for portable electronics, J Mater Chem A Mater. 6 (2018) 16101–16110. https://doi.org/10.1039/c8ta04612c.

[8] X. Yang, W.A. Daoud, Synergetic effects in composite-based flexible hybrid mechanical energy harvesting generator, J Mater Chem A Mater. 5 (2017) 9113–9121. https://doi.org/10.1039/c7ta01524k.

[9] N.P. Maria Joseph Raj, N.R. Alluri, G. Khandelwal, S.J. Kim, Ferroelectric flexible composite films based on morphotropic phase boundary for self-powered multisensors, Chemical Engineering Journal. 414 (2021). https://doi.org/10.1016/j.cej.2021.128840.

[10] S.P. Muduli, S. Veeralingam, S. Badhulika, Multilayered Piezoelectric Nanogenerator Based on Lead-Free Poly(vinylidene fluoride)-(0.67BiFeO3-0.33BaTiO3) Electrospun Nanofiber Mats for Fast Charging of Supercapacitors, ACS Appl Energy Mater. 5 (2022) 2993–3003. https://doi.org/10.1021/acsaem.1c03648.

[11] T. Avanish Babu, W. Madhuri, A hybrid microwave sintered PZT composite as a flexible piezoelectric nanogenerator, RSC Adv. 12 (2022) 34454–34462. https://doi.org/10.1039/d2ra05570h.

[12] M. Anithkumar, A.P.S. Prasanna, N.R. Alluri, S. Kim, Self-Powered Smart Touchpad using Novel Intrinsic Piezo–Tribo Hybrid Nanogenerator, Adv Funct Mater. (2023) 2213907. https://doi.org/10.1002/adfm.202213907.

[13] D. Wang, Z. Fan, G. Rao, G. Wang, Y. Liu, C. Yuan, T. Ma, D. Li, X. Tan, Z. Lu, A. Feteira, S. Liu, C. Zhou, S. Zhang, Ultrahigh piezoelectricity in lead-free piezoceramics by synergistic design, Nano Energy. 76 (2020). https://doi.org/10.1016/j.nanoen.2020.104944.

[14] Q. Zhao, H. Xiao, G. Huangfu, Z. Zheng, J. Wang, F. Wang, Y. Guo, Highly-efficient piezocatalytic performance of nanocrystalline BaTi0.89Sn0.11O3 catalyst with Tc near room temperature, Nano Energy. 85 (2021). https://doi.org/10.1016/j.nanoen.2021.106028.

[15] L.F. Zhu, B.P. Zhang, X.K. Zhao, L. Zhao, F.Z. Yao, X. Han, P.F. Zhou, J.F. Li, Phase transition and high piezoelectricity in (Ba,Ca)(Ti 1-xSnx)O3 lead-free ceramics, Appl Phys Lett. 103 (2013). https://doi.org/10.1063/1.4818732.

[16] J. Wu, Perovskite lead-free piezoelectric ceramics, J Appl Phys. 127 (2020) 190901. https://doi.org/10.1063/5.0006261.

[17] S.M. Mukhopadhyay, T.C.S. Chen, Surface chemical states of barium titanate: Influence of sample processing, J Mater Res. 10 (1995) 1502–1507. https://doi.org/10.1557/JMR.1995.1502.

[18] Y. Bao, B. Huang, K. Zhou, J. Roscow, E. Roake, M. Hopkins, D. Zhang, Y. Zhang, C. Bowen, Hierarchically structured lead-free barium strontium titanate for low-grade thermal energy harvesting, Ceram Int. 47 (2021) 18761–18772. https://doi.org/10.1016/j.ceramint.2021.03.211.

[19] H. Jena, V.K. Mittal, S. Bera, S. V. Narasimhan, K.V.G. Kutty, T.R.N. Kutty, X-ray photoelectron spectroscopic investigations on cubic BaTiO 3 , BaTi 0.9 Fe 0.1 O 3 and Ba 0.9 Nd 0.1 TiO 3 systems, Appl Surf Sci. 254 (2008) 7074–7079. https://doi.org/10.1016/j.apsusc.2008.05.316.

[20] C. Cui, Y. Pu, Effect of Sn substitution on the energy storage properties of 0.45SrTiO3–0.2Na0.5Bi0.5TiO3–0.35BaTiO3 ceramics, J Mater Sci. 53 (2018) 9830–9841. https://doi.org/10.1007/s10853-018-2282-8.

[21] M.E. Pilleux, C.R. Grahmann, V.M. Fuenzalida, Hydrothermal Strontium Titanate Films on Titanium: An XPS and AES Depth-Profiling Study, Journal of the American Ceramic Society. 77 (1994) 1601–1604. https://doi.org/10.1111/j.1151-2916.1994.tb09763.x.

[22] T. Tanaka, M. Kozako, N. Fuse, Y. Ohki, Proposal of a multi-core model for polymer nanocomposite dielectrics, IEEE Transactions on Dielectrics and Electrical Insulation. 12 (2005) 669–681. https://doi.org/10.1109/TDEI.2005.1511092.

[23] A. Sasmal, S. Sen, P.S. Devi, Frequency dependent energy storage and dielectric performance of Ba-Zr Co-doped BiFeO3loaded PVDF based mechanical energy harvesters: Effect of corona poling, Soft Matter. 16 (2020) 8492–8505. https://doi.org/10.1039/d0sm01031f.

[24] C. Zhao, H. Wang, J. Xiong, J. Wu, Composition-driven phase boundary and electrical properties in (Ba0.94Ca0.06)(Ti1-xMx)O3 (M = Sn, Hf, Zr) lead-free ceramics, Dalton Transactions. 45 (2016) 6466–6480. https://doi.org/10.1039/c5dt04891e.

[25] P. Manchi, S.A. Graham, B. Dudem, H. Patnam, J.S. Yu, Improved performance of nanogenerator via synergetic piezo/triboelectric effects of lithium niobate microparticles embedded composite films, Compos Sci Technol. 201 (2021). https://doi.org/10.1016/j.compscitech.2020.108540.

[26] W. He, Y. Qian, B.S. Lee, F. Zhang, A. Rasheed, J.E. Jung, D.J. Kang, Ultrahigh Output Piezoelectric and Triboelectric Hybrid Nanogenerators Based on ZnO Nanoflakes/Polydimethylsiloxane Composite Films, ACS Appl Mater Interfaces. 10 (2018) 44415–44420. https://doi.org/10.1021/acsami.8b15410.

[27] D.H. Kim, B. Dudem, J.S. Yu, High-Performance Flexible Piezoelectric-Assisted Triboelectric Hybrid Nanogenerator via Polydimethylsiloxane-Encapsulated Nanoflower-like ZnO Composite Films for Scavenging Energy from Daily Human Activities, ACS Sustain Chem Eng. 6 (2018) 8525–8535. https://doi.org/10.1021/acssuschemeng.8b00834.

[28] D. Bhattacharya, S. Mukherjee, A.N. Pal, R.K. Mitra, S.K. Ray, Two-Dimensional MoxW1−xS2 Alloys for Nanogenerators Producing Record Piezo-Output and Coupled Photodetectors for Self-Powered UV Sensor, Adv Opt Mater. 10 (2022). https://doi.org/10.1002/adom.202200353.

[29] S. Ippili, V. Jella, A.M. Thomas, C. Yoon, J.S. Jung, S.G. Yoon, ZnAl-LDH-induced electroactive β-phase and controlled dielectrics of PVDF for a high-performance triboelectric nanogenerator for humidity and pressure sensing applications, J Mater Chem A Mater. 9 (2021) 15993–16005. https://doi.org/10.1039/d1ta02966e.

[30] J. Wang, C. Wu, Y. Dai, Z. Zhao, A. Wang, T. Zhang, Z.L. Wang, Achieving ultrahigh triboelectric charge density for efficient energy harvesting, Nat Commun. 8 (2017). https://doi.org/10.1038/s41467-017-00131-4.

[31] M. Sahu, S. Hajra, J. Bijelic, D. Oh, I. Djerdj, H.J. Kim, Triple perovskite-based triboelectric nanogenerator: a facile method of energy harvesting and self-powered information generator, Mater Today Energy. 20 (2021). https://doi.org/10.1016/j.mtener.2021.100639.

[32] K. Shi, H. Zou, B. Sun, P. Jiang, J. He, X. Huang, Dielectric Modulated Cellulose Paper/PDMS-Based Triboelectric Nanogenerators for Wireless Transmission and Electropolymerization Applications, Adv Funct Mater. 30 (2020). https://doi.org/10.1002/adfm.201904536.

[33] S.H. Shin, Y.E. Bae, H.K. Moon, J. Kim, S.H. Choi, Y. Kim, H.J. Yoon, M.H. Lee, J. Nah, Formation of Triboelectric Series via Atomic-Level Surface Functionalization for Triboelectric Energy Harvesting, ACS Nano. 11 (2017) 6131–6138. https://doi.org/10.1021/acsnano.7b02156.

[34] B. Zhang, Y. Tang, R. Dai, H. Wang, X. Sun, C. Qin, Z. Pan, E. Liang, Y. Mao, Breath-based human–machine interaction system using triboelectric nanogenerator, Nano Energy. 64 (2019). https://doi.org/10.1016/j.nanoen.2019.103953.

[35] Z.L. Wang, On Maxwell's displacement current for energy and sensors: the origin of nanogenerators, Materials Today. 20 (2017) 74–82. https://doi.org/10.1016/j.mattod.2016.12.001.

[36] L. Gu, J. Liu, N. Cui, Q. Xu, T. Du, L. Zhang, Z. Wang, C. Long, Y. Qin, Enhancing the current density of a piezoelectric nanogenerator using a three-dimensional intercalation electrode, Nat Commun. 11 (2020). https://doi.org/10.1038/s41467-020-14846-4.

[37] H. Zhang, L. Yao, L. Quan, X. Zheng, Theories for triboelectric nanogenerators: A comprehensive review, 9 (2020) 610–625. https://doi.org/doi:10.1515/ntrev-2020-0049.

[38] S. Hajra, A.M. Padhan, M. Sahu, P. Alagarsamy, K. Lee, H.J. Kim, Lead-free flexible Bismuth Titanate-PDMS composites: A multifunctional colossal dielectric material for hybrid piezo-triboelectric nanogenerator to sustainably power portable electronics, Nano Energy. 89 (2021). https://doi.org/10.1016/j.nanoen.2021.106316.

[39] Y.H. Kwon, S.H. Shin, Y.H. Kim, J.Y. Jung, M.H. Lee, J. Nah, Triboelectric contact surface charge modulation and piezoelectric charge inducement using polarized composite thin film for performance enhancement of triboelectric

generators, Nano Energy. 25 (2016) 225–231. https://doi.org/10.1016/j.nanoen.2016.05.002.

[40] B. Shi, Q. Zheng, W. Jiang, L. Yan, X. Wang, H. Liu, Y. Yao, Z. Li, Z.L. Wang, A Packaged Self-Powered System with Universal Connectors Based on Hybridized Nanogenerators, Advanced Materials. 28 (2016) 846–852. https://doi.org/10.1002/adma.201503356.

[41] B. Dudem, L.K. Bharat, H. Patnam, A.R. Mule, J.S. Yu, Enhancing the output performance of hybrid nanogenerators based on Al-doped BaTiO3 composite films: A self-powered utility system for portable electronics, J Mater Chem A Mater. 6 (2018) 16101–16110. https://doi.org/10.1039/c8ta04612c.

[42] M. Sahu, V. Vivekananthan, S. Hajra, K. Khatua, S.-J. Kim, Porosity modulated piezo-triboelectric hybridized nanogenerator for sensing small energy impacts, (2020). https://doi.org/10.1016/j.apmt.2020.10.

[43] P.K. Yang, Z.H. Lin, K.C. Pradel, L. Lin, X. Li, X. Wen, J.H. He, Z.L. Wang, Paper-based origami triboelectric nanogenerators and self-powered pressure sensors, ACS Nano. 9 (2015) 901–907. https://doi.org/10.1021/nn506631t.

[44] X. He, Y. Zi, H. Yu, S.L. Zhang, J. Wang, W. Ding, H. Zou, W. Zhang, C. Lu, Z.L. Wang, An ultrathin paper-based self-powered system for portable electronics and wireless human-machine interaction, Nano Energy. 39 (2017) 328–336. https://doi.org/10.1016/j.nanoen.2017.06.046.

[45] S. Parandeh, M. Kharaziha, F. Karimzadeh, An eco-friendly triboelectric hybrid nanogenerators based on graphene oxide incorporated polycaprolactone fibers and cellulose paper, Nano Energy. 59 (2019) 412–421. https://doi.org/10.1016/j.nanoen.2019.02.058.

[46] S. Chen, J. Jiang, F. Xu, S. Gong, Crepe cellulose paper and nitrocellulose membrane-based triboelectric nanogenerators for energy harvesting and self-powered human-machine interaction, Nano Energy. 61 (2019) 69–77. https://doi.org/10.1016/j.nanoen.2019.04.043.

[47] X. Shi, S. Chen, H. Zhang, J. Jiang, Z. Ma, S. Gong, Portable Self-Charging Power System via Integration of a Flexible Paper-Based Triboelectric Nanogenerator

and Supercapacitor, ACS Sustain Chem Eng. 7 (2019) 18657–18666. https://doi.org/10.1021/acssuschemeng.9b05129.

[48] X.S. Zhang, M. Su, J. Brugger, B. Kim, Penciling a triboelectric nanogenerator on paper for autonomous power MEMS applications, Nano Energy. 33 (2017) 393–401. https://doi.org/10.1016/j.nanoen.2017.01.053.

[49] X. Gao, L. Huang, B. Wang, D. Xu, J. Zhong, Z. Hu, L. Zhang, J. Zhou, Natural Materials Assembled, Biodegradable, and Transparent Paper-Based Electret Nanogenerator, ACS Appl Mater Interfaces. 8 (2016) 35587–35592. https://doi.org/10.1021/acsami.6b12913.

[50] K. Xia, H. Zhang, Z. Zhu, Z. Xu, Folding triboelectric nanogenerator on paper based on conductive ink and teflon tape, Sens Actuators A Phys. 272 (2018) 28–32. https://doi.org/10.1016/j.sna.2018.01.054.

[51] M. Sahu, V. Vivekananthan, S. Hajra, K.S. Abisegapriyan, N.P. Maria Joseph Raj, S.J. Kim, Synergetic enhancement of energy harvesting performance in triboelectric nanogenerator using ferroelectric polarization for self-powered IR signaling and body activity monitoring, J Mater Chem A Mater. 8 (2020) 22257–22268. https://doi.org/10.1039/d0ta06215d.

[52] C. Zhang, J. Chen, W. Xuan, S. Huang, B. You, W. Li, L. Sun, H. Jin, X. Wang, S. Dong, J. Luo, A.J. Flewitt, Z.L. Wang, Conjunction of triboelectric nanogenerator with induction coils as wireless power sources and self-powered wireless sensors, Nat Commun. 11 (2020). https://doi.org/10.1038/s41467-019-13653-w.

[53] M. Haghi, K. Thurow, R. Stoll, Wearable devices in medical internet of things: Scientific research and commercially available devices, Healthc Inform Res. 23 (2017) 4–15. https://doi.org/10.4258/hir.2017.23.1.4.

[54] Basar M. R,; Ahmad M. Y,; Cho J,; and Ibrahim F. An Improved Wearable Resonant Wireless Power Transfer System for Biomedical Capsule Endoscope, in IEEE Transactions on Industrial Electronics, 2018, 65, 10, 7772-7781, DOI: 10.1109/TIE.2018.2801781.

[55] R. Das, H. Yoo, A Multiband Antenna Associating Wireless Monitoring and Nonleaky Wireless Power Transfer System for Biomedical Implants, IEEE Trans Microw Theory Tech. 65 (2017) 2485–2495. https://doi.org/10.1109/TMTT.2017.2647945.

[56] Shinohara N.; The Wireless Power Transmission: Inductive Coupling, Radio Wave, and Resonance Coupling, Wiley Interdiscip. Rev. Energy Environ. 2012, 1(3), 337–346, DOI: 10.1002/wene.43.

[57] M.A. Houran, X. Yang, W. Chen, Magnetically coupled resonance wpt: Review of compensation topologies, resonator structures with misalignment, and emi diagnostics, Electronics (Switzerland). 7 (2018). https://doi.org/10.3390/electronics7110296.

Related video file links

Walking
https://pubs.acs.org/doi/suppl/10.1021/acsaem.3c00635/suppl_file/ae3c00635_si_002.mp4

Jogging

https://pubs.acs.org/doi/suppl/10.1021/acsaem.3c00635/suppl_file/ae3c00635_si_003.mp4

Jumping

https://pubs.acs.org/doi/suppl/10.1021/acsaem.3c00635/suppl_file/ae3c00635_si_004.mp4

Writing patterns

https://pubs.acs.org/doi/suppl/10.1021/acsaem.3c00635/suppl_file/ae3c00635_si_005.mp4

Led glowing

https://pubs.acs.org/doi/suppl/10.1021/acsaem.3c00635/suppl_file/ae3c00635_si_006.mp4

Chapter 6

Conclusions and Future Perspectives

6.1. Conclusions

In this dissertation, the major research accomplishments achieved during Ph.D. studies are presented. The primary research objectives centered on the development of high-performance piezoelectric assisted triboelectric hybrid energy harvesters (HEH) with specific attributes, including increased output properties in terms of output voltage and current, flexibility, and versatile functionality. Another key aim was to discover innovative applications for HEH technology that can offer cost-effective, safe, convenient solutions to address energy challenges, specific sensing, as well as smart applications. In this chapter, a concise summary of achievements and a proposal of the roadmap for future HEH research for further exploration and advancement in this field were explored. Through the literature review and background study which is covered in Chapter 1, it is evident that there are various types of approaches to augment the power generation capability of piezoelectric and triboelectric energy harvesters. One of the best strategies to manipulate output properties was to load the functional polymer layers with piezoelectric ceramic materials. Therefore, the portion of synthesis of ceramic materials and ceramic/polymer composite films, fabrication of piezoelectric, triboelectric, and hybrid energy harvesters and the characterizations of various parameters which were carried out during my dissertation work are depicted in Chapter 2.

In Chapter 3, Barium Strontium Titanate/ PVDF-based composite films were studied for piezoelectric energy harvesting. This chapter deals with the connection between the structural attributes and multifunctional properties within the $Ba_{(1-x)}Sr_xTiO_3$ System (where, x=0.0, 0.2, 0.4, 0.6, 0.8, 1.0) and the optimization of the composition which will be used for the synthesis of polymer composite. For this purpose, $Ba_{(1-x)}Sr_xTiO_3$ (x=0.0, 0.2, 0.4, 0.6, 0.8, 1.0) particles were synthesized using solid state method. XRD study proved a structural phase transition from a non-centrosymmetric ferroelectric state to a centrosymmetric paraelectric phase near x = 0.4. Raman spectra of all the samples supported the XRD results and also confirmed the presence of polar nanoregions for $Ba_{0.6}Sr_{0.4}TiO_3$ (BST40) sample. Among all these

compositions, BST40 showed maximum room temperature dielectric permittivity (~ 4000 at 1 kHz) with good frequency and thermal stability. Moreover, this sample exhibited a comparatively lower value of dielectric loss tangent than that of undoped $BaTiO_3$. Along with these advantageous attributes, leakage current density is also very low which makes it a worthy filler material for composite synthesis. Then this BST40 was utilized as the filler material which was embedded in the PVDF matrix. Taking the advantage of negative Zeta potential of BST40, the $-CH_2$ dipole of PVDF interacted with it and resulted in an increment in the electroactive polar phase. Then that composite was employed for piezoelectric energy harvesting and self-powered mechanosensing applications. This composite film was capable of generating maximum output voltage and output power density of 15 V and 6.75 $\mu W/cm^2$ respectively on repeated human finger tapping. In the context of energy harvesting, the BST40/PVDF-based composite film displayed limited promise, primarily due to the constraints imposed by BST40's centrosymmetric crystal structure.

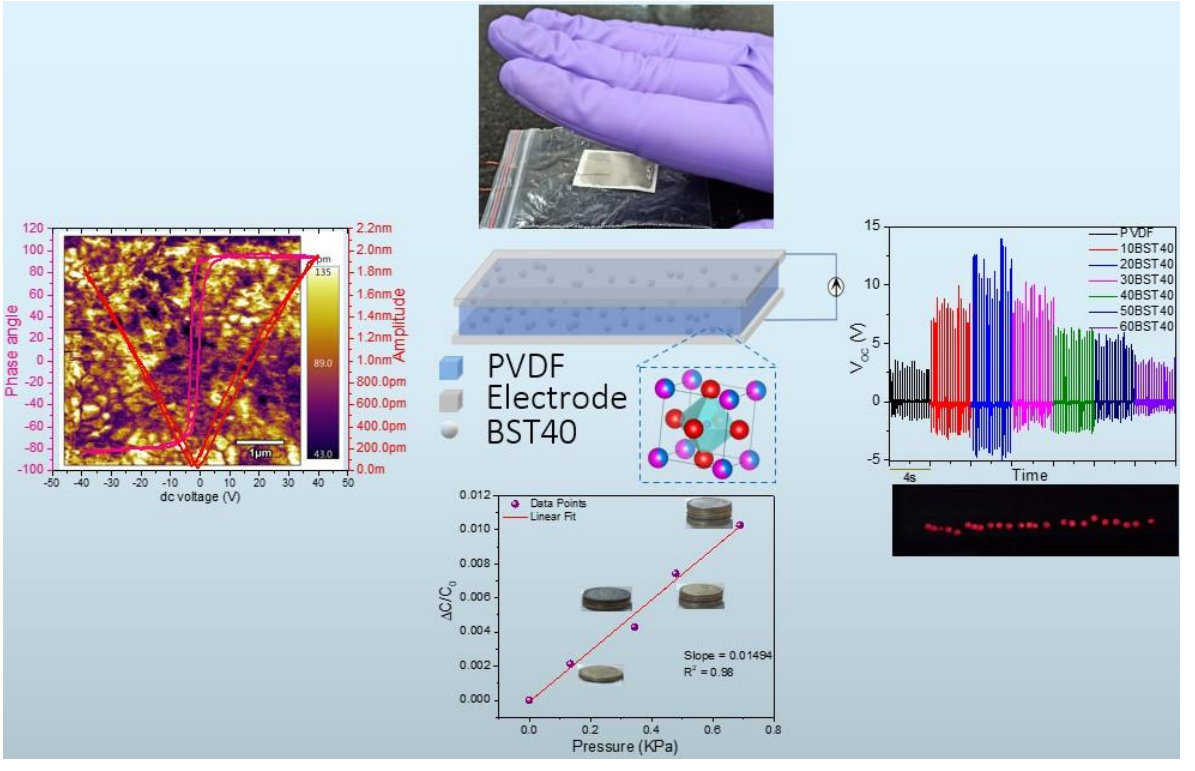

Fig. 6.1 *Summarization of Chapter 3.*

In Chapter 4, the limitation posed by BST40's centrosymmetric crystal structure was addressed by introducing $(Ba_{0.85}Ca_{0.15})(Ti_{0.90}Hf_{0.10})O_3$ (BCHT) particles. These BCHT particles had a notably high piezoelectric charge coefficient of 333 pC/N

and were incorporated as fillers to create flexible BCHT/PVDF composites. This strategic addition significantly bolstered the piezoelectric energy harvesting capabilities as perovskite BCHT particles served as nucleation centers, aligning the PVDF polymer chains in a trans conformation. This alignment increased the fraction of electroactive phases within the composite and enhanced its ability to trap electrons. The infusion of piezoelectric BCHT fillers resulted in notable improvements in both the piezoelectric and dielectric properties of the composite films. The enhanced piezoelectric properties of these composites, in turn, had a positive impact on the performance of the energy harvesting (HEH) device. By effectively harnessing the triboelectric effect within the system, the HEH device achieved a maximum output voltage of approximately 396 V and a current of about 30 μA, highlighting an instantaneous power density of 1.72 mW/cm^2. This remarkable performance boost was attributed to the successful synergy between the piezoelectric and triboelectric effects. Furthermore, the HEH device exhibited efficient electromechanical conversion capabilities, enabling it to capture energy from various body movements, such as those of the heel, toe, wrist, elbow, and even fine finger motions. Ultimately, the fabricated HEH device found practical application as a self-powered sensor in the development of smart home and smart parking systems. With its impressive power generation capacity and emphasis on wireless technology, this HEH device emerged as an adaptable and portable energy source for flexible smart electronics.

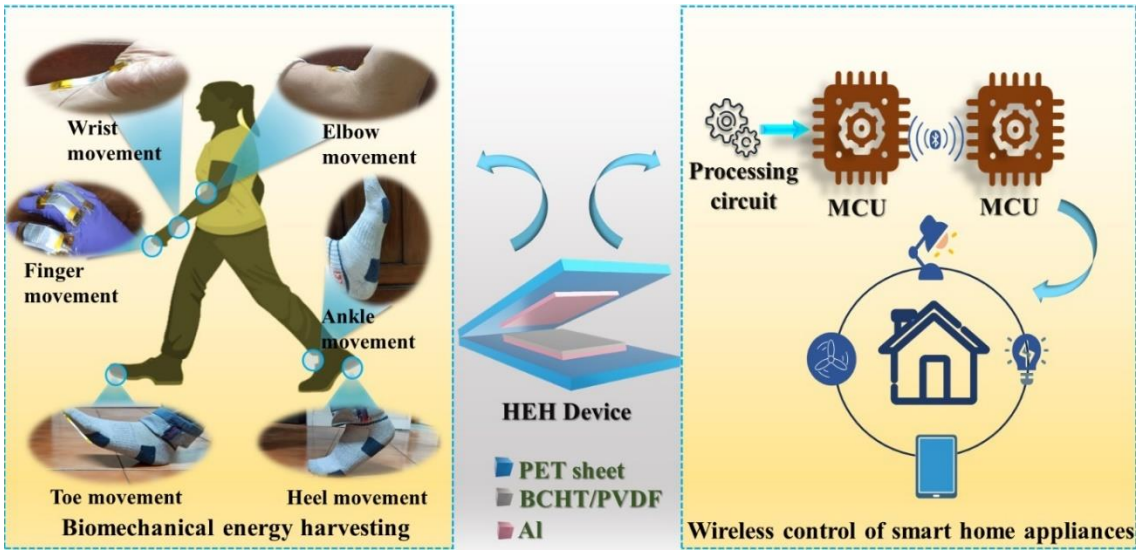

Fig. 6.2 *Summarization of Chapter 4.*

Now in Chapter 5, the idea of piezoelectric-assisted triboelectric hybrid energy harvester was again implemented in another HEH device where lead-free morphotropic phase boundary composition $BaTi_{0.89}Sn_{0.11}O_3$ (BTS) was synthesized via the modified Pechini method. Due to four phase coexistence, BTS showed a piezoelectric charge coefficient (d_{33}) of ~ 412 pC/N. Here, this time our focus was shifted towards another negative triboelectric polymer matrix which is PDMS instead of PVDF. BTS-incorporated PDMS-based composite films were further arranged suitably with normal printer paper to fabricate a piezo tribo hybrid energy harvester device. The generated optimized output voltage, output current, and instantaneous power density by the HEH device were ~358 V, 36 μA, and 1.08 mW/cm², respectively. Moreover, the optimized device was used for different biomechanical energy harvesting like walking, jogging, and running. It was found to be very suitable for analyzing writing patterns written on it which could be suitably used in smart robotics and code-language communication for security purposes. Furthermore, the device was successfully utilized as a power source for induction-based real-time wireless power transmission. The real-life application of wirelessly transmitted output power was experimentally confirmed by charging capacitors, powering low-powered electronic gadgets such as digital watches, electronic calculators, slide calipers, and lighting up LEDs. Thus, the present technology paves the way for different real-life applications including biomedical fields.

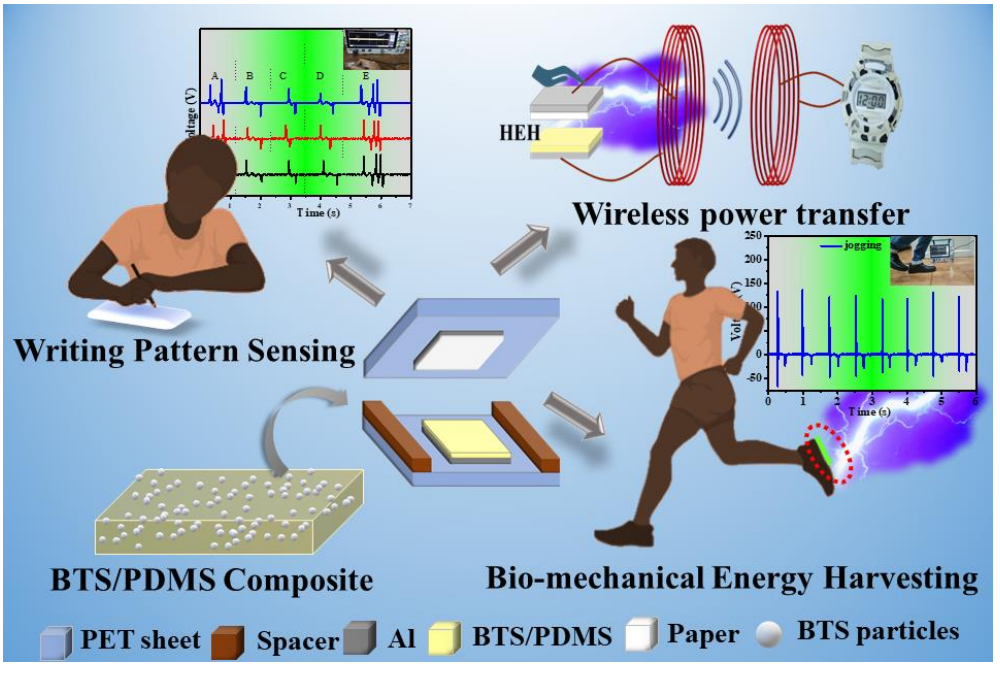

Fig. 6.3 *Summarization of Chapter 5.*

6.2. Future perspectives

This interdisciplinary study placed a significant emphasis on presenting methods for optimizing the performance of piezoelectric assisted triboelectric hybrid energy harvester. Nevertheless, there are several critical areas that require additional research efforts to address, enhance, and further refine the conclusions in this thesis.

1. Firstly, the filler material possesses a very high dielectric permittivity whereas, PVDF/PDMS is characterized with a low permittivity polymer material. That is why there is a significant gap in dielectric permittivity between these two materials, which deteriorates the homogeneity of the filler material inside PVDF matrix and simultaneously decreases breakdown strength. To compromise this effect, approaches like several coatings (SiO_2, TiO_2, Al_2O_3 etc.) of lower dielectric permittivity materials around the filler material can be pivotal solution which will enhance the uniformity of filler material as well as the breakdown strength. In the meantime, this effect will enhance the durability of the functional material as well as the energy harvesting device.

2. Though the output voltage generated from HEH device is high but output current generated from the HEH device is of μA range. The limited current output does not provide an adequate power supply for larger electronic devices or applications that demand significant energy. To overcome this shortcoming and to enhance the output current towards few hundreds of μA or in mA range, various approaches including conducting material incorporation and ion implantation on the functional layer can be done.

3. Generally, the output generated from the HEH device is of AC pattern. For application purposes we convert it to a dc and then utilize it for several real-life applications. Now, fabrication of dc hybrid energy harvester device can be done with the help of structural modification and simple engineering.

4. The present dissertation deals with the solid-solid interface energy harvester devices. However, for rain water energy harvesting, ocean energy harvesting solid – liquid interface energy harvester device can be structured.

5. Finally, fabrication of a single setup where energy harvesting as well as energy storage can be done. To put it simply, energy storage plays a vital role in energy harvesting systems, allowing for effective, dependable, and adaptable energy utilization. It guarantees the ability to capture, store, and deploy energy as required, even when dealing with sporadic and fluctuating energy sources.

Appendix

List of Publications

SCI Journal Publications

(i) From this Thesis work

1. **S. Maity**, E. Kar, A. Kar, and S. Sen. "Multiphase Coexisted Perovskite/PVDF Composite Derived Wearable Piezo-Tribo Hybrid Energy Harvester for Wireless Smart Applications". **Chemical Engineering Journal,** 2023, 474, 145959**.**
2. **S. Maity**, A. Sasmal, E. Kar, and S. Sen. "Morphotropic Phase Boundary-Assisted Lead-Free $BaTiO_3$/PDMS Composite-Based Hybrid Energy Harvester: A Portable Power Source for Wireless Power Transmission." **ACS Applied Energy Materials**, 2023, 6 (13), 7052-7064.
3. **S. Maity**, A. Sasmal, S. Sen, "Barium Titanate based paraelectric material incorporated Poly(vinylidene fluoride) for Biomechanical Energy Harvesting and Self-Powered Mechanosensing", **Materials Science in Semiconductor Processing**, 2023, 153, 107128.
4. **S. Maity**, A. Sasmal, S. Sen, Comprehensive characterization of $Ba_{(1-x)}Sr_xTiO_3$: Correlation between structural and multifunctional properties. **Journal of Alloys and Compounds**, 2021, 884, 161072.

(ii) Not from this Thesis work

1. S. Sen, **S. Maity**, S. Kundu "Fabrication of Fe doped reduced graphene oxide (rGO) decorated WO_3 based low temperature ppm level acetone sensor: Unveiling sensing mechanism by impedance spectroscopy", **Sensors and Actuators B: Chemical** 2022, 361, 131706.
2. A. Sasmal, A. Patra, **S. Maity**, S. Pratihar, and S. Sen, "Multiferroic $BiFeO_3$-based hydrophobic polymer composites for polarization rationalization-induced piezo-tribo hybrid energy harvesting and versatile self-powered mechanosensing" **Sustainable Energy Fuels**, 2022,6, 4652-4668.
3. A. Sasmal, P. Maiti, **S. Maity**, S. Sen, and A. Arockiarajan, "Air-plasma discharged PVDF based binary magnetoelectric composite for simultaneously

enhanced energy storage and conversion efficiency". **Applied Physics Letters**, 2023, 122, 083902.

4. A. Sasmal, **S. Maity**, P. Maiti, A. Arockiarajan, S. Sen, "Nano to micrometer range particle size effect on the electrical and piezoelectric energy harvesting performances of hydroxide mediated crosslinked PVDF composites" **Chemical Engineering Journal** 2023,468, 143794
5. S. Sen, **S. Maity**, S. Kundu, "Reduced graphene oxide (rGO) decorated NiO-SnO_2 nanocomposite based sensor towards room temperature diabetic biomarker detection" **Journal of Alloys and Compounds**, 2023, 966(3) 171553.
6. A. Sasmal, **S. Maity**, A. Arockiarajan, S. Sen, "Electroactive properties and piezo-tribo hybrid energy harvesting performances of PVDF-$AlFeO_3$ composites: role of crystal symmetry and agglomeration of fillers" **Dalton Transactions**, 2023,52, 14837-14851.

Conference Papers

1. **S. Maity**, S Sen, “Structural, microstructural and dielectric properties of Sr^{2+} doped $BaTiO_3$” International Virtual Conference on Advances in Functional Materials (AFM 2020), 26-28 August, 2020 at KIIT, Orissa, India.
2. **S. Maity**, S Sen, “Effect of Strontium addition on the crystal structure, grain size and dielectric properties of $BaTiO_3$ ceramics” National Seminar on “Propelling Innovations in Glass and Ceramics for Atmanirbhar Bharat”, Indian Ceramic Society, Kolkata Chapter & CSIR-CGCRI, 11-12 December, 2020, CSIR-CGCRI, Kolkata, WB, India.
3. **S. Maity**, S Sen, “Donor Acceptor co-doped $BaTiO_3$ as an efficient dopant in the output voltage enhancement of PVDF nanogenerator”, International Symposium on Materials of the Millennium: Emerging Trends and Future Prospects, 19-21 November, 2021, Department of Chemistry & Physics, School of Technology, Pandit Deendayal Energy University, Gandhinagar, Gujarat, India.
4. **S. Maity**, S Sen, “Optimization of output power of PVDF nanogenerator through ionic pair doped $BaTiO_3$ as filler”, International Conference on Advanced Materials & Mechanical Characterization (ICAMMC- 2021), Virtual Mode (2-4 December, 2021), Department of Physics and Nanotechnology and Department of Mechanical Engineering, SRM Institute Of Science And Technology in association with the Indian Institute Of Science (IISc), Indian Institute of Technology (IIT) Delhi, IIT Madras, IIT Hyderabad, IIT Indore, Indian Institute Of Metals Chennai Chapter, ASM International Chennai Chapter, Indian Ceramic Society, Indian Physics Association, and American Ceramic Society India Chapter.

Journal of Alloys and Compounds 884 (2021) 161072

Contents lists available at ScienceDirect

Journal of Alloys and Compounds

journal homepage: www.elsevier.com/locate/jalcom

Comprehensive characterization of $Ba_{1-x}Sr_xTiO_3$: Correlation between structural and multifunctional properties

Sourav Maity, Abhishek Sasmal, Shrabanee Sen*

Functional Materials and Devices Division, CSIR – Central Glass and Ceramic Research Institute, Kolkata 700032, West Bengal, India

ARTICLE INFO

Article history:
Received 22 April 2021
Received in revised form 14 June 2021
Accepted 4 July 2021
Available online 6 July 2021

Keywords:
Sr doped $BaTiO_3$
Phase transition
Dielectric
Impedance
Band gap

ABSTRACT

Considering the superior multifunctional performance and beautiful structural tunability, $Ba_{(1-x)}Sr_xTiO_3$ ($0 \le x \le 1$) samples were synthesized in this work by following a conventional solid state reaction technique. The structural, vibrational, optical and dielectric properties of the synthesized materials were characterized extensively throughout the work. Band gap energy of all the materials was evaluated from optical characterizations and correlated with structural properties. Study of leakage characteristics rendered fruitful explanation for electrical properties. At x = 0.4, a structural phase transition from ferroelectric to paraelectric state was observed. All the functional properties were correlated with structural properties. The $Ba_{0.6}Sr_{0.4}TiO_3$ sample showed maximum room temperature dielectric permittivity (~4000 at 1 kHz) with good frequency and thermal stability. The dielectric loss tangent of this composition was reduced to ~0.0098 (at 1 kHz) which was even much lower than that of undoped $BaTiO_3$. The detail temperature dependent dielectric and impedance characteristics of this sample were also evaluated. The activation energy, calculated from dielectric characterizations, was found to be ~1 eV suggesting the governance of doubly ionized oxygen vacancy for conduction and relaxation mechanism.

1. Introduction

$BaTiO_3$ is the most widely studied material which shows excellent ferroelectric and piezoelectric performance [1–4]. This class of materials find their huge applications in different fields of development of technological electric devices such as energy storage, memory and switching device [5,6]. Furthermore, $BaTiO_3$ and $BaTiO_3$ based ceramics show auspicious dielectric properties too, which make these materials useful in different fields like, development of multilayer and voltage-tunable capacitor, electro-optic device, infrared sensors and efficient transducers [7–9]. Owing to its superior piezoelectric properties, now-a-days $BaTiO_3$ based materials are being widely used for the development of piezoelectric actuators for energy harvesting [10]. Furthermore, this material is very suitable as an eco-friendly replacement of lead based piezoelectric material 'lead zirconate titanate (PZT)'. Therefore, the investigation of the electrical properties of this material is of immense interest to the researchers all over the world. Despite being studied widely, researchers are still attracted to study and tune the properties of this material by following several techniques.

Numerous techniques such as alloying this material with other perovskite oxides, cite engineering, domain engineering etc. have been followed till date to tailor the performance of $BaTiO_3$ [11–13]. Due to the capability of perovskite lattice of $BaTiO_3$ to host ions with different size, there is ample scope of addition of different dopant ions to this material deliberately [14]. In this regard, alloying of $BaTiO_3$ with perovskite oxides like, $BiFeO_3$ [15], $KNbO_3$ [13], $BiYbO_3$ [11], $CaTiO_3$ [16], $SrTiO_3$ [17], $Bi_{0.5}Na_{0.5}TiO_3$-$NaNbO_3$ [18], $CaTiO_3$-$BaHfO_3$ [19], $CaTiO_3$-$BaZrO_3$ [20], etc. have already been extensively studied earlier. On the other hand, Ba-site and/or Ti-site doping with Sm^{3+} [21], Sr^{2+} [22], Ca^{2+} [23], Li^{+}-Ho^{3+} [12], Mn^{4+} [24], Ni^{2+} [25], Fe^{2+}-W^{6+} [26], Fe^{3+} [27], Ca^{2+}-Zr^{4+} [14], Ca^{2+}-Zr^{4+}-Mn^{4+} [28], Zr^{4+} [29], Sn^{4+} [29], Hf^{4+} [30], etc. have also been previously studied extensively. Among all these techniques, the studies of Sr^{2+} doped $BaTiO_3$ have drawn much attention in recent years due its robust non-linear dielectric permittivity, small dielectric loss tangent and highly tunable and sensible thermal stability of dielectric permittivity which are very useful during the development of tunable microwave devices [7,8]. Moreover, the structural properties of $BaTiO_3$ strongly depends on the concentration of Sr^{2+} ion doping in Ba^{2+} site which in turn greatly affects its electrical properties [31,32]. Besides, the appearance of ferroelectricity in Sr^{2+} doped $BaTiO_3$ in paraelectric centrosymmetric phase (for a particular composition) has made this material worthy of investigation [33].

* Corresponding author.
E-mail address: shrabanee@cgcri.res.in (S. Sen).

https://doi.org/10.1016/j.jallcom.2021.161072
0925-8388/

Materials Science in Semiconductor Processing 153 (2023) 107128

Contents lists available at ScienceDirect

Materials Science in Semiconductor Processing

journal homepage: www.elsevier.com/locate/mssp

Barium titanate based paraelectric material incorporated Poly(vinylidene fluoride) for biomechanical energy harvesting and self-powered mechanosensing

Sourav Maity, Abhishek Sasmal, Shrabanee Sen *

Functional Materials and Devices Division, CSIR– Central Glass and Ceramic Research Institute, Kolkata, 700032, West Bengal, India

ARTICLE INFO

Keywords:
PVDF
Paraelectric filler
Piezoelectric energy harvesting
Self-powered sensing

ABSTRACT

Being a superior dielectric material exhibiting low loss, x = 0.4 composition of $Ba_{1-x}Sr_xTiO_3$ nanoparticles have been widely used as fillers in poly(vinylidene fluoride) (PVDF) for efficient flexible dielectric and electrical energy storage application. The mentioned composition of the material is also very attractive choice of interest to the researchers due to its ability of ferroelectric to paraelectric phase transition. Due to its paraelectric nature, $Ba_{0.6}Sr_{0.4}TiO_3$ has not been used for mechanical energy harvesting application till date. Here we have used $Ba_{0.6}Sr_{0.4}TiO_3$ particles as fillers in PVDF matrix for efficient mechanical energy harvesting purpose. In the present work, along with the flexible dielectric, ferroelectric and energy storage applications, the developed composite films have been explicitly used for efficient biomechanical energy harvesting, powering small electronic devices and pressure sensing. The fabricated nanogenerator successfully generated a maximum output voltage and output power density of 15 V and 6.75 μW/cm^2 respectively on repeated human finger tapping. The obtained output power has been clearly explained on the basis of polar phase formation and consideration of stress concentration effect.

1. Introduction

With the advancement of modern civilization, the uses of portable electronic devices are growing up day by day in our daily life. Most of the portable electronic devices utilize conventional batteries as their power source. But, considering the limitations of conventional batteries such as, requirement of periodic replacement and environmental pollution during disposal, researchers are focused on the development of energy sources in portable and self-powered manner [1–3]. In this regard, nanogenerators are considered one of the best known technology that can be used for these type of applications. In recent times, harvesting ambient waste mechanical energy into electricity by utilizing nanogenerator devices is one of the most attractive research topics all over the world [3]. For ambient mechanical energy harvesting, piezoelectric and triboelectric nanogenerators are commonly used [3,4]. Researchers are now engaged to develop these devices in flexible manner so that they can be easily used in various real life applications. Therefore, polymer based materials have become the best choice of interest to the researchers. The present work is also focused on developing flexible polymer based composites for nanogenerator application. Both the piezoelectric and triboelectric devices can be prepared by using flexible polymer based composites. But, owing to their special type of device formulation, triboelectric nanogenerators cannot be effectively used in various multifunctional electronic purposes other than mechanical energy harvesting and self-powered sensing. On the other hand, though the piezoelectric nanogenerators exhibit comparatively lower mechanical energy harvesting performance, they can be effectively used in several other multifunctional electronic applications including dielectric, ferroelectric, electrical energy storage and supercapacitor performance [5–7]. Therefore, the present work is mainly focused on the development of polymer based flexible composite films for multifunctional applications including dielectric, ferroelectric, energy storage and mechanical energy harvesting performance. For this purpose, such polymer material is needed to be chosen that, the material exhibits inherent dielectric, ferroelectric and piezoelectric properties. That's why poly(vinylidene fluoride) (PVDF) and its co-polymers are the best choice to fulfil the desired requirements [3]. Therefore, PVDF was chosen as the base polymer matrix in the present study.

PVDF is perhaps the most widely used flexible material for efficient dielectric, ferroelectric, electrical energy storage and mechanical energy

* Corresponding author.
E-mail address: shrabanee@cgcri.res.in (S. Sen).

https://doi.org/10.1016/j.mssp.2022.107128
Received 22 June 2022; Received in revised form 31 August 2022; Accepted 20 September 2022

ACS APPLIED ENERGY MATERIALS

www.acsaem.org Article

Morphotropic Phase Boundary-Assisted Lead-Free $BaTiO_3$/PDMS Composite-Based Hybrid Energy Harvester: A Portable Power Source for Wireless Power Transmission

Sourav Maity, Abhishek Sasmal, Epsita Kar, and Shrabanee Sen*

Cite This: ACS Appl. Energy Mater. 2023, 6, 7052−7064 Read Online

ACCESS | Metrics & More | Article Recommendations | Supporting Information

ABSTRACT: Here, in this present work, the development of a lightweight, flexible hybrid energy harvester using a composite $BaTi_{0.89}Sn_{0.11}O_3$ (BTS)/polydimethylsiloxane (PDMS) has been proposed. A significantly enhanced output performance of hybrid energy harvester (HEH) was achieved by strategically coupling the piezoelectric effect with the triboelectric output. Thus, multiphase coexisted BTS particles as confirmed by the structural and dielectric properties, with a high value of d_{33} coefficient ∼412 pC/N, were used as filler for the functional layer (PDMS) of the device. The hybrid energy harvesting device can harvest a maximum voltage of ∼358 V with an instantaneous power density of 1.08 mW/cm^2 from human finger imparting (force ∼ 100 N, frequency ∼ 4 Hz). The fabricated device harvests energy from handwriting and differentiates fine patterns of different letters by using it as a writing pad. In addition to that, a wireless system utilizing an inductor-based resonant coupling mechanism was developed for wireless power transmission. The easy processability, flexibility, high output performance, and alignment toward a power source for wireless power transmission make the fabricated HEH device a promising candidate for various applications for portable smart flexi-electronics.

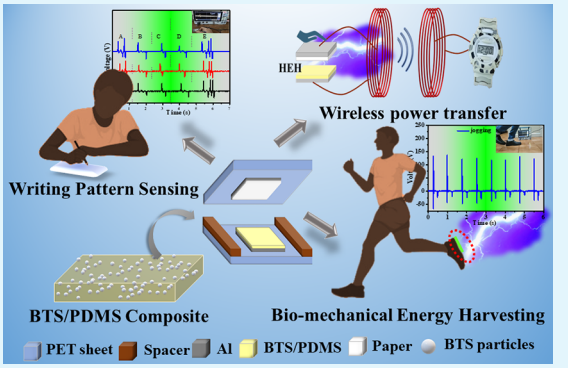

KEYWORDS: *piezoelectric, triboelectric, hybrid, biomechanical energy harvesting, wireless power transfer*

INTRODUCTION

Hydrocarbon-based traditional fossil fuels are the major source of energy for the development of our human civilization. Of late various countries are facing serious scary issues regarding the difference between energy requirements and production. Along with this lack of resources, fossil fuels are highly responsible for climate change and environmental pollution resulting in the serious problem of global warming. To tackle these issues and to meet worldwide energy demand, rigorous research is in progress focusing on renewable and clean energy resources. In this regard, sustainable energy resources like solar, mechanical, wind, chemical, etc., can be a vital solution to make this world eco-friendly.[1−3] Among these, mechanical energy sources are available everywhere in the form of human activities, ocean waves, breezes, etc., and this energy is converted to usable electrical energy through energy harvesters (piezoelectric and triboelectric).

With the advancement in Internet of Things, the requirement for self-powered sensors, medical monitoring devices, and handy electronic devices are in desperate need, which makes low-energy harvesting devices a research worthy topic in recent times. A triboelectric energy harvester (TEH), which works on triboelectric charging and electrostatic induction theory, has gained tremendous attention due to its higher output generation capability than a piezoelectric energy harvester (PEH). In TEH, there are two triboelectric material layers with a difference in their electron affinity, which upon contact with each other generates opposite static charges, whereas PEH transforms mechanical energy into electrical energy with the help of the piezoelectric effect. In this case, due to its intrinsic non-centrosymmetric structure, piezoelectric material generates a charge on the application of mechanical stimuli.

To date, various approaches (doping,[4,5] defect engineering,[6,7] etc., for ceramic materials and ceramic filler inclusion,[8−10] electrospinning,[11,12] etc., for polymer materials) have been utilized to amplify the output properties of PEH. On the other hand, for TEH, output power density, which is a measure of its superiority, mainly depends on the dielectric constant and surface charge density of the triboelectric layers.[13]

Received: March 9, 2023
Accepted: June 15, 2023
Published: June 27, 2023

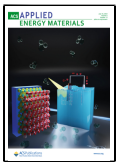

https://doi.org/10.1021/acsaem.3c00635
ACS Appl. Energy Mater. 2023, 6, 7052−7064

Chemical Engineering Journal 474 (2023) 145959

Contents lists available at ScienceDirect

Chemical Engineering Journal

journal homepage: www.elsevier.com/locate/cej

Multiphase coexisted perovskite/PVDF composite derived wearable piezo-tribo hybrid energy harvester for wireless smart applications

Sourav Maity, Epsita Kar, Animesh Kar, Shrabanee Sen *

Functional Materials and Devices Division, CSIR– Central Glass and Ceramic Research Institute, Kolkata 700032, West Bengal, India

ARTICLE INFO

Keywords:
Structural properties
Dielectric properties
Piezoelectric properties
Piezoelectric energy harvester
Hybrid energy harvester
Bio-mechanical energy harvesting

ABSTRACT

With the unprecedented advancement of smart, wearable, and flexible electronics the modern world is advancing towards the Internet of Things (IoT) era. To cope with this ever-increasing demand for smart electronics, a wearable and sustainable energy solution is highly desirable. Thus, the present work reports on a high-performance wearable power source assisted with piezoelectricity coupled triboelectricity based hybrid energy harvesting (HEH) phenomenon. A compatible $(Ba_{0.85}Ca_{0.15})(Ti_{0.90}Hf_{0.10})O_3$ (BCHT) impregnated poly(vinylidene) fluoride (PVDF) composite was used as the functional layer for the HEH device. The excellent piezo nature (d_{33} ~333 pC/N) of the incorporated fillers improves the electromechanical performance of the functional layer of HEH. This sustainable HEH shows excellent energy harvesting performance with an output voltage, current, and power density of ~396 V ± 10 V, ~ 30 μA ± 2 μA, and 1.72 mW/cm^2, respectively. This excellent output performance of HEH is attributed to the synergistic phenomena occurring between the piezoelectric and triboelectric effects inside the device. This HEH shows excellent energy harvesting performance in scavenging bio-mechanical energies. Further, the fabricated HEH was utilized as a smart switch which acts as a source of signal generation for wireless smart home operations. In order to develop a Bluetooth enabled smart home connection, a 2 X 2 array of smart switches were assembled which can efficiently generate signals distinctively to control different equipment of a smart home such as light, fan, mobile charger, etc. Further, the fabricated HEH was used as a self-powered sensor to develop a smart parking system. Thus, with this excellent power generation capability and alignment towards wireless technology enables the designed HEH as the pervasive energy solution for flexible smart electronics.

1. Introduction

Of late with the swift advancement of Internet of Things (IoT), there is an upsurging urgency in the development of sensors as well as different electronic gadgets. To maintain and uplift their lifestyle, human civilization is bending towards electronic gadgets embedded in smart clothes [1,2], smart homes [3–5], smart agriculture [6], health-care monitoring [7], remotely controlling emergency situations [8], etc. consequently, the interaction between human and machines are increasing through human–machine correlated systems day by day. This ever-increasing demand for electronic equipment which act as the building blocks for IoT technology leads to massive power requirement. In today's world, most of this power demand is fulfilled by commercial batteries or grid power cords. As far as commercial batteries are concerned, they possess limitations like charging after a specific time, replacement issues, and the presence of toxic elements. Whereas power from the electric power grid mainly comes from non-renewable energy resources. Owing to high carbon emissions, extensive use of such non-renewable energy sources results in severe detrimental effects of global warming. To cope with these adversities, researchers are concentrating their hubs on the development of self-powered sensor networks, which can operate without any external energy sources [9–11].

In this scenario, several easily accessible mechanical energy sources such as human motion-based bio-mechanical energy, wind energy, ocean wave energy, etc. can act as considerable substitutes. These mechanical energy sources can be used to generate electrical energy using different mechanical energy harvesters, which can be a feasible solution for such increasing demand for portable power supply [11,12]. Depending upon the working mechanism, the most widely used mechanical energy harvesters are named piezoelectric [13–16], triboelectric [1–4], electromagnetic nanogenerators [17], etc. Out of these

* Corresponding author.
E-mail address: shrabanee@cgcri.res.in (S. Sen).

https://doi.org/10.1016/j.cej.2023.145959
Received 7 June 2023; Received in revised form 1 September 2023; Accepted 7 September 2023
Available online 9 September 2023

Sensors & Actuators: B. Chemical 361 (2022) 131706

Contents lists available at ScienceDirect

Sensors and Actuators: B. Chemical

journal homepage: www.elsevier.com/locate/snb

Fabrication of Fe doped reduced graphene oxide (rGO) decorated WO_3 based low temperature ppm level acetone sensor: Unveiling sensing mechanism by impedance spectroscopy

Sovandeb Sen, Sourav Maity, Susmita Kundu *

Functional Materials and Devices Division, CSIR-Central Glass & Ceramic Research Institute, Kolkata 700032, India

ARTICLE INFO

Keywords:
Sol-gel synthesis
Fe doped rGO decorated WO_3
Thin film sensors
ppm level acetone sensing
Low operating temperature
Impedance spectroscopy

ABSTRACT

Chemiresistive MOS-based acetone sensing device is a futuristic pathway for non-invasive diagnosis of diabetes. Although their potential deployment is restricted till now due to lack of selective, low temperature operated ppm-level sensors. In this work, we demonstrated synthesis of iron doped reduced graphene oxide (rGO) decorated WO_3 nanocomposites in a facile, environment friendly wet chemical sol-gel process. The as-synthesized nanocomposites were comprehensively characterized by using different characterization techniques. A maximum ~78% sensing response was obtained for the optimized composition of ~10 wt% Fe doped 3 wt% rGO decorated WO_3 based thin film (thickness ~700 nm) sensor towards ~10 ppm acetone gas. This sensing performance was observed at comparatively low working temperature of ~130 °C with fast response (~20 s) and recovery (~75 s) time. The efficacy of the fabricated sensors was established by their capabilities to sense a very low concentration of ~1 ppm acetone under similar working environment. Further illustration of versatility of the sensors revealed that, the sensors could be able to manifest a repeatable and reproducible sensing performance with prolong stability and superior selectivity for acetone over other interfering gases. The acetone sensing mechanism was illustrated with the help of electron depletion model and impedance spectroscopy study. Impedance spectroscopy quantifies different electrical properties and enlightens the smooth electronic transition mechanism between analyte and sensing material.

1. Introduction

At present, several toxic gases and volatile organic compounds (VOCs) evolved from our different habitual style of living; impart an adverse effect on environment and raise a great concern for human health [1–4]. On the other hand, some of them are generated in human body due to different metabolic processes and recently identified as potential biomarker [5–8] for early stage non-invasive detection of diseases. It has been observed that under certain pathological conditions, in ppm level concentration, acetone is breath biomarker for diabetes [9,10], ammonia for kidney disorder [11,12], hydrogen sulfide for asthma [13,14] etc. In this respect, real time monitoring of these gaseous species in minute concentration is utmost necessity. Generally, analytical technologies involving spectroscopy and chromatography are in use for their detection. Although, they are significantly accurate but seemed to be complicated, non-portable and tedious. In order to avail cost effective and hand-held user-friendly device with good accuracy, reproducibility and fast response/recovery time, several research works are in progress. Worldwide researchers are interested in metal oxide semiconductors (MOSs) based chemiresistive sensors [15–20] because of their excellent reproducibility, non-toxicity and ease of production. However, their practical applications are challenging due to poor selectivity and high temperature of operation. At elevated operating temperature range the sensors consume high power and leads to complication in device fabrication. The temperatures also degrade the sensing behavior through grain coalescence and thus shorten their lifetime. Hence, recent research studies are devoted almost entirely in fabrication of low temperature sensors.

From this viewpoint, WO_3, an n-type metal oxide semiconductor, is considered as one of the significant candidate for gas sensing [21–24]. The superiority of WO_3 prevails due to its different crystalline nanostructures with high oxygen vacancies and excellent electrical conductivity. In spite of that, WO_3 based sensors suffer from drawbacks like poor sensitivity and high working temperature. With this viewpoint,

* Corresponding author.
E-mail addresses: ksusmita4@gmail.com, ksusmita@cgcri.res.in (S. Kundu).

https://doi.org/10.1016/j.snb.2022.131706
Received 12 November 2021; Received in revised form 1 March 2022; Accepted 10 March 2022
Available online 24 March 2022

Sustainable Energy & Fuels

ROYAL SOCIETY OF CHEMISTRY

PAPER

View Article Online
View Journal | View Issue

Cite this: *Sustainable Energy Fuels*, 2022, **6**, 4652

Multiferroic $BiFeO_3$-based hydrophobic polymer composites for polarization rationalization-induced piezo-tribo hybrid energy harvesting and versatile self-powered mechanosensing†

Abhishek Sasmal, [a] Aniket Patra, [b] Sourav Maity, [a] Shewli Pratihar [a] and Shrabanee Sen *[a]

Received 10th July 2022
Accepted 5th September 2022

DOI: 10.1039/d2se00947a

rsc.li/sustainable-energy

$BiFeO_3$-poly(vinylidene fluoride) (BFO-PVDF) and $BiFO_3$-polydimethylsiloxane (BFO-PDMS) piezoelectric composite films have been fabricated herein and used to develop flexible piezoelectric-triboelectric hybrid nanogenerators by forming different combinations with aluminium (Al) electrodes (PVDF-Al, PDMS-Al and PDMS-PVDF) using the contact-separation mode. The dielectric permittivity of both the PVDF- and PDMS-based composites has been found to increase from ~9 and 3.2 for a filler loading of 3 wt% to ~16.6 and 4.7, respectively, for 10 wt% BFO concentration within their matrix. The mechanical stimulus-driven output voltage has also been found to be increased from ~7.5 V and 35 V to ~18 V and 100 V for the respective films. The rational augmentation of the polarization of PVDF and PDMS induced by the gradually increased BFO filler concentration in their matrix, as confirmed from the above-mentioned results, have been found to significantly affect the output performance of the fabricated piezo-tribo hybrid nanogenerators. Among the three types of fabricated hybrid devices, the combination of 10 wt% BFO-incorporated PDMS with an aluminium electrode shows the best output performance both theoretically and experimentally. Hence, this combination has been used to develop a flexible multi-unit hybrid nanogenerator (M-HNG), which shows further performance enhancement (output power density: ~600 μW cm^{-2}). The M-HNG was then used for biomechanical energy harvesting, powering small electronics and different self-powered mechanosensing applications including motion sensing, pressure sensing, water drop counting and phonation monitoring.

1 Introduction

The energy crisis is increasing day by day with the advancement of modern civilization. Therefore, researchers all over the world are attempting to develop new energy sources in various eco-friendly ways. For this purpose, renewable energy such as solar energy, wind energy, geothermal energy, biomass energy, and ocean wave energy have been already developed and are under extensive research all over the world. However, all of these energy sources require a very large area and cost of installation and are not portable in nature. Moreover, due to progress in the modern era, the use of portable electronic devices is increasing very rapidly. Thus, the development of new and green energy sources in a portable and wearable manner is an attractive prospect for researchers. For this purpose, nanogenerators are the best known technology, which can convert ambient irregular mechanical or thermal energy into electricity. Although the power outputs from nanogenerators are low compared to those of renewable energy sources, they are sufficient to drive low-power-consumption electronic devices.

Considering the easy availability of different mechanical energy sources in our surroundings, piezoelectric nanogenerators (discovered in 2006)[1] and triboelectric nanogenerators (discovered in 2012)[2] have drawn much attention due to their unique feature of converting any irregular mechanical vibration into electricity. Therefore, the development of self-powered, portable and wearable electronic skin, smart electronics and healthcare monitoring devices using piezoelectric or triboelectric nanogenerators has become one of the most attractive topics of interest to researchers in recent times. Although the output power from triboelectric nanogenerators is sufficient enough to drive smart electronic devices, piezoelectric nanogenerators suffer from low electrical power output. In this regard, researchers have recently focused on the development of triboelectric nanogenerators by incorporating piezoelectric features into them, so that a higher power

[a]*Functional Materials and Devices Division (FMDD), CSIR-Central Glass & Ceramic Research Institute (CSIR-CGCRI), Kolkata700032, West Bengal, India. E-mail: shrabanee@cgcri.res.in*

[b]*Dipartimento di Fisica, Università della Calabria, Rende 87036, Italy*

† Electronic supplementary information (ESI) available. See https://doi.org/10.1039/d2se00947a

Applied Physics Letters ARTICLE scitation.org/journal/apl

Air-plasma discharged PVDF based binary magnetoelectric composite for simultaneously enhanced energy storage and conversion efficiency

Cite as: Appl. Phys. Lett. **122**, 083902 (2023); doi: 10.1063/5.0137968
Submitted: 7 December 2022 · Accepted: 13 February 2023 ·
Published Online: 22 February 2023

Abhishek Sasmal,[1,a)] Payel Maiti,[1] Sourav Maity,[2] Shrabanee Sen,[2] and A. Arockiarajan[1,3,a)]

AFFILIATIONS

[1]Department of Applied Mechanics, Indian Institute of Technology Madras (IIT Madras), Chennai 600036, India
[2]Functional Materials and Devices Division, CSIR-Central Glass & Ceramic Research Institute, Kolkata 700032, India
[3]Ceramic Technology Group, Center of Excellence in Materials and Manufacturing Futuristic Mobility, Indian Institute of Technology Madras (IIT Madras), Chennai 600036, India

Note: This paper is part of the APL Special Collection on Energy Conversion and Storage in Functional Dielectrics.
[a)]**Authors to whom correspondence should be addressed:** absk102@gmail.com and aarajan@iitm.ac.in

ABSTRACT

Different nanomaterials and their modified forms are very often added into a poly(vinylidene fluoride) (PVDF) matrix in order to improve the energy storage and conversion efficiency of the system. The improvement in energy storage density caused by this secondary nanomaterial addition is most often found to be accompanied by the reduction in energy storage efficiency due to increased amounts of space charges. Here, we show that both the capacitive energy storage density and efficiency can be simultaneously improved by air-plasma discharging on the PVDF based composite system. The energy storage density and efficiency of a 5 wt. % $BiFeO_3$ loaded PVDF film (5BF) have been found to be increased to ~1.55 J/cm^3 and ~73%, respectively, from the values of ~1.36 J/cm^3 and 59% after air-plasma discharging. The dipole rotation caused by air-plasma discharging also helped in improving the mechanical to electrical energy conversion efficiency and magnetoelectric coupling of the studied composite system. Upon similar periodic applied stress, the pristine and air-plasma discharged 5BF film showed ~3 and 9.6 μW/cm^2 of output electrical power density with ~13.5 and 19.2 V of open circuit output voltage, respectively. The air-plasma discharged 5BF film (5BFD) has also shown an excellent magnetoelectric coupling coefficient (α_{33}) of ~35 mV cm^{-1} Oe^{-1} at 1 kHz frequency of fixed AC magnetic field (~3 Oe) and 4 kOe of DC bias field. The simultaneous improvement of all of these parameters of the studied composite system caused by air-plasma discharging proves its multifunctional applicability in a variety of real life applications.

Poly(vinylidene fluoride) (PVDF) is perhaps the best known flexible and cost-effective polymer material which shows excellent ferroelectric and piezoelectric characteristics. Thus, it is being used very widely all over the world for the development of efficient flexible energy storage and mechanical energy harvesting devices for next generation wearable electronics.[1–3] It is worth mentioning that both of the above-mentioned performances can be significantly tuned by the usage of secondary inorganic nanomaterials into a PVDF matrix.[4–6] Though the addition of secondary nanomaterials can improve these performances, the improvement of energy storage density (U_{stored}) of PVDF based binary composite films caused by rational loading of nanomaterials is very often accompanied by the reduction in storage efficiency (η).[5,6] In order to resolve this issue, various surface modification techniques of filler nanomaterials and the modification techniques of filler–polymer interfaces have widely been explored by the researchers all over the world.[6–8]

The decrease in η in PVDF based binary composites along with their increased value of U_{stored} is mainly driven by the increased space charges within the composite films due to the increased amount of filler loading. On the other hand, the existence of space charges within the PVDF based composites have recently been found to show better mechanical energy harvesting activity.[9] Therefore, such technique is needed to be utilized by which the amount of space charges can be reduced without any significant reduction in energy harvesting

Chemical Engineering Journal 468 (2023) 143794

Contents lists available at ScienceDirect

Chemical Engineering Journal

journal homepage: www.elsevier.com/locate/cej

Nano to micrometer range particle size effect on the electrical and piezoelectric energy harvesting performances of hydroxide mediated crosslinked PVDF composites

Abhishek Sasmal [a,b], Sourav Maity [a], Payel Maiti [c], A. Arockiarajan [b,d], Shrabanee Sen [a,*]

[a] Functional Materials and Devices Division, CSIR-Central Glass & Ceramic Research Institute (CSIR-CGCRI), Kolkata, West Bengal 700032, India
[b] Department of Applied Mechanics, Indian Institute of Technology Madras (IIT Madras), Chennai, Tamil Nadu 600036, India
[c] Department of Metallurgical and Materials Engineering, Indian Institute of Technology Kharagpur (IIT Kharagpur), Kharagpur, West Bengal 721302, India
[d] Ceramic Technology Group, Center of Excellence in Materials and Manufacturing Futuristic Mobility, Indian Institute of Technology Madras (IIT Madras), Chennai, Tamil Nadu 600036, India

ARTICLE INFO

Keywords:
Particle size
Hydroxide filler
Hydrogen bonding
PVDF
Piezoelectric energy harvesting
Space charge polarization

ABSTRACT

The polar phase and piezoelectric response of filler-loaded PVDF-based composites very often depend on the interfacial interaction between the filler surface and PVDF dipoles. In this regard, hydrogen bonding interaction has shown a much stronger effect compared to other interactions. In order to induce hydrogen bonding interaction, the filler surface is commonly modified by various modifiers. In the present work, instead of filler surface modification, we introduce $ZnSn(OH)_6$ filler (hydroxide filler having a high number of –OH groups) into the PVDF matrix in order to facilitate the hydrogen bonding interaction. Not only the hydroxide fillers but the effect of wide particle size variation (from nano to micrometer range) into PVDF has also been shown here for the very first time. $ZnSn(OH)_6$ fillers with similar morphology but different sizes have been synthesized by using a variety of techniques and then incorporated into the PVDF matrix. The microstructural defects of the composite films have been found to be gradually increased with the increase in filler size which in turn caused to gradually increase their space charge polarization. Filler, with 915 nm size has shown the best polar phase formation (~84 %), dielectric permittivity (~10 at 1 kHz), and piezoelectric energy harvesting performance (output voltage ~20 V) of the resulting PVDF-based composite and hence has been used for various real-life applications. All of these results have been suitably explained here on the basis of interfacial interaction, microstructural defect, and the mechanism of formation of space charge polarization.

1. Introduction

Owing to their superior ferroelectricity and piezoelectric characteristics among the polymer materials, Poly(vinylidene fluoride) (PVDF) and its copolymers and terpolymers are perhaps the most widely studied materials in present days, especially in the field of flexible energy storage and piezoelectric energy harvesting. Apart from good piezoelectric characteristics, their chirality-induced relaxor ferroelectric behaviour makes them very suitable for capacitive energy storage purposes [1,2]. The output energy storage and energy harvesting activities of PVDF are very often tuned by incorporating suitable filler materials in its matrix through the proper tuning of the interfacial effect [3,4]. Various inorganic fillers like ZnO [5], $BaTiO_3$ [6], $Pb(ZrTi)O_3$ [7], $CsPbBr_3$ [8], SiO_2 [9], $BiFeO_3$ [10], $ZnSnO_3$ [11], etc. have been most widely used for this purpose. The improvement of output dielectric, ferroelectric, energy storage, and energy harvesting activity of PVDF-based composites are mainly governed by two factors. Firstly, the improvement of output performance of the composite system (compared to neat PVDF) may arise due to the enhancement of their polarity caused by the improved dipole orientation resulting from strong interfacial interaction between the filler surfaces and the dipoles of the PVDF matrix [10]. Secondly, the improvement of output performance of the composite system compared to neat PVDF may also occur due to the existence of the inherent ferroelectric and piezoelectric characteristics within the filler materials. Most often it has been found that the first factor renders the most prominent effect in enhancing the output performance of PVDF-based composites [12].

Therefore, researchers have utilized several techniques in order to

* Corresponding author.
E-mail address: shrabanee@cgcri.res.in (S. Sen).

https://doi.org/10.1016/j.cej.2023.143794
Received 24 February 2023; Received in revised form 1 May 2023; Accepted 26 May 2023
Available online 27 May 2023

Journal of Alloys and Compounds 966 (2023) 171553

Contents lists available at ScienceDirect

Journal of Alloys and Compounds

journal homepage: www.elsevier.com/locate/jalcom

Reduced graphene oxide (rGO) decorated NiO-SnO_2 nanocomposite based sensor towards room temperature diabetic biomarker detection

Sovandeb Sen, Sourav Maity, Susmita Kundu *

Functional Materials and Devices Division, CSIR, Central Glass & Ceramic Research Institute, Kolkata 700032, India

ARTICLE INFO

Keywords:
Sol-gel synthesis
Taguchi type sensors
Room temperature sensing
Non-invasive diabetic biomarker
Impedance spectroscopy

ABSTRACT

In the present work, reduced graphene oxide (rGO) decorated NiO-SnO_2 nanocomposites were synthesized by using a facile sol-gel process and their structural (XRD, FTIR, Raman), morphological (BET, FESEM, TEM), and optical (UV-Vis, PL) characterizations were carried out. The as-synthesized NiO-SnO_2 nanocomposite exhibited an enhancement of surface area after the incorporation of rGO and this substantial increment was expected to be beneficial for gas sensing at room temperature. Therefore, Taguchi-type sensors were fabricated and deployed for the detection of VOCs. The optimized sensor containing ~ 3 wt% rGO in NiO-SnO_2 nanocomposite demonstrated an excellent sensing response (R_g/R_a ~ 7.8) towards ~ 10 ppm acetone at room temperature (30 ± 5 °C) with response and recovery time of ~ 10 s and ~ 30 s respectively. It also exhibited good reproducibility and stability over ~ 3 months. Additionally, this sensor selectively detected trace concentration (< 1 ppm) of acetone in exhaled human breath (ethanol present in a healthy person's exhaled breath is insignificant), which is a non-invasive biomarker of diabetes. The sensing performance was analyzed from an electronic transportation point-of-view and consequent band structure modulation. The electrical property of the sensing material was illustrated using impedance spectroscopy to support the sensing mechanism.

1. Introduction

In the twentieth century, fast-track advancements in science and technology have adversely affected human health due to releasing of several toxic gasses and volatile organic compounds (VOCs) [1–8]. However, some VOCs (present in ppb/ppm level in exhaled breath) have recently been considered biomarkers for early-stage non-invasive detection of different diseases. Under certain pathological conditions, detecting a specific exhaled VOC can identify a particular disease [9–12]. The gas sensors are very promising to identify these VOCs, but the real challenge is their trace concentration. Acetone in exhaled breath has been recognized as a biomarker for the non-invasive detection of diabetes [13–16] at a concentration > 1 ppm. Therefore, developing a selective acetone sensor with good sensing response at low concentrations and fast response/recovery time is imperative.

Among various types of metal oxide semiconductors (MOSs) based chemiresistive gas sensors [17,18], SnO_2 is used extensively owing to its chemical stability and good sensitivity [19–22]. Nevertheless, its commercialization has constraints due to high operating temperature, lack of selectivity, low precision, and sluggish response/recovery time. To solve these problems, worldwide researchers are employing different strategies like microstructure modification, functionalization with noble metals [23–25], heterojunction formations [26–28] etc. Combining two semiconductor materials to form a binary heterojunction might be a fruitful successor as it can provide fluent electronic transportation via hole-electron recombination pathways. From this perspective, the introduction of p-type NiO in n-type SnO_2 matrix develops a p-n heterojunction which can effectively attune charge carriers' concentration across heterojunction barrier and thereby elevate sensing performance [29,30], e.g., Zhang et al. [31] demonstrated 500 ppm methane sensing at 330 °C by porous NiO nanosheets decorated with SnO_2, Wei et al. [32] showed NO_2 sensing performance of hydrothermally synthesized SnO_2 nanoneedle-anchored NiO microsphere at 230 °C. These literature studies reveal that NiO-SnO_2 sensors can detect gases efficiently but operate at high working temperatures. However, high temperature operated sensors need more power consumption and grain coalescence leads to a shortening of lifetime, restricting them from commercial applications. Henceforth, researchers are devoted to fabricate sensors operated at ambient temperature [33,34].

It is worth mentioning that enhancement of the surface area of

* Corresponding author.
E-mail addresses: ksusmita4@gmail.com, ksusmita@cgcri.res.in (S. Kundu).

https://doi.org/10.1016/j.jallcom.2023.171553
Received 15 June 2023; Received in revised form 25 July 2023; Accepted 26 July 2023
Available online 28 July 2023

Dalton Transactions

ROYAL SOCIETY OF CHEMISTRY

PAPER

View Article Online
View Journal | View Issue

Cite this: *Dalton Trans.*, 2023, **52**, 14837

Electroactive properties and piezo-tribo hybrid energy harvesting performances of PVDF-$AlFeO_3$ composites: role of crystal symmetry and agglomeration of fillers†

Abhishek Sasmal, [a,b] Sourav Maity,[a] A. Arockiarajan[b,c] and Shrabanee Sen *[a]

Received 7th August 2023,
Accepted 21st September 2023

DOI: 10.1039/d3dt02547k

rsc.li/dalton

Inorganic filler-loaded PVDF-based composites have been very widely used for electrical and energy harvesting applications in recent times. In this regard, the effects of different parameters of fillers like size, shape, chemical states, distribution, functional properties, and many others on the output performance of PVDF have been widely studied. However, the effect of another important parameter, namely the crystal symmetry of the filler, in tuning the energy harvesting performance of PVDF has been rarely explored. Therefore, to explore this fact, here we develop PVDF-based composite films by using two types of $AlFeO_3$ fillers, one with rhombohedral $R\bar{3}c$ symmetry (AFRH) and another with an orthorhombic $Pc2_1n$ structure. Ferrite-based oxides have been chosen here as fillers due to their good dielectric compatibility with PVDF. On the other hand, $AlFeO_3$ has been chosen due to the simplicity of synthesizing it with both centrosymmetric and non-centrosymmetric crystal structures and the scarcity of reports exploring the energy-harvesting performance of $AlFeO_3$-based polymer composites. A significant difference in particle agglomeration has also been observed here between the mentioned two types of $AlFeO_3$ fillers which was mainly due to their specific synthesis conditions. The electroactive properties of PVDF have been observed to be mostly dependent on filler agglomeration. However, the crystal symmetry has shown a strong effect on the piezoelectric energy harvesting performances. As a result of these facts, the piezo-tribo hybrid energy harvesting performance, which depends on both the dielectric permittivity and piezoelectric activity, has been observed to be better for the AFRH5-based hybrid device (AFRH5H) (with ~72 V open circuit voltage and ~45 μW cm^{-2} power density) compared to that of the AFOR5-based hybrid device (AFOR5H). The real-life applications of all the energy harvesting devices have also been demonstrated here.

1. Introduction

Poly(vinylidene fluoride) (PVDF) is perhaps the most widely studied electroactive polymer in the last few years. It can be used in a variety of electroactive applications including flexible dielectrics and ferroelectrics, capacitive energy storage, piezoelectric and triboelectric energy harvesting leading to self-powered mechanosensing, and many others.[1–5] The introduction of various filler materials in the PVDF matrix has been widely reported to enhance its electroactive properties.[6] Along with the improvement of the electro-activity, the included filler material can serve to induce various other properties in the PVDF-based matrix if the filler exhibits specific inherent properties. For example, the introduction of magnetostrictive fillers into PVDF can introduce magnetoelectric performance into the resulting composite by coupling their magnetostrictive nature with the inherent piezoelectricity of the host polymer matrix.[7] Similarly, if the included filler exhibits good optoelectronic properties, it can induce the piezo-phototronic effect in the resulting PVDF-based composites.[8] Due to the excellent piezoelectric property of PVDF, especially in a flexible form, it has gained tremendous attention in recent times in the field of flexible electronics. This excellent inherent property of PVDF has made it possible to couple various other inherent properties of fillers with its piezoelectricity. As a result of this fact, PVDF loaded with different inorganic fillers is being widely used in a variety of real-life applications in recent times including gas sensing,[9]

[a]*Functional Materials and Devices Division, CSIR-Central Glass & Ceramic Research Institute, Kolkata – 700032, India. E-mail: shrabanee@cgcri.res.in*
[b]*Department of Applied Mechanics, Indian Institute of Technology Madras, Chennai – 600036, India*
[c]*Centre of Excellence in Ceramics Technologies for Futuristic Mobility, Indian Institute of Technology Madras (IIT Madras), Chennai, Tamil Nadu – 600036, India*
† Electronic supplementary information (ESI) available. See DOI: https://doi.org/10.1039/d3dt02547k